

PIEZOELECTRIC CERAMICS AND THEIR APPLICATIONS  
IN SMART AEROSPACE STRUCTURES

119520

A THESIS SUBMITTED TO  
THE GRADUATE SCHOOL OF NATURAL AND APPLIED SCIENCES  
OF  
THE MIDDLE EAST TECHNICAL UNIVERSITY

BY

119520

TARKAN ÇALIŞKAN

T.C. YÜKSEKÖĞRETİM KURULU  
DOKÜMANTASYON MERKEZİ

IN PARTIAL FULFILLMENT OF THE REQUIREMENTS FOR THE DEGREE OF  
DOCTOR OF PHILOSOPHY

IN

THE DEPARTMENT OF AERONAUTICAL ENGINEERING

SEPTEMBER 2002

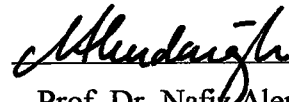
Approval of the Graduate School of Natural and Applied Sciences



Prof. Dr. Tayfur Öztürk

Director

I certify that this thesis satisfies all the requirements as a thesis for the degree of  
Doctor of Philosophy



Prof. Dr. Nafiz Alemdaroğlu

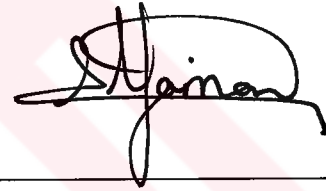
Head of Department

This is to certify that we have read this thesis and that in our opinion it is fully  
adequate, in scope and quality, as a thesis for the degree of Doctor of Philosophy



Dr. Volkan Nalbantoğlu

Co-Supervisor



Prof. Dr. Yavuz Yaman

Supervisor

Examining Committee Members

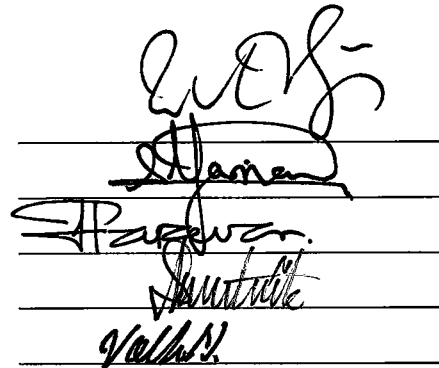
Prof. Dr. Mehmet A. Akgün

Prof. Dr. Yavuz Yaman

Assoc. Prof. Dr. Levend Parnas

Assoc. Prof. Dr. Kenan Y. Şanlıtürk

Dr. Volkan Nalbantoğlu



## **ABSTRACT**

### **PIEZOELECTRIC CERAMICS AND THEIR APPLICATIONS IN SMART AEROSPACE STRUCTURES**

Çalışkan, Tarkan

Ph.D., Department of Aeronautical Engineering

Supervisor: Prof. Dr. Yavuz Yaman

Co-Supervisor: Dr. Volkan Nalbantoğlu

September 2002, 279 pages

This thesis investigates some applications of smart structures in aerospace engineering. The smart structures considered are finite and flat aluminum beam-like and plate-like structures with surface bonded PZT (Lead-Zirconate-Titanate) patches. The smart structures are studied in cantilevered configuration.

The thesis gives the theoretical and experimental studies conducted on the smart structures with particular attention given to the vibration control aspects.

In the determination of the structural models of the smart structures, the finite element package program ANSYS® (v.5.6) is used. During the analysis and the design of the vibration controllers both finite element approach and the experimental system identification techniques are utilized.

The thesis first determines the structural models of smart beam-like and plate-like structures. By using those models, the study extensively analyzes the static and dynamic behaviour of the smart structures by considering the effects of the smart elements like the size, placement and the actuation voltages of the PZT patches in detail.

The study then proceeds to obtain the models of PID and  $H_\infty$  vibration controllers, which are intended to be used in the suppression of the vibrations of the smart structures due to their first two flexural modes. The closed-loop control characteristics of the smart structures are studied. It was shown that the designed controllers ensure robust performance of the system in the presence of uncertainties.

Keywords: Smart structure, finite element modeling, system identification, vibration control, PID and  $H_\infty$  controllers, robust performance

## ÖZ

### PIEZOELEKTRİK SERAMİKLER VE AKILLI UZAY YAPILARINDAKİ UYGULAMARI

Çalışkan, Tarkan

Doktora, Havacılık Mühendisliği Bölümü

Tez Yöneticisi: Prof. Dr. Yavuz Yaman

Ortak Tez Yöneticisi: Dr. Volkan Nalbantoğlu

Eylül 2002, 279 sayfa

Bu tez akıllı yapıların havacılık ve uzay mühendisliğindeki bazı uygulamalarını araştırmaktadır. Çalışmada kullanılan akıllı yapılar, düz, sonlu kiriş ve plak geometrisindeki alüminyum yapılardan ve bunların yüzeylerine yapıştırılan PZT (Lead-Zirconate-Titanate) yamalardan oluşturulmuştur. Çalışmada kullanılan akıllı yapılar bir kenarı tutturulmuş diğer kenarları serbest olarak alınmıştır.

Bu tezde, akıllı yapıların özellikle titreşim kontrolüne yönelik teorik ve deneysel çalışmaları sunulmaktadır.

Çalışmada yapısal modellemeler ANSYS® (sürüm 5.6) yazılımının kullanıldığı sonlu elemanlar tekniği ile yapılmıştır. Denetçi tasarım ve analizi esnasında sonlu elemanlar yaklaşımı ve deneysel system tanımlama teknikleri kullanılmıştır.

Bu tezde öncelikle akıllı kiriş ve plakların yapısal modellemeleri yapılmıştır. Elde edilen modeller, akıllı elamanların boyut, yerleşim ve piezoelektrik uyarı gerilimi gibi etkileri düşünülerek, akıllı yapıların statik ve dinamik davranışlarının detaylı analizlerinde kullanılmıştır.

Çalışmanın daha sonraki aşamasında, akıllı yapıların ilk iki frekansından dolayı oluşan titreşimlerinin sönümlenmesinde kullanılacak olan PID ve  $H_{\infty}$  denetçileri tasarımına yönelinmiş ve akıllı yapıların kapalı döngü karakteristikleri araştırılmıştır. Tasarlanan denetçilerin belirsizliklerin varlığında gürbüz performans özelliğine sahip olduğu gösterilmiştir.

Anahtar sözcükler: Akıllı yapılar, sonlu elemanlar modellemesi, titreşim, system modeli tanımlama, aktif titreşim kontrolü, gürbüz performans.

This work is dedicated to my mother Leyla, and my brother Kenan alıřkan, who have given me the most generous support that any parents could possibly give.

Bu alıřma, bana bir ailenin saęlayabileceęi en geniř desteęi saęlayan annem Leyla ve aęabeyim Kenan alıřkan'a ithaf edilmiřtir.

## ACKNOWLEDGMENTS

The author wishes to acknowledge his indebtedness to his supervisor, Prof. Dr. Yavuz Yaman for the guidance, supervision, encouragement and patience given during this long process.

The author also wishes to express his gratitude to his co-supervisor, Dr. Volkan Nalbantođlu for his close support of sharing the difficulties of the work.

The author would like to thank Assoc. Prof. Dr. Levend Parnas for his support, constructive criticism and advices.

Thanks are also extended to the president of Sensor Technologies limited, Dr. Eswar Prasad and his staff, for their close cooperation.

The author expresses his sincere appreciation to his uncles, Ali and Celal Yüncü, for their support and understanding throughout his long-term endeavors.

This thesis is supported by Turkish State Planning Organization project, METU-AFP-03-13-DPT-98K-122630 ‘Establishment of Aeronautical Engineering Research and Development Center’ and NATO/Research and Technology Organization/Applied Vehicle Technology Panel Project, T-121 ‘Application of Smart Materials in the Vibration Control of Aeronautical Structures’. The support given is gratefully acknowledged.



## TABLE OF CONTENTS

ABSTRACT.....	iii
ÖZ.....	v
ACKNOWLEDGEMENTS.....	viii
TABLE OF CONTENTS.....	ix
LISTS OF TABLES.....	xv
LIST OF FIGURES.....	xvi
LIST OF SYMBOLS.....	xxviii
CHAPTER	
1 INTRODUCTION.....	1
1.1 Background to the Study.....	1
1.2 Contents and Scope of this Study.....	3
1.3 The Limitations of the Study.....	5
2 LITERATURE SURVEY.....	7
2.1 Introduction.....	7
2.2 Smart Structures with Different Smart Materials.....	7
2.3 Smart Structures with Piezoceramic Actuators.....	13
2.3.1 Structural Modeling of Smart Structures.....	16
2.3.2 Active Vibration Control Strategies Applied to the Smart Structures.....	21
2.4 The Applications of Smart Structures in Active Aeroelastic Control.....	26
2.5 Structural Health Monitoring By Using Smart Structures.....	29
3. MODELING AND DESIGN OF SMART STRUCTURES.....	35
3.1 Introduction.....	35

3.2	Theory of Piezoelectricity .....	36
3.2.1	The Analytical Modeling of the Piezoelectric Materials .....	36
3.2.2	Finite Element Modeling of Piezoelectric Materials....	40
3.2.3	The Limitations in the Finite Element Modeling of Piezoceramic Materials .....	44
3.3	The Finite Element Modeling and Design of Smart Structures.	46
3.4	Finite Element Modeling of Smart Beam-Like Structure.....	46
3.4.1	The Influences of the Element Type Selection.....	49
3.4.2	The Effects of Polarization and Placement of Piezoelectric Patches .....	56
3.4.3	Effects of Piezoelectric Patch Position .....	59
3.4.4	The Influence of the Piezoelectric Patch Size.....	60
3.4.5	Effects of the Actuation Voltage Variation and the Maximum Admissible Piezoelectric Actuation Value...	61
3.4.6	The Influence of the Transverse and Normal Stresses ..	63
3.4.7	The Influence of the Placement of the Patches on the Natural Frequencies of the Smart Beam .....	67
3.4.8	Sensor Placement.....	68
3.5	Finite Element Modeling of the Smart Fin .....	69
3.5.1	The Effects of Piezoelectric Patch Position.....	72
3.5.2	The Influence of the Piezoelectric Patch Size.....	75
3.5.3	The Maximum Admissible Piezoelectric Actuation Value.....	76
3.5.4	The Influence of the Transverse and Normal Stresses.....	76
3.5.5	Placement of Strain Gage Sensors.....	78
3.6	Conclusions.....	81
4	THEORY OF ACTIVE VIBRATION CONTROL FOR SMART STRUCTURES.....	83

4.1	Introduction.....	83
4.2	Finite Element Based System Modeling Technique for Smart Structures: State-Space Representation.....	84
4.2.1	The Formulation in Nodal Coordinates.....	85
4.2.2	The Formulation in Modal Coordinates.....	88
4.2.3	The Determination of the Spatial Model: Spatial Reduction of the Models.....	93
4.2.4	The System Model Reduction: The Reduced Order Models.....	98
4.3	Control Design Techniques.....	99
4.3.1	Series Compensators: PID Compensator.....	102
4.3.2	The Analysis and Synthesis of Smart Structures for Robust Control.....	104
4.3.2.1	The Classical Robust Stability Analysis of Control Systems.....	105
4.3.2.2	The Classical Robust Performance Analysis of Closed-loop Systems.....	109
4.3.2.3	Modern Robust Stability Analysis of Control Systems: Uncertainty and Robustness.....	110
4.3.2.4	Modern Robust Performance Analysis of Control Systems.....	114
4.3.3	$H_\infty$ Optimal Control.....	116
4.4	Conclusions.....	118
5	SYSTEM IDENTIFICATION TECHNIQUES FOR SMART STRUCTURES.....	120
5.1	Introduction.....	120
5.2	Test Articles.....	121
5.2.1	The Smart Beam.....	123
5.2.2	Smart Fin.....	124
5.3	Nonparametric Identification for the Smart Structures.....	125

5.3.1	Data Acquisition.....	126
5.3.1.1	The Smart Beam Experiments.....	127
5.3.1.2	The Smart Fin Experiments.....	131
5.3.2	Signal Processing.....	134
5.3.2.1	Nonparametric Identification for the Smart Beam.....	138
5.3.2.2	Nonparametric Identification for the Smart Fin.....	143
5.4	Frequency Domain Least Squares Curve Fitting Technique.....	145
5.4.1	System Identification for the Smart Beam.....	149
5.4.2	System Identification for the Smart Fin.....	151
5.5	The Validation of the Finite Element Models of Smart Structures.....	153
5.6	The Response of the Smart Beam by Assumed-Mode Summation Method.....	154
5.7	The Tuning of the Finite Element Model of the Smart Beam...	157
5.7.1	The Influences of The Hysteresis Effect: LVDT Tests on the smart Beam.....	158
5.7.2	The Influences of the Cable Masses on the Response of the Smart Beam.....	161
5.7.3	The Influences of the Damping on the Response of the Smart Beam.....	165
5.8	Overview of Finite Element and System Identification Techniques Applied to Smart Structures.....	173
5.9	Conclusions.....	175
6	DESIGN FOR ACTIVE VIBRATION CONTROL OF SMART STRUCTURES.....	178
6.1	Introduction.....	178
6.2	The Series Compensator Design for the Vibration Control of the Smart Beam: PID Compensators.....	179
6.2.1	Proportional Compensator.....	180

6.2.2	Proportional and Integral Controller.....	182
6.2.3	Proportional and Derivative Compensator.....	185
6.2.4	Proportional, Integral and Derivative Compensators....	188
6.2.5	Robustness Analysis of PID Compensators.....	197
6.2.5.1	The Classical Frequency Response Analysis of the PID-Compensated System.....	197
6.2.5.2	The Modern Frequency Response Analysis of the PID-Compensated System.....	204
6.3	$H_{\infty}$ Optimal Control design for the Smart Beam.....	209
6.3.1	The Robustness analysis of the $H_{\infty}$ -Controlled System for the Smart Beam.....	213
6.3.2	The Comparison of the PID Compensator and the $H_{\infty}$ Controller for the Smart Beam.....	214
6.4	Vibration Control of the Smart Fin.....	219
6.4.1	$H_{\infty}$ Optimal Controller Design for the smart fin.....	219
6.4.2	Robustness Analysis of the $H_{\infty}$ Controller.....	224
6.5	The Real time implementation of $H_{\infty}$ Controller the Smart Beam.....	225
6.6	Conclusions.....	227
7	CONCLUSIONS.....	230
7.1	General Conclusions.....	230
7.2	Recommendations for Future Work.....	234
	REFERENCES.....	235
	APPENDICES	
A.	PIEZOELECTRIC, DIELECTRIC AND MATERIAL PROPERTIES OF BM500 PZTPATCHES.....	254
A.1.	Dielectric Constant, $[\epsilon]^s$ (Relative Permittivity).....	255
A.2.	Piezoelectric Stress Constant Matrix.....	255
A.3.	Stiffness Matrix .....	256
A.4	Curie Temperature:.....	256

B	THE EFFECTS OF ELEMENT TYPE SELECTION ON THE NATURAL FREQUENCIES.....	257
C	THE COMPUTER CODES FOR SYSTEM IDENTIFICATION.	259
C.1	Nonparametric Identification.....	259
C.2	The Least Square Curve fitting.....	264
D	THE COMPUTER CODE USED IN REAL TIME IMPLEMENTATION OF $H_{\infty}$ CONTROLLER.....	265
D-1	The $H_{\infty}$ CONTROLLER.....	265
D-2	The Computer code.....	266
VITA.....		279



## LIST OF TABLES

### TABLE

3.1	The influences of the element type selection on the natural frequencies of the smart beam (Legend of Figure 3.7).....	54
3.2.	The influence of the piezoelectric patches on the natural frequencies of the passive beam-like structure.....	67
4.1	The interrelations of the finite element based system modeling techniques for active vibration control of smart structures.....	93
5.1.	The tests conducted for the nonparametric identification of smart beam.....	140
5.2.	The comparison of the theoretical and experimental frequencies of the smart beam.....	153
5.3.	The comparison of the theoretical and experimental frequencies of the smart fin.....	154
5.4.	The properties of BM500 type piezoelectric patches .....	155
5.5	The comparison of the frequencies of the smart beam.....	156
5.6.	The comparison of the finite element and experimental frequencies of the smart beam.....	165
5.7.	The comparison of the parameters of the smart beam.....	173
5.8.	The system modeling techniques for smart structures.....	174
6.1.	The comparison of the effectiveness of the PID-compensator and $H_{\infty}$ controller on the vibration control of the smart beam.....	216
6.2.	The comparison of the attenuation levels achieved by the $H_{\infty}$ controller designed for the smart fin .....	223

## LIST OF FIGURES

### FIGURES

- 3.1. The piezoelectric patch and the positive sign convention used in the study..... 37
- 3.2. The comparison of the geometry, node locations and coordinate system for the element having coupled magnetic, thermal, electric and structural capability in ANSYS® (v.5.6)..... 41
- a. PLANE13
- b. SOLID5
- c. SOLID98
- 3.3. The deformation of a single C-C-C-C piezoelectric crystal at 300V ( $\Delta T=0$ ) ..... 43
- a. Side view
- b. Top view
- 3.4. The first two theoretical natural frequencies and mode shapes of a single C-C-C-C piezoelectric crystal. .... 43
- 3.5. The piezoelectric actuation of a bimorph cantilevered smart beam... 48
- a. The configuration and the polarization of the piezoelectric actuators
- b.  $V_o < V_i$ , top actuators in tension, bottom actuators in compression
- c.  $V_o > V_i$ , top actuators in compression, bottom actuators in tension



3.6	Elements used in the modeling of the passive portion of the smart beam.....	50
	a. SOLID45	
	b. SOLID95	
	c. SHELL93	
3.7.	The comparison of the effects of the element type selection on the deformation of the smart beam by piezoelectric actuation at 300V (model1: SOLID5 and SOLID45, model 2: SOLID5and SOLID95, model 3: SOLID5 and SHELL93).....	52
3.8.	The comparison of the influence of the actuator thickness on the response of the two theoretical models .....	53
3.9.	The geometry and the finite element model of the smart beam (solid-solid hybrid model).....	56
	a. Top view	
	b. Side view	
3.10.	The comparison of the effects of the actuator polarization and the electric field on the deformation of the smart beam by, .....	58
	a. Piezoelectric actuation of -300 V ( $V_i=0, V_o=300$ V)	
	b. Piezoelectric actuation of 300V ( $V_i=0, V_o=-300$ V)	
3.11.	The unimorph smart beam .....	59
	a. Side view of the finite element model	
	b. The deformation of the model at 300V actuation ( $V_i=0, V_o=300$ V)	
3.12.	The effects of the patch position on the response of the smart beam..	60
3.13.	The influences of the patch size variation on the response of the smart beam-like structure. ....	61
3.14.	The influences of the piezoelectric actuation voltage variation .....	62
	a. The displacement response of the smart beam	
	b. The Von-Mises stresses developed on the piezoelectric actuators	

3.15.	The influences of the voltage variation on the maximum stresses developed on the passive portion of the smart beam .....	64
3.16.	The influence of the piezoelectric patch size on the maximum transverse normal and shear stress developed on the passive portion of the smart beam .....	65
3.17.	The influence of the piezoelectric patch thickness on the maximum transverse normal and shear stress developed on the passive portion of the smart beam.....	66
3.18.	The first two natural frequencies and mode shapes of the smart beam.....	68
3.19.	The position and the configuration of the strain gages on the smart beam.....	69
3.20.	The finite element model of the smart fin.....	70
	a. Top view	
	b. Side view	
3.21.	The theoretical response of the smart fin to various piezoelectric actuation values.....	71
	a. Bending by 300V	
	b. Twisting by +300V and -300V	
3.22.	The first two theoretical mode shapes of the smart fin .....	71
	a. The first mode ( $f_1=14.963$ Hz)	
	b. The second mode ( $f_2=45.737$ Hz)	
3.23.	The effects of the patch position on the response of the smart fin. ...	73
	a. Bending (by 300V)	
	b. Twisting (by +300V and -300V)	
3.24.	The influences of the patch position on the first two theoretical natural frequencies of the smart fin.....	74
	a. First natural frequency	
	b. Second natural frequency	

3.25.	The comparison of the effects of the patch size variation on the right tip displacement response of the smart fin.....	75
3.26.	The effect of the piezoelectric actuation voltage on the Von Mises stresses developed within the piezoelectric patches of the smart fin...	76
3.27.	The comparison of the effects of the voltage variation on the maximum stresses developed in the passive portion of the smart fin due to the piezoelectric bending .....	77
	a. The normal stresses	
	b. The shearing stresses	
3.28	The comparison of the effects of the voltage variation on the maximum stresses developed on the passive portion of the smart fin due to the piezoelectric actuation twisting actuation .....	78
	a. The normal stresses	
	b. The shearing stresses	
3.29.	The placement and the configuration of the strain gages and piezoelectric patches on the smart fin .....	79
3.30.	The comparison of the response of the smart fin (location (1): $\epsilon_x$ , locations (2) and (3): $\epsilon_y$ ).....	80
	a. Bending by 300V	
	b. Twisting +300V and -300V	
4.1	The spatial model reduction algorithm used in the study.....	97
4.2.	The block diagram representation of typical open-loop and closed-loop controllers.....	101
	a. Open-loop system	
	b. Closed-loop system	
4.3.	The block diagram representation of PID controller applied to smart structures.....	104
4.4.	The plots used in Nyquist stability theorem (open-loop system: The smart beam model of [77]).....	107

4.5.	The algorithm used for the classical robustness analysis for the PID controllers designed in the study ( $f_l$ : The lower frequency of interest, $f_h$ : The upper frequency of interest).....	111
4.6.	The descriptions of the modeling uncertainties used in the thesis.....	112
	a. Additive uncertainty, $\tilde{P} = P + \Delta W_2$	
	b. Multiplicative uncertainty, $\tilde{P} = (1 + \Delta W_2)P$	
4.7.	The algorithm used for the modern robustness analysis of the PID controllers designed in the study (for additive uncertainties).....	115
4.8.	The closed loop architecture of the $H_\infty$ controller.....	117
4.9.	The modeling of the uncertainties in $H_\infty$ controller .....	117
5.1.	The smart beam used in the thesis.....	123
5.2.	The smart fin used in the thesis.....	124
5.3.	The configuration of the strain gages on the smart structures and the schematic representation of the Wheatstone bridge used in the thesis	
	a. The placement of the strain gages on the smart beam.....	127
	b. The half Wheatstone bridge connection of the strain gages	
5.4.	The data acquisition for smart beam.....	129
	a. The data acquisition system	
	b. The connection of the piezoelectric actuators to a bipolar power amplifier	
5.5.	The block diagram of the computer program used during the data acquisition.....	130
5.6.	Sample time domain representations of the signals measured during the tests for the smart beam.....	130
	a. A portion of the chirp signal for 10s	
	b. An output of the smart beam for 120s	
5.7.	The data acquisition for smart fin.....	132
	a. The data acquisition system	
	b. The connection of the piezoelectric actuators to a bipolar power amplifier	

5.8.	Sample time domain representations of the signals measured during the tests for the smart fin .....	133
	a. A portion of the chirp signal for 10s	
	b. An output of the smart fin for 30s (strain gages at location (1))	
	c. An output of the smart fin for 30s (strain gages at location (2))	
5.9.	The block diagram of the computer program used in the multi channel data acquisition for smart fin.....	134
5.10.	The algorithm for the method of spectral estimation of nonparametric identification used in the thesis.....	139
5.11.	Sample power spectral densities of the input and the output of the smart beam.....	141
	a. The spectral density of the input, $S_{xx}$	
	b. The spectral density of the output, $S_{yy}$	
	c. The cross spectral density, $S_{xy}$	
5.12.	Bode plot of a sample experimental transfer function of the smart beam .....	142
5.13.	The influences of the overlap averaging number on the experimental transfer function of the smart beam.....	142
	a. Magnitude	
	b. Phase	
5.14.	The comparison of the influences of the different measurements on the experimental transfer function of the smart beam.....	143
5.15.	Sample power spectral densities of the input and the output of the smart fin (dotted: Strain gage measurements at location (1). solid: Strain gage measurements at location (2)).....	144
	a. The spectral density of the input, $S_{xx}$	
	b. The spectral density of the output, $S_{yy}$	
	c. The cross spectral density, $S_{xy}$	

5.16.	The bode plots of sample experimental transfer functions of the smart fin (dotted: Strain gage measurements at location (1), solid: Strain gage measurements at location (2)).....	145
5.17.	The algorithm used for the application of frequency domain least squares curve fitting technique to the smart structure.....	148
5.18.	The influences of the order selection for the identified models of the smart beam.....	150
	a. Magnitude	
	b. Phase	
5.19	The comparison of the frequency responses of the experimental and 6 <sup>th</sup> order identified models (Strain gage measurements at location (1)).....	151
5.20	The comparison of the experimental and 6 <sup>th</sup> order identified models of the smart fin (Strain gage measurements at location (2)).....	152
5.21	The comparison of the responses of the smart beam (the mid-tip displacement response with $\zeta_1=7.730910^{-2}$ , $\zeta_2=1.778410^{-2}$ and $\zeta_3=7.060510^{-3}$ ).....	156
5.22	The data acquisition of the LVDT tests for the smart beam.....	159
5.23	The hysteresis nonlinear behavior of the smart beam: The samples of the LVDT tests conducted.....	160
5.24	The positive sign convention and the orientation of the point mass element, MASS21 used in the thesis.....	161
5.25.	The smart beam and the configuration of the mass elements on the finite element model of the smart beam ( $m_1=6\text{gr}$ , $m_2=4\text{gr}$ , $m_3=1\text{gr}$ )...	162
	a. Smart beam	
	b. The finite element model of the smart beam (93 MASS21, 420 SOLID45, 72 SOLID5 elements)	

5.26.	The effects of the cable mass on the response of the smart beam (the response at the strain gage location of $x_s = 97\text{mm}$ , $y_s = 25.5\text{mm}$ , the theoretical model with damping values of $\gamma = 2 \times 10^{-4}$ and $\beta = 1 \times 10^{-4}$ ).	164
	a. Magnitude	
	b. Phase	
5.27.	The comparison of the strain and displacement transfer functions of the smart beam at the strain gage location ( $\gamma = 2 \times 10^{-4}$ and $\beta = 2 \times 10^{-4}$ ).	167
5.28.	The first three theoretical mode shapes of the smart beam (flexural displacement).....	168
5.29.	The first three theoretical mode shapes of the smart beam (longitudinal strain evaluated on aluminum beam, $\epsilon_x$ ).....	168
5.30.	The algorithm used in the determination of the tuned theoretical response of the smart beam.....	170
5.31.	The transfer functions of the smart beam obtained in the thesis (the response at the strain gage location of $x_s = 97\text{mm}$ , $y_s = 25.5\text{mm}$ ).....	171
	a. Displacement transfer function, $G_\delta(s)$	
	b. Displacement-strain transfer function, $G_\tau(s)$	
	c. Strain transfer function, $G_\theta(s)$	
5.32.	The comparison of the theoretical, tuned theoretical and experimental transfer functions of the smart beam.....	172
	a. Magnitude	
	b. Phase	
6.1.	The block diagram representation of the P-compensated system for the smart beam.....	180
6.2.	The comparison of the effects of the proportional gain on the P-compensated system for the smart beam.....	181
6.3.	The block diagram representation of the PI-compensated system for the smart beam.....	182

6.4.	The comparison of the effects of the proportional gain $K_p$ on the PI-compensated system for the smart beam.....	183
6.5.	The comparison of the effects of the proportional gain $K_i$ on the PI-compensated system for the smart beam.....	185
6.6.	The block diagram architecture of the PD-compensated system for the smart beam.....	185
6.7.	The comparison of the effects of the proportional gain $K_p$ on the PD-compensated system for the smart beam.....	187
6.8.	The comparison of the effects of the proportional gain $K_d$ on the PD-compensated system for the smart beam.....	187
6.9.	The block diagram architecture of the PID-compensated system for the smart beam.....	188
6.10.	The comparison of the effects of the proportional gain $K_p$ on the PID-controlled system for the smart beam.....	189
6.11.	The comparison of the effects of the proportional gain $K_i$ on the PID-compensated system for the smart beam.....	190
6.12.	The comparison of the effects of the proportional gain $K_d$ on the PID-compensated system for the smart beam.....	191
6.13.	The comparison of the open and closed-loop frequency responses for the beam (PI: $K_p=30$ , $K_i=70$ ), (PD: $K_p=30$ , $K_d=3/1000$ ), (PID: $K_p=30$ , $K_i=70$ , $K_d=3/1000$ ).....	192
6.14.	The comparison of the frequency responses of the series compensators used in the thesis (P: $K_p=30$ ), PI: $K_p=30$ , $K_i=70$ ), (PD: $K_p=30$ , $K_d=3/1000$ ) and (PID: ( $K_p=30$ , $K_i=70$ , $K_d=3/1000$ )).....	193
6.15.	The comparison of the time domain responses of PID-compensated systems.....	194
	a. PID compensator with the gain of $K_p=50$ , $K_i=60$ , and $K_d=3/1000$	
	b. PID compensator with the gain of $K_p=150$ , $K_i=150$ , $K_d=3/1000$ )	
	c. PID compensator having the gain of $K_p=300$ , $K_i=300$ , and $K_d=5/1000$	



6.16.	The influences of the gain variations on the relative error for the PID-compensated system models of the smart beam.....	196
	Compensator 1: $K_p = 50$ , $K_i = 60$ and $K_d = 3/1000$ ,	
	Compensator 2: $K_p = 100$ , $K_i = 100$ and $K_d = 3/1000$ ,	
	Compensator 3: $K_p = 300$ , $K_i = 300$ and $K_d = 5/1000$	
6.17.	The influences of the higher frequencies on the PID-controlled system for the smart beam ( $K_p=100$ , $K_i=150$ , $K_d=1/1000$ ).....	198
	a. The comparison of the open and closed-loop frequency response	
	b. The comparison of the open and closed-loop impulse response	
6.18.	The comparison of the loop gains of the identified and the theoretical models of the smart beam for PID compensator with the gain values of $K_p=50$ , $K_i = 60$ , and $K_d = 3/1000$ .....	200
6.19.	The comparison of the loop gains of the identified and the theoretical models of the smart beam for PID compensator with the gain values of $K_p=300$ , $K_i = 300$ and $K_d = 5/1000$ .....	201
6.20.	The comparison of the effects of the gain variations on the sensitivity function of the PID- compensated systems for the smart beam.....	202
	a. $K_p = 50$ , $K_i = 60$ and $K_d = 3/1000$	
	b. $K_p = 300$ , $K_i = 300$ and $K_d = 5/1000$	
6.21.	The comparison of the effects of the gain variations on the complementary sensitivity functions of the PID- controlled systems for the smart beam.....	203
	a. $K_p = 50$ , $K_i = 60$ and $K_d = 3/1000$	
	b. $K_p = 300$ , $K_i = 300$ and $K_d = 5/1000$	
6.22.	The block diagram representation of the perturbed model for the smart beam.....	205
6.23.	The comparison of the performance weight $W_1(s)$ and the open-loop transfer function of the smart beam.....	206

6.24.	The comparison of the additive weight $W_2(s)$ and the open-loop transfer function of the smart beam.....	206
6.25.	The effects of the gain variations on the robust stability and performance of the PID-compensated system model for the smart beam (compensator 1: $K_p=50$ , $K_i=60$ and $K_d=3/1000$ , compensator 2: $K_p=150$ , $K_i=150$ and $K_d=3/1000$ , compensator3: $K_p=200$ , $K_i=200$ and $K_d=3/1000$ , compensator 4: $K_p=300$ , $K_i=300$ and $K_d=5/1000$ )... a. Robust stability: $ W_2(s)T(s) $ b. Robust performance: $ W_1(s)S(s)  +  W_2(s)T(s) $	208
6.26.	The $H_\infty$ control formulation for the smart beam.....	210
6.27.	The 6 <sup>th</sup> order $H_\infty$ controller designed for the smart beam.....	212
6.28.	The comparison of the open and closed-loop responses of $H_\infty$ - controlled system for the smart beam.....	213
6.29.	The structured singular value ( $\mu$ ) of the closed-loop system for the smart beam..... a. Robust performance b. Robust stability c. Nominal Performance	214
6.30.	The comparison of the responses of the PID-compensator with the gains of $K_p=0.5$ , $K_i=9.6$ and $K_d = 1/1000$ and the optimal $H_\infty$ controller for the smart beam.....	215
6.31.	The comparison of the open and closed-loop responses of the smart beam.....	216
6.32.	The robust stability and performance tests for the PID-compensated model with the gains of $K_p=0.5$ , $K_i=9.6$ and $K_d = 1/1000$ for the smart beam..... a. Robust stability: $ W_{add}(s)T(s) $ b. Robust performance: $ W_{per}(s)S(s)  +  W_{add}(s)T(s) $	218

6.33.	The block diagram formulation of the $H_\infty$ control problem for the smart fin.....	220
6.34.	The comparison of the performance weight $W_{per}$ and the experimental smart fin transfer functions at the strain gage locations	221
	a. Location (1)	
	b. Location (2)	
6.35.	The comparison of the performance weight $W_{add}$ and the experimental smart fin transfer functions at the strain gage locations	221
	a. Location (1)	
	b. Location (2)	
6.36.	The comparison of the open and closed loop responses of the smart fin for the strain gage at location (1).....	222
6.37.	The comparison of the open and closed loop responses of the smart fin for strain gage location (2).....	222
6.38.	The comparison of the frequency responses of the 12 <sup>th</sup> order $H_\infty$ controllers applied to the strain gage locations.....	223
6.39.	Structural singular value ( $\mu$ ) of the closed loop system of the $H_\infty$ controller designed for the smart fin.....	224
	a. Robust performance	
	b. Robust stability	
	c. Nominal performance	
6.40.	The block diagram representation of the experimental setup for active vibration control of the smart beam.....	225
6.41.	The comparison of the open and closed responses of the $H_\infty$ controlled smart beam (response to the initial tip displacement of 2 cm).....	227

## LIST OF SYMBOLS

$W(s)_{\text{add}}$	Additive uncertainty weight
$\xi_i$	Applied electric field
$\omega$	Circular frequency
$T(s)$	Complementary sensitivity
$S$	Compliance
$\gamma$	Constant mass matrix multiplier for Rayleigh damping model
$\beta$	Constant stiffness matrix multiplier for Rayleigh damping model
$K(s)$	Controller transfer function
$[D_o]$	Damping matrix of a finite element model
$K_d$	Derivative gain constant associated with the PID compensators
$[\Lambda]$	Diagonal matrix formed by formed by the natural frequencies
$\epsilon$	Dielectric constant of the piezoelectric material
$u, v, w$	Displacements along $x, y, z$ coordinates
$[C_o]$	Elastic moduli
$D_i$	Electric flux density vector
$\psi$	Electric scalar potential function
$e(s)$	error signal used in series compensator design
$q_m$	Generalized modal coordinate
$q, \dot{q}, \ddot{q}$	Generalized displacement, velocity and acceleration
$I$	Identity
$g(t)$	Impulse response function
$[B]$	Input matrix
$K_i$	Integral gain constant associated with the PID compensators
$S$	Laplace variable

$L(s)$	Loop gain
$F_l$	Lower linear fractional transformation
$[M]$	Mass matrix of a finite element model
$[\Psi]$	Mass normalized modal matrix
$S_{ii}$	Maximum normal stresses component along $i$ direction ( $i=x,y,z$ )
$S_{ij}$	Maximum shearing stress component on $ij$ plane ( $i, j=x, y, z$ )
$\zeta$	Modal damping ratio or loss factor
$P(s)$	Nominal system model of the smart structures
$\Delta(s)$	Norm bounded uncertainty block
$k$	Number of actuators
$p$	Number of degrees of freedom associated with each node
$p$	Number of degrees of freedoms
$m$	Number of modes contributing the response
$t$	Number of reduced degrees of freedoms such that $t < p$
$n$	number of reduced nodes in the finite element model
$r$	Number of sensor on the smart structure
$y(s)$	Output
$[C]$	Output matrix
$W(s)_{per}$	Performance weight
$\tilde{P}(s)$	Perturbed model of the nominal system $P(s)$
$u$	Piezoelectric actuation value
$e$	Piezoelectric stress constant
$S_{xx}(\omega)$	Power spectral density function of input
$S_{yy}(\omega)$	Power spectral density function of output signal
$S_{xy}(\omega)$	Cross power spectral density function
$x_1, x_2, x_3$	Principal coordinate system
$K_p$	Proportional gain constant associated with the PID compensators

$\alpha(s)$	Receptance
$x,y,z$	Rectangular coordinate system
$R(s)$	Reference command
$\omega_r$	$r^{\text{th}}$ natural frequency of the structure
$S(s)$	Sensitivity
$N(s)$	Sensor signal
$x$	State vector
$[K]$	Stiffness matrix of a finite element model
$\mu$	Structured singular values for a system
$[A]$	System matrix
$\Delta T$	Temperature difference
$\alpha$	Thermal expansion coefficients
$[F]$	Unit piezoelectric voltage generalized force transformation matrix
$V_i$	Voltage applied to the inner electrodes of piezoelectric actuators
$V_o$	Voltage applied to the outer electrodes of piezoelectric actuators
	$\partial/\partial t$
$\cdot\cdot$	$\partial^2/\partial t^2$
$  $	Absolute value

$\{$	Column matrix
$]$	Square matrix
$   \ \infty$	Infinity norm of a signal or system
$\bar{\sigma}(M)$	Maximum singular value of matrix M

Other parameters are clearly defined wherever applicable.

## **CHAPTER 1**

### **INTRODUCTION**

#### **1.1 Background to the study**

Recent developments in the field of piezoelectric materials have encouraged many researchers to work in the field of smart structures. The smart structure can be defined as the structure that can sense external disturbance and respond to that with active control in real time to maintain mission requirements. Smart structures consist of highly distributed active devices and processor networks. The active devices are primarily sensors and actuators either embedded or attached to an existing passive structure.

In the smart materials technologies, the developments are realized by two approaches. While the first approach concentrates on the improvements in the smart materials for their suitability as sensors and actuators at the molecular level, the second approach involves the applications of the known smart materials in the design of the smart structures.

The smart structures are expected to provide new and innovative capabilities in military and civilian aerospace applications. This is done by specific applications in terms of system functional enhancements such as, active vibration control and/or health monitoring. These functional enhancements also lead to overall benefits like reduced life cycle costs.

The future aircrafts are expected to take advantages from smart materials and smart structures technologies. These structures may include aircraft wing, rotorcraft blades, air inlets and engine nozzles. Some of the expected benefits include enhancing the performance by manipulating the lift and drag, by changing the shape of the control surface or by affecting flow conditions over the lifting surface producing twist in aircraft wings or rotor blades, reducing the vibrations such as panel flutter, tail buffet and blade vortex interaction.

The role of smart structures for space systems indicates the direct applicability of the smart structures technologies to resolve many of the current and future space challenges. Its value to the space program can be described as providing design options to the direct applicability which leads to the rapid insertation of the smart structures into flight experiments and space missions.

The use of smart structures offers a potential for precision shape control and correction in the deformation of space structures. The structures and systems considered for space applications are usually flexible, deployable, lightweight and remotely operated, which makes them expensive and their maintenance difficult. These structures are constantly exposed to the harsh environment of space that subjects them to low gravity, vacuum, thermal cycling, large temperature gradients, radiation, impact from space particles. These conditions results in undesired shape deformation and uncontrolled vibrations which can adversely affects the performance and shorten the useful life of the structure.

The applications of smart materials in aerospace structures technologies are not limited to shape and active vibration control. The use of the smart structures in health monitoring is very popular among the researchers working in smart structure technologies. The high frequency vibration signature based techniques for example, are considered to be very effective in detecting the very minor damage that may grow or exist in the structure on which piezoelectric material is mounted.



Depending on the characteristics of the smart structures involved and the expected operating conditions, the selection of the sensors and actuators vary considerably. The most promising smart materials that can be considered in smart structures technologies include piezoelectric materials, electrostrictive materials, magnetostrictive materials, shape memory alloys, optical fibers, electrorheological fluids and magnetorheological fluids.

## **1.2. Contents and Scope of this Study**

Aerospace structures are complex assemblages of structural components that are mainly in the geometry of beams, plates and shells. These components operate under severe and uncertain service environments and require high reliability and performance.

The objectives of this thesis are first to present the structural dynamics of smart structures that are composed of aluminum beam-like and plate-like structures modeled in cantilevered configuration with surface bonded piezoelectric patches. Active vibration control strategies applied to smart structures are also developed.

Since the determination of the accurate model of the system that is as close as possible to the realistic smart structure is an essential step in the design of a high performance control system, the thesis focuses on accurate representation of the electromechanical coupling inherent to the piezoelectric materials and their effects on the smart structures. In the determination of these models both theoretical and experimental approaches are considered and the factors influencing the accuracy of the theoretical models are investigated.

Based on the theoretical and experimental models, the thesis examines PID and  $H_\infty$  control design techniques for their effectiveness in active vibration control of the

smart structures with special attention paid to the modelling of the uncertainties and robustness issues.

Chapter 2 gives the detailed survey of the trends in the applications of the smart structures. In this chapter, the specific assumptions in the modeling, design and the active vibration control of smart structures are given. Although the focus is basically on the modeling and the active vibration control of the smart structures having piezoelectric patches, other types of smart structures and the work on the active aeroelastic control and structural health monitoring are also explained for completeness.

Chapter 3 investigates the effectiveness of the finite element method in the modeling and the design of smart structures. In the theoretical analysis, the commercial finite element program ANSYS® (v.5.6) is used to model the smart structures. During the development of the smart structure models, parametric design capabilities are considered. By using these models, the study gives the effects of the piezoceramic patches on the static response and explains the influences of actuator size, placement and determines the maximum piezoelectric actuation value to ensure the integrity of the piezoelectric patches. The effects of the element type selection are also dealt with.

Chapter 4 describes the finite element based system modeling techniques for the determination of the state-space representation of the smart structures. It explains the robust control design and analysis applied to the smart structures and serves to combine the methods of structural dynamics and the control design and analysis techniques.

Chapter 5 explains the experimental work and system identification algorithms applied to determine the experimental models of the smart structures. This chapter details on the determination of the factors influencing the accuracy of the theoretical models obtained through the applications of the methods developed in

Chapters 3 and 4. Furthermore, the methods to tune the accuracy of the theoretical models by using the experimentally identified models of the smart structures are also described in detail.

The design of the robust active vibration controllers that effectively suppresses the vibrations of the smart structures due to the first two flexural modes are presented in Chapter 6. In this thesis, the vibration suppression is achieved by the application of robust PID and  $H_\infty$  controllers. The effectiveness of the controllers in the vibration suppression and the modeling of the uncertainties are also compared. The real time implementation of the  $H_\infty$  controller designed for the smart beam is also demonstrated.

Finally, the general conclusions drawn from the study are given in Chapter 7.

### **1.3 The Limitations of the Study**

The flexible smart structures considered in the study consist of finite aluminum beam-like and plate-like structures modeled in cantilevered configurations with surface bonded piezoelectric patches.

The thesis extensively uses finite element software ANSYS<sup>®</sup> (v.5.6) to model the smart structures.

The theoretical calculations of the study are performed within the linear range of the elasticity and piezoelectricity. Since the smart structures are not designed to withstand large temperature gradients, the effects of possible thermal loads on the response of the piezoelectric materials are excluded in the theoretical analyses conducted. Furthermore, the damping of the piezoelectric patches are ignored during the theoretical calculations

The smart structures involved in this thesis have non-clustered, complex poles with small real parts. Hence, the influences of the heavy damping and the cluster of modes are not included in the analyses.

It is further assumed that the possible incompatibilities between the theoretical and the true models due to changes in the system parameters arising from the time dependence of the components, aging, damages or environmental changes and unmodeled nonlinearities can be represented in terms of the model uncertainties.



## **CHAPTER 2**

### **LITERATURE SURVEY**

#### **2.1. Introduction**

This chapter aims to detail the advances and trends for the smart engineering structures. The first section gives the literature survey about the smart structures with different smart materials. The second section describes the work on the modeling and the active vibration control strategies with piezoelectric patches. Finally for the completeness of the smart structures studies, the work done on the active aeroelastic control and structural health monitoring by using smart structures are also explained.

#### **2.2. Smart Structures with Different Smart Materials**

Advanced smart materials are being developed for sensors and actuators to be integrated with smart structures. Typical smart structure sensors include fiber optics and piezoelectric ceramics and polymers. Either surface bonded or embedded sensors can be used in discrete or distributed locations to measure the performance of the system. The typical actuators used in the smart materials technologies structure include shape memory alloys (SMAs), piezoelectric ceramics, piezoelectric polymers (PVDF), electrostrictive and magnetostrictive(MS)

and electro-rheological (ER) and magneto-rheological (MR) fluids.

Depending on the mission requirements the actuator devices can be dynamic for vibration suppression or static for shape control.

Clauser first published the idea of producing smart materials and structures in a broad and conceptual form in 1968 [1]. By 1970's the idea had received an international interest and many researchers published articles on the smart materials and structures. Crowe and Sater [2] presented a paper for the evaluation of the materials together with sensing and actuation techniques, design, and control algorithms, fabrication and test of the smart structures.

In 1999, Koko *et al.* [3] presented the detailed survey on the sensor and actuator materials that are currently used in smart structures technologies. In this work, the advantages and disadvantages of the smart materials were discussed.

Shape memory alloys (SMA) like Nitinol, are the materials that undergo shape changes due to phase transformation associated with the application of the thermal field. When a shape memory alloy is deformed in its low temperature condition and the stresses are removed, it regains its original shape by phase transformation to its high temperature condition when heated.

The ability of the SMA to recover its preset shape upon heating can provide a low mass and power mechanism. The utilization of SMAs allow large force generation with low power requirements. Furthermore, SMAs have high resistance to corrosion and dust. SMA devices can be controlled such that very smooth maneuvers can be performed. The use of SMA as actuators for shape correction in space industries provide several advantages [4]. However, SMA can only be suited for low frequency (0-10Hz) and low precision applications. The SMAs also exhibits complex constitutive behavior with large hysteresis [3,5].

Zhong and Mei [6] investigated thermal deflection and random response of composite plates with embedded SMA fibers. They presented a finite element based modeling technique to account for the nonlinearities in the geometry and the material properties. By using their modeling technique, they numerically demonstrated that SMA can effectively be used to reduce the thermal deflection of composite plates at elevated temperature.

Jiang *et al.*[7] studied the feasibility of SMA actuator to control the dynamic response of a cantilevered beam. They proposed experimentally that the SMAs can be used to shift the fundamental frequency up by 7%. In another study, by using appropriate SMA elements available in NASTRAN<sup>®</sup> Jiang *et al.* [8] presented the method of optimal design and dynamic analysis of shape memory alloy strips. They showed that the damping capacity of the smart beam increases with the size of the SMA but the damping rate slows down.

Electrostrictive materials (Lead-Magnesium Niobate, PMN) differ from the piezoelectric materials in their response to the electric field. While the response of the piezoelectric materials to the applied electric field are proportional, that of electrostrictive materials is proportional to the square of the applied field. Therefore, electrostrictive materials always produce positive displacements regardless of the polarity. That is the electrostrictive materials always produce compression under the action of electric field. Although the electro restrictive materials exhibit quicker response time and hysteresis compared to piezoelectric materials, the electrostrictive materials are more sensitive to temperature variation compared to piezoelectric materials [2,3].

Magnetostrictive materials like Terfenol-D are the materials that experience mechanical stress when subjected to magnetic field or vice versa. The main advantage of these materials is the high force capability. The main disadvantages include its brittleness, heavy weight and high hysteresis in their response to the

applied magnetic field. Furthermore, only the compression components are available [2,3].

Electro-rheological fluids (ER) like Alumino-silicate in Paraffin oil, are a class of controllable fluids that respond to an electric field with radically change in its rheological (viscosity, elasticity and plasticity) behavior. The essential characteristic of these fluids is their ability to reversibly change from free-flowing linear viscous fluid to semi solids with controllable yield strength.

Electrorheological fluids are the suspensions of fine dielectric particles in insulating carrier media, typically nonconducting oils which exhibit dramatic and reversible changes in rheological behavior in their response to the electric field [3,9]. When they are subjected to electric field they turn into a gel-like solid as the electric field is removed, they quickly to liquid state (typically within 0.0001 to 0.001 second). Furthermore, the gelling phenomenon is proportional to the electric field strength, so by changing the electric field any rheological state from the liquid to solid or vice versa can be smoothly or instantly reached. A smart structure based upon electrorheological fluid [10,11] can be considered for suppressing vibrations in a smart beam with the proper selection and the combination of actuator materials such as piezoceramic actuators. Various hybrid sensor and actuator systems can be designed. Hybrid smart structures consisting of several different classes can easily be configured for vibration suppression applications [12]. The electrorheological fluids however, are suitable in low frequency applications and not suitable for low temperature applications. Furthermore, its highly nonlinear behavior in the formulation of the reciprocal relations and very high voltage requirements (2-10kV, [3]) limits their use in the smart structures technologies.

Magneto-rheological Fluids (MR) like are similar to ER. These materials respond to an applied magnetic field with the change in its rheological behavior. These materials have extremely higher densities and lower voltage requirements than ER. Similar to ER, these materials exhibit highly nonlinear response to the applied field.



Wereley *et al.* [13,14] involved analytical and experimental studies for the determination of the active vibration control studies using magnetorheological fluids and elastomeric materials. The magnetorheological fluids combine the flexibility for altering structural response with low voltage requirements within wide range of temperatures. Similar to the electrorheological fluids, they exhibit highly nonlinear response [3,14]. The density of MR is larger than that of ER which may bring additive mass effect on a smart structure.

Optical fibers such as Fabry-Perot and Bragg grating, offer very high accuracy, temperature stability and very short response time. Despite those advantages their delicacy in handling, bulky control systems and cost make them unpopular. The fiber optic materials are suitable only for sensing.

Sensors based on fiberoptic technology offer distinct advantages over conventional sensors in the synthesis of smart structures [2,3]. In 1999, the applications of fiber optic materials were briefly overviewed by Mrad *et al.* [15]. The bulky control units and their fragility in handling limit their use in smart structures technologies.

The strong piezoelectric effect is observed in PVDF (Polyvinylidene Fluoride) polymer was discovered in 1969. This material is characterized by such properties as flexibility, ruggedness, softness, light weight [16]. PVDF differs from crystalline piezoelectric materials in a way that PVDF has the common properties of polymers such as, flexibility, softness and low acoustic impedance. PVDF are available in sheets of thin films and inexpensive to produce, easy to cut or shape in complex configurations. Unlike PZT type of transducers, they can easily be integrated into an existing structure. However, PVDF foil sensors and actuators are unattractive for most of the engineering applications because of their very low passive stiffness value and their extreme sensitivity to environmental conditions, such as humidity and especially temperature. [3,16].

In 1985, Bailey and Hubbard [17] initiated the research on the application of the smart structures in active vibration control by using PVDF as an actuator for the smart beam.

A vibration damper by using thin layer of PVDF film was designed by Burke and Hubbard [18]. In their model, the transducer was bonded on a complete side of the structure and an accelerometer on opposite side close to the root. They showed both theoretically and experimentally that the spatial variation of the polarization profile allows the simultaneous control of all modes or selective control of modal subsets. In their analysis, however, there were many issues that still need to be resolved before the application appropriate control strategies. Specifically, for the piezoelectric material (PVDF), electromechanical coupling had to be included in the development of the reciprocal relations between the sensor and the actuator. In another study, Burke and Hubbard developed formulation to the vibration control of thin elastic Kirchoff plates by using PVDF foil sensors and actuators [19]. This work is the extension of their theory developed for Euler-Bernoulli beams [18]. In their analysis by including electromechanical coupling of the transducers, they also proposed the design criteria that guarantee active vibration control of such plates. This leads to the design flexibility that the active vibration control is a function of the spatial variation of the transducer weighting function.

Starting from four basic design parameters in the dynamic analysis of fully anisotropic plates, Lee [20] developed a theory that is capable of incorporating the piezoelectric properties of the PVDF laminates completely into the classical laminate theory. The laminates were mounted symmetrically to both up and bottom sides of existing structure as collocated sensor and actuator pairs. The reciprocal relations between sensor and actuator laminates have been derived.

The formulation provided in [20] was used to define the new control design strategy for active vibration control of anisotropic plates by Miller *et al.* [21]. They briefly explained the destabilizing effect of the presence of anisotropy. The strategy is

based on the second method of Lyapunov. Asymptotic stability is shown to be ensured as long as the three design criteria proposed are met. The design criteria are: (1) for each piezoelectric actuator above the composite midplane there exists corresponding identically polarized sensor laminate also located above midplane (2) a linear control law governing each conjugate actuator/sensor pair is enforced such that the input to each actuator is proportional and opposite in sign to current induced by the corresponding sensor (3) for each conjugate pair above the midplane there exists an identical pair below the midplane. This work, however, includes purely theoretical considerations. The numerical and experimental verifications were left for future studies.

### **2.3 Smart Structures with Piezoceramic Actuators**

More than a century has passed since Pierre Curie first discovered the piezoelectric effect in 1880. This effect is now a branch of crystal physics, and this owes much to Woldemar Voigt, who did pioneering studies many years ago [16,22]. The piezoelectricity also finds wide application in the electrical and mechanical and aerospace engineering field. Jones *et al.* [22] explained the characteristics and the applications of the currently available piezoelectric materials in engineering.

Piezoelectricity is a fundamental process of electromechanical interaction and is representative of linear coupling in energy conversion. The discovery of the piezoelectricity dates back the 19<sup>th</sup> century in which the piezoelectric effect is found in ferroelectric materials. These materials are known in the form of ceramics and anisotropic crystals (like quartz, barium titanate, lead zirconate titanate). These materials are currently used in many transducers such as accelerometers and pressure transducers. Among the piezoelectric crystalline the most widely used one is PZT (Lead-Zirconate-Titanate).

A piezoelectric transducer when subjected to an input voltage changes its dimensions that in turn generates a force exerted on adjacent structural member (direct piezoelectric effect). In contrast, a piezoelectric transducer generates voltage due to an applied strain (converse piezoelectric effect).

The major advantage of piezoelectric transducers are realized when they are used as collocated sensor and actuator pair for active vibration control. The use of highly distributed piezoceramics combines tunability with quick response time over wide frequency range together with high stiffness, relative temperature insensitivity and relatively low hysteresis. The piezoelectric actuators are easily controlled due to their near linear response with applied voltage

The piezoceramic actuators are found in a variety of forms like thin plates, multiplayer stacks and injection molded shapes. Many actuator configurations are reliable and have low cost. The tubular actuators containing multilayer PZT stacks offer many advantages in linear positioning and pointing applications. Thin plate type actuators are also a standard product that has been utilized in many active noise and vibration suppression applications. The piezoceramic actuators exhibit excellent response to the applied electric field over very large range of frequencies. The sensing quality of the piezoelectric patches, however are limited to moderate frequency applications (typically >10 Hz).

Piezoelectric actuator can be used beneficially for the applications in active vibration control of smart structures. The piezoelectric actuators can easily be controlled due to their nearly linear response with the actuation voltage. Although piezoelectric actuators are expected to find many applications in smart structures technologies, precise material characterization is particularly difficult due to various possible mechanical compliances and thermal management situations. Therefore, the configurations and the performances of the piezoelectric actuators for their use in the design of smart structures must be examined [22].

Steel *et al.* [23] worked on the theoretical treatment of the quasistatic response of a thin piezoelectric PZT plate. In their work, the features dealt with include electrical poling, hysteresis behavior, transverse and longitudinal mechanical strain of the bimorph crystal subjected to electric field. An experimental work was also conducted to validate the modeling technique.

The realization of smart structures with active components greatly depends on the reliability of its integral components. In this terminology, the reliability is the probability of which an actuator will perform its specified function under a set of external function for a specified time. Among the three components, sensors, actuators and the passive structure, the functionality of the actuators is anticipated to be limiting factor governing the design and life of the structure. Yoshikawa *et al.* [24] discussed the reliability of piezoelectric actuators by considering the stress and strain requirements and material issues of various piezoceramic materials. Uchino [25] approached the piezoelectric actuator reliability issues from a slightly different point of view. He considered the reliability in three categories such as the reliability of the ceramic material, reliability of the device design like Yoshikawa, as well as the actuator drive technique with a particular focus on the multilayer actuators. He further established the possibilities to improve the reliability of the actuators for their future wide commercialization. In 1995 a comparative study [26], was released for the identifications of the recent developments in the ceramic actuators among USA, Japan and Europe. The aim of the work was to investigate the trends in the development, design, production techniques and their applications mainly on the smart structures technologies. Various piezoelectric materials, driving techniques and their performances were illustrated.

For many years, piezoelectric and electrostrictive ceramic materials have been considered for use as solid state actuators for small displacements and precise mechanical movement devices. Many applications like loudspeakers and noise canceling devices however, require actuators with larger displacements. Hence novel techniques of strain amplification are required to satisfy these demands for

high displacement actuation [22]. The novel piezoelectric bending actuators include RAINBOW<sup>®</sup> (standing for Reduced And Internally Biased Oxide Wafer)[27], CERAMBOW<sup>®</sup> (stands for CERAMic Oxide Wafer) and THUNDER<sup>®</sup> (standing for Thin layer Driver and sensor) [28].

Kugel *et al.* [27-29] discussed the linear and nonlinear performances of the shear and bending mode actuators in three papers. A year later, Kugel *et al.* [30] presented a comparative analysis to study the dynamical performances of these actuators in terms of the mechanical displacement, electrical impedance and mechanical quality factor for piezoelectric bending mode actuators. The aim of the work was to gain knowledge of the dynamic behavior of the bending and shear mode actuators including hysteresis and the change in the slope of the displacement versus actuation. They further estimated that because of the nonlinearities the resonant frequency of the bending mode depends on the driving field. Near [31] summarized general design guidelines for the selection and the use of piezoelectric actuators for active vibration control. In this work, several examples of the current actuators are given for each actuator case. In one of the recent studies, Mukherjee *et al.* [32] showed the nonlinear effects in piezoelectric ceramics. They detailed that the properties for various piezoceramic materials were depend on applied fields such as, AC and DC and stress.

### **2.3.1 Structural Modeling of Smart Structures**

The determination of an accurate model is an essential step in the design of a high performance active vibration control. This section briefly explains the work done in the modeling of the coupled response of the piezoelectric patches and the interactive response of the smart structures. This section also outlines the analytical, numerical and experimental techniques for the development of the system model suitable for the design of active vibration control.

One of the first studies of smart structures, was performed by Swiger and Forward [33] in 1981. They conducted a theoretical and experimental study that involved an electronic damper implementing a system of electromechanical transducers made from PZT as the elements of the electronic feedback loops to control the mechanical vibration of an end supported mast. The structure consisted of a hollow fiberglass cylinder called an omni antenna mast, and the concept was to apply electronic damping with surface mounted piezoelectric sensors and actuators. The outputs of the sensors were amplified and appropriately processed in time to provide inputs for the actuators positioned symmetrically on the cylindrical surface. By the early 1980's various papers have appeared on the modeling and active vibration control on various combinations of PZT, passive structures and control algorithms.

By using the variational principles in piezoelectricity, Dökmeci presented theories of vibrations of coated thermopiezoelectric laminae in two papers [34,35]. In his first paper, he constructed a system of the three dimensional approximate governing equations of coated laminate for the case when the mechanical displacement, electric potential and temperature fields vary linearly across laminae thickness. In his formulation, he also included the effects of elastic stiffness and the interaction between layers of laminae and its electrodes. Later, Dökmeci removed the apparent restriction of his first paper by including the equations of nonlinear piezoelectricity in his formulation. Dökmeci presented novel formulations in the linear and nonlinear descriptions of the piezoelectric laminae. However, his work is confined by the formulations and not supported by neither numerical nor experimental results.

The utilization of discrete piezoelectric actuators has been shown to be a viable concept for vibration suppression by Crawley and de Luis [36]. They proposed an analytical solution for a static case including various actuator geometries by considering perfect and finite bonding layers for surface bonded piezoelectric actuators. Because the interlaminar layer is considered to be negligibly small, in the case of embedded actuators, perfect bonding case was considered alone. At each

case, the static models derived, were compared. These static models were then integrated into the dynamic models of a cantilevered Euler-Bernoulli beam. The validity of the theoretical models was also confirmed by the experimental results. They concluded that the discrete piezoelectric actuators could be considered in vibration suppression of some modes of vibration of flexible structures. However, the exclusion of the mass of the piezoelectric actuators in their modeling technique limits the use of the modeling to the actuators that are very thin or having very low densities.

The vibration excitation of thin plates by using piezoelectric patches has been analyzed by Dimitridis and Fuller [37,38]. This work is the extension of the one-dimensional theory proposed in [36] to two-dimension. In this work, however the directional properties of the actuator patches that are essentially anisotropic and electromechanical coupling effects are ignored. Furthermore, similar to Crawley's approximation [36] their model is limited to the actuators made from thin patches of negligible mass. They have derived static formulation by following the observations of Crawley and applied their models to the dynamic model of the structure. Pan *et al.* [39] improved the static modeling technique of Crawley [36] by incorporating the dynamics of the smart beam. This work however, is limited to simply supported beams. Furthermore, no experimental justifications were presented to confirm the validity of their modeling technique. Kwak *et al.* [40] worked first on the reduction of the three dimensional piezoelectric theory to one dimensional one in order to comply with the Euler-Bernoulli beam. They then presented the formulation of flexible multibody systems.

Kalaycıoğlu [41] developed a new dynamic modeling technique for the vibration excitation and suppression of plate structures with surface bonded PZT actuators by relaxing the apparent restriction on the thickness and the density of the actuator patches of the previous work. The modal analysis based technique incorporates geometrical and mechanical properties of the actuator with the structures on which they mounted.



A wave modeling technique for a dynamic system consisting of smart beam in cantilevered configuration with surface bonded PZT actuators and PVDF sensors, was introduced by Koma and Vukovich [42]. In this work, they first described the transverse vibration of the beam with respect to the traveling waves and then incorporating the wave model of the piezoelectric actuators and piezoelectric sensors, a state-space model of the integrated smart structure was derived. The modeling technique however, did not include the three dimensional electromechanical coupling of piezoelectric actuators and sensors instead, one dimensional coupling equation was incorporated to their modeling. Furthermore, the experimental validation of the modeling technique was not included.

In the analysis of piezoelectric structural elements, many finite element models have been proposed since early 70's. But, they are mainly devoted to the design of ultrasonic transducers [43,44]. By the late 80's the interests have been directed towards the application of smart materials and structures [45-49]. The application of the finite element modeling techniques in the smart materials technologies is in continuous growth during the last decade. Hence it gains a certain evolution so that some piezoelectric elements have become available in a commercial finite element programs like ANSYS® [50].

Wang [51] worked on the effectiveness of the finite element code ANSYS® in the modeling of the smart structures. In this work, the finite element method was proven to be a very effective tool for the analysis of the smart structures. Unlike the analytical techniques, the method offers fully coupled thermo-mechanical-electrical analysis of the smart structures. This allows the prediction of the reciprocal relations between the sensors and actuators. This allowance makes the development of the closed loop controller for active vibration control possible, Prasad *et al.* [52].

The truss type structures are widely used in aerospace engineering. The space station main structural backbone for example, is a three dimensional space truss. The design and analysis of a smart truss structure has of particular importance. The

smart trusses consist of active and passive strut members that are commonly made of tubular electrostrictive (PMN) or piezoceramic actuators (PZT). Utku [53] proposed the applications of finite element technique in the modeling and design of the smart trusses.

The design and analysis of smart trusses currently used in space structures, were summarized by Bravo *et al.* [54]. In this work, by using IDEAS<sup>®</sup> software they also presented a finite element based modeling technique for the design and analysis of smart trusses. Since the commercial program IDEAS<sup>®</sup> do not contain elements suitable for the analysis of electro mechanical coupling, these effects were simulated by the thermal deformations of the rod elements. In this work, the experimental justification of the modeling was not included. This assumption may lead to improper calculation of the deformation of the smart truss.

Hydraulic actuators are commonly used as high force linear actuators. The disadvantages of these actuators like toxic fluids and flammability limits their use in aerospace actuators. The utilization of solid state piezoelectric (PZT) or electroresistive materials (PMN) combines the high force capability with no toxic and flammability problems. In one of the recent research studies for the actuator design, the inchworm actuator (the actuator that uses small incremental steps to reach large displacements) design was conducted by using ANSYS<sup>®</sup> and the experimental results were used to confirm the validity of the finite element modeling technique [55,56].

In the modeling of the smart structures analytical methods such as variational approach and modal expansion, wave analysis or numerical methods like finite element modeling are available. Alternatively an experimental approach was also adopted in the modeling of the smart structures, Bai and Lin [57]. When an accurate analytical or finite element model is not available, an experimentally identified model was typically used [58-60]. Furthermore, Dosch *et al.* [59] proposed that the

experimentally identified models could also be used for tuning the accuracy of the finite element models.

### **2.3.2 Active Vibration Control Strategies Applied to Smart Structures**

This section presents the current trends and the methodologies applied to the active vibration control of smart structures

Hanagoud and Obal [61] developed an optimal control procedure based on the minimization of the quadratic performance index which chosen to be the total strain energy of the system. State and control vectors for a system consists of sensors and actuators occupying discrete subdomain of elastic cantilevered beam. The method they proposed makes use of the output feedback methods. In this work, they considered the actuator patches as point actuators that increase the spill over problem. The effect of spill over due to the unmodeled modes on the control procedure and the optimal number of actuators and their positions not attended to.

The Linear Quadratic Regulator (LQR), and controllability measure, were compared for the determination of the optimal actuator size and placement for vibration suppression of a simply supported smart beam by Devasia *et al.* [62]. In this paper, it was proposed that the LQR based measures more suitable than the controllability measures for placement and sizing of the actuators. Sunar and Rao [63] approached the optimal placement problem of the actuators on a cantilevered beam with symmetrically placed PZT actuators from a different point of view. By using a finite element based modeling technique, they observed the magnitude of the structural vibrations for various actuator configurations to determine the optimal location of the actuators. In this work, it was shown that the placement of the actuator closer to the root is more efficient than the pair further away.

The effectiveness of Linear Quadratic Gaussian Algorithm (LQG) on the experimentally identified beam was shown by Bai and Lin [57]. The experimental results obtained in this study shows that the algorithm provides significant attenuation of the vibration signal.

Based on the dynamic modeling described in [41], Kalaycıoğlu and Misra [64] discussed the suitability of the applications of the various control strategies to the problem of shape control of spacecraft appendages. They presented the improved version of an efficient method developed to handle vibrations in the flexible structures by Singer [65] for calculating optimum voltage profile causing minimum vibrations. They justified their work both experimentally and numerically. Using the time-delay techniques presented in [41,64] Kalaycıoğlu *et al.* showed the effectiveness of the model on the active control of space structures in which fiber-optic materials are chosen as sensors and PZT patches are chosen as actuators [66].

The optimum placement of piezoelectric sensor/actuator for active vibration control of the laminated beam, was investigated by Kang *et al.* [67]. In this work, they firstly identified the optimal locations by selecting the modal damping ratios as their performance index, then identified the optimal sensor/actuator locations as the points where the performance index reaches its maximum.

Xu and Igusa [68] presented a new optimal design method for the actuator placement. In this method, the gains of the actuators and sensors are considered as an output control system. They explored the efficiency of their model by considering several numerical studies for two dimensional membrane structures.

Hwang *et al.* [69] presented a technique that allows the optimal design of the size and the location of the collocated pair of the piezoelectric sensors and actuators together with the composite layer angles. By using a modal analysis based technique, they stated that an efficient control algorithm could be designed for the active vibration control of the layered composites in cantilevered configuration. The

work however includes only the numerical results. Experimental justifications were not made and issues on the robustness performance were not included.

A new control algorithm for eliminating structural vibrations is presented in [70]. The developed algorithm so-called Pulse Active Damping is applied to eliminate the residual oscillations of space shuttle remote manipulator system (RMS). In this study, simulation results presented both in plane and out-of-plane vibrations are cancelled effectively by injecting appropriate torque pulses at shoulder yaw and shoulder pitch joints of RMS. By using the concept of integral manifolds and singular perturbation theory, Moallem et al [71] presented a nonlinear control strategy for tip position tracking of a class of structurally flexible multi-link manipulators

Ge and Jouaneh [72] proposed a PID control with nonlinear model in driving the piezoelectric actuator to resolve the hysteresis problem. However, they did not consider system uncertainties in the formulation of feedback controllers. A Preisach model that captures hysteresis in a stacked piezoceramic actuator was developed and experimentally validated by Hu and Mrad [73].

Choi *et al.* [74] proposed the Quantitative Feedback Theory (QFT) that is a frequency domain design technique to reach the robust performance within the frequency range of interest for a smart structure consisting of composite beam with a surface bonded piezoceramic actuator.

By using the experimentally identified model of flexible ribbed antenna Dosch *et al.* [59] developed Multi Input Multi Output (MIMO) and Single Input Single Output (SISO) models. They showed the necessity of the application of MIMO models in the case of the presence of the repeated eigenvalues and designed a positive position feedback and  $H_\infty$  controller that increases damping in all modes of vibrations.

Nalbantoğlu [60] studied robust control and system identification for flexible structure that is considered to be a four stories space truss with active components. In his study, system identification, performance criteria selection and optimal sensor placement for flexible structures were examined within the  $H_\infty$  and  $\mu$  analysis framework and the ideas developed were tested on the flexible structure.

In another study, Bravo *et al.* [54] also considered  $H_\infty$  controller for the vibration suppression of a truss by using finite element modeling [54]. Their finite element modeling was not capable of electromechanical coupling and their controller was designed by considering the uncertainty structure as a full block [60,75]. This approach may yield to conservative results [60].

A control criterion based on the absorption of the traveling waves of the sensing area was introduced by Koma and Vukovich [42]. Based on the global wave absorbing technique a controller for active vibration control of smart beams in cantilevered configuration with surface bonded PZT actuators. It was shown that the technique had unique advantage over more common dynamic model based controllers such as LQR. In this technique, the utilization of PVDF polymers as strain rate sensors eliminates the necessity of integration and differentiation. They also included experimental results to validate the effectiveness of the controller. Although the controller design greatly depends on the accurate modeling of the system no information was provided for the validation of the modeling and the robustness issues [75].

Mei and Mace [76] studied the reduction of spillover in active vibration control. They combined an optimal damping feedback wave control strategy with LQG and showed the robust performance of the controller. Their work however, was limited to the active vibration control of smart beams and the analysis of more complex structures was not included.

By using ANSYS<sup>®</sup>, Yaman *et al.* [77] worked on the finite element modeling technique based for the determination of the smart beam. Based on this model they designed a controller that effectively suppressed the vibrations of the beam due to its first two modes. In their work, the effectiveness of  $H_\infty$  design technique in the modeling and the evaluation of the robust performance were also demonstrated.

In another study, Yaman *et al.* [78] extended their finite element modeling technique and the robust controller design approaches developed for the analysis of smart beams [77] to the analysis of a flat fin (flat plate with surface bonded piezoelectric actuators). This study, first gave the effects of the piezoelectric actuators on the response of the smart fin, then explained the influence of the actuator size and placement and also determined optimum sensor location. The smart fin was then used in the determination of an experimentally identified model. Based on this model, a single input two outputs  $H_\infty$  controller was designed to suppress the in-vacuo vibrations due to the first two modes of the smart fin. The effectiveness of the technique in the modeling of uncertainties was also given. It was shown that the controller designed guaranteed the robust performance in the presence of the uncertainties.

In one of the recent studies Sivrioğlu *et al.* [79] discussed the effectiveness of  $H_\infty$  output feedback control technique on the acoustic power suppression of a panel structure. In this paper, a robust control system was designed to suppress the radiated acoustic power emitted from vibrating planar structure, and the spill over effects due to unmodeled frequencies of the structure were presented.

## 2.4 The Applications of Smart Structures in Active Aeroelastic Control

Aeroelastic effects and related problems have considerable importance in the design and analysis of aeronautical structures. These effects are felt by the structure in the form of changes in the aerodynamic load and lift distribution. These changes affect structural integrity of the vehicle as well as flight stability, effectiveness of the control surfaces and overall performance. This section outlines the current applications of smart structures in active aeroelastic control.

Active aeroelastic concepts deal with the treatment of static or dynamic aeroelastic deficiencies with respect to stability, maneuverability, loads and aerodynamic response. The goals of applying smart devices to aeroelastic problems are to control the aerodynamic and/or structural characteristics of aeronautical structures, to improve flutter, gust, buffet and maneuver load behavior of fixed wing vehicles and to reduce the loads on rotorcrafts. In many cases, applications of smart materials will create more efficient structural designs. Several analytical and experimental studies clearly demonstrated that the piezoelectric devices can be used as actuators to actively control the vibratory response including the aeroelastic response [80-82].

Suleman [83] discussed the feasibility of employing passive control methodology by using piezoelectric actuators to control the panel flutter. In order to achieve best performance, there exists an optimum patch size and configuration. However, a compromise needs to be determined between the advantages of an increased actuation capability and the disadvantages of an increased weight due to the addition of the piezoelectric materials. These questions left untouched for further studies. In another study, Suleman *et al.* [84] proposed the effectiveness of the piezoceramic sensor and actuators on the suppression of vibrations on an experimental wing due to the gust loading. They showed, experimentally, the feasibility of the application of the smart structures in the suppression of vibrations due to the gust loading on the smart wing



By using frequency response fitting and a semi analytical model, P transform technique [85], Baker *et al.* [86] presented the aeroservoelastic modeling and design techniques for transport aircraft based on their experiences derived from several transport aircraft programs at Boeing

A joint research program in the field of aircraft structures was initiated between Daimler Chrysler Military Aircraft Division (DASA), Daimler Chrysler Research and Technology (DC-FT) and German Aerospace Center (DLR). Within these efforts various different concepts for active vibration suppression on vertical fins were developed investigated theoretically and experimentally [87]. Luber *et al.* [88,89] considered a method for the improvement on the design strategy of flight control system development through an algorithm that included the integrated design optimization involving the modeling of the coupled system of flight dynamics, the actuators, sensors and the effects of the processor network. In this work the aeroelastic and aeroservoelastic models were based on the theoretical finite element model representative of the stiffness and mass characteristics of European Fighter 2000 by means of dynamic assembly. By using NASTRAN<sup>®</sup>, the complete flutter model is assembled through the dynamic model components and included the unsteady aerodynamic components.

A comparable research program was initiated in the United States with a participation from Canadian and Australian institutions in which the active rudder and integrated piezoelectric actuators concept were investigated on a modified F/A-18 fighter aircraft. Nietzsche *et al.* [90] presented a finite element approach for the design of control algorithms for vertical fin buffeting by using strain actuation. Since for the first time the full scale aircraft (F/A-18) was tested at buffet control using the smart materials technologies, this work represents an important step in the development of smart structures. In this work, by using the commercial code NASTRAN<sup>®</sup> [91] the structural and the aeroelastic model of the vertical fin is modeled. Based on this model, a MIMO LQG based controller design was performed for the alleviation of the buffeting effects on the vertical fin. However,

since NASTRAN<sup>®</sup> has no elements for the analysis of the effects of the piezoelectricity, the actuation of the piezoelectric actuation was simulated by the deformations of the rod elements under constant temperature. Furthermore, the robust performance property of the controller design was not shown. Despite of the approximations considered in the modeling, very promising results were obtained.

In another study, Hanagoud *et al.* [92] presented a different approach for the tail buffet alleviation of the twin tail aircraft. By using the offset piezoceramic stack actuators and acceleration feedback concept, this study focuses on the reliability and maintainability of the actuator and the robustness of the controller. The theoretical model of the study was based on the single degree of freedom approximation for the system model. They also provided certain experimental validations for the effectiveness of the acceleration feedback concept on a full scale tail sub assembly and on a 1/16<sup>th</sup> scale wind tunnel model. These studies had shown that the active control systems offer a compromising solution to alleviate buffet induced strain and increase fatigue life of modern fighter aircrafts. The aeroservoelastic characteristics of the B2 bomber and its implications for future large aircraft was also discussed by Britt *et al.* [93].

Recent developments in the finite element modeling of smart structures for aeroservoelastic response, were presented by Nam *et al.* [94]. In this work, it was shown that, a commercial program ASTROS<sup>®</sup> [95] provides a successful means of integration as a result of the thermal versus PZT analogy and the control surface versus PZT equivalence principle. The capabilities of the software were also demonstrated by considering certain numerical examples. These included the neural net work based active flutter suppression of F-16 wing by using PZT actuators, the gust-load alleviation of a modeled F18 wing by using active control, and the trim reduction of TOMAHAWK missile with or without battle damage by using PZT actuators.

The present helicopter research is mainly directed towards the improvement of the aerodynamic efficiency and the acoustic emissions. The helicopter flight dynamics

are governed by many complex and still quite poorly understood phenomena [96]. This makes accurate modeling hard and consequently designing new controllers are challenging [97]. The applications of smart materials have also a high potential to significantly suppress noise, reduce vibration and increase the overall aerodynamic efficiency. The utilization of the smart materials provides means of direct approach aiming the alleviation of the problems at their physical sources [98-100].

In one of the recent studies, Suleman *et al.* [101] described the wind tunnel aeroelastic testing of a Remotely Piloted flight Vehicle (RPV). The aeroelastic response to gusts and performance of the RPV wing by using traditional aerodynamic control surface methods is compared to the ones obtained by using PZT actuation. Piezoelectric shunting, a passive form of control was used to create system redundancy and thus improving flight safety in the worst-case scenario.

## **2.5 Structural Health Monitoring By Using Smart Structures**

This section reviews and discusses the enhancements and developments in the applications of the smart materials for the structural health monitoring of aerospace structures.

The structural integrity of the critical connections or parts of the aerospace structures must be assured during its lifetime. Structural health monitoring of these regions has of primary importance and this is currently being fulfilled on aircraft externally and internally. When health monitoring is performed internally, the access to the locations of the critical parts by using traditional Non-Destructive-Inspection (NDI) techniques is rather limited or unavailable. In this case, the disassembly of the aircraft structure is required. These inspections are necessary during the service time of the aircraft to ensure the structural integrity of the aircraft

for flight-worthiness. The inspection of these structural elements by traditional methods, therefore, requires a lot of time and effort.

The application of smart structures technologies provides effective solutions to the problem by eliminating unnecessary aircraft structural disassembly for the structural health monitoring of the critical parts. Furthermore, in principle, the smart structures offer not only in-service inspections but also provides in-situ basis for continuous monitoring.

In structural health monitoring, the state of the structure is sensed during in-service life and measurements are compared with previously measured reference response levels. Therefore, it is essential to have basic understanding of expected response of the structures for which sensors can be used.

The structural health monitoring of the structure during its service life can be accomplished by sensing global as well as local parameters. The sensing of local parameters (deformation, strain, temperature and pressure) can give information on exact location. The extent of the damage to the structure however, can be understood from sensing global parameters (natural frequencies and damping factors). Typical response parameters that can be used in health monitoring are the natural frequencies and the strains caused by in service loading. The natural frequencies are affected by both distributed or localized mass and stiffness changes. The reduction of mass (e.g. impact damage) will increase natural frequencies while reduction in stiffness will reduce natural frequencies. However, the health monitoring strategies based on changes in structures global parameters require very sensitive sensors since, in most cases extensive damage is required before significant changes occur. Some modes may be significantly affected by the relatively small amounts of damage. However, which modes experience large changes in modal parameters depends on where the damage is located in the structure. If the damage is located at high strain region of a certain node, it will take

relatively little damage to produce a significantly changes in natural frequencies, Bicos and Tracy [102].

The aim in structural health monitoring is to provide means for warning before the actual failure occurs. In addition to the safety requirements, the target should be the reduction of the maintenance cost. One way to achieve this is to perform the maintenance only when it is necessary. This can also be achieved through the structural health monitoring

As it was mentioned in the previous sections, significant work conducted on the development of piezoelectric and fiber optic sensors that can be used to monitor the performances of the structures [102,103]. In the health monitoring, depending on the operating conditions, loading and the passive material type, different kind of smart materials are used.

When an alternating voltage drives the PZT bonded to the structure it imposes bending moment on the structure through its longitudinal expansion and contraction causing structure to vibrate. This vibration in turn modulates the current flowing through the patch and consequently the electric impedance which is defined as the ratio of the applied voltage to the resulting current of the bonded patch.

The idea to use the electric impedance in the dynamic analysis of smart structures is introduced by Liang *et al.* [104]. Since the method reflects the physical essence of the active material systems precisely, the technique has advantages over other conventional techniques like the static and dynamic finite element approaches. By using the observations of Liang, Sun *et al.* considered the measurement of the admittance of the PZT patch that is related to the mechanical impedance, (the ratio of the applied force to resulting velocity of the structure) for the on-line damage detection of the smart structures in two articles [105,106]. They first proposed an electrical impedance measurement based frequency response function acquisition technique for the flexible structures. Later they presented a novel vibration signal

recognition technique for the determination of the damage of the smart structures. In their work, the damage is obtained by using the statistical algorithm based on the difference in electrical impedance of a healthy and the damaged structure. This algorithm is then applied to extract an index of the health of the structure. In another study, Chaudhry *et al.* [107] further provided an experimental proof of the technique for the health monitoring of an assembled truss structure. In this work, it was shown that the local effects of the collocated PZT sensors /actuators greatly simplifies the determination of the location and the extent of the damage. The idea, used in the vibration signature sensing techniques described, is actually based on the fact that each part of the structure contributes to the impedance to some extent. Any variation in the structure integrity will cause a change in the measured electrical impedance of the patches. This approach works well for truss type structures. For the solid structures having high spatial mass distribution however, the number of the required sensors increases greatly. Thus, there seems a little feasibility for this approach [107].

By using results of [106] and [107], Chaudhry *et al.* [108], introduced the high frequency mechanical impedance technique to the local area health monitoring of the critical sections of an aircraft by using piezoceramics. In this application, because the size of the PZT transducer area limits the sensing and the actuation area, the impedance was affected only by the changes in structural properties close to the sensing/actuating and insensitive to the changes in the far-field boundary conditions and loading.

Since, at high frequencies the response is dominated by local modes, the incipient damages like small cracks, loose connections and delaminations can be identified at the locations where high structural integrity must be assured at all time. Chaudhry *et al.* [108] proposed that the technique developed can be applied to the critical parts on an aircraft, like the main fuselage joint, the engine to-fuselage joint and other critical regions. Because of the high frequency of the excitation, the analysis is very sensitive to minor damage that may exist in the structure. High frequency excitation

(typically in the order of 50 kHz) is critical for the success of this technique since it assures clearly visible change in the impedance. Because the wavelength of the oscillation should be less than that of the crack to detect, it is directly related to the accuracy of the model. Chaudhry *et al.* further showed that at such high frequencies the technique is comparable in sensitivity to sophisticated traditional NDI techniques.

The examination of the mechanical impedance of a structure at the location of interest has been proven to be an effective way to estimate the structural integrity of the structures. However, with the utilization of the conventional transducers such as accelerometer and force gauge, it is economically and technically impractical to implement in service or real time health monitoring of large structures composed of hundreds of joints and components. The vibration signature based techniques applied on the piezoceramic patch however, provides simple means of acquiring the vibration signature pattern that is much easier to measure than that of mechanical impedance. For the success of the vibration signature based technique however, the piezoelectric patches should be mounted to the surfaces of the critical parts of the structure on which health monitoring is necessary. Chaudhry *et al.* [109] further investigated the effectiveness of the vibration recognition technique on the monitoring of the integrity of the composite repair patches used in the aircrafts and showed that the technique assures a clearly visible change even for very minor changes.

Acoustic emission is also being considered for health monitoring of aeronautical structures [102,103]. In this technique, the fiber-optic sensors embedded to the structures are replaced with surface mounted piezoelectric sensors. The technique is reported to have advantages over other techniques, Rogowski [103]. Because an acoustic signal propagates for relatively long distances in many structural elements, the number of sensors required for the technique is minimum compared to other techniques. In this technique, the propagation of acoustic signals are modeled and compared with measurements, the relative signal arrival times are then used to localize the damage, Spillman and Fuhr [110]. A complete understanding of

fundamental physical process is required to allow proper interpretation of acoustic emission data to locate and identify structural defects.

Tsou and Shen [111] explored the application of the artificial neural networks to the structural damage detection and identification on the discrete structures. They proposed that the neural network's ability to learn the feature of the nonlinear mapping and their fast computational speed make the application of the neural networks in the structural health monitoring feasible. By using piezoelectric sensors and actuators, Islam and Craig [112] proposed a neural network based strategy for the detection of damage in composite structures. By using the back propagation neural network trained with the first five modes of the laminated composite beam, the technique was shown to yield accurate results in the determination of any delaminations.

McBride *et al.* [113] conducted a feasibility study for the determination of debris impact and damage assessment for space structures. They showed acoustic emission technique could provide a basis for the monitoring of debris impact and materials degradation in large, isolated space structures. Since the accuracy of the technique greatly depends on the selection of the sensors, currently available sensors should carefully be examined in terms of the characteristics of both passive and active components to contain both debris impact and materials damage requirements.

The flexible structures can experience structural integrity problems as a result of the damaged connections. Real time monitoring of the structures can be achieved by using piezoelectric actuator by sensing the global parameters of the structures. Nesculescu and Abreu [114] compared the effectiveness of frequency and transient response based health monitoring. They first obtained the damage index by considering different levels of loosening for the joints of the clamped smart beam with surface bonded piezoelectric actuators. Then by comparing with a healthy beam, they showed that the transient response could also be used effectively in the determination of the structural integrity problems.



## **CHAPTER 3**

### **MODELING AND DESIGN OF SMART STRUCTURES**

#### **3.1 Introduction**

This chapter is devoted to the modeling and the design of smart structures. By using ANSYS® (v.5.6) software, the study determines the effectiveness of the finite element modeling technique in the analysis of piezoelectric materials and the design of smart structures. The study first gives the effects of the piezoelectric patches on the response of the smart structures and also explains the influences of the actuator size, placement and the maximum admissible piezoelectric actuation value to secure the integrity of the piezoelectric patches. These models will then be reduced to the state space models of the smart structures necessary for active vibration control. This study focuses on the accurate representation of anisotropy and the electromechanical coupling inherent to the piezoelectric materials and their effects on the passive portion of the smart structures. The smart structures considered in this thesis consist of aluminum beam-like and plate-like structures modeled in cantilevered configuration with surface bonded PZT patches. The identically polarized piezoelectric patches are bonded symmetrically on top and bottom surfaces of the passive portion of the smart structures.

## **3.2 Theory of Piezoelectricity**

This section presents both analytical formulation and numerical technique for the analysis of piezoelectric materials in which there is an inherent coupling between the mechanical and electrical behavior. This section first describes the fundamental differential equations of linear piezoelectricity then gives a finite element based modeling technique for the analysis of the linear piezoelectricity.

### **3.2.1 The Analytical Modeling of the Piezoelectric Materials**

This part of the thesis gives a brief review of the three-dimensional equations governing the response of piezoelectric materials under the application of an electric field. During the course of work, the formulations are adapted to the dielectric, piezoelectric and anisotropic material properties of BM500, the piezoelectric material that is used throughout the study. The properties of BM500 are presented in Appendix A.

Piezoelectricity deals with the coupling of structural and electric fields, which is the natural property of anisotropic crystals. The analysis of the coupled field problems requires the incorporation of the piezoelectric interaction equations with strain displacement and the equations of the motion of the problem.

The actuation of a piezoceramic material is characterized by the three-dimensional deformations of the ceramics under the application of an electric field [16,20,22]. Depending on the polarization pattern of the ceramics and the actuation values, the applied electric field generates tension or compression in a piezoceramic material.

If one denotes the material or the body coordinates of the piezoelectric rectangular coordinate and the principal axes of the piezoelectric material by the axes  $(x, y, z)$  and  $(x_1, y_2, x_3)$  respectively, Figure 3.1 then gives the positive sign convention, which will be followed in the analysis of the piezoelectric materials. In that the actuation voltages applied to inner and outer electrodes of the piezoceramic material represented by  $V_i$  and  $V_o$  respectively. The equations to be solved in the analysis of the coupled field problem are summarized in equations (3.1.1) to (3.1.5)

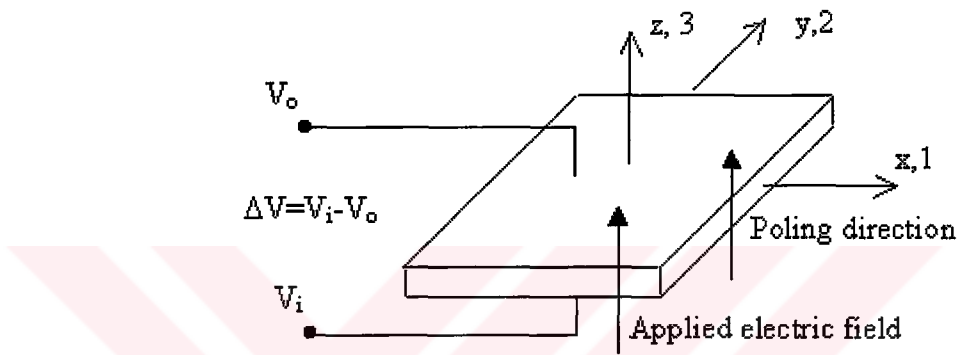


Figure 3.1. The piezoelectric patch and the positive sign convention used in the study

During the presentation of the equations  $(x, y, z)$  coordinates are used in the formulation of the strain-displacement and equilibrium equations. The constitutive equations and the transport equations however, are written in the principal coordinate system  $(x_1, x_2, x_3)$ . For the small displacement analysis of an elastic structure, the strain displacement equations are well known to be,

$$\begin{aligned} \epsilon_{xx} &= \frac{\partial u}{\partial x}, \epsilon_{yy} = \frac{\partial v}{\partial y}, \epsilon_{zz} = \frac{\partial w}{\partial z} \\ \gamma_{xy} &= \frac{\partial v}{\partial x} + \frac{\partial u}{\partial y}, \gamma_{yz} = \frac{\partial v}{\partial z} + \frac{\partial w}{\partial y}, \gamma_{zx} = \frac{\partial u}{\partial z} + \frac{\partial w}{\partial x}, \end{aligned} \quad (3.1.1)$$

where,  $u, v, w$  represent the displacements along  $x, y$  and  $z$  directions respectively. In the absence of the body forces, the equilibrium equations are given by equation (3.1.2).

$$\begin{aligned}\frac{\partial \sigma_{xx}}{\partial x} + \frac{\partial \sigma_{xy}}{\partial y} + \frac{\partial \sigma_{xz}}{\partial z} &= \rho_0 \frac{\partial^2 u}{\partial t^2} \\ \frac{\partial \sigma_{xy}}{\partial x} + \frac{\partial \sigma_{yy}}{\partial y} + \frac{\partial \sigma_{yz}}{\partial z} &= \rho_0 \frac{\partial^2 v}{\partial t^2} \\ \frac{\partial \sigma_{xz}}{\partial x} + \frac{\partial \sigma_{yz}}{\partial y} + \frac{\partial \sigma_{zz}}{\partial z} &= \rho_0 \frac{\partial^2 w}{\partial t^2}\end{aligned}\tag{3.1.2}$$

Here  $\sigma$  defines stress  $\sigma_{ii}$  where,  $i=x, y, z$ , stands for normal stress and  $\sigma_{ij}$ , where  $i$  and  $j=x, y, z$ , gives shearing stresses.  $\rho_0$  symbolizes the density per unit volume of the piezoceramic material and  $t$  stands for time. The transport equation, relates the electric field  $\xi_i$  to the scalar potential function  $\psi_i$  by the following relation,

$$\xi_i = -\frac{\partial \psi_i}{\partial x_i}\tag{3.1.3}$$

In the analysis of piezoelectric materials having constant thickness, the electric field is described by the ratio of the potential difference between the surface electrodes of the piezoelectric material to the distance between the surface electrodes. When the stress strain relations for a piezoceramic material [22,115] are adapted to BM500 type actuators [116]; these relations, in principal directions, take the form of equation (3.1.4).

$$\begin{Bmatrix} \sigma_1 \\ \sigma_2 \\ \sigma_3 \\ \sigma_4 \\ \sigma_5 \\ \sigma_6 \end{Bmatrix} = \begin{bmatrix} C_{11} & C_{12} & C_{13} & 0 & 0 & 0 \\ & C_{22} & C_{23} & 0 & 0 & 0 \\ & & C_{33} & 0 & 0 & 0 \\ & & & C_{44} & 0 & 0 \\ & \text{symmetry} & & 0 & C_{55} & 0 \\ & & & & 0 & C_{66} \end{bmatrix} \begin{Bmatrix} \epsilon_1 - \alpha_{11}\Delta T \\ \epsilon_2 - \alpha_{22}\Delta T \\ \epsilon_3 - \alpha_{33}\Delta T \\ \epsilon_4 \\ \epsilon_5 \\ \epsilon_6 - 2\alpha_{12}\Delta T \end{Bmatrix} \quad (3.1.4)$$

$$+ \begin{bmatrix} 0 & 0 & e_{31} \\ 0 & 0 & e_{32} \\ 0 & 0 & e_{33} \\ 0 & 0 & 0 \\ 0 & e_{52} & 0 \\ e_{61} & 0 & 0 \end{bmatrix} \begin{Bmatrix} \frac{\partial \psi}{\partial x} \\ \frac{\partial \psi}{\partial y} \\ \frac{\partial \psi}{\partial z} \end{Bmatrix}$$

where,  $C_{ij}$  defines the elastic moduli and  $e_{ij}$  is the piezoelectric stress constant of the actuators.  $\alpha_{ij}$  are the thermal expansion coefficients of the piezoelectric material in principal directions and  $\Delta T$  is the temperature difference during the process. The electric flux density vector,  $D_i$  can be found from equation as [22,50,115],

$$\begin{Bmatrix} D_1 \\ D_2 \\ D_3 \end{Bmatrix} = \begin{bmatrix} 0 & 0 & 0 & 0 & 0 & e_{16} \\ 0 & 0 & 0 & 0 & e_{25} & 0 \\ e_{31} & e_{32} & e_{33} & 0 & 0 & 0 \end{bmatrix} \begin{Bmatrix} \epsilon_1 \\ \epsilon_2 \\ \epsilon_3 \\ \epsilon_4 \\ \epsilon_5 \\ \epsilon_6 \end{Bmatrix} - \begin{bmatrix} \epsilon_{11} & & 0 \\ \epsilon_{12} & \epsilon_{22} & 0 \\ & & \epsilon_{33} \end{bmatrix} \begin{Bmatrix} \frac{\partial \psi}{\partial x} \\ \frac{\partial \psi}{\partial y} \\ \frac{\partial \psi}{\partial z} \end{Bmatrix} \quad (3.1.5)$$

Here,  $\epsilon_{ii}$  where  $i=1, 2, 3$  gives the dielectric constants of the piezoelectric material in the principal directions.

The three-dimensional analysis of a piezoelectric material consists of finding the displacement components  $u, v, w$  and the electric potential  $\psi$  satisfying equations (3.1.1) to (3.1.5), completed by adequate boundary and initial conditions.

### **3.2.2 Finite Element Modeling of Piezoelectric Materials**

This section aims to investigate the effectiveness of the finite element technique in the analysis of the piezoceramic materials. Since these materials are generally used as the actuators in smart structures, their analysis has of primary importance in the determination of accurate models of smart structures. During the analysis, the modeling incapacibilities of the finite element technique that inevitably limits the accuracy of the results are also stated.

The finite element method was shown to be a very effective tool for the analysis of the piezoelectric materials since the method offers coupled thermo-mechanical-electrical analysis of the structures [50,52,55,77].

In the analysis of thermo-mechanical-electrical coupling field problems ANSYS®(v.5.6) has only three elements. These elements are, PLANE13, SOLID5 and SOLID98. These elements have magnetic, thermal, electrical, piezoelectric and structural field capabilities with coupling between these fields [50]. While PLANE 13 can be used in two-dimensional problems, SOLID5 and SOLID98 are considered in the analysis of three-dimensional coupled field problems. The geometry node locations and coordinate system for these elements are shown in Figure 3.2.

The piezoelectric actuation of a smart structure is characterized by the three-dimensional deformations of the piezoelectric actuators under the application of electric field [22,23,34]. Thus, in the finite element analysis of smart structures utilization of the prismatic or solid elements is common [52,56,77].

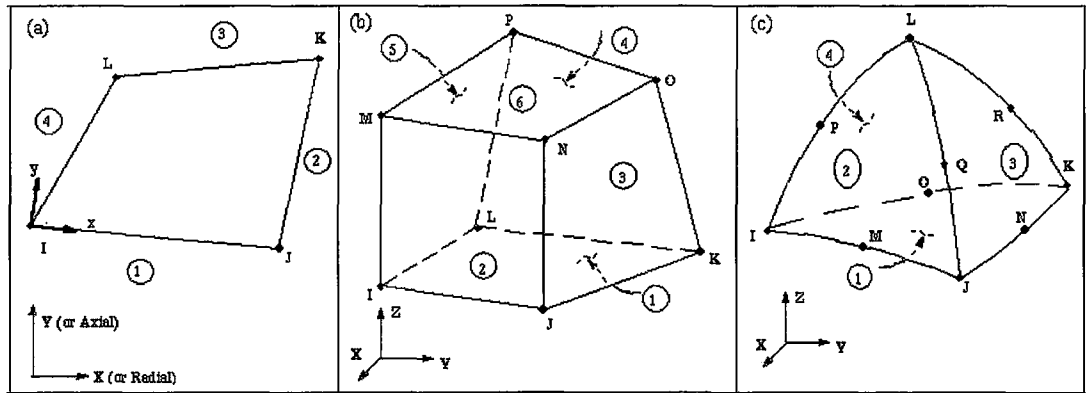


Figure 3.2. The comparison of the geometry, node locations and coordinate system for the element having coupled magnetic, thermal, electric and structural capability in ANSYS® (v.5.6).

- a. PLANE13
- b. SOLID5
- c. SOLID98

The prismatic elements, SOLID5 and SOLID98 are the suitable elements in three-dimensional coupled field problems available in ANSYS® (v.5.6). These elements have three displacement degrees of freedoms per node. In addition to these degrees of freedoms, the elements have also potential degrees of freedom. SOLID5 can be used to model regular meshes involving thin and flat geometries. The element has extra displacement shapes and uniform mass distribution [50,52,77]. SOLID98 is the 10 node tetrahedral version of 8 node SOLID5. The element has a quadratic displacement behavior and well suited to model thick and irregular meshes [55,56].

SOLID98 however, has non-uniform mass distribution such that the mid-nodes of the element always have larger mass [50]. The non-uniform mass distribution may influence the accuracy in the sub-structuring analysis which is the analysis conducted to condense the properties of the finite element to a single element or modal analysis that requires the condensation of the voltage degrees of freedoms at certain nodes in the finite element model called master degrees of freedoms [50].

Despite of the quadratic displacement behavior defined, SOLID98 has linear potential variation through thickness.

In order to avoid the inclusion of extra degrees of freedoms and non-uniform mass distribution, the smart material models of this study are created by using the regular meshes that allows the efficient use of SOLID5 for the theoretical modeling of piezoelectric patches throughout the study. The utilization of this element also guaranties the uniform mass distribution within an element during the dynamical and sub-structuring analyses [50].

The proper interpretation of the static and dynamic characteristics of the piezoelectric actuator is one of the most important steps in the analysis of the smart structures. For this reason, by using SOLID5 element, the theoretical model of a single piezoceramic crystal (25×25×0.5 mm, type: BM500) is obtained. In this thesis the sizes of the rectangular models are described in terms of their Length×Width×Height. The model is then used in the static and dynamic analysis of the patch modeled in mechanically clamped (C-C-C-C) configuration. The deformation of the piezoelectric patch under the application of 300V ( $V_i=300$  and  $V_o=0$ ) is calculated and the result is shown in Figure 3.3. Since, the boundaries of C-C-C-C patch is highly constrained, the deformations are found to be symmetric with respect to the x-y plane.

The mechanically clamped configuration for the actuators are considered to simulate the electro-mechanical behavior of the surface bonded PZT actuators closer than other possible boundary conditions such as, free and simply supported and elastic boundary conditions. Hence during the theoretical calculations the properties like dielectric and stress constant of the actuators are measured in its mechanically clamped configuration [52,51,116]. Figure 3.4 gives the first two theoretical natural frequencies and the mode shapes of a single piezoceramic crystal in mechanically clamped configuration. When all resonances of the actuator are higher than the frequencies of interest for the smart structures, the actuator acts



quasistatically compared to the smart structure. In this case, the dynamics of the actuator and the smart structure can be decoupled [35,36] and hence the numerical accuracy of the model is improved.

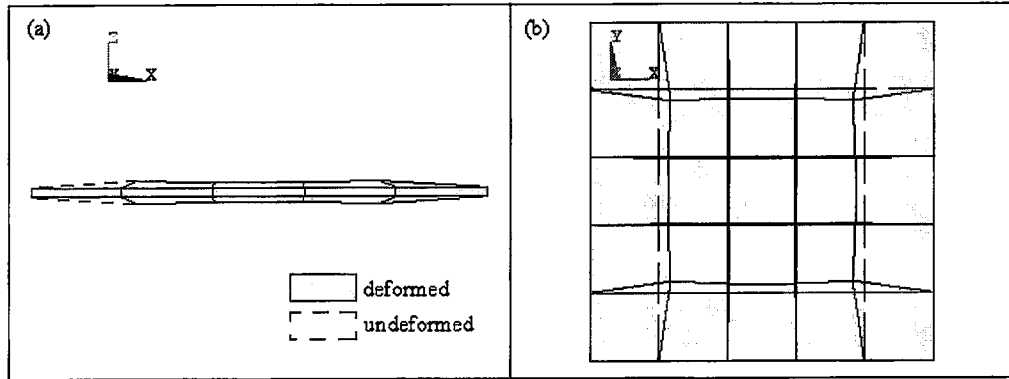


Figure 3.3. The deformation of a single C-C-C-C piezoelectric crystal at 300V ( $z=0$ ;  $V_i=0$ ,  $z=t_{pzt}$ ;  $V_o=300$  and  $\Delta T=0$ )

- a. Side view
- b. Top view

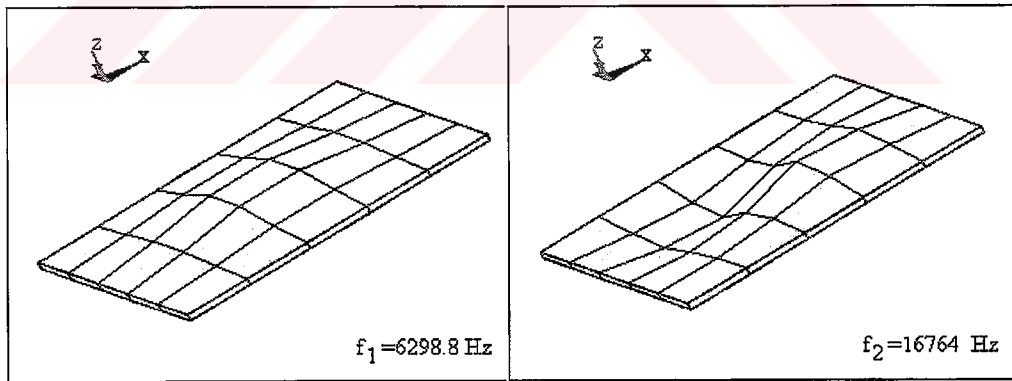


Figure 3.4. The first two theoretical natural frequencies and mode shapes of a single C-C-C-C piezoelectric crystal

### **3.2.3 The Limitations in the Finite Element Modeling of Piezoceramic Materials**

The inherent electromechanical coupling which exist in the smart structures and the required surface compatibility and continuity characteristics can be handled through the three-dimensional finite element modeling with an extended nodal degrees of freedom vector containing both mechanical and potential degrees of freedoms. This is generally done, by assuming the linear variation of the electric potential [50,117,118]. However, the assumption of linear variation of the electric potential neglects the induced potential. Depending on the type of the piezoceramic material and loading, this assumption may lead to the incomplete treatment of the electromechanical coupling [35].

The effect of the induced potential on the response of the smart structures is closely related to the extent of the elastic deformation of the piezoelectric material such that, the assumption of the linear variation of the electric potential across the thickness of the piezoelectric material ceases its validity for the smart material undergoing large deformations. In this case, the linear approximation should accordingly be modified [35]. Therefore, the influences of the initial stresses on the piezoceramic material must be investigated prior to the analysis.

In the finite element modelling of the smart structures, although the element SOLID98 is designed to have quadratic displacement behaviour, similar to SOLID5, the element assumes linear potential variation through thickness so ignores the effects of the induced potential. ANSYS® (v. 5.6) does not have elements suitable for the analysis of the effects of the induced potential and the large deformations by using scalar potential field approximation.

In the solution of electromechanical coupling problems, the method of the direct coupled field is used [50,117]. This method handles the highly nonlinear field

coupling by calculating the element matrices or the element load vectors containing the necessary terms for the solution. The technique is iterative for both matrix and vector coupling. Because the method calculates the results in single solution, this method has the advantage to avoid the use of enlarged nodal unknowns vector but still neglects the induced potential [50,117,118].

The theoretical calculations of the study are performed within the linear range of the elasticity and piezoelectricity. Therefore, the influences the large deformation (or large rotations) consequently the influences of the induced potential are not included in the current analysis. The linearity assumption provides an accurate description of the small amplitude waves in, and the small amplitude vibrations of the piezoelectric material [25,35,116].

The validity of the small deformation assumption is confirmed at the design stage by considering maximum transverse displacement ( $w$ ) to thickness ratio ( $h$ ) [119,120]. The linear plate and piezoelectric theories are not valid if this ratio is large, that is if it exceeds a few tenths. Although the practical limit of this ratio is case dependent, large  $w/t$  yields to deflections which are significantly different than those predicted by the linear theories. During the design stages of the smart materials the  $w/t$  ratio, for both active and passive portions undergoing bending deformations, is kept fairly below 10 to secure the validity of the linear piezoelectricity and elasticity theories. Furthermore, the piezoelectric material was also selected among the crystals from which the influences of the induced potential under small deformations are considered to be negligible. The validity of this assumption was shown in [52,55,116].

Since the piezoelectric or voltage degrees of freedom have no mass, the only option in the modal analysis for the models including coupled-field elements is the reduced method. The method uses Householder-Bisection-Inverse iteration algorithm to calculate the natural frequencies and mode shapes. Since the method works with a small subset of the degrees of freedoms called master degrees of freedoms, the

accuracy of the method depends largely on the number and location of the freedoms. Furthermore, the method does not allow the specification of the damping. Hence only undamped natural frequencies and mode shapes can be found by using modal analysis.

In the harmonic response analysis of the coupled field problems, the damping can only be included through the specification of the Rayleigh damping coefficients, the modal damping ratios associated with the modes of the smart material can not be specified.

### **3.3 The Finite Element Modeling and Design of Smart Structures**

This section presents a finite element based modeling technique for the analysis and the design of the smart structures. The technique used in this section is the appropriate extension of the theory developed for the analysis of the piezoelectric materials. During the analysis the effects of the electromechanical coupling are incorporated in the modeling of passive structures. The design of the smart structures was conducted by developing models having the parametric design capabilities that consequently allow variation in the location and the size of the actuators.

### **3.4 Finite Element Modeling of Smart Beam-Like Structure**

The smart beam-like structure considered in this study is composed of an aluminum beam modeled in cantilevered configuration with eight surface bonded piezoelectric patches (PZTs). In the study, it is generally referred to as smart beam.

Depending on the mission requirements and the surface characteristics of the passive structure, the selection of either unimorph or the bimorph configurations is common in the design of the smart structures. In the monomorph configuration, the actuators are bonded to one face of the passive structure. In the bimorph configuration however, the identically polarized piezoelectric actuators are symmetrically bonded to the top and bottom surfaces of the passive structure. The bimorph configuration doubles the forcing capacity of the piezoelectric actuators and improves symmetry [22,31,37]. The bimorph configuration is favorable when the forcing levels and the power requirements are critical [22,31]. Throughout this thesis, the bimorph configuration is considered in the design of the smart structures.

When piezoceramic crystals are bonded to the passive structure, their responses to the voltage actuation are modulated by the presence of the passive structure. Therefore, the mathematical model to be used in the analysis should be capable of appropriately modeling of active components and their interaction with the passive components.

Depending on the polarization pattern of the actuators and the actuation values, the applied electric field generates bending moments on the smart structure by inducing tension and compression on the opposite sides of the smart structure modeled in bimorph configuration. In Figure 3.5, this situation is represented for a smart beam-like structure subjected to different piezoelectric actuation. In this case, the net potential difference between the top and the bottom actuators is given as.

$$\begin{aligned}\Delta V^T &= V_o - V_i \\ \Delta V^B &= V_i - V_o\end{aligned}\tag{3.4.1}$$

Here the subscripts T and B denote the top and bottom actuators respectively.

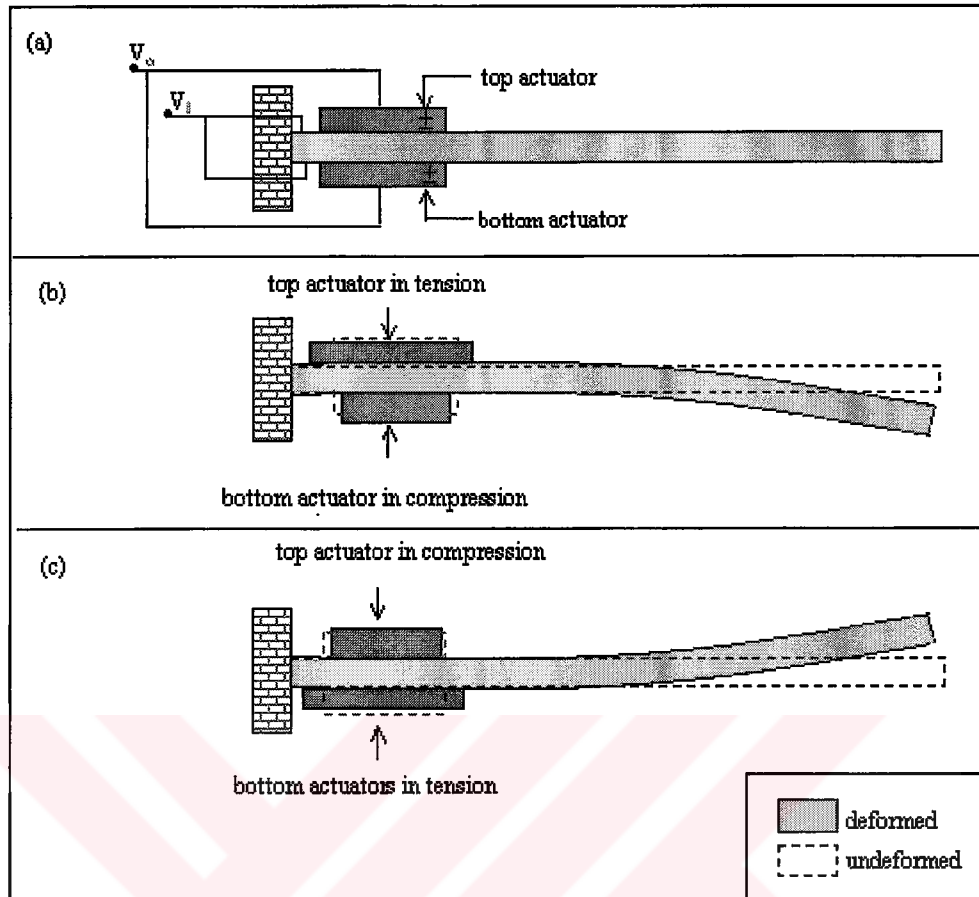


Figure 3.5. The piezoelectric actuation of a bimorph cantilevered smart beam.

a. The configuration and the polarization of the piezoelectric actuators

b.  $V_o < V_i$ , top actuators in tension, bottom actuators in compression

c.  $V_o > V_i$ , top actuators in compression, bottom actuators in tension

### **3.4.1 The Influences of the Element Type Selection**

In finite element modeling, the selection of the element type profoundly affects the accuracy of the problem. Therefore, in modeling of smart structures, it is imperative to understand the effects of the geometry, the loading conditions and the capabilities of the finite element program.

Because piezoceramic actuators exhibit anisotropy and yields three dimensional spatial variation in their response to the piezoelectric actuation, the models developed for the passive portion should also include consistent spatial degrees of freedoms with the actuator elements where the active and passive elements interface.

Piezoelectric patches strain in both directions in their plane. Hence, the passive portion of the smart beam-like structure should also be able to incorporate these deformations in its model. Thus, the smart beam-like structure is not an Euler-Bernoulli nor a Timoshenko beam but actually a plate strip and works in accordance with plate theory.

Theoretically, the plate elements (shell or solid) can be considered in the modeling of the passive portion of a smart structure. While the shell elements are used in accordance with the thin plate theories, the prismatic or solid elements work with the three dimensional elasticity theories [50,115,120].

Depending on the problem linear shell, prismatic, or their higher order versions may be used to model structures consisting of the thin plate strip or plates. In many situations however, the results obtained by using linear elements is known to yield results, which are not very accurate [50,120]. The utilization of linear elements with extra displacement shapes or the ones having quadratic displacement behavior is favored for the modeling of such structures [50].

In the modeling of piezoelectric patches, the typical elements used are the prismatic elements, whereas in the modeling of the passive portions, which are in the geometry of thin plates or plate strips, the quadratic shell elements may also be considered as an alternative to the prismatic structural elements [51,52]. The shell elements, in addition to the three displacement degrees of freedom, also have three rotational degrees of freedom per node. The use of elements possessing different degrees of freedoms in the same model requires coupling of the consistent degrees of freedoms at the contact surfaces where these elements interface. Although the application of the coupling strategies guaranties the appropriate transfer of the nodal forces between the active and passive portions at the interface, the nodal moments corresponding to nodal rotations do not transfer [50].

The geometry, node locations and coordinate system for the elements that are used to model the passive portion is given in Figure 3.6. Appendix B compares the effects of the element types by calculating the natural frequencies of the passive portion of the smart beam.

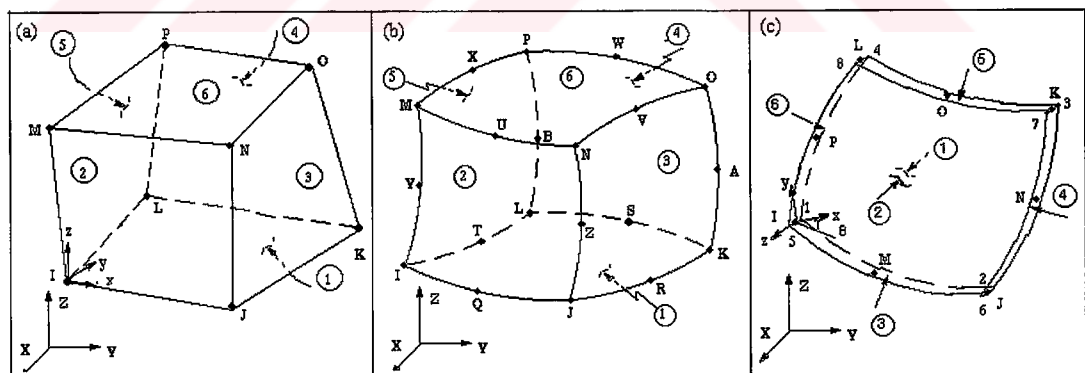


Figure 3.6. Elements used in the modeling of the passive portion of the smart beam structure [50]

- a. SOLID45
- b. SOLID95
- c. SHELL93



The appropriate model of the smart beam considered in this study is decided by considering two approaches [52,77].

In the first approach, the prismatic elements (SOLID5) are used for modeling the active portion (piezoelectric patches) and two different cases, which correspond to the modeling of the passive portion of the smart beam with different prismatic elements, are considered. In case 1, the passive portion of the smart beam is modeled by using the structural elements that are compatible with actuator elements (SOLID5). The element considered for this purpose is a linear prismatic element with extra displacement shapes (SOLID45). This model is called 'model 1'. In the second case, the structural quadratic elements (SOLID95) are used to model the passive portion. The model so obtained, is called 'model 2'. The element SOLID95 is a higher order version of the 8 node structural prismatic element SOLID45. The element has 20 nodes.

Then the passive structure is modeled with quadratic shell elements (SHELL93) whereas the piezoelectric elements are still prismatic elements (SOLID5). This hybrid model is denoted by 'model 3'.

The smart beam models obtained are then subjected to a piezoelectric actuation of 300V and the deformation results of the three different models are shown in Figure 3.7. Significant differences are observed between the solid-solid hybrid models (model 1 and model 2) and shell-solid hybrid model (model 3). It can also be seen from Figure 3.7 that the results obtained from the model consisting of linear elements having extra displacement shapes (model 1) are very close to that of the model with quadratic elements (model 2) such that, for the piezoelectric actuation of 300V, the maximum deviation in the deformation patterns of the solid-solid hybrid models are in the order of 1 percent.

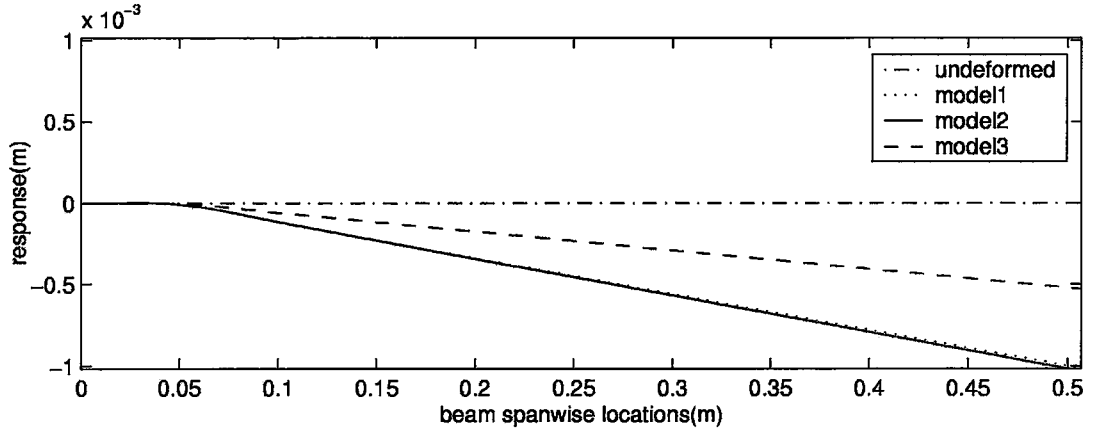


Figure 3.7. The comparison of the effects of the element type selection on the deformation of the smart beam by piezoelectric actuation at 300V (model1: SOLID5 and SOLID45, model 2: SOLID5 and SOLID95, model 3: SOLID5 and SHELL93)

The previous analytical studies revealed that the response of the smart beams [36,74] and plates [34,38,41] depends largely on the actuator thickness such that the increase in the actuator thickness reduces the response of the smart beam-like and plate-like structures. Thus, the influences of the patch thickness variation on the response of the smart beam-like structure models are investigated.

Figure 3.8 shows the dependency of the response on the patch thickness for three hybrid models, which are subjected to a piezoelectric actuation of 300V. In that figure the theoretical responses, in terms of the tip deflection values for twelve patch thickness values calculated by using the smart beam models, are plotted against actuator thickness. It can be seen from figure 3.8 that, as the patch thickness increases, the response reduces for the solid-solid hybrid models (model 1 and model 2), within the range of the actuator thickness values. The solid-shell hybrid model, (model 3), however, exhibits an unexpected behavior in its response to the piezoelectric actuation. The response increases for the patch thickness values between 0.1 and 0.75 mm. Thus, similar to the observations of Yaman, *et al.*

[77], the contradictory results are obtained from the shell-solid hybrid model, (model 3). These differences observed in model 3 may be attributed to the improper modeling of the element stiffness matrix in the determination of the global stiffness matrix for the shell-solid hybrid model.

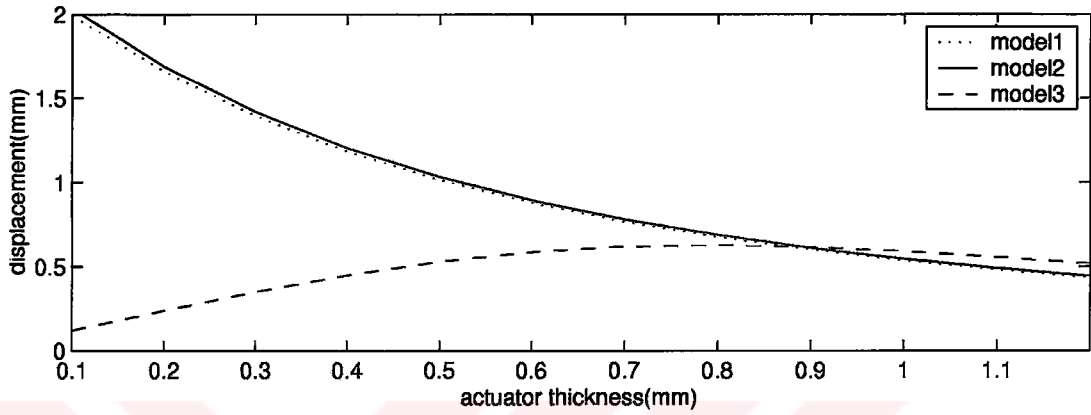


Figure 3.8. The comparison of the influence of the actuator thickness on the response of the theoretical models (legend of Figure 3.7)

The influences of the element type selection on the natural frequencies of the smart beam are also investigated. By using modal analysis, the first three natural frequencies are calculated and the results are shown in Table 3.1. During the theoretical calculations, since the voltage degrees of freedom associated with the coupled field analysis have no mass, these degrees of freedoms are condensed out through the application of the reduced method with master degrees of freedom chosen only for the structural degrees of freedom [50].

In order to avoid the inaccurate calculation of the mass matrix in the reduced analysis, the master degrees of freedoms are selected at the locations having larger mass and relatively low stiffness [50,120,122]. Hence, during the analysis, the master degrees of freedoms are selected at the mid-nodes that have greater mass for the quadratic elements. Since the highest stiffness of the smart structures are

observed at the locations where the piezoelectric patches are bonded to the passive structures, the master degrees of freedoms are selected at the locations which are sufficiently away from these locations.

During the theoretical calculations, the surface electrodes of the piezoelectric patches are assumed to be grounded ( $\Delta V=0$ ). Hence, the effects of the prestressing due to the piezoelectric actuation of the smart beam on the natural frequencies are excluded in the analysis.

It can be seen from Table 3.1 that while solid-solid hybrid models (model 1 and 2) yields to the closer results, the ones obtained from the solid-shell hybrid model (model 3) differs significantly. This expected result is due to the mismatches between the prismatic piezoelectric and shell structural elements used in the smart beam model. The slight differences observed between the solid-solid hybrid models may be attributed to the non-uniform mass distribution of the quadratic elements used in model 2. This statement will further be justified in Chapter 5 by considering the experimental results.

Table 3.1. The influences of the element type selection on the natural frequencies of the smart beam (Legend of Figure 3.7)

Model 1	Model 2	Model 3
Frequencies (Hz)	Frequencies (Hz)	Frequencies (Hz)
7.3047	7.3595	6.76
44.112	44.50	42.164
117.28	121.38	100.04

Because of the inevitable compatibility problems identified in the solid-shell hybrid model, in the modeling and analysis of the smart structures of this study always solid-solid hybrid models are used.

The smaller order prismatic elements having extra displacement shapes in the modeling of the passive portion of the smart beam is found to yield results nearly as good as those of the higher order elements. Hence, in order to avoid the inclusion of the extra degrees of freedoms, the study considers the smaller order prismatic elements with extra displacement shapes to model the passive portion of the smart beam. The inclusion of the extra degrees of freedoms is well known to increase the computing time.

The preliminary analysis conducted, indicates that higher strain gradients are observed in the vicinity of the regions where piezoelectric patches interfaces with the aluminum beam. Hence, finer meshes in x and y directions without wedges or tetrahedral forms are generated in these regions to improve the accuracy of the model. Furthermore, because the smart beam model is composed of thin components, single elements is considered to model piezoelectric patches and the aluminum beam in z direction. Figure 3.9 gives the geometry, dimensions and the finite element model of the smart beam used in the study.

Although the use of prismatic elements in the modeling of the passive portion of the smart structures inevitably increases the number of nodes to account for the calculation of through thickness variation of the normal and transverse stresses hence increase the computing time, the regular geometries of the smart structures involved in this thesis allow the creation of the models consisting of small number of nodes and gives accurate results within reasonable computing time.

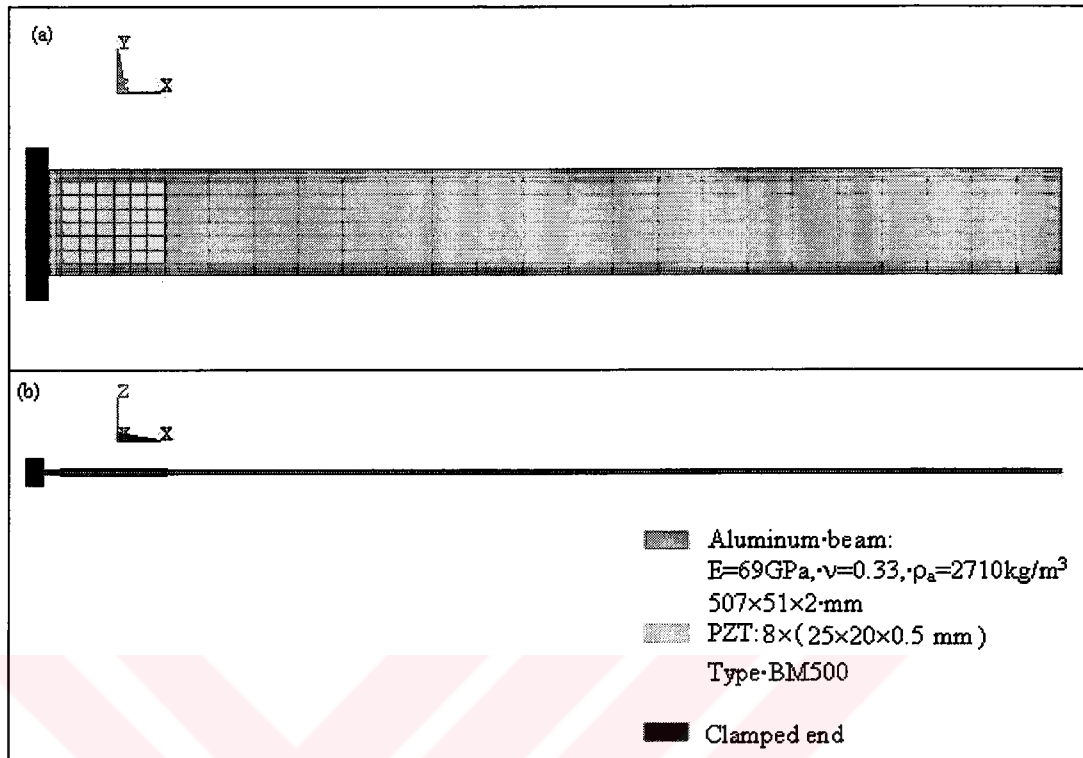


Figure 3.9. The geometry and the finite element model of the smart beam (solid-solid hybrid model with 1192 nodes and 420 SOLID45 and 72 SOLID5 type elements)

- a. Top view
- b. Side view

### 3.4.2 The Effects of Polarization and Placement of Piezoelectric Patches

This section explains the effects of the polarization, and the symmetrical placement of the piezoelectric patches on the response of the smart beam. Depending on the polarization pattern of the piezoelectric patches and the direction of the applied electric field, the patches induce bending moments by generating tensile and compressive stresses on the opposite sides of the smart beam if the beam is modeled in bimorph configuration. This configuration requires the symmetric placement of the piezoelectric actuators on top and bottom surface of the smart beam.

The utilization of the bimorph configuration for smart structures allows the simultaneous control of the magnitude and the direction of the response of the smart structure. In this configuration, the bending moments induced on the opposite sides of the smart beam have the same magnitude. Furthermore, the direction of the response is directly related to the polarization of the actuators and the direction of the electric field applied. Hence, the same amount of response but in the opposite direction can simply be obtained by reversing the direction of the applied field.

Figure 3.10.a shows the deformation of the smart beam to the piezoelectric actuation of -300V ( $V_i=0$ ,  $V_o=300$  V), and Figure 3.10.b gives the response of the same beam to a piezoelectric actuation of 300V ( $V_i=0$ ,  $V_o=-300$  V). It is evident from this figure that simply by reversing the direction of the electric field, the response equal in magnitude but opposite direction can be obtained.

The symmetric placement of the patches on the top and bottom surfaces of the smart beam increases the actuation power of the patches [36,38]. In order to investigate the effects of the symmetric placement of the patches on the response of the smart beam, a case is considered. That involves the modeling of the smart beam in unimorph configuration. The unimorph model of the smart beam shown in Figure 3.11.a. This model is obtained by removing the bottom actuators of the bimorph smart beam model shown in Figure 3.9. The response of the unimorph smart beam to the piezoelectric actuation of 300V is calculated and the resulting deformation of the unimorph beam is shown in Figure 3.11.b. The comparison of Figure 3.10.a and Figure 3.11.b reveals that despite the reduction obtained in the stiffness of the structure, the removal of the actuators from one face significantly reduces the response from 1.015 mm to 0.689 mm.

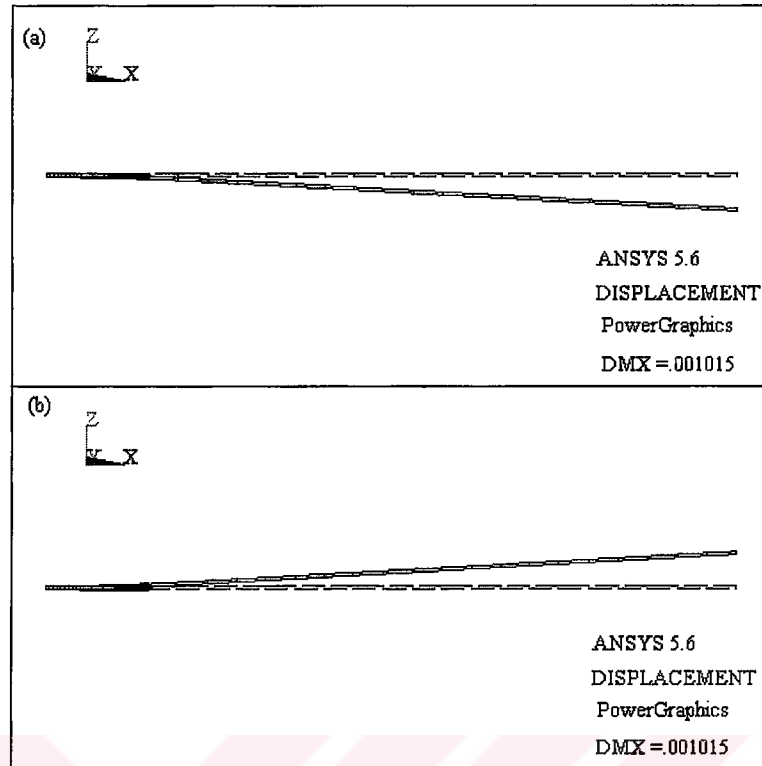


Figure 3.10. The comparison of the effects of the actuator polarization and the electric field on the deformation of the smart beam by,  
 a. Piezoelectric actuation of -300 V ( $V_i=0$ ,  $V_o=300$  V)  
 b. Piezoelectric actuation of 300V ( $V_i=0$ ,  $V_o=-300$  V)



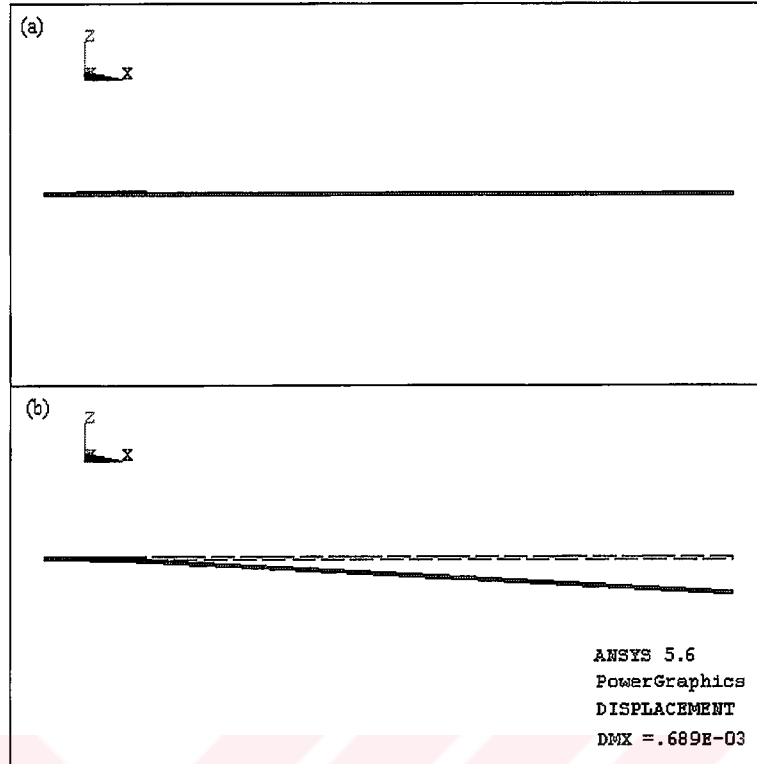


Figure 3.11. The unimorph smart beam  
 a. Side view of the finite element model  
 b. The deformation of the model at 300V actuation ( $V_i=0$ ,  $V_o=300$  V)

### 3.4.3 Effects of Piezoelectric Patch Position

In this section, the influence of the positions of  $8 \times (20 \times 25 \times 0.5)$  mm BM500 type patches on the smart beam is considered. For this reason, the positions of the patches relative to the clamped end are varied. During the analysis, the tip displacement responses of the smart beam are calculated at eight different patch locations for a piezoelectric actuation value of 300V and the results are plotted in Figure 3.12. It can be seen from the figure that as the patches move away from the clamped end, the response decreases. This is due to the higher strain developed near the fixed end. For this reason, the patches should be placed on the beam as close as possible to the fixed end.

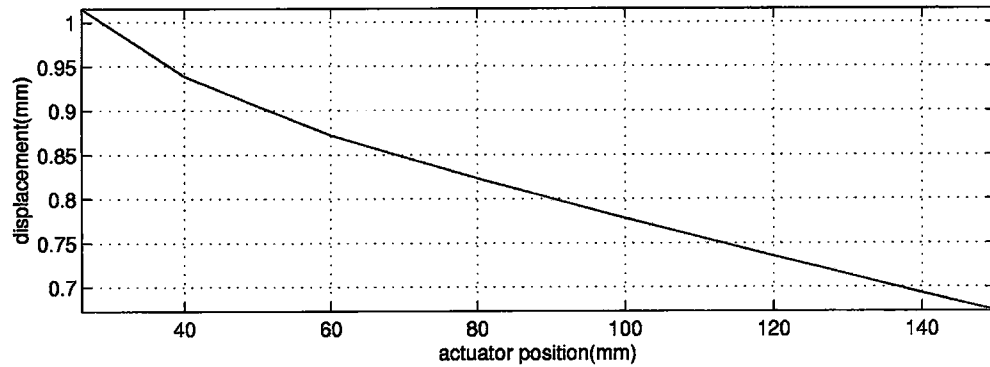


Figure 3.12. The effects of the patch position on the response of the smart beam

#### 3.4.4 The Influence of the Piezoelectric Patch Size

Depending on the mission requirements the size of the piezoelectric patches can be altered. The effects of the increase in the size of the patches on the response are investigated in terms of the coverage ratio. The coverage ratio is defined as the ratio of the area covered by the piezoelectric patches to the surface area of the passive structure. The coverage ratio of the initial configuration of the smart beam given in Figure 3.9 is increased during the analysis by enlarging the actuator length. The tip displacement results for eight coverage ratio values obtained by the application of piezoelectric actuation at 300V are shown in Figure 3.13. Although the increase in the size of the actuator makes the smart structure stiffer, it also increases the energy transmitted to the structure thereby giving a rise to the energy transmitted to the structure. That consequently increases the response of the smart structure.

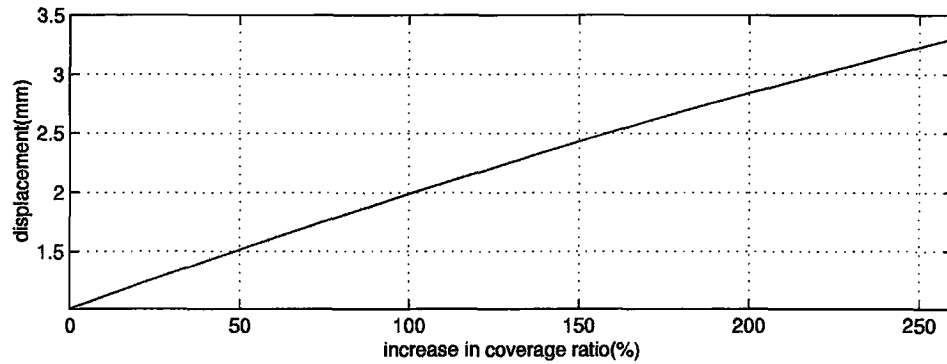


Figure 3.13. The influences of the patch size variation on the response of the smart beam.

### 3.4.5 Effects of the Actuation Voltage Variation and the Maximum Admissible Piezoelectric Actuation Value

This section aims to determine the effects of the actuation voltage variation on the response of the smart beam and on the integrity of the piezoelectric actuators.

The tip displacement responses of the smart beam are calculated for eight piezoelectric actuation values and the results are plotted against the piezoelectric actuation voltages as shown in Figure 3.14.a. Since the theoretical model is in the linear range of piezoelectricity and the influences of the large deformations are negligible [116,119], the response of the structure is found to vary linearly with the actuation voltage.

Piezoelectric material used in this study is brittle and has tensile strength value, which is in the order of 63 MPa [116]. The level of the stress, which will develop in the piezoelectric material, can be critical in adverse applications. In order to determine the maximum possible piezoelectric actuation value that can safely be applied, the variation of the Von Mises stresses developed in the actuators due to the piezoelectric actuation is analyzed. For this reason, the Von misses stresses

developed on the piezoelectric patches are calculated for eight piezoelectric actuation voltages and the results are shown in Figure 3.14.b. Similar to the tip displacement results, the Von Mises stresses developed are also found to vary linearly with the actuation voltage. Since the Von Mises stresses developed in the piezoelectric actuators are in the order of 7-8 MPa for normal operating conditions of the smart beam (200-400V), the piezoelectric actuators are not expected to fail.

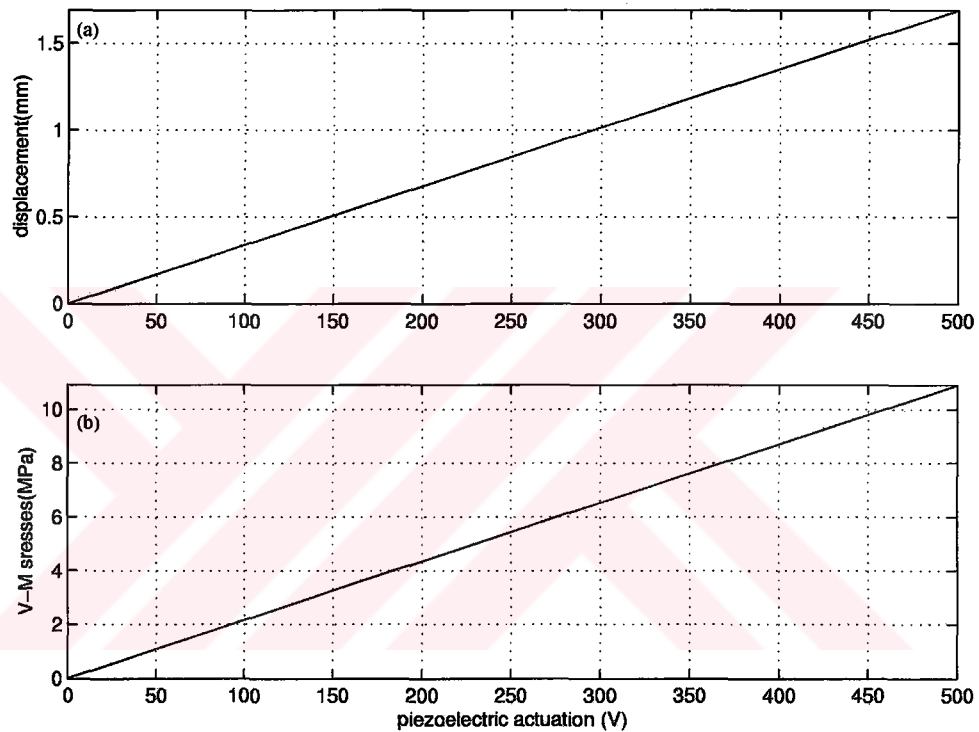


Figure 3.14. The influences of the piezoelectric actuation voltage variation  
a. The tip displacement response of the smart beam  
b. The Von-Mises stresses developed in the piezoelectric actuators

### **3.4.6 The Influence of the Transverse and Normal Stresses**

The modeling of the passive portion by using compatible prismatic elements not only guarantees the proper transfer of the nodal forces generated by the active elements on the passive elements at the interface where these elements meet, but also allows the computation of the through thickness variation of the transverse shear and normal stresses developed on the passive portion of the smart beam due to the piezoelectric actuation.

In this section, the factors influencing the generation of the transverse and normal stresses are investigated by considering the variation of the three parameters. These parameters are the piezoelectric actuation voltage, the patch size described in terms of the coverage ratio, and the patch thickness. During the analysis, the maximum stress values on the passive portion (aluminum beam) of the smart beam, are found to be in the vicinity of the locations where the piezoelectric patches bonded on the aluminum beam for all cases considered in the study.

The influences of the piezoelectric actuation voltage variation on the maximum transverse and normal stresses developed in the passive portion of the smart beam is analyzed by considering the response of the smart beam to eight piezoelectric actuation values and the results obtained are shown in Figure 3.15. It can be seen from the figure that the actuation of the piezoelectric patches results in the generation of the significant normal and transverse stresses. These stresses are found to vary linearly with the piezoelectric actuation voltage.

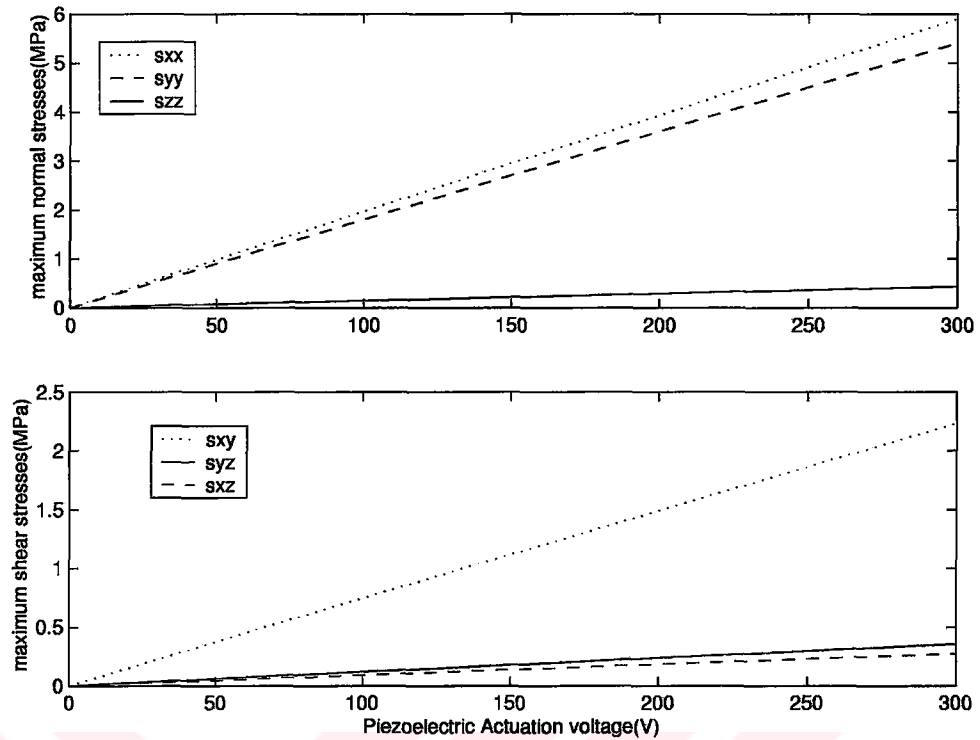


Figure 3.15. The influences of the voltage variation on the maximum stresses developed on the passive portion of the smart beam ( $S_{xx}$ ,  $S_{yy}$ ,  $S_{zz}$  are the maximum normal stress component along x, y and z directions respectively ,  $S_{xy}$ ,  $S_{yz}$ ,  $S_{xz}$  are the maximum shearing stress component on xy, yz and xz planes respectively)

In addition to the piezoelectric actuation voltage variation, the variations in the patch size and thickness also affect the generation of the transverse and normal stresses on the passive portion of the beam. Figure 3.16 and Figure 3.17 show the influences of the piezoelectric patch size and thickness on these stresses for a piezoelectric actuation of 300V.

The response of the smart beam is calculated by using eight coverage ratio values and the results obtained are shown in Figure 3.16. Since the increase in the size of the piezoelectric patches yields to an increase in the energy transmitted to the smart beam for a specified piezoelectric actuation value the stresses developed also increases with the size of the patches.

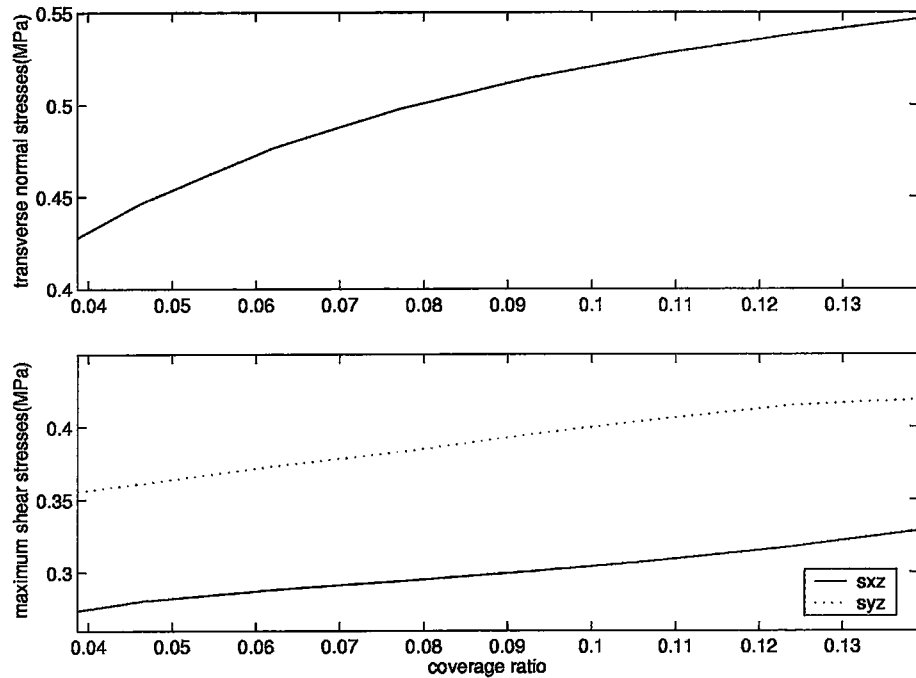


Figure 3.16. The influence of the piezoelectric patch size on the maximum transverse normal and shear stress developed on the passive portion of the smart beam ( $S_{zz}$  is the maximum normal stress component along z direction, and  $S_{yz}$ ,  $S_{xz}$  are the maximum shearing stress component on yz and xz planes respectively).

The influences of the piezoelectric patch thickness are also analyzed by considering twelve actuator thickness values. The results obtained are plotted in Figure 3.17. Because the increase in the thickness of the piezoelectric patches effectively reduces the actuation power of the piezoelectric patches, it decreases the transverse stresses developed in the passive portion of the smart beam.

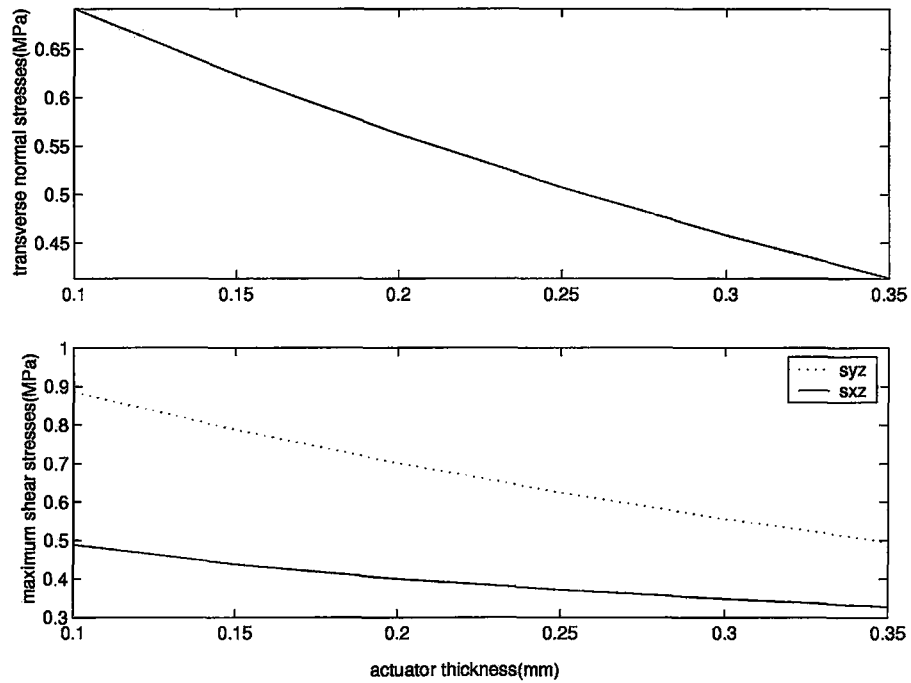


Figure 3.17. The influence of the piezoelectric patch thickness on the maximum transverse normal and shear stress developed on the passive portion of the smart beam.

By considering the results of the parametric study conducted for the determination of the factors affecting the generation of the transverse normal and shear stresses, it can be concluded that the generation of these stresses depends largely on the piezoelectric actuation power transmitted to the passive portion rather than the local stiffening effects which is closely related to the size and thickness of the piezoelectric patches. It can be seen from these figures that the piezoelectric actuation generates significant amount of transverse and normal stresses on the passive portion of the smart beam in the vicinity of the regions where the patches interfaces with the passive beam. Hence any exclusion of these stresses may yield to erroneous results



### 3.4.7 The Influence of the Placement of the Patches on the Natural Frequencies of the Smart Beam

This section, investigates the effects of the placement of the actuators on the natural frequencies of the aluminum beam-like structure. For this reason, the natural frequencies of 507×51×2 mm aluminum beam-like structure are determined by removing the piezoelectric patches of the smart beam shown in Figure 3.9 and are compared with the resonance frequencies of the smart beam. The results are shown in Table 3.2.

Table 3.2. The influence of the piezoelectric patches on the natural frequencies of the passive beam-like structure

Frequency (Hz)	Passive beam	Smart Beam (*)	Increase
$f_1$	6.679	7.3047	%9.37
$f_2$	41.858	44.112	%5.38
$f_3$	117.20	117.22	%0.1

(\*): The theoretical results obtained without prestressing,  $\Delta V=0$

The presence of the patches, as expected, shifts the natural frequencies to higher values. This effect is known as the stiffening effects of the patches and is more prominent at lower frequencies. The first two mode shapes of the smart beam are shown in Figure 3.18.

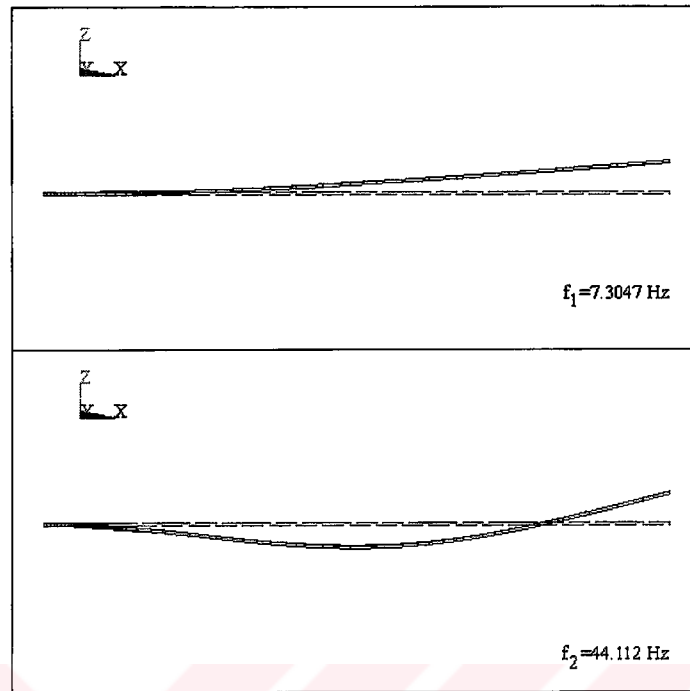


Figure 3.18. The first two natural frequencies and mode shapes of the smart beam.

#### 3.4.8. Sensor Placement

In this thesis, the strain gage sensors are considered to sense vibrations due to the first two flexural modes of the smart beam. The finite element method allows the determination of the most suitable location for the strain gage sensors. By using the modal analysis results, the location for the collocated strain gage sensor pair is determined. In order to determine location for the strain gages, which will be used to sense first two modes of vibrations modal strain values are considered. The location of the sensor is determined at the location where the strain values attain their highest value for the first two modes of vibrations. Figure 3.19 shows the position and the configuration of the strain gage sensors on the smart beam.

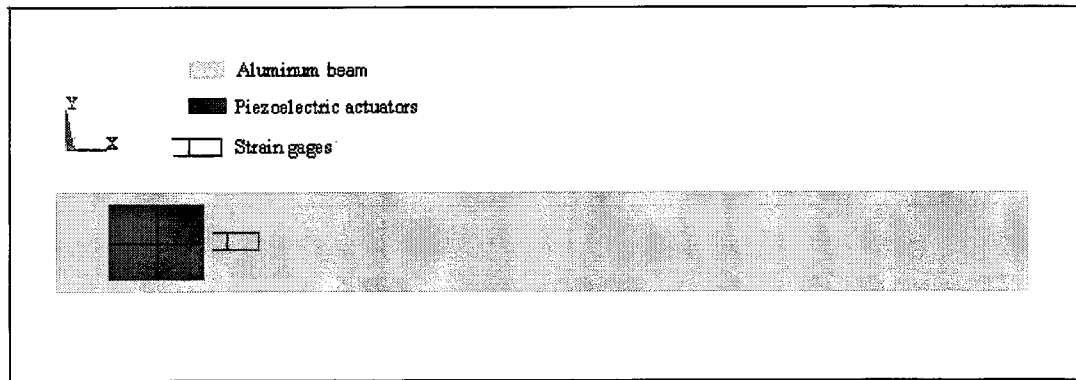


Figure 3.19. The position and the configuration of the strain gages on the smart beam.

### 3.5 Finite Element Modeling of Smart Fin

Based on the finite element modeling technique presented for the smart beam, this section presents the finite element modeling technique for the design and analysis of the smart fin. The smart fin is actually a plate with symmetrically placed piezoelectric patches and modeled according to the plate theory. Since its shape looks like the typical vertical tail of an aircraft, it is called smart fin.

During the development of the smart fin model, a model having parametric design capability is created. The design parameters include the actuator size and their positions. Prismatic elements (SOLID5) are used for the modeling of the active portion (piezoelectric patches) and compatible solid elements (SOLID45) are considered for the modeling of the passive portion (aluminum plate). By using the modal analysis results, which were obtained by the finite element modeling,  $24 \times (25 \times 25 \times 0.5 \text{ mm})$  BM500 type patches are placed on the aluminum fin at the locations where the modal strain values reaches their maximum values at its first two modes of vibration. The identically polarized patches are bonded symmetrically on top and bottom surfaces of the fin.

An additional symmetrically placed piezoelectric BM500 type sensors are also considered to sense bending and torsional vibrations. The finite element model developed in the study is shown in Figure 3.20. The smart fin is modeled in C-F-F-F (Clamped-Free-Free-Free) configuration. The smart fin considered to be clamped along  $y=0$  edge.

The theoretical static transverse displacements of the smart fin to various piezoelectric actuation values are given in Figure 3.21. The first two theoretically determined natural frequencies and mode shapes are shown in Figure 3.22.

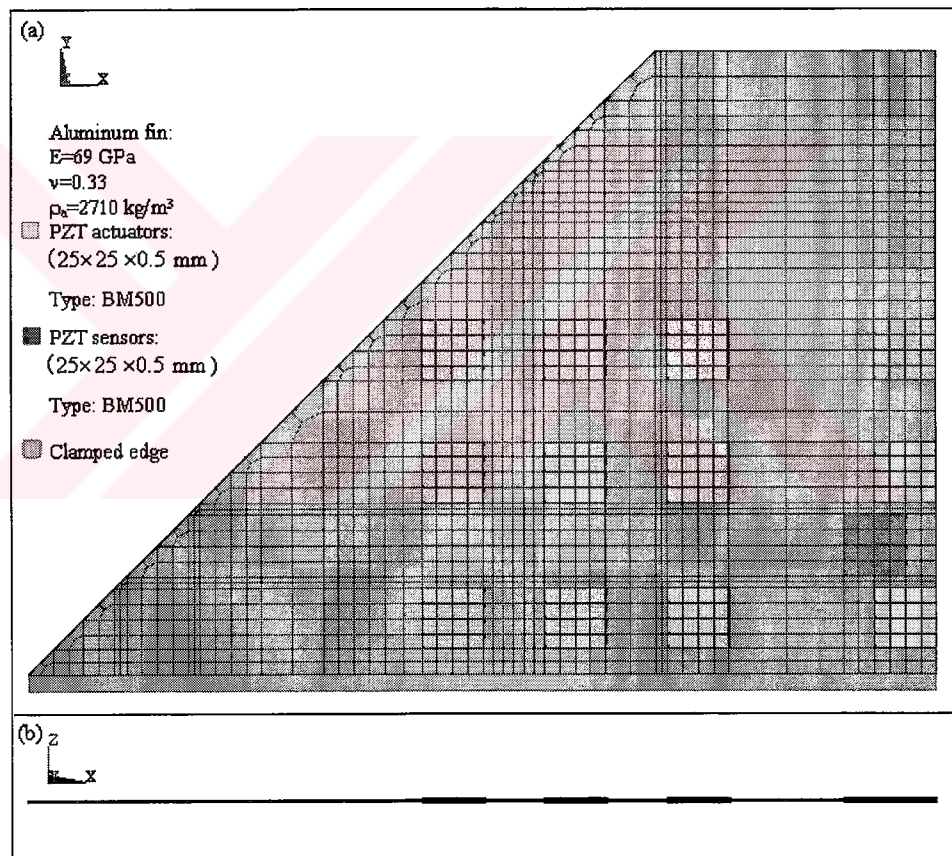


Figure 3.20. The finite element model of the smart fin (4438 nodes and 416 SOLID5 and 1491 SOLID45 elements)

- a. Top view
- b. Side view

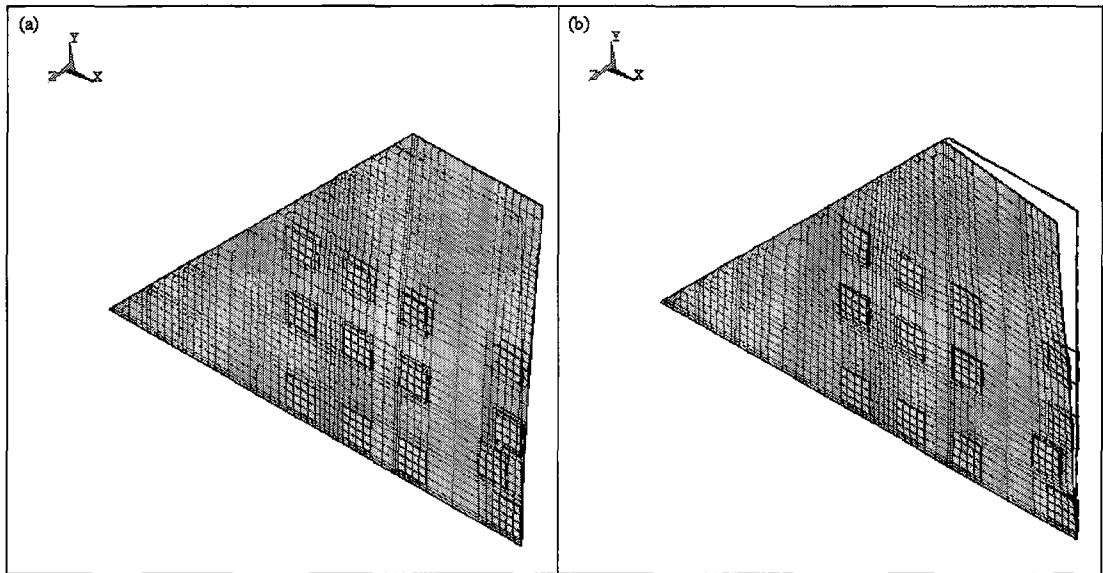


Figure 3.21. The theoretical transverse displacements of the smart fin to various piezoelectric actuation values

a. Bending by 300V

b. Twisting by +300V and -300V

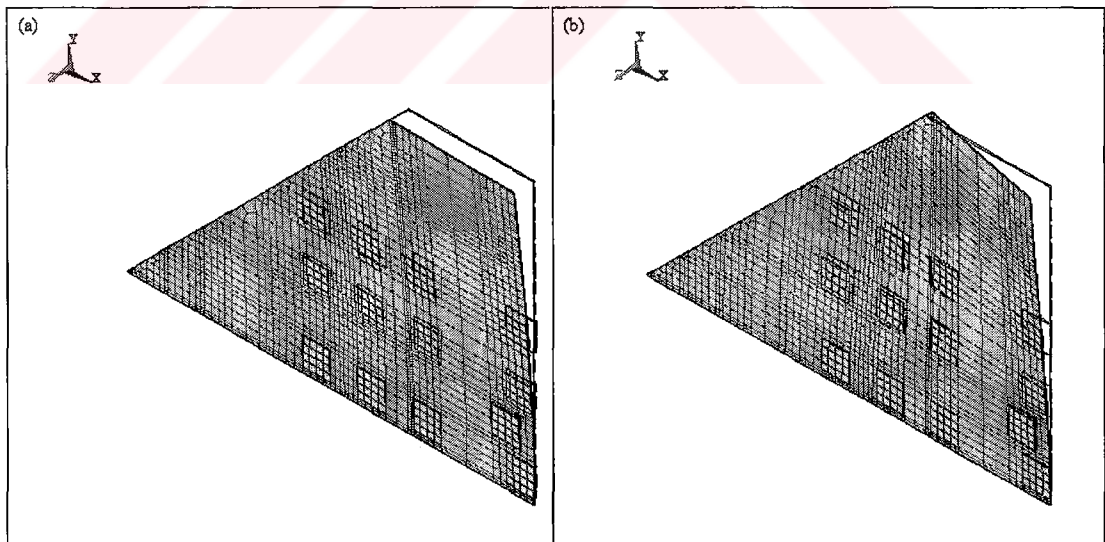


Figure 3.22. The first two theoretical mode shapes of the smart fin, ( $\Delta V=0$ )

a. The flexural first mode ( $f_1=14.963$  Hz)

b. The torsional second mode ( $f_2=45.737$  Hz)

Since the main idea behind the vibration suppression is to excite the smart structure with an opposite vibration relative to the observed one so that vibration cancellation will be achieved, the resemblances between the static deformation patterns and the mode shapes are considered to confirm the configuration of the piezoelectric patches on the aluminum fin for exciting or suppressing the vibrations due to the first two modes of the smart fin.

### **3.5.1 The Effects of Piezoelectric Patch Position**

In order to determine the effects of the patch position on the response, two cases are considered. At each one, by keeping the relative distance between the piezoelectric patches constant, the x or y positions of all patches are varied from their original configuration given in Figure 3.20. During the theoretical calculations, the variations in the positions of the patches are expressed in terms of the percent increase from the original configurations. The right-tip corner transverse displacement results are obtained for eight patch locations and the results are plotted in Figure 3.23.

It is evident from the Figure 3.23 that as the patches are moved away from the root ( $y=0$ ) along y direction, the response of the smart fin, reduces for both bending and twisting actuation. This is due to the higher strain developed near the root. For this reason, the patches should be placed on the fin as close as possible to the root. Furthermore, as the patches are moved away from the leading edge ( $x=0$ ) the bending response remains less affected but the twisting response reduces due to the reduction of the twisting arm that is the x distance between the patches. In order to improve the twisting response this distance should be maximized.

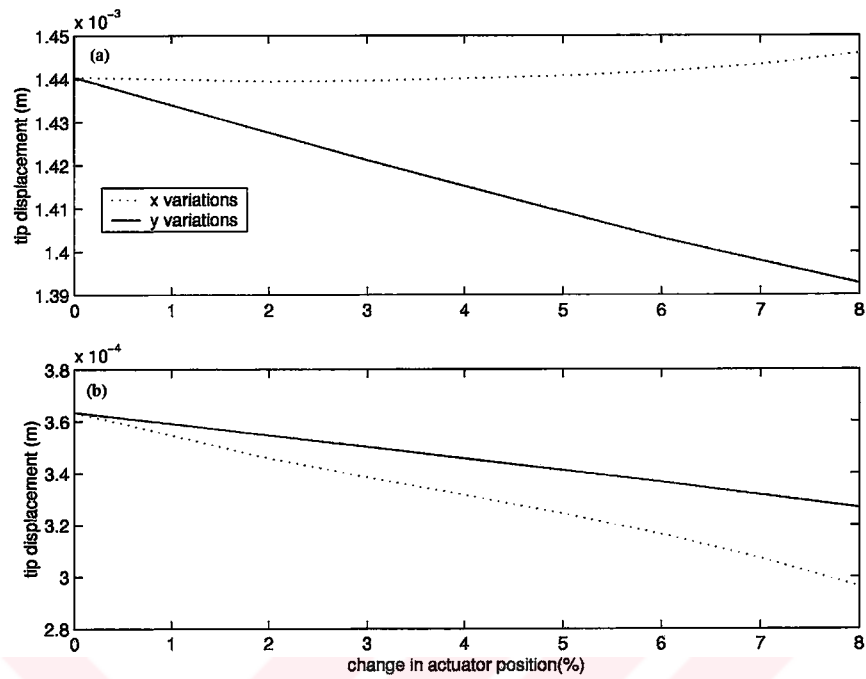


Figure 3.23. The effects of the patch position on the response of the smart fin  
a. Bending (by 300V)  
b. Twisting (by +300V and -300V)

The effects of the patch location on the first and second natural frequencies of the smart fin are also investigated for the same eight actuator locations and the results are shown in Figure 3.24.a and Figure 3.24.b respectively.

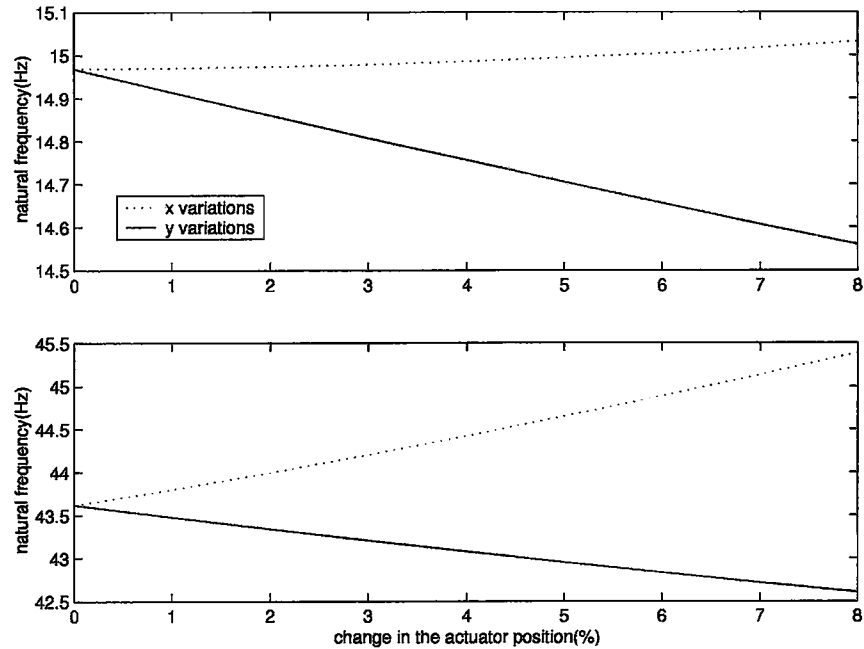


Figure 3.24. The influences of the patch position on the first two theoretical natural frequencies of the smart fin, ( $\Delta V=0$ )

a. First natural frequency ( $f_1 = 14.963$  Hz)

b. Second natural frequency ( $f_2 = 45.737$  Hz)

It can be seen from Figure 3.24 that, while the x variations of the actuator positions do not appreciably affect the first natural frequency, it increases the second natural frequency. The y variations in the actuator positions however, reduce both first and the second natural frequencies. These results can be attributed to the variations in the flexural and torsional stiffness values of the smart fin associated with the x or y variations. This occurs in a way that, as the patches are moved away from the root the flexural stiffness of the smart structure decreases. Thus, the frequencies reduce. Since the flexural stiffness variations remain less sensitive to the x variations, the first frequency of the smart fin remains almost unaffected. Conversely, as the patches get close to the trailing edge the torsional stiffness significantly increases giving rise to an increased second frequency.



### 3.5.2 The Influence of the Piezoelectric Patch Size

According to the mission requirements, the size of the piezoelectric actuators can be altered. The effects of the increase in the size of the actuator on the response in terms of the change in the coverage ratio are investigated. By using the original configuration of the smart fin, the coverage ratio is increased and the results in terms of the right tip corner displacement, for the piezoelectric actuation of 300V are calculated for eight coverage ratio values and the results are shown in Figure 3.25. Although the increase in the size of the actuators makes smart fin stiffer, it also increases the energy transmitted to the smart fin giving a rise to the response for the specified piezoelectric actuation value.

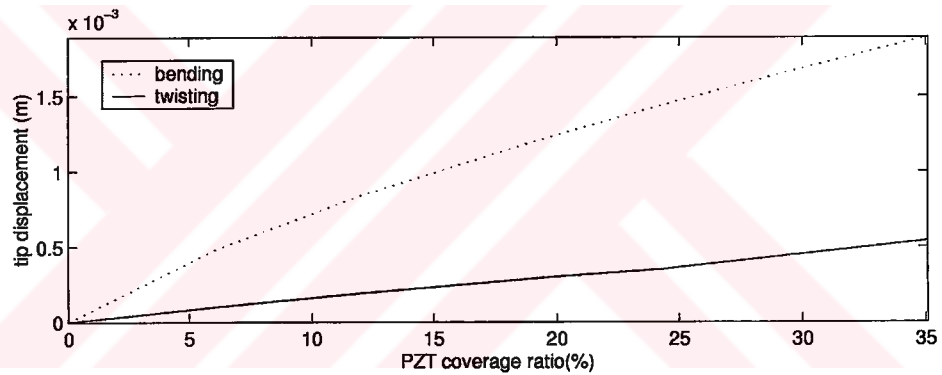


Figure 3.25. The comparison of the effects of the patch size variation on the right tip displacement of the smart fin

### 3.5.3 The Maximum Admissible Piezoelectric Actuation Value

In order to determine the maximum possible piezoelectric actuation value, the Von Mises stresses developed in the patches for various actuation types and values should be investigated prior to the operation. The Von Mises stresses for various actuation types and voltages are calculated and the results are shown in Figure 3.26. Since the resultant Von Mises stresses developed in the patches are in the order of 10 MPa for normal operating conditions (200-300V), the piezoelectric actuators are not expected to fail.

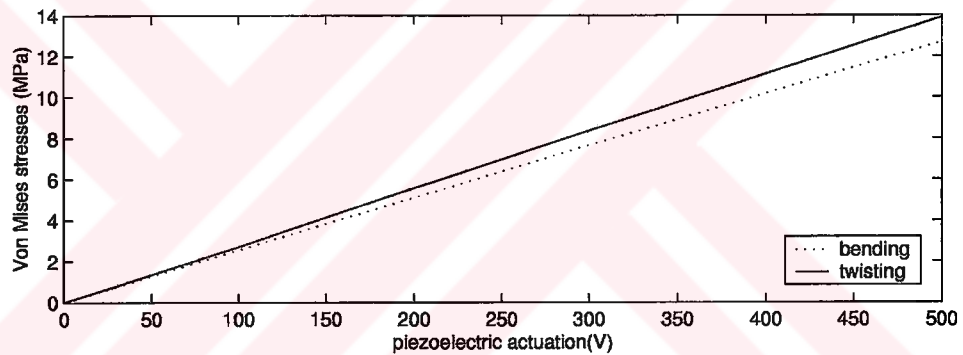


Figure 3.26. The effect of the piezoelectric actuation voltage on the Von Mises stresses developed within the piezoelectric patches of the smart fin.

### 3.5.4 The Influence of the Transverse and Normal Stresses

The modeling of the passive portion by using the compatible solid elements not only guarantees the proper transfer of the nodal forces generated by the active elements to the passive elements at the interface, but also allows the computation of the through thickness variations of the transverse and normal stresses developed on the passive portion of the smart fin due to the piezoelectric actuation.

In order to investigate the importance of the transverse and normal stresses, the smart fin is actuated for bending and twisting. Figures 3.27 and 3.28 give the variation of the resultant stress components as a function of the piezoelectric actuation voltage. For the twisting actuation, shear stress in yz plane is the maximum stress component. Therefore, any exclusion of these stresses may lead to the inaccurate results.

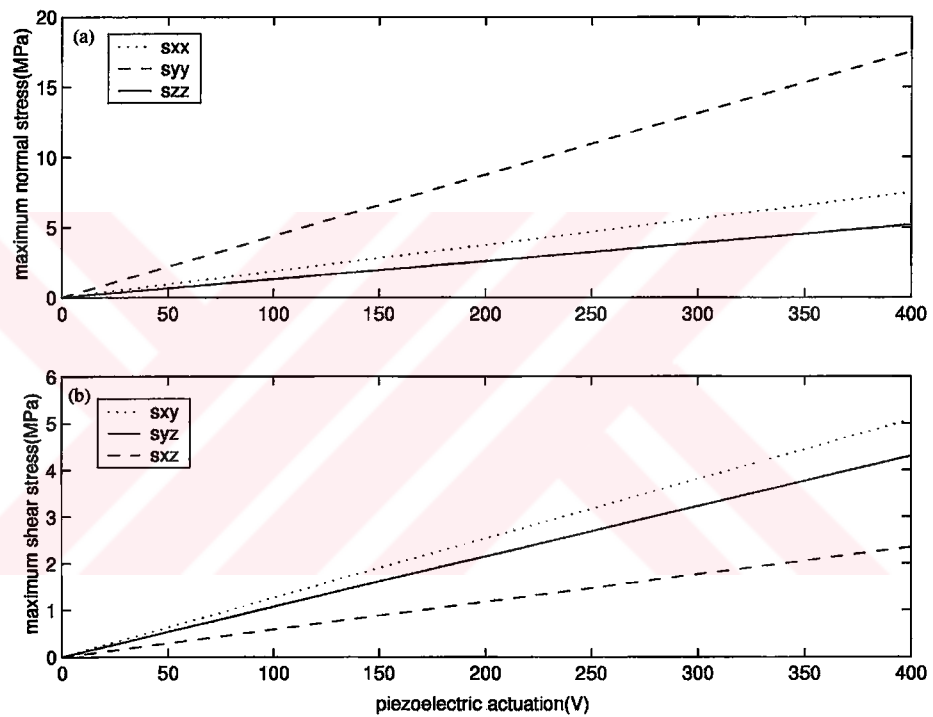


Figure 3.27. The comparison of the effects of the voltage variation on the maximum stresses developed in the passive portion of the smart fin due to the piezoelectric bending actuation ( $S_{xx}$ ,  $S_{yy}$ ,  $S_{zz}$  are the maximum normal stress component along x, y and z directions respectively  $S_{xy}$ ,  $S_{yz}$ ,  $S_{xz}$  are the maximum shearing stress component on xy, yz and xz planes respectively)

- a. The normal stresses
- b. The shearing stresses

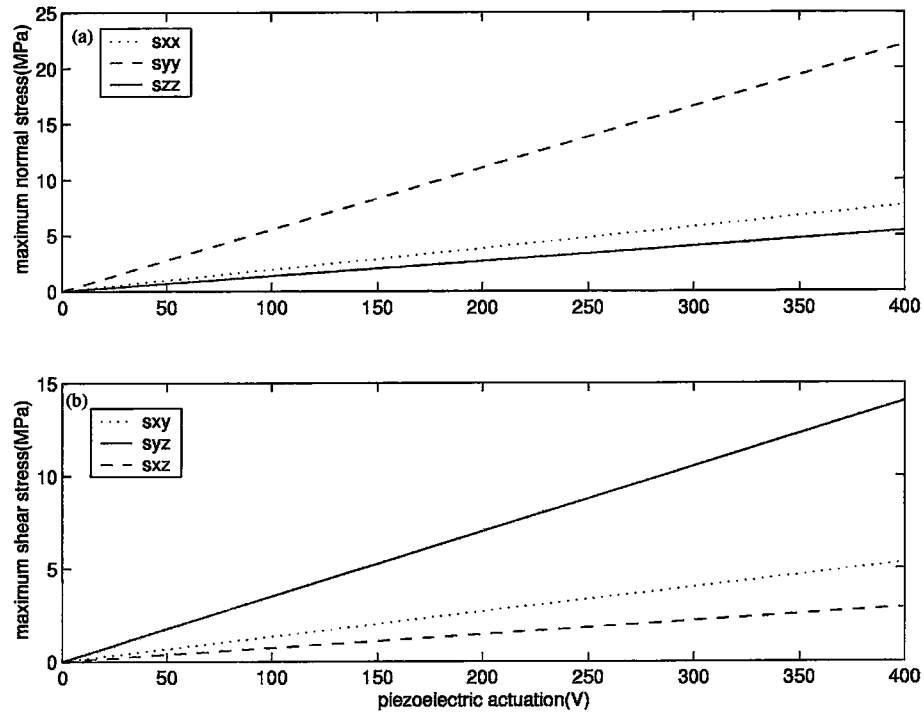


Figure 3.28. The comparison of the effects of the voltage variation on the maximum stresses developed in the passive portion of the smart fin due to the piezoelectric twisting actuation (Legend of Figure 3.27)

a. The normal stresses

b. The shearing stresses

### 3.5.5 Placement of Strain Gage Sensors

Finite element method allows the determination of the suitable locations of the sensors for vibration sensing. These locations can be determined by the utilization of mode shapes of the smart structure. In this thesis, by using the modal strain distribution for the smart fin at its first two modes, three locations where the strain components reach their maximum values are determined. These locations are then considered for attachment of the strain gage sensors to sense the vibrations of the smart fin. The locations so obtained are shown in Figure 3.29. In this model, while the strain gage at location (1) is used for the measurement of strain in x direction,

locations (2) and (3) are considered in the measurement of the strain in y direction. Figure 3.29 also includes a pair of symmetrically placed piezoelectric patch, which are intended to be used as a sensor.

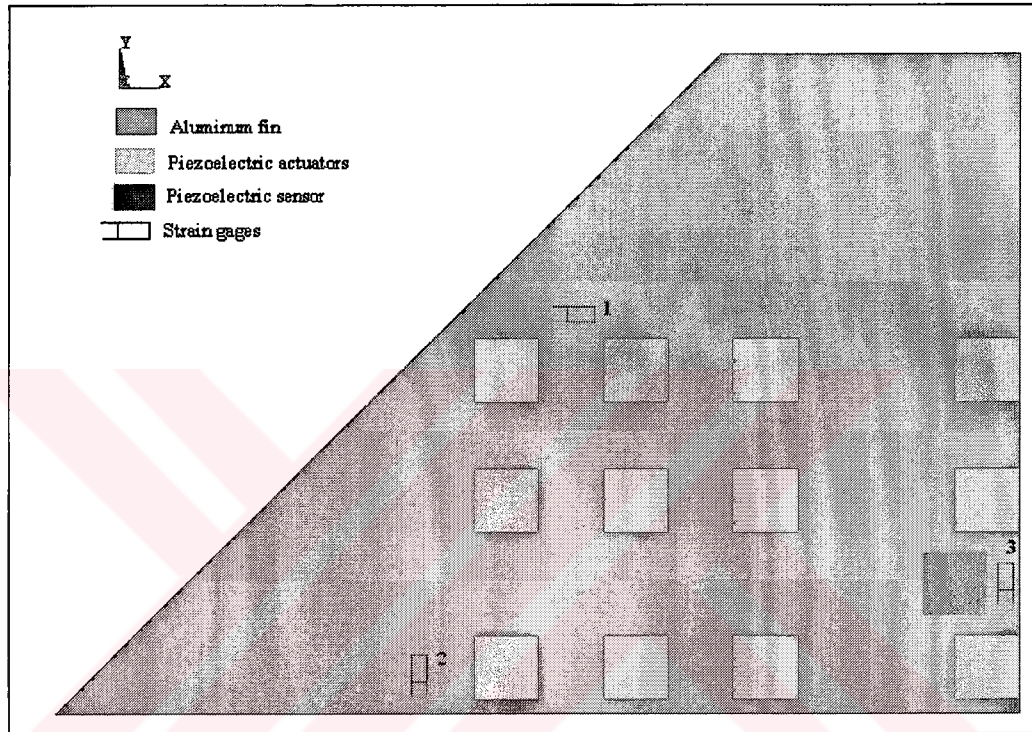


Figure 3.29. The placement and the configuration of the strain gages and piezoelectric patches on the smart fin

The influences of the piezoelectric actuation voltage variation on the responses at the three strain gage sensor locations are calculated for both bending and twisting piezoelectric actuations. Figure 3.30 gives the results in terms of the magnitude of the strain at the measurement locations. It can be seen from these figures that for bending and twisting actuation the highest response is calculated at location (2).

Since the theoretical model is in the linear range of the piezoelectricity and the effects of the large deflections are considered to be negligible, the response of the smart fin is also found to vary linearly with the actuation voltage.

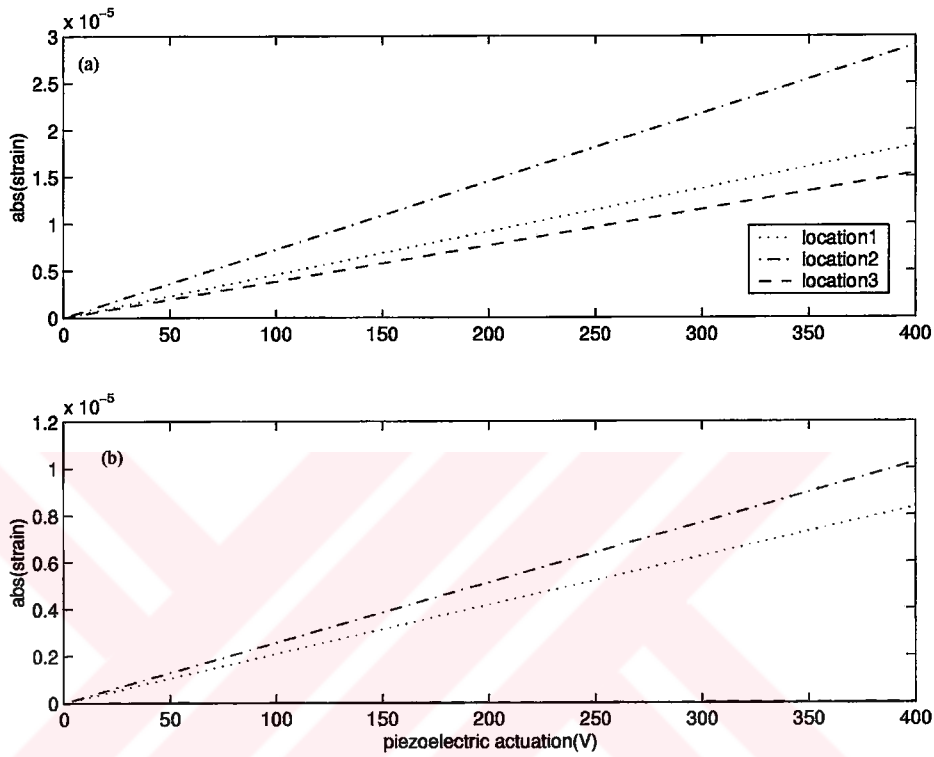


Figure 3.30. The comparison of the response of the smart fin (location (1):  $\epsilon_x$ , locations (2) and (3):  $\epsilon_y$ )  
 a. Bending by 300V  
 b. Twisting +300V and -300V

### 3.6 Conclusions

This chapter, by using ANSYS® (v.5.6) software, presented the effectiveness of the finite element modeling technique in the analysis and design of smart structures. During the course of the work, basic analytical formulations for the analysis of piezoelectric materials were also given for the completeness. The formulations were adapted to BM500 type piezoelectric patches and the limitations of the modeling techniques were outlined as well.

The finite element method offers fully coupled three-dimensional, thermo-mechanical-electrical analysis of the smart structures. This allows the prediction of the reciprocal relations between the sensors and actuators. The simulation of the smart structures also provides the necessary information for the design of the closed loop controllers, which suppress the vibrations of the smart structures.

The smart structures designed in this thesis, consisted of aluminum beam-like and plate-like structures modeled in cantilevered configuration with surface bonded PZT patches. The identically polarized piezoelectric patches were bonded symmetrically on top and bottom surfaces of the passive portion of the smart structures to achieve the bimorph configuration.

The finite element method was shown to be especially advantageous in handling the multiple design parameters of piezoelectric patches and sensors. By enabling the parametric design feature of the technique, the influences of the piezoelectric patch placement and size on the responses of the smart structures can be obtained. The technique also allows the determination of the maximum admissible piezoelectric actuation value, hence effectively gives the actuator limits. Based on these models, the sensor locations can be found.

This thesis focused on the accurate representation of anisotropy and the electromechanical coupling inherent to the piezoelectric materials and their effects on the passive portion of the smart structures. The influences of the element type selection on the response and the importance of the transverse stresses and normal stresses on the passive portions of the smart structures were dealt with.

It was shown in this chapter that the utilization of inconsistent hybrid finite element models including shell-solid elements yield erroneous results in the analysis of the smart structures.

The modeling of the passive portions of the smart structures by using linear prismatic elements with extra displacement shapes is shown to be a correct approach for the simple smart structures considered in the thesis, but the difficulties in the modeling of the irregular geometries with these elements and the increased computing time limit their potential applications on realistic aerospace structures.

In order to eliminate these difficulties, the offset modeling techniques for the shell-solid hybrid models should be improved or shell piezoelectric elements having quadratic displacement and voltage behavior must be developed.

The modal analysis based sensor and actuator placement technique considered in the thesis does not form a basis for a formal optimization. It gives satisfactory results for the simple structures such as the ones considered in the thesis. The extension of the technique to the realistic structures is known to be very difficult.



## CHAPTER 4

### THEORY OF ACTIVE VIBRATION CONTROL FOR SMART STRUCTURES

#### 4.1 Introduction

This chapter describes the finite element based system modeling techniques and the robust control design and analysis applied to the smart structures. This thesis combines the methods of structural dynamics and the structural control design and analysis techniques. Thus, it aims to form a link between the structural and control engineering disciplines by incorporating the methods of structural dynamics into the control concepts.

In the design of aerospace structures and flight control systems, the inevitable interaction between the flight mechanics, structural dynamics and flight control system dynamics must always be considered. This is necessary to improve the handling qualities and travel comfort. The utilization of smart structure technologies is believed to offer effective means of shape and active vibration control of aerospace structures within acceptable reliability and cost margins.

The active vibration control of smart aerospace structures that inherently exhibit flexibility becomes more important, when the designers attempt to push with,

the state of the art, faster and lighter structures for aerospace applications. Generally two steps are necessary for the control of a flexible smart structure.

First a precise mathematical model, which is capable of handling the electromechanical coupling effects, must be developed. Second, a robust controller that successfully incorporates the possible modeling uncertainties must be designed.

#### **4.2 Finite Element Based System Modeling Technique for Smart Structures: State-Space Representation**

The system models of smart structures can be obtained by using the finite element modeling technique. The aim in the system modeling is to obtain the mathematical description of the structure which is suitable for the design of the control system. The system modeling technique involves the determination of the state space representation of the system. The model of the system can also be found by using the system identification approach [58,59,60]. The system model obtained from experimental data may also be used to tune the accuracy of the model derived from the finite element method [59]. This approach will be briefly explained in Chapter 5.

In the dynamical analysis of the smart structures, the theoretical models are represented by the second order linear differential equations with constant coefficients. In that analysis, the system is modeled by the generalized coordinates. In the controller design however, the dynamics of the structure is modeled by the first order equations which are in terms of states. The approach used in the controller design is known as the state-space representation.

Although the choice of the coordinates used in the state-space representation of the model is arbitrary; the use of two coordinate systems, namely, nodal (or physical)

and modal coordinates is common [122,123]. While the nodal coordinates are defined through the displacements and velocities of the structural locations called the nodes, the modal coordinates are defined in terms of the displacements and velocities at the structural modes.

#### 4.2.1 The Formulation in Nodal Coordinates

The finite element method can effectively be used in the modeling of smart structures. This section describes the application of the nodal coordinates approach in the modeling of smart structures. The governing differential equation of motion for a smart structure subjected to the piezoelectric actuation can be represented as [77,123],

$$[M]\{\ddot{q}\} + [D_o]\{\dot{q}\} + [K]\{q\} = [F]\{u\} \quad (4.2.1)$$

here, by defining  $N$  as the number of nodes of the finite element model and  $p$  as the number of degrees of freedoms associated with each node (for the finite element models of this thesis which are consisting of prismatic elements,  $p=3$ ),  $[M]$ ,  $[D_o]$  and  $[K]$  give  $Np \times Np$  mass, damping and stiffness matrices respectively. In this representation, the vector  $\{q\}_{Np \times 1}$  represents the generalized vector of displacements,  $\{\dot{q}\}_{Np \times 1}$  symbolizes the generalized vector of velocities and  $\{\ddot{q}\}_{Np \times 1}$  defines the generalized vector of accelerations for each node. Defining  $k$  as the number of piezoelectric actuators  $[F]_{Np \times j}$  is the unit piezoelectric voltage generalized force transformation matrix from  $j^{\text{th}}$  ( $j=1$  to  $k$ ) actuator applicable to each node and  $\{u\}_{j \times 1}$  is the piezoelectric actuation voltage vector associated with the  $j^{\text{th}}$  piezoelectric actuator.

In the nodal coordinates based system modeling approach for smart structures, Rayleigh damping model is generally used. Rayleigh damping is effectively a proportional damping where viscous damping matrix  $D_o$  is directly proportional to mass matrix, stiffness matrix or both [121,122] and given as,

$$[D_o] = \gamma[M] + \beta[K] \quad (4.2.2)$$

where,  $\gamma$  is the constant mass matrix multiplier and  $\beta$  defines constant stiffness matrix multiplier. When only the stiffness damping is used ( $\gamma=0$ ) with the  $i^{\text{th}}$  ( $i=1$  to  $N$ ) natural frequency  $\omega_i$  of the system, the modal loss factor  $\zeta_i$  takes the form of equation (4.2.3)

$$\zeta_i = \frac{\omega_i}{2} \beta \quad (4.2.3)$$

In order to obtain a state space representation of a smart structure, the differential equation of motion described by equation (4.2.1) is premultiplied with  $[M]^{-1}$  (for nonsingular mass matrix)

$$\begin{aligned} \{\ddot{\mathbf{q}}\}_{Np \times 1} + [M]_{Np \times Np}^{-1} [D_o]_{Np \times Np} \{\dot{\mathbf{q}}\}_{Np \times 1} + \\ [M]_{Np \times Np}^{-1} [K]_{Np \times Np} \{\mathbf{q}\}_{Np \times 1} = [M]_{Np \times Np}^{-1} [F]_{Np \times j} \{\mathbf{u}\}_{j \times 1} \end{aligned} \quad (4.2.4)$$

where

$$p = 1 \text{ to } 3, j = 1 \text{ to } k$$

Furthermore, selection of the state vector  $\{\mathbf{x}\}$ , as  $\{\mathbf{q} \quad \dot{\mathbf{q}}\}^T$  leads to the formation of the specific form given in equation (4.2.5)

$$\begin{aligned} \left\{ \begin{array}{c} \dot{\mathbf{x}} \\ \mathbf{x} \end{array} \right\}_{2Np \times 1} = \begin{bmatrix} [0] & [I] \\ -[M]^{-1}[K] & -[M]^{-1}[D_o] \end{bmatrix}_{2Np \times 2Np} \left\{ \begin{array}{c} \mathbf{x} \end{array} \right\}_{2Np \times 1} + \begin{bmatrix} [0] \\ [M]^{-1}[F]\{\mathbf{u}\} \end{bmatrix}_{2Np \times 1} \end{aligned} \quad (4.2.5)$$

where  $[0]$  and  $[I]$  defines zero and identity matrices respectively. In this case, defining  $r$  as the number of sensors, the output  $\{y\}$  of the system can be written in the form of equation (4.2.6)

$$\{y\}_{i \times 1} = [C_q]_{i \times N_p} \{q\}_{N_p \times 1} + [C_v]_{i \times N_p} \{\dot{q}\}_{N_p \times 1}, \quad (i = 1 \text{ to } r) \quad (4.2.6)$$

where,  $[C_q]$  and  $[C_v]$  give the displacement and velocity output matrices respectively. The displacement and velocity output matrices represent the nodes where the response is measured. Such that, if no measurement is made on a node in the finite element model, its value is set to zero otherwise taken to be unity. The forms of equations (4.2.5) and (4.2.6) allow the representation of the governing differential equation of motion given in equation (4.2.1), to be cast into the state space form that is generally used in the controller design of a linear time invariant systems. The linear time invariant systems are the systems consisting of the differential equations with constant coefficients [121,122]. The standard form of the state space representation is given as [122],

$$\{\dot{x}\} = [A]\{x\} + [B]\{u\}, \quad \{y\} = [C]\{x\} \quad (4.2.7)$$

In this representation,  $[A]$  describes the system matrix and  $[B]$  gives the input matrix,  $[C]$  defines the output matrix and  $\{u\}$  symbolizes the vector of inputs to the system. The matrices  $(A, B, C)$  are real constant matrices, and  $(A, B, C)$  is the system triple. The triple is called the state space representation of the system.

The equations from (4.2.5) to (4.2.7) allows the determination of the state-space representation for a smart structure consisting of  $k$  piezoelectric actuators and  $r$  sensors in nodal coordinates as,

$$\begin{aligned}
[A] &= \begin{bmatrix} [0] & [I] \\ -[M]^{-1}[K] & -[M]^{-1}[D_o] \end{bmatrix}_{2Np \times 2Np}, \quad [B] = \begin{bmatrix} [0] \\ [M]^{-1}[F] \end{bmatrix}_{2Np \times j} \\
[C] &= \begin{bmatrix} [C_q] & [C_v] \end{bmatrix}_{i \times 2Np}, \quad (i=1 \text{ to } r \text{ and } j=1 \text{ to } k)
\end{aligned} \tag{4.2.8}$$

Equation 4.2.8 gives the description of the nodal coordinates based state-space model for the smart structures that can be used in controller design.

#### 4.2.2 The Formulation in Modal Coordinates

In the determination of the state-space representation, the alternative approach is to use the modal coordinates in the second order form.

Define a diagonal matrix  $[\Lambda]$  with order  $mp$  ( $mp \leq Np$ ) formed by the natural frequencies of the  $N$  nodes within the frequency range of interest, each with  $p$  degrees of freedoms ( $mp \leq Np$ ) as,

$$[\Lambda] = \text{diag}(\omega_j), \quad (j = 1 \text{ to } mp) \tag{4.2.9}$$

In this formulation, the mass normalized  $Np \times mp$  modal matrix formed by the mode shapes of the system, symbolized by  $[\Psi]$ , diagonalizes the mass, stiffness and damping matrices of the system considered.

$$\begin{aligned}
[\Psi]^T [M] [\Psi] &= [I] \\
[\Psi]^T [K] [\Psi] &= [\Lambda]^2 \\
[D_m] &= [\Psi]^T [D_o] [\Psi] = \text{diag}(2\omega_j \zeta_j)
\end{aligned} \tag{4.2.10}$$

where,  $[I]$  is  $mp \times mp$  identity matrix and  $[D_m]$  is a  $mp \times mp$  diagonal modal damping matrix. Defining a new vector  $\{q_m\}$  as,

$$\{q_m\}_{mp \times 1} = [\Psi]_{mp \times np}^T \{q\}_{np \times 1} \quad (4.2.11)$$

and by using equation (4.2.11) in equation (4.2.1) and then by premultiplying equation (4.2.1) with  $[\Psi]^T$  results in the following form.

$$[\Psi]^T [M] [\Psi] \{\ddot{q}_m\} + [\Psi]^T [D_o] [\Psi] \{\dot{q}_m\} + [\Psi]^T [K] [\Psi] \{q_m\} = [\Psi]^T [F] \{u\} \quad (4.2.12)$$

By using equations (4.2.10) and (4.2.12) and also defining the new state variable  $x$  as the modal displacements  $\{q_m \dot{q}_m\}^T$ , the state-space representation of the smart structures can be obtained as,

$$\begin{Bmatrix} \dot{x} \\ x \end{Bmatrix}_{mp \times 1} = \begin{bmatrix} [0] & [I] \\ -[\Lambda]^2 & -[D_m] \end{bmatrix}_{mp \times mp} \begin{Bmatrix} x \\ \dot{x} \end{Bmatrix}_{mp \times 1} + \begin{Bmatrix} [0] \\ [\Psi]_{np \times mp}^T [F]_{np \times j} \{u\}_{j \times 1} \end{Bmatrix}_{mp \times 1} \quad (4.2.13)$$

(j = 1 to k)

Furthermore, the substitution of equations (4.2.11) to (4.2.6) yields the output of the system, in modal coordinates. The output vector obtained is given in equation (4.2.14).

$$\{y\}_{ix \times 1} = [C_q]_{ix \times np} [\Psi]_{np \times mp} \{q_m\}_{mp \times 1} + [C_v]_{ix \times np} [\Psi]_{np \times mp} \{\dot{q}_m\}_{mp \times 1}, \quad (i = 1 \text{ to } r) \quad (4.2.14)$$

Together with the general form of the state space realization given in equations 4.2.7, equations (4.2.13) and (4.2.14) allows the determination of the components of the state-space realization of the smart structures in the modal coordinate based modeling technique. The components of the state space realization for the smart structures in modal coordinate based systems are given in equation (4.2.15).

$$\begin{aligned}
[A_m] &= \begin{bmatrix} 0 & I \\ -\Lambda^2 & -D_m \end{bmatrix}_{2mp \times 2mp} \\
[B_m] &= \begin{bmatrix} 0 \\ [\Psi]^T [F] \end{bmatrix}_{2mp \times j}
\end{aligned} \tag{4.2.15}$$

$$[C_m] = \left[ [C_q] [\Psi] \quad [C_v] [\Psi] \right]_{i \times 2mp}, \quad (i = 1 \text{ to } r, j = 1 \text{ to } k)$$

In this formulation,  $[A_m]$  describes the system,  $[B_m]$  gives input and  $[C_m]$  symbolizes the output matrices in modal coordinates.

The state-space representation provides necessary and sufficient information for the design of the controllers that aim to suppress the vibrations due to the modes of the smart structures.

The modal coordinates based system model retains the physical correspondence between the theoretical model and the test structure, a relation that is somehow lost in nodal coordinates based modeling technique. The modal coordinates based technique also allows the specification of the desired number of modes contributing to the response under consideration. This allowance always results in smaller order models than those of nodal coordinate based technique. Another advantage is that, by assigning different modal damping ratios associated with the modes of the structure, the modal coordinate based technique offers greater flexibility in tuning the theoretical model to the experimental data [59,121].

By using the state space realization developed for the smart structures, the transfer functions of a system can also be found. The transfer function of linear time invariant systems can be defined as the ratio of the Laplace transform of the response (or output) of the system to the Laplace transform of the actuation (or input) under the assumption of zero initial conditions. The transfer function of a smart structure is analogous to the receptance function,  $\alpha(s)$  of the structure in classical modal analysis techniques. The receptance matrix can also be found by using equation 4.2.7 [121,122] as follows,



$$\begin{aligned}
\{\dot{x}\} &= [A]\{x\} + [B]\{u(s)\} \\
y &= [C]\{x\} \\
y(s) &= C(s[I] - [A])^{-1}[B]\{u(s)\} \text{ or,} \\
y(s) &= \alpha(s) u(s) \\
\alpha(s) &= C(s[I] - [A])^{-1}[B]
\end{aligned} \tag{4.2.16}$$

where,  $s$  defines the variable of Laplace transform.

The substitution of equation (4.2.15) in equation (4.2.16) allows the formulation of the receptance matrix of the smart structures in modal coordinates. Equation (4.2.17) gives the receptance function of the smart structure that relates  $k$  piezoelectric actuators to  $r$  sensors in partitioned form as follows,

$$[\alpha(s)] = \begin{bmatrix} [C_q][\Psi] & [C_v][\Psi] \\ i \times j & i \times 2mp \\ & & [s[I] - [A_m]]^{-1} \\ & & & \begin{bmatrix} [0] \\ [\Psi]^T [F] \\ 2mp \times j \end{bmatrix} \end{bmatrix} \tag{4.2.17}$$

( $p = 1$  to  $3$ ), ( $m = 1$  to  $N$ ) and ( $i = 1$  to  $r$ ,  $j = 1$  to  $k$ )

The transfer function or the frequency response of the smart structures is characterized by two factors: The resonances where natural frequencies reside in; and the antiresonances or minima between the resonances. In the transfer function representation, while the roots of the polynomial appearing on the numerator of the transfer function are called the zeros of the system, those of the denominator are called the poles of the system.

The smart structure system models having poles on the positive real axis give rise to the exponential term that increases in time. That is, more positive real part of the pole the faster the rate of growth is. The systems in which a transient term increases indefinitely with time are called unstable. Conversely, systems in which all transient terms die out with time are called stable system. Any pole having a positive real part leads to a transient term that increases with time. For a stable system, the

system settles into steady state after all the transient terms in the response decay to zero. Therefore, for a system to be stable all the system poles must lie in the negative left half of the  $s$  plane giving the plot of the poles and the zeros of the system along the real and imaginary axes. The location of zeros does not affect the stability of the system [121,122]. The systems with no poles in the right half plane but one or more on the imaginary axis are known as marginally stable.

The poles of the transfer function are responsible for the transient response. The zeros however, have an effect on the magnitude of these terms. For this reason, the aim in the closed-loop controller design for the active vibration control is to increase damping ratios of the dominant poles without reaching the instability limits of the system [122]. Therefore, the controller design should start with the investigation of the open loop behavior of the system to be controlled. This can be achieved only by extracting accurate system model of the smart structure to be controlled.

The transfer function describes the property of the system that relates output to input. The transfer function approach maintains the physical correspondence between the theoretical models and the actual test structure that is implicit in state space models [59]. Therefore, the transfer function approach can effectively be used to investigate the nature of the system.

In the active vibration control of the smart structures, depending on the nature of the problem, both transfer function approach and state space approach are utilized. While the classical control design techniques like PID controllers considers the transfer function approach, modern optimal controller design schemes like  $H_\infty$  use the state space realizations [126]. Table 4.1 summarizes the interrelationship between the finite element based system modeling techniques.

Table 4.1 The interrelations of the finite element based system modeling techniques for active vibration control of smart structures

Model	nodal coordinates	modal coordinates
state variable vector $\{x\}$	$\{q \ \dot{q}\}_{Np \times 1}^T$	$\{q_m \ \dot{q}_m\}_{mp \times 1}^T$
Parameters	$K_{Np \times Np}, [M]_{Np \times Np}, \gamma, \beta$ $[D_o] = \gamma[M] + \beta[K]$	$[\Lambda]_{mp \times mp}, [\Psi]_{np \times mp}, \zeta_{mp}$ $[D_m]_{mp \times mp}$
output matrix, [C]	$\begin{bmatrix} [0] \\ [M]^{-1}[F] \end{bmatrix}_{2Np \times j}$ (j=1 to k)	$\begin{bmatrix} 0 \\ [\Psi]^T[F] \end{bmatrix}_{2mp \times j}$
input matrix, [B]	$\begin{bmatrix} [C_q] & [C_v] \end{bmatrix}_{j \times 2Np}$ (i=1 to r)	$\begin{bmatrix} [C_q][\Psi] & [C_v][\Psi] \end{bmatrix}_{j \times 2mp}$
System matrix, [A]	$\begin{bmatrix} [0] & [I] \\ -[M]^{-1}[K] & -[M]^{-1}[D_o] \end{bmatrix}_{2Np \times 2Np}$	$\begin{bmatrix} 0 & I \\ -\Lambda^2 & -D_m \end{bmatrix}_{2mp \times 2mp}$
Transfer function matrix, [G(s)]	$[C](s[I]-[A])^{-1}[B]$	$[C_m](s[I]-[A_m])^{-1}[B_m]$

(N: the number of nodes in the finite element model , p: The number of degrees of freedom (p=1 to 3), m: The number of modes contributing the response (m=1 to Np), k: The number of piezoelectric actuators, r: The number of sensor)

#### 4.2.3 The Determination of the Spatial Model: Spatial Reduction of the Models

In the finite element modeling, the structure is generally modeled by using large number of degrees of freedoms for better accuracy. In active vibration control of smart structures however, the use of higher order models has considerable computational difficulties. This limitation requires the order of the model to be reduced to a level which is as small as possible. This is generally achieved by reducing the order of the model to a restricted set of nodes and degrees of freedoms.

The application of the spatial model reduction techniques results in the formulation of the reduced model having  $t$  ( $t \leq p$ ) reduced degrees of freedoms associated with  $n$  number of ( $n \leq N$ ) nodes. This leads to the formulation of reduced or condensed models. In this technique, the full model of the system is used for the determination of the master degrees of freedoms describing the accurate dynamical characteristics of the model. In the determination of the spatial model, a transformation matrix, which relates the master degrees of freedoms to the remaining degrees of freedoms called secondary or slave degrees of freedom, is used to reduce the order of the system.

The reduction process is performed upon a transformation, which neglects inertia or static contributions of the secondary degrees of freedoms, then deriving  $n_t \times n_t$  spatial matrices of the condensed system as the reduced mass matrix,  $[M^R]$  and the reduced stiffness matrices  $[K^R]$ .

The equation of equilibrium for an undamped system subjected to the forces due to unit piezoelectric actuation voltage,  $F_t$ , acting only on the primary degrees of freedoms can be written in the following partitioned form [121,122].

$$\begin{bmatrix} [M_{ss}] & [M_{st}] \\ [M_{ts}] & [M_{tt}] \end{bmatrix} \begin{Bmatrix} \{\ddot{q}_s\} \\ \{\ddot{q}_t\} \end{Bmatrix} + \begin{bmatrix} [K_{ss}] & [K_{st}] \\ [K_{ts}] & [K_{tt}] \end{bmatrix} \begin{Bmatrix} \{q_s\} \\ \{q_t\} \end{Bmatrix} = \begin{Bmatrix} \{0_s\} \\ \{F_t\} \end{Bmatrix} \quad (4.2.18)$$

Where,  $s$  defines the number of secondary degrees of freedom ( $s < 3$ ) and  $t$  is the number of primary degrees of freedom ( $t \leq p$ ). In this formulation,  $\{q_s\}$  is  $n_s \times 1$  vector of secondary degrees of freedoms and  $\{q_t\}$  defines  $n_t \times 1$  vector of primary degrees of freedoms defined on  $n$  ( $n < N$ ) nodes in the finite element model. In this technique, all secondary degrees of freedom can be related to the primary degrees of freedom by using the following transformation

$$\{q_s\}_{ns \times 1} = [T]_{ns \times nt} \{q_t\}_{nt \times 1} \quad (4.2.19)$$

in this formulation, the transformation matrix relating the primary degrees of freedoms to the secondary degrees of freedoms,  $[T]_{ns \times nt}$ , is given by

$$[T]_{ns \times nt} = (1 - \beta) \left( -([K]_{ss})^{-1} [K]_{st} \right) - \beta ([M]_{ss}^{-1} [M]_{st}) \quad (4.2.20)$$

where,  $\beta$  defines the reduction coefficient whose value is zero for static reduction (Guyan reduction) and one for dynamic reduction. By using the matrix reduction techniques, the reduced mass and reduced stiffness matrices, describing the reduced spatial model for both static and dynamic condensation, can be found. Hence, the reduced mass matrix to be used in the analysis becomes,

$$[M^R]_{nt \times nt} = \begin{bmatrix} [T]_{ns \times nt}^T & [I]_{nt \times nt} \end{bmatrix} \begin{bmatrix} [M_{ss}] & [M_{st}] \\ [M_{ts}] & [M_{tt}] \end{bmatrix} \begin{bmatrix} [T]_{ns \times nt} \\ [I]_{nt \times nt} \end{bmatrix} \quad (4.2.21)$$

$\begin{matrix} Np \times Np & & \\ & Np \times nt & \end{matrix}$

and the reduced stiffness matrix takes the following form.

$$[K^R]_{nt \times nt} = \begin{bmatrix} [T]_{ns \times nt}^T & [I]_{nt \times nt} \end{bmatrix} \begin{bmatrix} [K_{ss}] & [K_{sp}] \\ [K_{ps}] & [K_{pp}] \end{bmatrix} \begin{bmatrix} [T]_{ns \times nt} \\ [I]_{nt \times nt} \end{bmatrix} \quad (4.2.22)$$

$\begin{matrix} Np \times Np & & \\ & Np \times nt & \end{matrix}$

In this thesis, the computer code ANSYS<sup>®</sup> (v.5.6) is used for the calculation of the reduced mass and stiffness matrices through Guyan matrix reduction technique [50].

The key assumption in this procedure is that for lower frequencies ( $f < 150\text{Hz}$ ), inertia forces on the secondary degrees of freedoms are negligible compared to the elastic forces transmitted by the primary degrees of freedoms. Therefore, the total mass of the structure is only allocated among the primary degrees of freedoms [50].

During this procedure the group of the finite elements is condensed into a single element whose mass and stiffness matrices and load vectors are calculated at the master degrees of freedom of the model. Because the accuracy of the reduced mass matrix depends solely on the selection of the correct number of degrees of freedoms, the selection of the appropriate master degrees of freedoms is the most important step in this analysis. The procedure applied in the determination of the spatial model is summarized in Figure 4.1.

The effectiveness of the nodal and modal coordinates based techniques applied to the smart beam is compared in Chapter 5. In this thesis, while the nodal coordinates are considered in the determination of the spatial models for the smart structures, the modal coordinate based techniques utilized in the extraction of the system model.



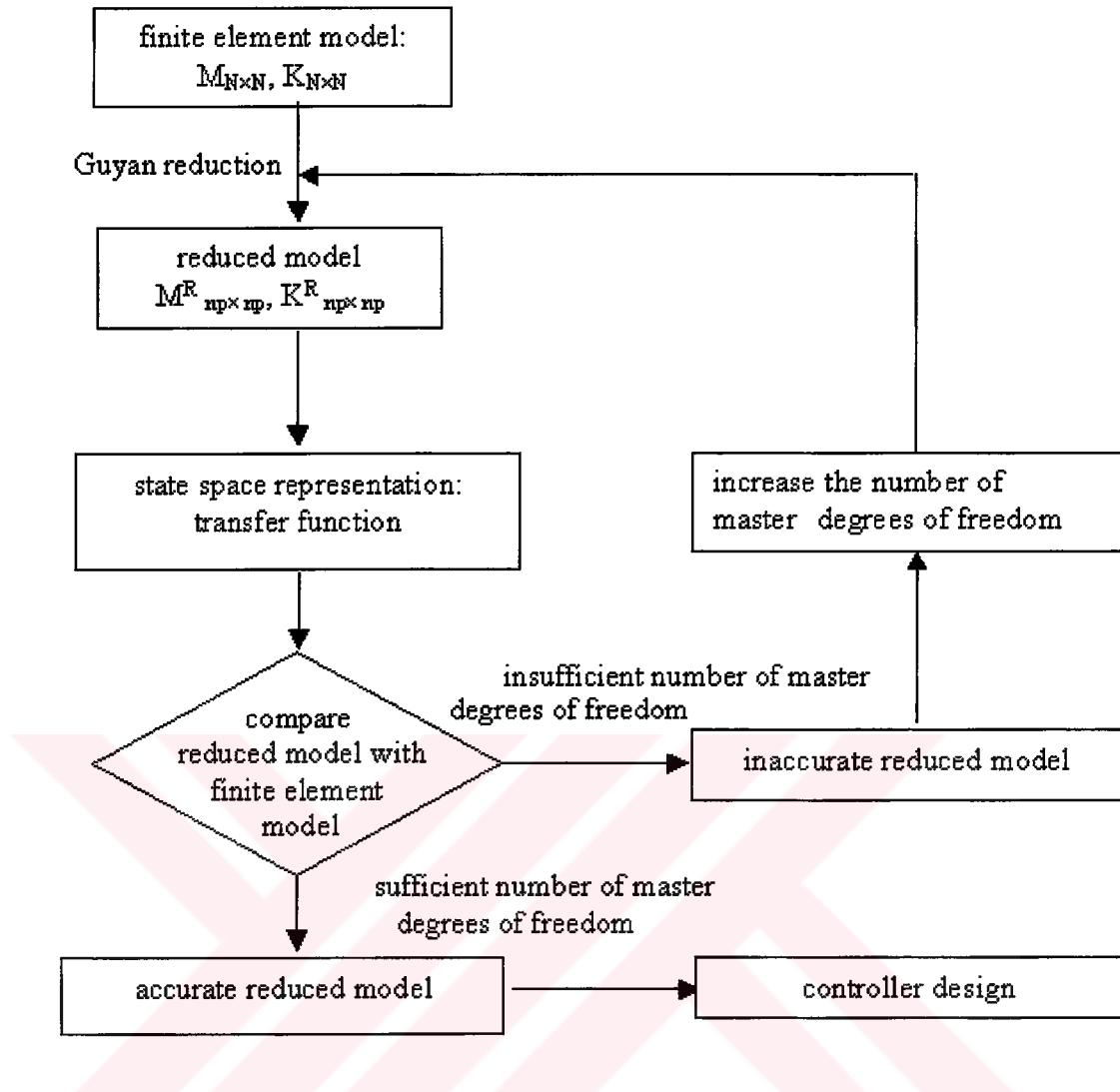


Figure 4.1. The spatial model reduction algorithm used in the study (p: the total number of degrees of freedoms of the model, t: the reduced number of degrees of freedom, N: the number of nodes of the model, n: the reduced number of nodes associated with the model).

#### **4.2.4 The System Model Reduction: The Reduced Order Models**

In the active vibration control of the smart structures, the complexity and the performance of the finite element based control model depends on the order of the structural model. The oversized model not only brings extra computational difficulties but also may cause the inclusion of the unwanted signals in the form of the noise. Therefore, the model reduction is one of the most important parts of the analysis and the design.

In the finite element based system models the application of the static reduction technique provides an effective means for the calculation of the reduced order spatial model. But since the spatial model reduction does not necessarily yield the minimal order system models necessary for the controller design, the extraction of a minimal order model of the system that sufficiently describes the dynamics of the system is required.

Among the reduction techniques developed for the flexible structures, the balanced realization and modal reduction techniques offer nearly optimal solutions within reasonable computational efforts. [123,127]. This study makes use of the balanced realization technique developed for stable systems. The system models are reduced to the minimal order using  $\mu$  analysis and synthesis toolboxes of the numerical analysis code of Matlab<sup>®</sup> (v.5.2.).



### 4.3 Control Design Techniques

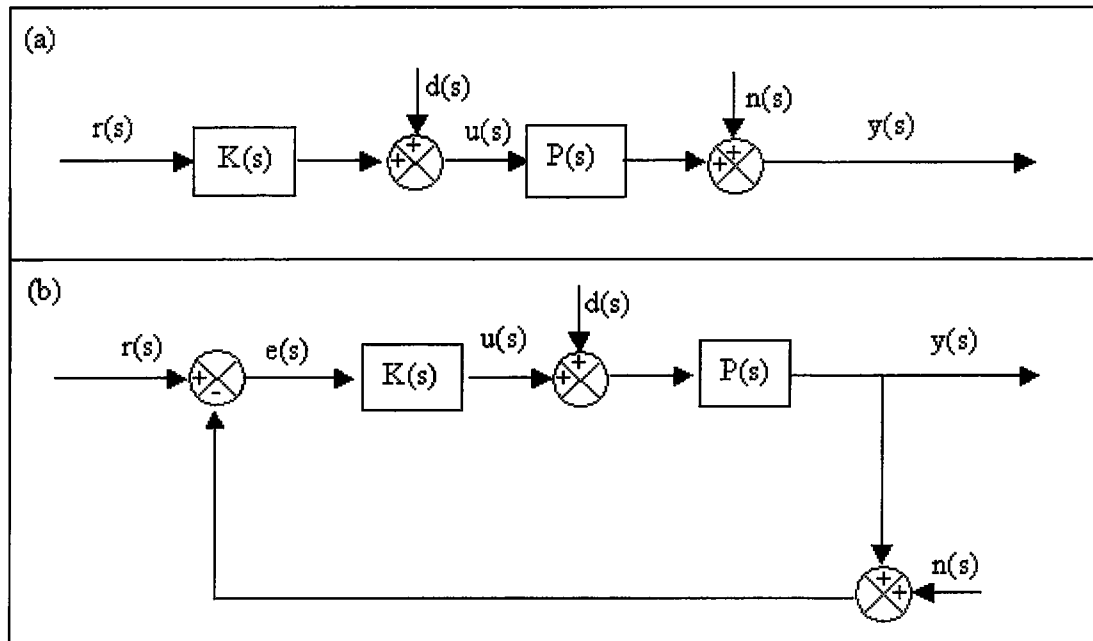
In this thesis, the objective of the controller design is to improve the performance of the controllers that are intended to suppress the flexural vibrations of the smart structures. During the study, the deviations of the theoretical models from the actual models are represented through system uncertainties. PID and  $H_\infty$  techniques are used for designing the controllers. Classical and modern frequency response, robust control and  $\mu$  analysis techniques quantifying stability and performances are considered in the analysis of the controllers.

This thesis deals with closed loop control systems, but it is best to describe both open and closed loop systems first. An open loop system is the one which neither the output nor any of the other system variables has any effect on the control of the output. The closed-loop systems however, provide means of control over the output. In a closed-loop system (often referred to as feedback control system) the actuation error, which is defined as the difference between the input signal and the feedback signal which can either be the actual output signal or a function of the output signal, is fed to the controller so as to reduce the error and bring the output to the desired value. The term closed loop control implies the use of the feedback control to reduce the system error.

The advantage of the closed loop control arises from the fact that the use of the feedback makes the system response relatively insensitive to the external disturbances and any possible internal variations in the system parameters. Thus it is theoretically possible to use the relatively inaccurate and inexpensive components to obtain precise control of a given system. This is not realizable in the case of open-loop controllers [124]. From the stability point of view, in the open-loop controller the system's stability is not the major problem. On the other hand, stability is the major problem in closed-loop controllers such that the system may overcorrect the errors which can cause oscillations [124,125]. The block diagram

representation of typical open-loop and closed-loop systems are shown in Figure 4.2.

In any open-loop control system such as the one shown in Figure 4.2.a, the controller  $K(s)$  processes the reference input  $r(s)$  which represents a fixed operating conditions and directly feeds to the system  $P(s)$  to obtain the desired output  $y(s)$  for the system. In an open-loop system, because the output of the system is not compared with any condition, the accuracy of the system depends only on the calibration of the actuators. For this reason, the open-loop system can not maintain the performance requirements in the presence of the disturbances  $d(s)$  and the sensor noises  $n(s)$ . This limits the applications of open-loop control schemes to the cases where the relationship between the input and the output is known and no disturbance acts on the system only [124]. In the closed loop systems however, despite the presence of the sensor noises and the disturbances, the controller  $K(s)$  processes the error signal  $e(s)$  in a useful manner and feeds back to the system to reduce the error. Figure 4.2.b gives the block diagram representation of a closed loop system.



$P(s)$ : System  
 $K(s)$ : Controller  
 $r(s)$ : Reference command  
 $u(s)$ : Control signal  
 $d(s)$ : Input disturbance  
 $n(s)$ : Sensor noise  
 $y(s)$ : Output  
 $e(s)$ : Error signal

Figure 4.2. The block diagram representation of typical open-loop and closed-loop controllers

a. Open-loop system

b. Closed-loop system

By assuming the  $P(s)$  is unalterable and zero initial conditions of the state variables, the performance of the closed-loop system is mainly characterized by the three closed-loop transfer functions. The transfer functions include  $G_{yr}$  (the transfer function relating the reference signal to the output),  $G_{yd}$  (the transfer function describing the relation between the output and the disturbance),  $G_{yn}$  (the transfer function which gives the relation between the output and the sensor noise)

Defining the loop gain  $L(s)$  as,

$$L(s) = P(s)K(s) \quad (4.3.1)$$

The transfer functions that can be used to describe the performance of the closed-loop system then have the following forms:

$$\begin{aligned} G_{yd} &= \frac{y(s)}{d(s)} = \frac{P(s)}{1 + L(s)} \\ G_{yn} &= \frac{y(s)}{n(s)} = -\frac{L(s)}{1 + L(s)} \\ G_{yr} &= \frac{y(s)}{r(s)} = \frac{L(s)}{1 + L(s)} \end{aligned} \quad (4.3.2)$$

### 4.3.1 Series Compensators : PID Compensators

Early in the design of the control systems, it was thought that many systems can be adequately controlled with a simple series compensator. This approach is specially applicable to the chemical and manufacturing processes. This simple series compensator called a PID (Proportional Integral Derivative) compensator. The compensator has three components and the transfer function of the compensator is well known to be [124,128],

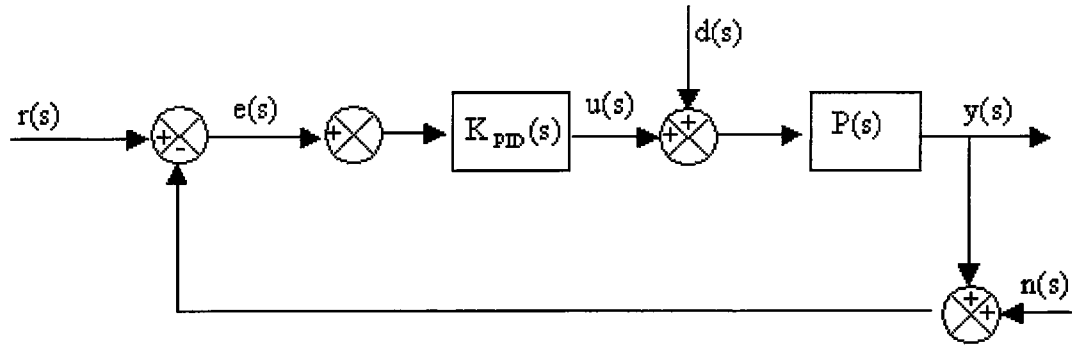
$$K(s) = K_p \left( 1 + \frac{K_i}{s} + K_d s \right) \quad (4.3.3)$$

where  $K_p$  defines the proportional gain,  $K_i$  is the integral gain and  $K_d$  symbolizes the derivative gain. The integral and derivative constants can be related to the physical parameters like the integral or reset time  $T_i$  and the derivative term  $T_d$  [128] by using,

$$K_i = \frac{1}{T_i}, \text{ and } K_d = T_d \quad (4.3.4)$$

There are commercially available modules that have knobs for the user adjust the set of values of each of the three constants [128]. The commercial success of PID controllers lies in their ease in the implementation and general applicability to most controllable systems [124]. In the field of process control systems, it is also a well-known fact that the basic and modified PID control schemes have proved their usefulness in providing satisfactory control, although they may not provide optimal control in many situations [124,126,128]. Depending on the performance requirements of the control system, certain combinations of the proportional, integral and derivative gains such as, P (Proportional), PI (Proportional plus Integral) and PD (Proportional plus Derivative) compensators may also be considered in the design. These combinations are obtained by setting the relevant gains of PID compensators to zero. In this thesis, PID control scheme is applied to the smart structure models

Now, let the block diagram of the closed-loop system shown in Figure 4.2 be modified to include the proportional, derivative and integral actions of the PID controller with the sensor noise and disturbances. Then, the block diagram of the PID controlled closed-loop system is obtained. Figure 4.3 gives the block diagram representation of the PID controller algorithm used in the thesis.



$$K_{PID}(s) = K_p \left( \frac{s + K_d s^2 + K_i}{s} \right)$$

Figure 4.3. The block diagram representation of PID controller applied to smart structures

### 4.3.2 The Analysis and Synthesis of Smart Structures for Robust Control

It is a well known fact that the feedback control systems reduce the effect of disturbances and moderate modeling errors or parameter changes on the performance of a control system. In certain cases however, the extend of the modeling errors, disturbances and sensor noises may influence both stability and the performance of the feedback control systems. Therefore, the control system design must satisfy the stability and the desired performance specifications in the presence of the parameter changes and disturbances. The robust control of the linear time invariant systems is generally realized by the analysis or the synthesis of the control systems. In this terminology, while the robustness analysis of a linear time invariant control system deals with the evaluation of the stability and the performance of the system in the presence of a set modeling errors and disturbances for a given feedback controller, the synthesis of a system involves the design of the controller that satisfies the stability and the performance requirements for a set of modeling errors and disturbances.

The ideas to evaluate the robustness of a control system based on the frequency response methods dates back to 1930's. In the classical frequency response techniques, the robustness analysis of a control system was addressed mostly by trial and error. These techniques were considered mainly for SISO applications and their applications in MIMO systems are very difficult [129]. In 1980's the developments in the  $H_\infty$  and robust control gave the classical robust performance analysis a new modern look. In the modern robust analysis and synthesis techniques, the modeling errors and the performance requirements are included in the analysis systematically [60]. In this thesis, the classical and modern robustness analysis and  $H_\infty$  design and synthesis techniques are used.

Since the standard PID controller design is not able to include the modeling errors and disturbances which may be present in the system at the design stage, the determination of the proportional, integral and derivative gains is iterative for the robust control [124,128]. In this case, for each gain specification, the robust stability and performance analysis should be conducted to secure the success of the PID controllers. In  $H_\infty$  controller design and synthesis technique however, modeling errors and disturbances are included in the synthesis of the controllers systematically [60,129].

#### **4.3.2.1 The Classical Robust Stability Analysis of Control Systems**

The stability analysis of a linear time invariant control system is generally performed at two stages. These stages involve the determination of the absolute and relative stability of the system. The absolute stability analysis investigates whether the control system is stable or not. The relative stability analysis however, gives how stable is the system and how much can it be perturbed within the range of stability. In the design of a controller the most important requirement is the

preservation of the absolute stability. Furthermore, the system must also have adequate relative stability [124,125].

The closed response of the systems can be determined from the frequency response characteristics of the loop gain including the stability. In the frequency response of the loop gain, there exists a critical point which separates the stable and unstable systems where the phase shift is  $-180^\circ$  and the loop gain is 1. This point corresponds to  $s=-1$  point on the Nyquist diagram. Nyquist diagram presents a polar plot of a complex number that gives the frequency response at each frequency. The frequency at which the open loop system contributes  $180^\circ$  phase lag is known as the phase cross over frequency [124]. Nyquist theorem is generally used in the determination of the absolute stability of the closed loop system [125]. The theorem states that, the closed loop system is stable if and only if the net number of the clockwise encirclements of point  $s=-1$  plus the number of poles of  $G(s)$  in the right hand plane is zero. Thus in the absolute stability analysis of open-loop and closed-loop systems it is necessary to analyze pole-zero map and Nyquist plots simultaneously. Figure 4.4 illustrates such a stable open loop system. For this system, the lack of encirclements around  $s=-1$  and right hand zeros ensures the stability.



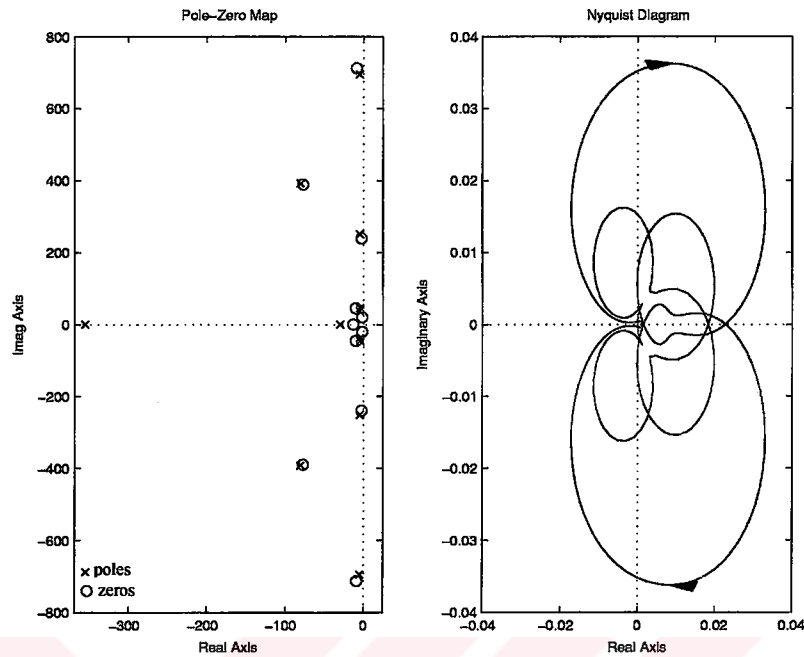


Figure 4.4. The plots used in Nyquist stability theorem (open-loop system: The smart beam model of [77])

This thesis makes the effective use of the Nyquist theorem to ensure the absolute stability of the control systems including PID controllers.

In the classical frequency response techniques, the relative stability concept is applied in the characterization of the behavior of the system by using mainly two relative stability measures. These measures are the gain and phase margins [124,125].

The gain margin (GM) of the system can be defined as the gain that can be increased before the system is marginally stable. The gain margin is approximately the reciprocal of the open loop gain at the phase cross over frequency. In the classical robust stability analysis, the small gain margin indicates a Nyquist plot that approaches the  $s=-1$  point too closely such that the closed loop characteristics are oscillatory. That is, the controller may become unstable in the presence of modeling

errors and uncertainties [124,126]. The specification of the gain margin is generally not enough to express the relative stability of the control systems.

In addition to the gain margin the specification of the phase margin (PM), which is defined as the additional phase lag that will make the system marginally stable, allows the appropriate description of the relative stability of the systems. Similar to the gain margin, the phase margin can also be obtained from the loop gain frequency response. The phase margin in Nyquist plot is simply the angle between the negative real axis and the intersection  $L(s)$  locus with the unit circle.

In the classical robust stability of the control systems, the systems with the small gain and phase margins are not considered to be robust because a perturbation may force the system to be unstable [124,125].

In classical control usually gain and phase margins are used as a design criteria for good performance, PM values from  $30^\circ$  to  $60^\circ$  and the GM values larger than 6dB values are considered [130]. In general, for a design with good GM and PM is considered to be robust against the variations in the system components. In certain exceptional cases however, good margins may not imply robustness. That is, a minor change in the parameters of the system may influence the robustness of the system. Thus, the classical robust stability and performance analyses may not guarantee the robust stability and performance of the closed loop systems [129,130].

### 4.3.2.2 The Classical Robust Performance Analysis of Closed-loop Systems

Although the relative stability considerations are very important in the design of a controller for the desired performance; the controller design based on the nominal system model including the modeling errors should also satisfy the performance specification. Thus, the response of the actual system should be within the perturbed system response.

The control system is designed to be stable and perform well when used with the true physical system including disturbances. The output of the actual system can be expected to behave in a similar manner to the nominal model including the modeling errors. A controller design that works well with a large set of system models is said to be robust in the classical frequency response analysis.

In the classical frequency response analysis, the performance of a closed-loop system is analyzed by using the tracking,  $T$ , and sensitivity functions,  $S$  which are given in equations (4.3.5) and (4.3.6). The tracking performance of the system is analyzed by the transfer function  $G_{yr}$  (or complementary sensitivity function,  $T$ )

$$S = \frac{1}{1 + P(s)K(s)} \quad (4.3.5)$$

$$T = \frac{P(s)K(s)}{1 + P(s)K(s)} \quad (4.3.6)$$

Theoretically, the controller may be adjusted to achieve a good disturbance rejection. For a good disturbance rejection, the sensitivity function  $S$  should be small over a wide frequency range. In order to achieve good noise rejection, the complementary sensitivity function should also be small over a wide frequency range. Since  $S+T=1$ , this is conflicting. That is, no controller gain can make both  $T$

and  $S$  small. In practice, this conflict is resolved by keeping these functions small at different frequency ranges [124,128]. For instance, because the influences of the sensor noise is more prominent at higher frequencies, the adjustment of small  $T$  values at high frequencies results in good noise rejection. Similarly the selection  $T$  values close to 1 at lower frequencies improves the command tracking or disturbance rejection. The algorithm used in the classical robust performance analysis is shown in Figure 4.5.

#### 4.3.2.3 Modern Robust Stability Analysis of Control Systems: Uncertainty and Robustness

The presences of the measurement errors, the mismatches between the true and mathematical model and the time dependance of the parameters describing the system do not usually allow the exact representation of the real system models. In many cases the modeling error ultimately influence the stability and performance of the controller systems. In modern robust stability analysis techniques and  $H_\infty$  controller design and synthesis techniques, the possible deviations of the mathematical models from the real world system are represented by system uncertainties. This allows the representation of the model sets including uncertainties instead of a fixed model. This section starts with the definitions for the norms commonly used in robust control and  $H_\infty$  control theories. Signal norms serve as a measure of signal size. The performance of a control system can be described by the norms of the signals such as the size of the error signals.

The energy or the 2 norm of a signal  $x(t)$  is given as [80,129],

$$\|x(t)\|_2 = \left( \int_{-\infty}^{\infty} |x(t)|^2 dt \right)^{1/2} \quad (4.3.7)$$

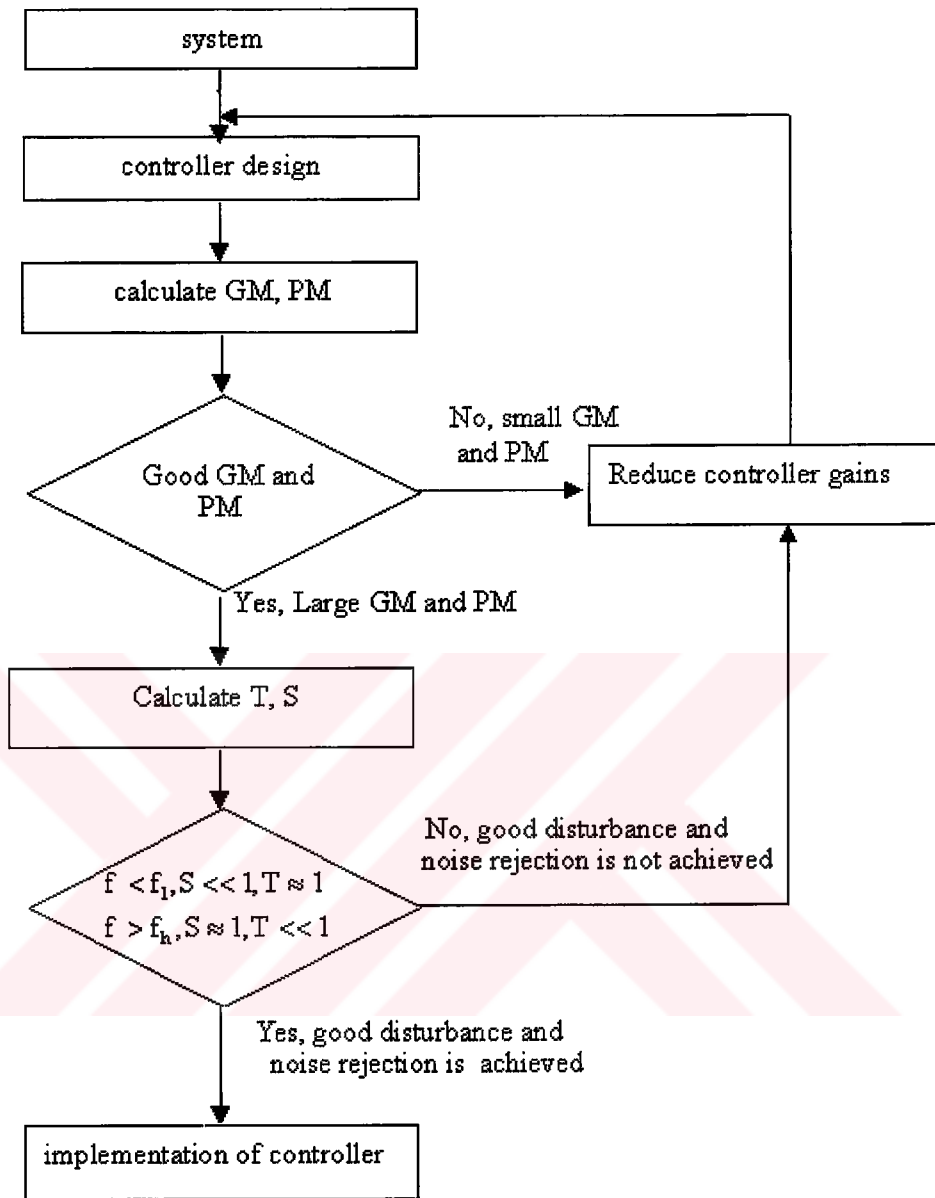


Figure 4.5. The algorithm used for the classical robustness analysis for the PID controllers designed in the study ( $f_l$  : The lower frequency of interest,  $f_h$  : The upper frequency of interest)

The  $\infty$  norm of a signal is defined as the least upper bound or the supremum of its absolute value [129].

$$\|x(t)\|_{\infty} = \sup_t |x(t)| \quad (4.3.8)$$

The  $H_\infty$  norm of a stable system is the supremum of the singular value when the transfer function is evaluated on  $i\omega$  axis [60,129]. For example,  $H_\infty$  norm of a single-input, single-output system is the peak value of the transfer function magnitude given as

$$\|G\|_\infty = \sup_{\omega} \bar{\sigma}(G(i\omega)) \quad (4.3.9)$$

here  $\sigma$  defines the singular value and  $\sup_{\omega} \bar{\sigma}(G(i\omega))$  symbolizes the largest singular value of  $G(i\omega)$ . In the modern robustness analysis and synthesis techniques, the uncertainties are assumed to influence the linear time invariant systems  $P(s)$ , by means of another norm bounded linear time invariant system  $\Delta(s)$ . Describing the perturbed system by  $\tilde{P}$ , the definitions of the modeling uncertainties, additive uncertainty and multiplicative uncertainty used in the thesis are given in Figure 4.6 [80,129].

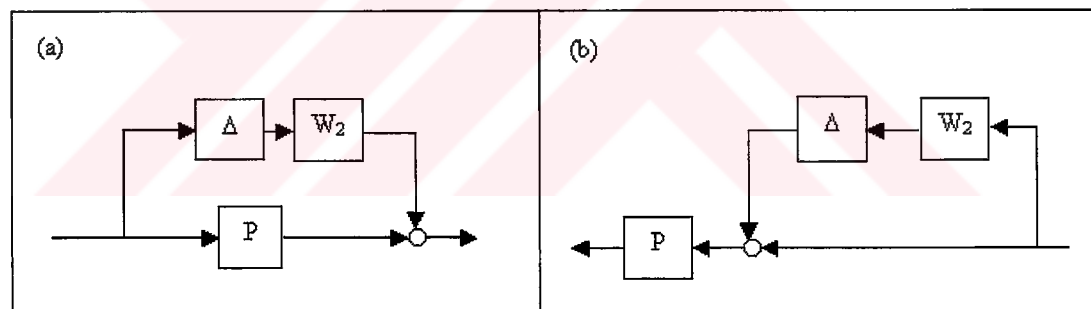


Figure 4.6 The descriptions of the modeling uncertainties used in the thesis

a. Additive uncertainty,  $\tilde{P} = P + \Delta W_2$

b. Multiplicative uncertainty,  $\tilde{P} = (1 + \Delta W_2)P$

In Figure 4.6  $W_2(s)$  is a fixed stable transfer function called weighting and  $\Delta(s)$  defines a norm bounded transfer function such that  $\|\Delta\|_\infty \leq 1$ . In the modern

robustness analysis and synthesis techniques, the description of the uncertainty structure  $\Delta(s)$  and the weighting function  $W_2(s)$  forms a basis for the modelling of the uncertainty present in the control system.

In order for a system to have robust stability, the system must be stable for all systems described by the uncertainty structure,  $\Delta(s)$  [129]. That is to say all the modeling errors are assumed to influence the nominal system model of the linear time invariant systems by another linear time invariant system  $\Delta(s)$ . The conditions for the robust stability of the closed loop controllers are given in equation (4.3.10) for additive uncertainty and in equation (4.3.11) for multiplicative uncertainty.

$$\|W_2KS\|_{\infty} < 1 \quad (4.3.10)$$

$$\|W_2T\|_{\infty} < 1 \quad (4.3.11)$$

The weighting function  $W_2$  is selected to account for the unmodelled dynamic characteristics, such as  $\omega_n$ 's, of the system. Therefore, this weight should have higher values in the frequency range of interest where modeling errors increases. In active vibration control of smart structures for example, this weight should increase as the frequency increases to include the effects of the unmodeled or truncated higher frequency modes [60,80,129].

#### 4.3.2.4 Modern Robust Performance Analysis of Control Systems

The nominal performance of a closed-loop system is achieved when the system satisfies the desired performance criteria. Similarly, the robust performance is obtained as the system satisfies the performance specifications for all systems described by the uncertainty set.

In order to achieve the desired performance specifications, the sensitivity function  $S$  should be small within the frequency range of interest. Because the transient response of the smart structures are dominated by the frequencies in the lower frequency range of interest, the sensitivity function kept small at low frequencies. This is assured by choosing a performance weight as a stable transfer function  $W_1(s)$ . In terms of  $\infty$  norm, the condition is formulated as [127,129]

$$\|W_1 S\|_{\infty} \leq 1 \quad (4.3.12)$$

By using weights  $W_1(s)$  and  $W_2(s)$ , the necessary and the sufficient condition for the robust performance criteria can be stated as follows [129],

$$\| |W_1 S| + |W_2 T| \|_{\infty} < 1 \quad (4.3.13)$$

or, equivalently

$$\|W_2 T\|_{\infty} < 1 \text{ and } \left\| \frac{W_1 S}{1 - |W_2 T|} \right\|_{\infty} < 1 \quad (4.3.14)$$

The algorithm for the modern robust performance analysis used in this thesis is given in Figure 4.7.



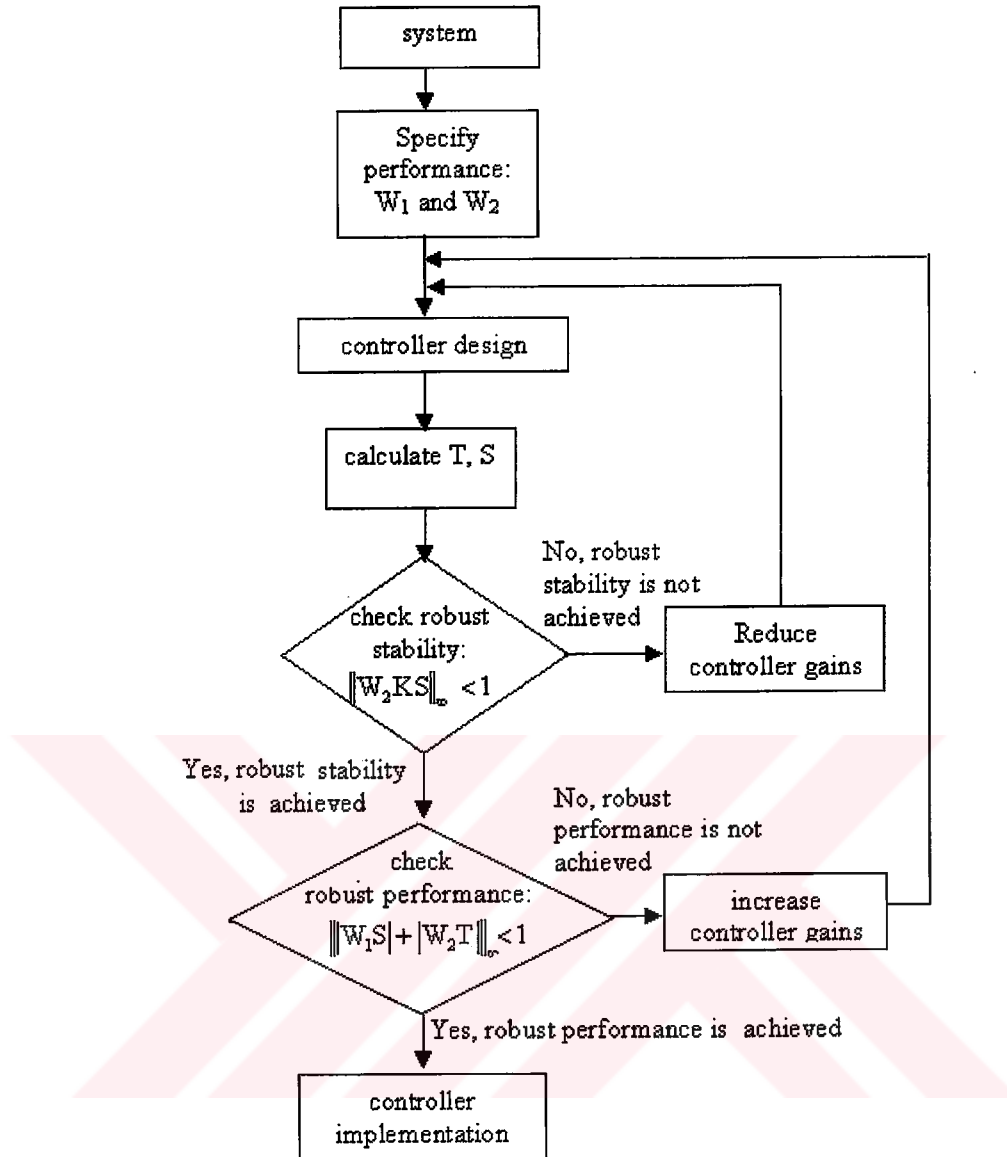


Figure 4.7. The algorithm used for the modern robustness analysis of the PID controllers designed in the study (for additive uncertainties).

### 4.3.3 $H_\infty$ Optimal Control

PID control schemes have proved their usefulness in providing satisfactory control for the SISO applications. The MIMO synthesis of PID controllers however, is very difficult. Furthermore, PID controllers generally do not yield optimal solutions. Another drawback of the application of PID controllers is observed in their robust performance calculations. Since the uncertainties, can not be included at the design stages, the robustness issues of the PID controllers are addressed by trial and error. The applications of  $H_\infty$  controllers however, eliminate the apparent restrictions of the PID controllers and more likely to yield optimal results within reasonable computing efforts.

The standard closed loop architecture of the  $H_\infty$  controller is shown in Figure 4.8. In this figure  $\{w\}$ ,  $\{v\}$ ,  $\{u\}$ ,  $\{e\}$ ,  $\{z\}$  and  $\{y\}$  are vector valued signals. The  $\{w\}$  and  $\{v\}$  are the exogenous inputs, typically consisting of command signals, disturbances, and sensor noises.  $\{u\}$  is the control signal,  $\{z\}$  is the output to be controlled and  $\{e\}$  symbolizes the error signals; their components typically being tracking errors, filtered actuator signal and  $\{y\}$  is the measured output.  $P(s)$  represents a generalized nominal transfer function of the system. In this architecture,  $K(s)$  processes the outputs and feeds back to the system. The  $H_\infty$  control problem consists of determining  $K(s)$  such that the  $H_\infty$  norm of the transfer function from  $\{w\}$ ,  $\{v\}$  to  $\{z\}$ ,  $\{e\}$  is minimized and the closed loop system is stable [77,80,127,129].

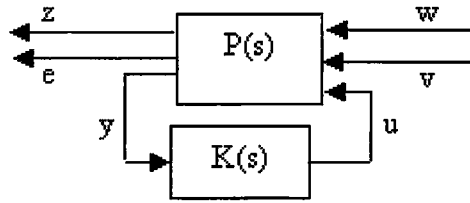


Figure 4.8. The closed loop architecture of the  $H_\infty$  controller

Unlike other conventional controller designs such as PID, the uncertainties present in the system can systematically be included in the modeling. In this technique, despite of the presence of the uncertainties  $\Delta(s)$  as shown in Figure 4.9, the controller minimizes the ratio of the signal energies  $\{e\}$  to  $\{v\}$  [80,127,130]

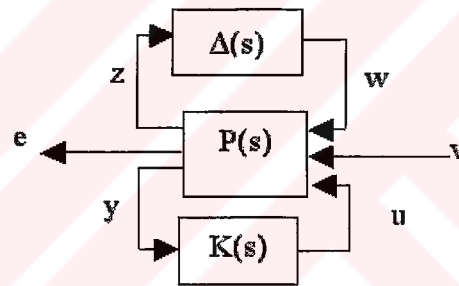


Figure 4.9. The modeling of the uncertainties in  $H_\infty$  controller

For the design purposes, the  $\Delta$  block is eliminated and the input-output map from  $[\{w\} \{v\}]^T$  to  $[\{z\} \{e\}]^T$  is expressed in lower linear fractional transformation form  $F_1(P, K)$  [78] as ,

$$\begin{bmatrix} \{z\} \\ \{e\} \end{bmatrix} = F_1(\mathbf{P}, \mathbf{K}) \begin{bmatrix} \{w\} \\ \{v\} \end{bmatrix} \quad (4.3.17)$$

where,  $F_1(P, K) = P_{11} + P_{12}K(I - P_{22}K)^{-1}P_{21}$ .  $P_{ij}$  represents the partitioned elements of  $[P]$  (according to the dimensions of the control, measurement, disturbance and error signals) as

$$[P] = \begin{bmatrix} P_{11} & P_{12} \\ P_{21} & P_{22} \end{bmatrix} \quad (4.3.18)$$

The objective is to find a stabilizing controller  $K$  that minimizes the  $\infty$ -norm of  $\|F_1(P, K)\|_{\infty}$ . For an uncertainty block satisfying  $\|\Delta\|_{\infty} < 1$ , the closed loop system in Figure 4.3.8 has robust performance if  $\|F_1(P, K)\|_{\infty} \leq 1$  is achieved [130].

This result, however, is conservative because it assumes that the delta block is a full block. The uncertainties in a realistic problem are due to the components of a system, and the representation of such uncertainties results in a block diagonal  $\Delta(s)$ . A less conservative robustness test for the closed loop system is given by examining the structured singular values ( $\mu$ ) of  $M = F_1(P, K)$ . For a given system  $M$  and an uncertainty structure, the structured singular value  $\mu$  is defined by Doyle and Zhou [130] and [127] as,

$$\mu_{\Delta} = \frac{1}{\min\{\sigma(\Delta) : \Delta \in \Delta', \det(I - M\Delta) = 0\}} \quad (4.3.19)$$

where  $\Delta'$  is the set of block diagonal matrices

If no  $\Delta \in \Delta'$  makes  $(I - M\Delta)$  singular then  $\mu_{\Delta}(M) = 0$  [80,130].

#### 4.4. Conclusions

This chapter was devoted to the finite element based system modeling techniques and the robust control design and analysis applied to the smart structures. This thesis attempted to introduce the methods of structural dynamics to the structural

control design and analysis techniques so as to serve as a link between the structural and control engineering disciplines.

In this thesis, the effectiveness of nodal and modal coordinates based system modeling approaches was illustrated. During the formulations, the theory and the basic assumptions underlying the method of the static reduction for the determination of the reduced spatial models of the smart structures was also outlined.

It was theoretically determined that the modal coordinates based technique allows the specification of the desired number of modes contributing to the response under consideration. This allowance always results in smaller order models than those of nodal coordinate based technique. Another advantage was appeared in the damping models. The modal analysis based technique offers greater flexibility in tuning the damping characteristics of the model by assigning different modal damping ratios associated with the modes of the structure.

This chapter was served to lay down the essence of the open and the closed-loop control systems and detailed on the robustness analyses of the closed-loop controllers. In this thesis, PID and  $H_\infty$  techniques were considered in the design of the controllers that suppresses vibrations of the smart structures. The classical and modern frequency response robustness analyses were introduced to evaluate the robustness issues of the PID controllers. The robust control design and the modeling of the system uncertainty within the framework of  $H_\infty$  controller design and  $\mu$  synthesis were also described. In this thesis, the deviations of the theoretical models from the actual models are represented through system uncertainties.

## CHAPTER 5

### SYSTEM IDENTIFICATION TECHNIQUES FOR SMART STRUCTURES

#### 5.1 Introduction

This chapter describes system identification techniques for the smart structures. Based on the theoretical analyses described in Chapter 3, the aluminum test articles with surface bonded piezoceramic actuators and strain gage sensors are fabricated to obtain the experimental characteristics of the smart structures for the development of active vibration control strategies.

The determination of the accurate model of the system is an essential step in the design of a high performance control system. The system models may be obtained from finite element model or system identification. System identification is a method of constructing a mathematical model for a system by using input-output data. The technique provides the appropriate description of the system, especially in the cases where the finite element modeling of the structures becomes insufficient to provide the accurate results.

Usually at the initial stages, the finite element model is sufficient. The finite element modeling allows the determination of the optimal actuator and sensor placement, actuator size and power requirements. Generally, finite element method accurately predicts the natural frequencies and mode shapes. But, since the technique makes no damping predictions [59], it usually does not determine the

transfer functions relating the inputs and outputs very accurately. Hence, because of the difficulties in the development of an accurate finite element model of the smart structures, the technique is generally considered at the design stage. For the controller design, usually experimentally identified models are considered [58,59,60]. The results obtained from system identification may also be used to tune the accuracy of the finite element modeling results.

Since the system identification techniques only require the specification of the input-output relations of the system, the accurate description of these relations has of vital importance for the success of the technique. The input-output relations can be synthesized from the frequency response data [58,122].

In this thesis, the finite element models are considered in the determination of the natural frequencies of the smart structures specifying the frequency range of interest. For the determination of the identified minimal order models of the smart structures the frequency domain identification technique, which is based on the least square curve fitting, is used.

## **5.2 Test Articles**

By using the results of Chapter 3, three test articles are produced and tested in Sensor Technologies Limited of Canada. These are called the smart beam and the smart fin in this thesis.

The smart structures consist of spatially distributed BM500 type piezoelectric patches bonded symmetrically on the top and bottom surfaces of the passive structures. The direction of polarization is in the thickness direction. The electric, dielectric and material properties of the piezoelectric patches are given in appendix A.

The response of a smart structure may be described in terms of displacement, strain, velocity or acceleration. Although accelerometers are the most common form of the transducers used in the measurements of the response of large structures, their considerable mass and local stiffening effects have negative effects on the response of the smart structures consisting of light components. The recent advances in the laser based transducer systems may also provide an extensive non-contacting measurement capacity. Laser doppler systems may be considered for the measurement of the vibration signals. However, their delicacy in handling, cost and the difficulties in the integration of the sensor units to the aerospace structures limit their potential use in the smart structures technologies. The piezoelectric sensors offer precise vibration measurements for smart structure applications [101]. But the accuracy of the piezoelectric sensors is limited to the relatively moderate frequencies ( $f > 10$  Hz) [116]. Furthermore, the piezoelectric sensors are very sensitive to the changes in the environmental conditions such that thermal fluctuations result in continuous drift in the measurements [106].

The utilization of strain gages in smart structure applications yields good performance at relatively low cost. They are also relatively insensitive to temperature changes and suitable for a frequency range of 0 to 150 Hz. In this thesis, the smart structures contain pairs of SG-7/350-LY13 type (Omega Engineering, CT) strain gages bonded top and bottom surfaces of the smart structures symmetrically to sense the vibration signals. During the tests the smart structures are firmly attached to the fixtures designed to provide the required clamped-free configuration.



### 5.2.1 The Smart Beam

The smart beam produced, consists of an aluminum beam (507×50×2 mm) with surface bonded BM500 type 8×(25×20×0.5 mm) symmetrically placed BM500 type piezoelectric patches. The smart beam further contains a pair of SG-7/350 type strain gages bonded symmetrically on the top and bottom surfaces of the structure to sense the vibrations. The test article used in the study is shown in Figure 5.1.

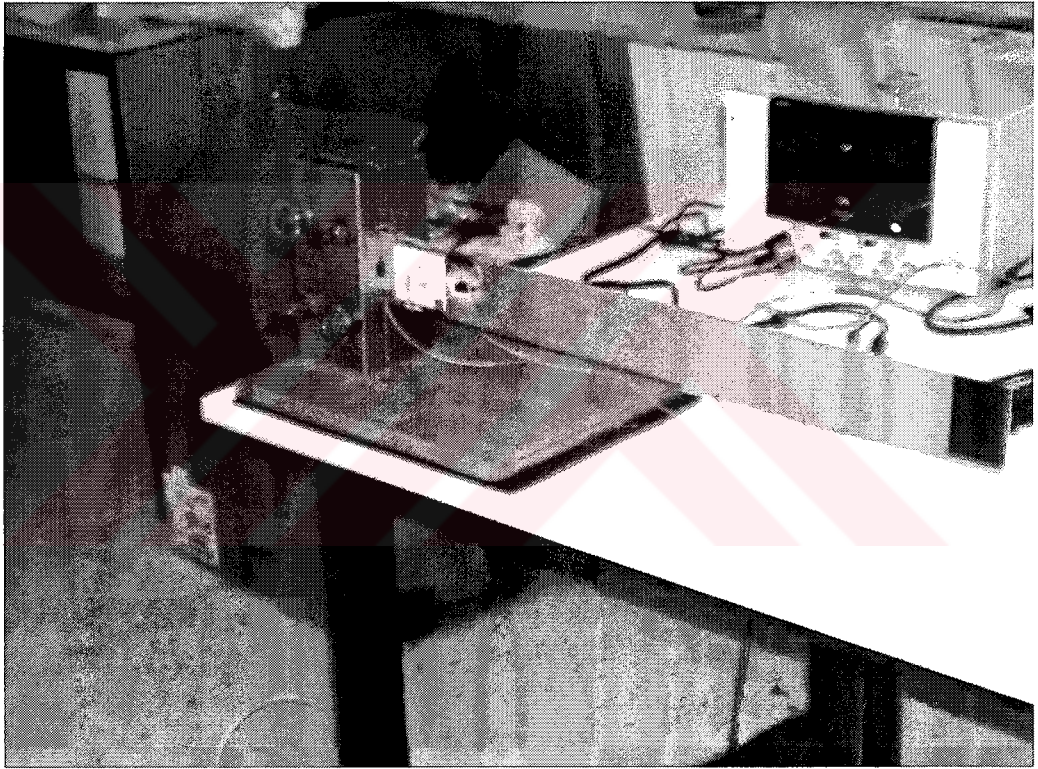


Figure 5.1. The smart beam used in the thesis

### 5.2.2 Smart Fin

The smart fin is actually a plate and designed according to the plate theory. Its shape resembles to a typical vertical fin. Hence it is called a smart fin. The smart fin consists of 24×(25×25×5 mm) symmetrically placed BM500 type piezoelectric actuators. It further contains 6 symmetrically placed SG-7 LY13 type strain gages to sense the flexural and torsional vibrations. An additional pair of PZTs, were also placed on the fin to work as sensors. The test article is shown in Figure 5.2.

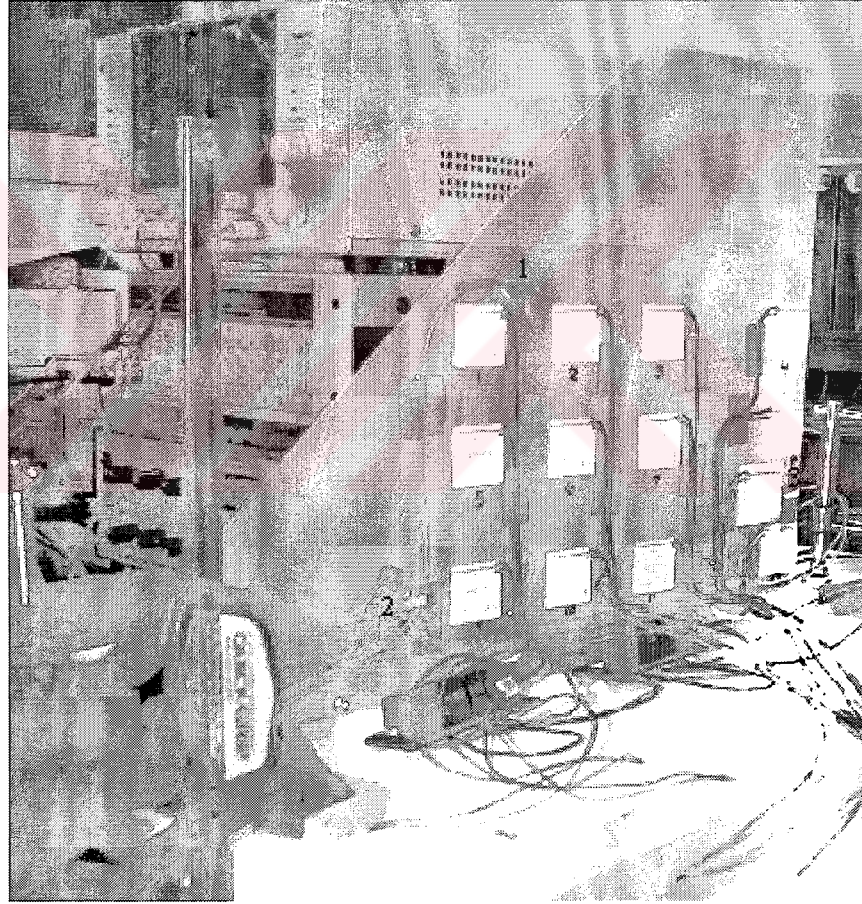


Figure 5.2. The smart fin used in the thesis

### 5.3 Nonparametric Identification for the Smart Structures

It was given in Chapter 4 that the existence of a mathematical model allows the determination of the state-space representation or equivalently, the transfer function of the system. This makes the calculations of the poles and zeros of the system possible. The systems are generally described by specifying the poles and zeros. In this, the numbers giving the poles and zeros are called the parameters of the models. These models provide the parametric description of the system. The existence of the parametric description of the system allows the computation of the frequency response and corresponding transfer function.

In certain cases however, the accurate parametric model may not be available. In such cases, the nonparametric system identification defines the input-output relation of the system without parameters, so there is no finite set of numbers that describe the system exactly [58,60]. In the determination of the nonparametric description for a system, the Fourier transform of the impulse response function or equivalently the frequency response function is considered in most system identification techniques. The methods of determining the experimental frequency response function from the input-output measurements are called nonparametric identification. In this thesis, the spectral estimation method of nonparametric identification is applied to the smart structures. The other common methods of nonparametric identification are the impulse response and step response analyses in time domain and sine wave testing in frequency domain [58, 60, 121, 122].

The nonparametric identification of the smart structures considered in this thesis is achieved at two stages. The first stage involves the excitation of the system to be identified with an input signal  $x(t)$  and the measurement of the output signals  $y(t)$ . The second stage deals with the determination of the resulting transfer function through the application of the appropriate signal processing techniques [58,60].

For the nonparametric identification technique applied in the thesis, the input signal  $x(t)$  should continuously excite the system within the frequency range of interest. A band limited white noise or a chirp signal usually used as input signal [58,60]. The chirp is a sinusoidal function with a frequency that grows from an initial value to a final value so as to cover the frequency range of interest.

### **5.3.1 Data Acquisition**

This section describes various experiments that were conducted to determine the dynamic characteristics of the smart structures. During the experiments PZT actuators were excited by the chirp signals. The signal generator (Stanford Research DS 345) was used for generating the  $\pm 10V_{pp}$  (peak to peak) chirp signals. The chirp signals so generated were amplified to the desired levels by using the power amplifier (KROHN-HITE 7602M) before they were fed to the PZT actuators. The responses of the smart structures were measured by using the strain gages in the half bridge configuration. The symmetric placement of the strain gages allows the construction of a half Wheatstone bridge circuit that eliminates the temperature effects and doubles the vibration signal [131]. The schematic representation of the half bridge configuration considered in the thesis is shown in Figure 5.3.

During the tests, the sensor signals were preamplified and to eliminate the noise present in the environment. The analog sensor signals were then converted to digital ones by a 16 bit Analog to Digital Converter (ADC) board (NI-PCI16XE-50) and stored in the host computer. The ADC board has 16 channel analog and 8 channel digital input-output channels and can stream data up to 20kS/s. The commercial software LabVIEW<sup>®</sup> (v.5.1) was used.

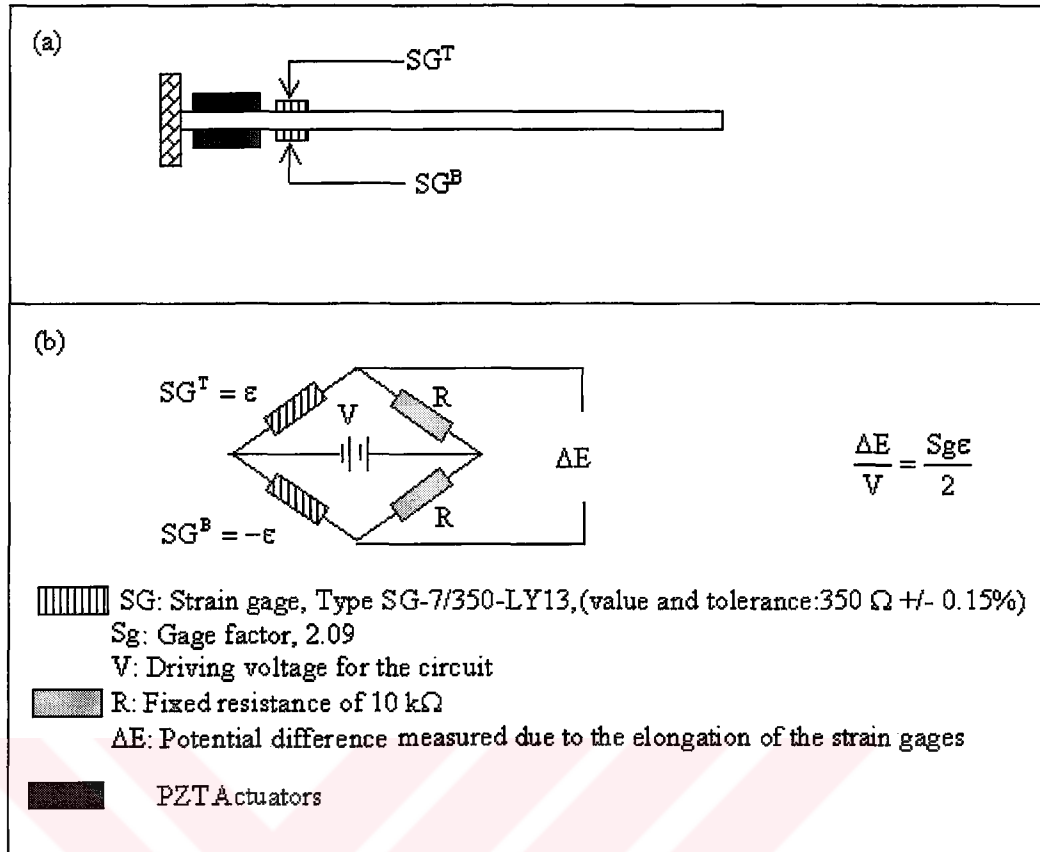


Figure 5.3. The configuration of the strain gages on the smart structures and the schematic representation of the Wheatstone bridge used in the thesis

- The placement of the strain gages on the smart beam
- The half Wheatstone bridge connection of the strain gages

### 5.3.1.1 The Smart Beam Experiments

The frequency range of interest for the nonparametric identification of the smart beam was determined by using the theoretical analysis conducted in Chapter 3. The frequency range of interest was selected to span the first three flexural frequencies of the smart beam. During tests, the smart beam was continuously excited by a chirp signal changing from 0.1 Hz to 150 Hz in 120s. The magnitude of the 10V peak to peak (pp) chirp signal was increased to 165V through a power amplifier and the

response of the smart beam was measured. The preamplified strain gage signals and the output of the signal generator were converted to the digital signals by using the ADC board at the rate of 4096 sample/s and stored in the host computer that includes LabVIEW® (v.5.1).

The detailed description of the data acquisition system is shown in Figure 5.4. In this setup, the passive portion of the smart beam was appropriately grounded and the smart beam firmly attached to the fixture throughout the tests. The LabVIEW® (v.5.1) program used for the acquisition of the data is shown in Figure 5.5. Figure 5.6 gives a sample time domain representation of the chirp signal and the output of the smart beam for nonparametric identification. The first three resonance frequencies of the smart beam show up in the form of three sharp peaks in the sample output of the smart beam shown in Figure 5.6.b.



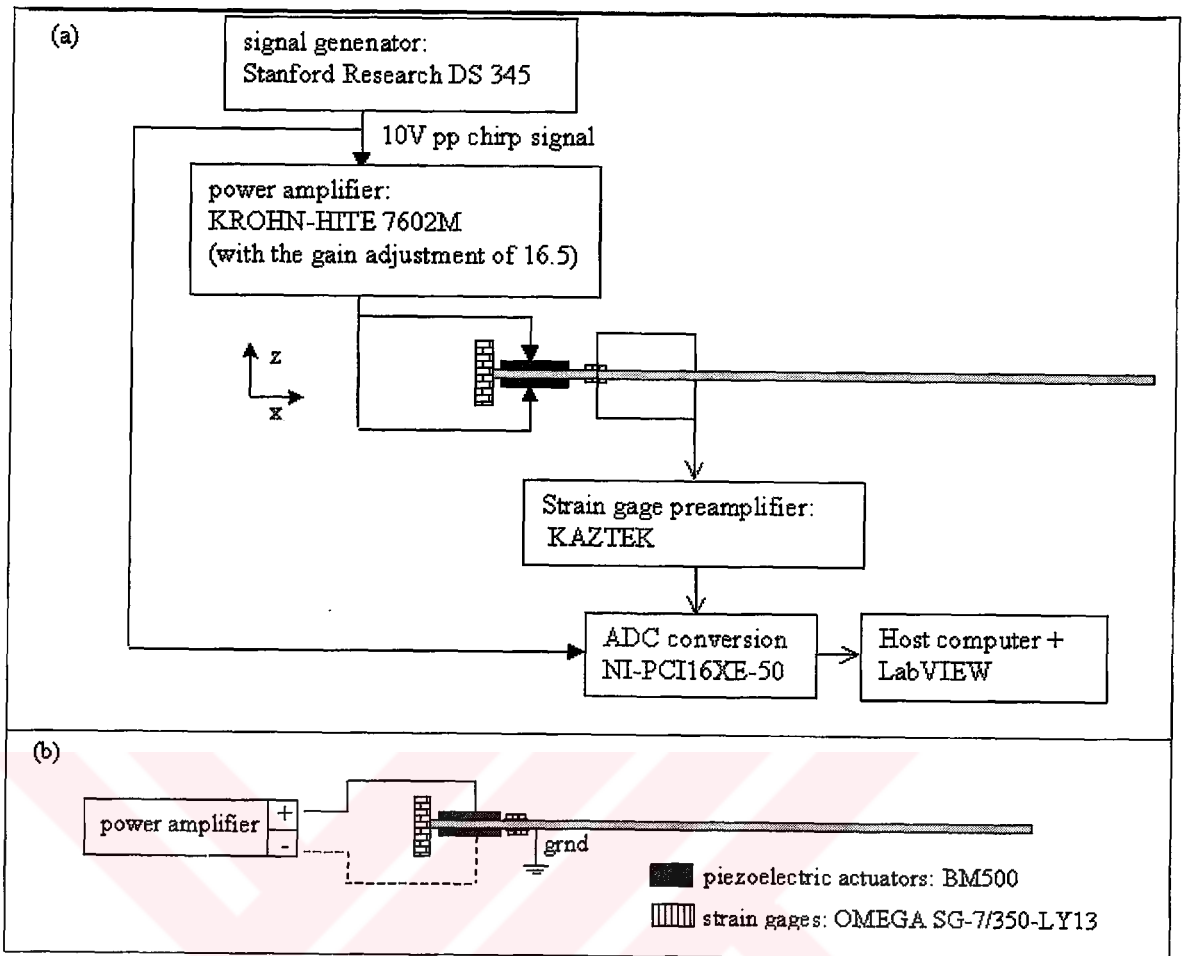


Figure 5.4. The data acquisition for smart beam

a. The data acquisition system

b. The connection of the piezoelectric actuators to a bipolar power amplifier

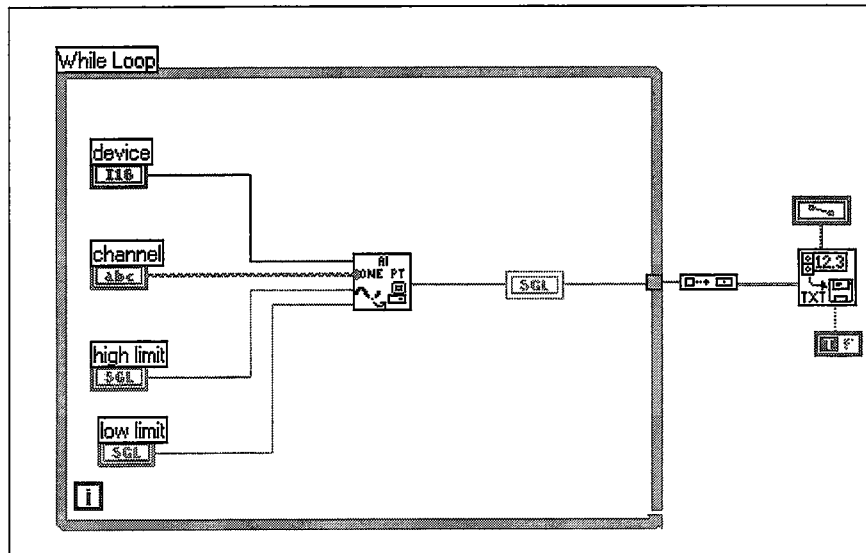


Figure 5.5. The block diagram of the computer program used during the data acquisition

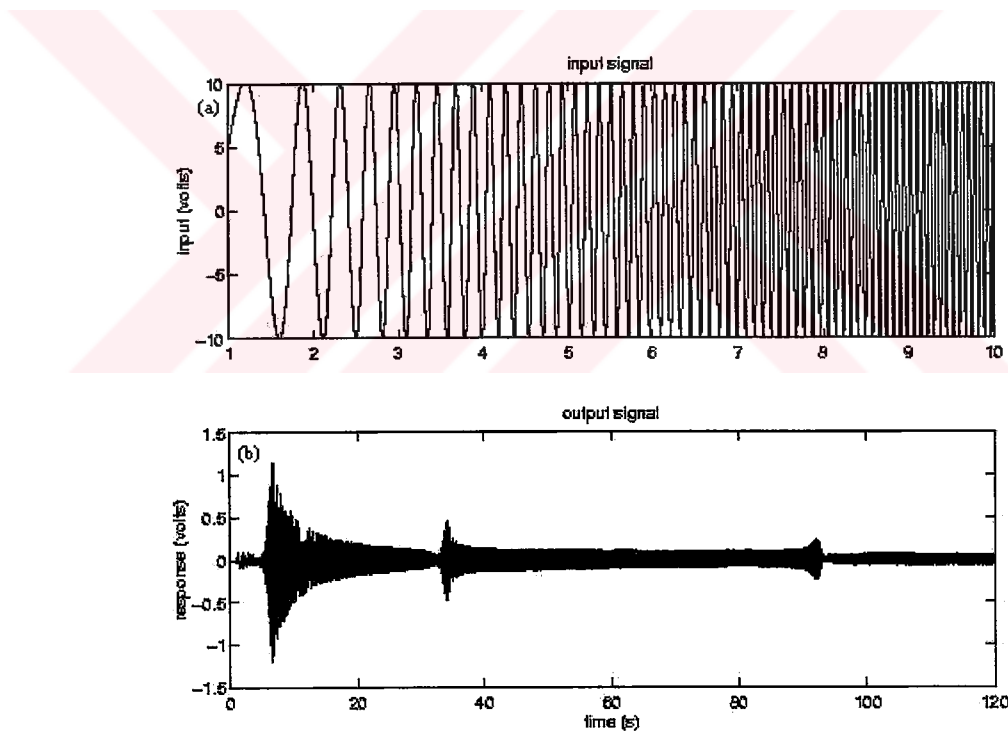


Figure 5.6. Sample time domain representations of the signals measured during the tests for the smart beam

- a. A portion of the chirp signal for 10s
- b. An output of the smart beam for 120s



### 5.3.1.2 The Smart Fin Experiments

In this thesis, as a result of the analysis explained in Chapter 3, only the strain gage pairs labeled (1) and (2) were considered for the nonparametric identification of the smart fin. Furthermore, the actuation was only applied to the PZTs on one face of the fin. Figure 5.7 gives the details of the data acquisition system used for the smart fin

During the tests, the PZT actuators the piezoelectric actuators were connected to the positive port of the power amplifier and the aluminum fin was joined to the negative port of the power amplifier. Figure 5.8 gives a sample time domain representation of the chirp signal whose frequency changes from 1Hz to 100 Hz in 30s and the outputs of the smart fin for nonparametric identification. The data was collected at a rate of 1024 samples/s for 30 s throughout the tests. The computer program used in the storage of the data is shown in Figure 5.9. During the tests, in order to improve the signal to noise ratio, the DC offsets of 8V and 9V were applied to the strain gages at location (1) and location (2) respectively.

In Figure 5.8, the first three resonance frequencies of the smart fin can be seen as the peaks shape of which are different for each output channel. These differences are due to the sensing of the response of the smart fin at different locations. It is evident from the figure that while the strain gages at location (1) have better response characteristics at the second and third modes than that of the first mode, the strain gages at location (2) have superior response characteristics at the first and the second modes compared to the third mode. Hence, the dynamic characteristics of the smart fin at its three modes of vibration can be estimated by using the current configuration of the strain gages on the smart fin.

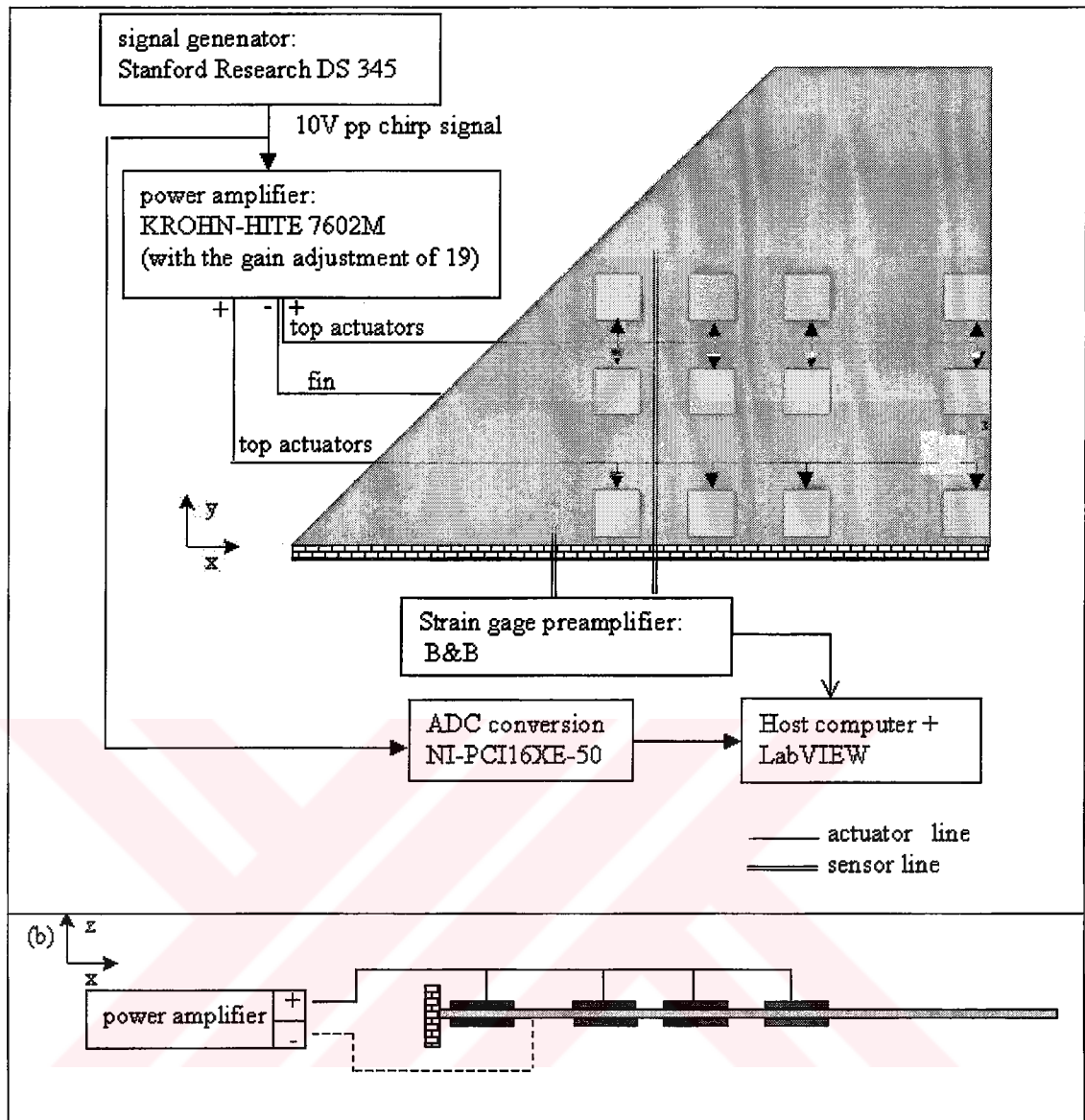


Figure 5.7. The data acquisition for smart fin

a. The data acquisition system

b. The connection of the piezoelectric actuators to a bipolar power amplifier

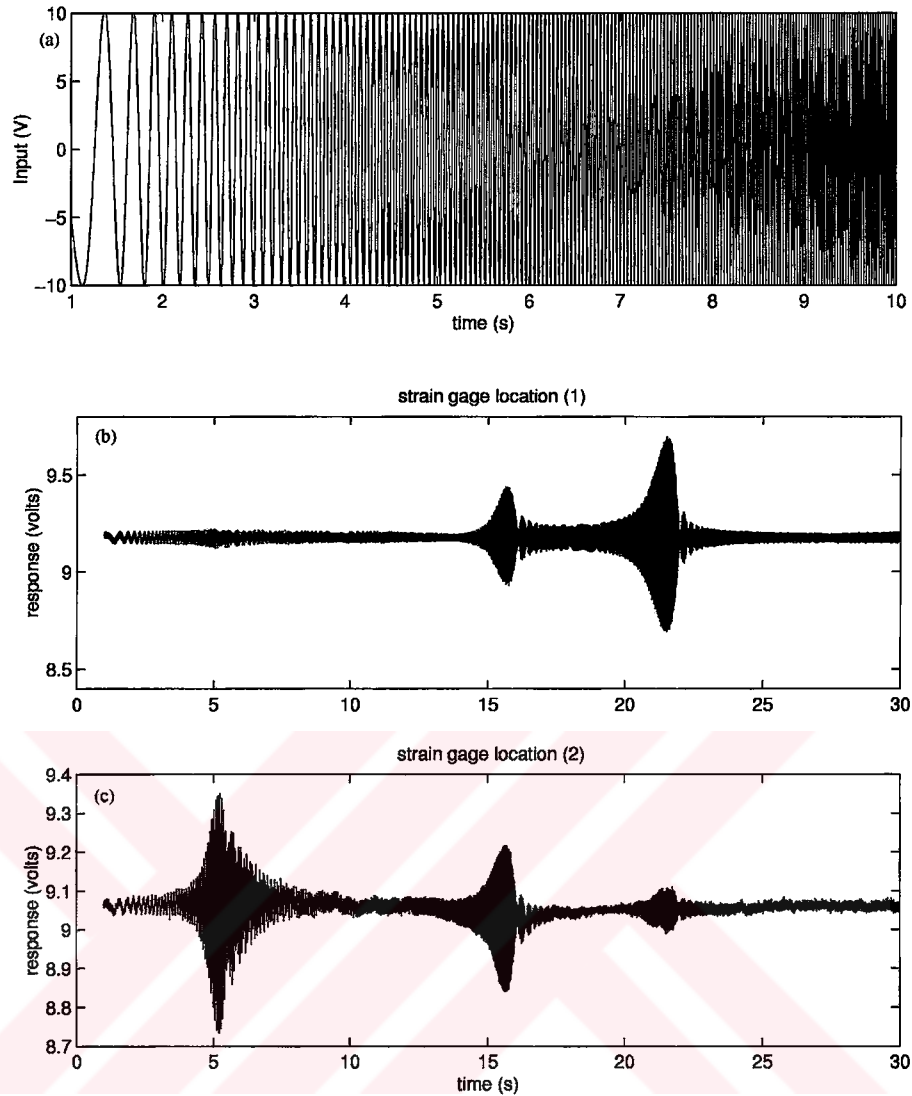


Figure 5.8. Sample time domain representations of the signals measured during the tests for the smart fin

- a. A portion of the chirp signal for 10s
- b. An output of the smart fin for 30s (strain gages at location (1))
- c. An output of the smart fin for 30s (strain gages at location (2))

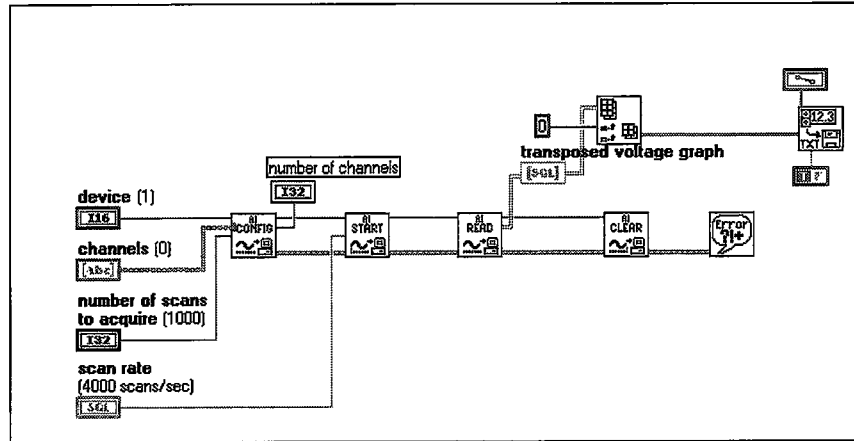


Figure 5.9. The block diagram of the computer program used in the multi channel data acquisition for smart fin

### 5.3.2 Signal Processing

The impulse response of a linear time invariant systems characterizes the dynamics of that system. In order to determine the nonparametric description of the system, the input and output relation of the system must be determined. The input/output relation of a linear time invariant system is given by the convolution integral [58,60].

$$y(t) = \int_0^{\infty} g(\tau)x(t - \tau)d\tau \quad (5.2.1)$$

$$R_{xy}(\tau) = \int_0^{\infty} g(\gamma)R_{xx}(\tau - \gamma)d\gamma \quad (5.2.2)$$

$$R_{xx}(\tau) = \lim_{T \rightarrow \infty} \frac{1}{T} \int_0^T x(t)x(t + \tau)dt$$

$$R_{xy}(\tau) = \lim_{T \rightarrow \infty} \frac{1}{T} \int_0^T x(t)y(t + \tau)dt$$

By taking the Fourier transform of the convolution integrals given (5.2.2), the corresponding power spectral density functions of  $S_{xx}$  and  $S_{xy}$  are obtained. In this case, the spectral densities and the transfer function  $G(\omega)$  can be related as,

$$S_{xy}(\omega) = G(\omega)S_{xx}(\omega) \quad (5.2.3)$$

where

$$S_{xy}(\omega) = \int_{-\infty}^{\infty} R_{xy}(\tau) e^{-i\omega\tau} d\tau$$

$$S_{xx}(\omega) = \int_{-\infty}^{\infty} R_{xx}(\tau) e^{-i\omega\tau} d\tau$$

In most of the recent signal processing softwares, like Matlab<sup>®</sup> (v.6.0), due to the numerical advantages [60,127] the power spectral density functions are calculated from the Discrete Fourier Transform (DFT) of  $x(t)$  and  $y(t)$  rather than using the correlation functions.

This thesis presents the method of spectral estimation method of nonparametric identification for the smart structures. The thesis uses Matlab<sup>®</sup>(v.6.0) package program to calculate the DFT of the input and output signals that are used to determine the spectral estimates. The study first finds out the data set in which the input signal influences the output effectively without measurement errors. These errors may arise when the response times of the actuation and measurement devices are not synchronized properly. The data set is obtained by considering the power spectral densities of the input and output signals. The thesis then, by using the data set, computes the experimental transfer functions for the smart structures.

During the theoretical calculations involving the Fourier transform, the windowing of the data is considered to avoid the leakage problem. The leakage is a direct consequence of the need to take a finite length of time history coupled with the

assumption of the periodicity. The windowing involves the imposition of a prescribed profile on the time prior to the Fourier transform. In this thesis, the Hanning windows are considered to reduce the leakage problem. The Hanning windows are typically used for continuous signals like those produced by steady periodic or random vibration [121,122,134].

In order to obtain the estimates for the spectral densities or correlation functions that are used to characterize the output signals, there are additional considerations concerning their accuracy and statistical reliability. Generally, it is necessary to perform the averaging process involving several time records or samples before an obtained result can be used in confidence. The two major considerations, that determine the number of averages required, are the statistical reliability and the removal of spurious noise from the signals. In this thesis, the overlap averaging technique is considered to remove the noise from the output data.

In overlap averaging technique, the input and output signals have time duration of  $T_{tot}$  with  $n$  number of samples. The signals measured are then separated into the  $M$  overlapping segments each of which has duration of  $T$ . Denoting the fraction of overlap time by  $q$  and the overlap time by  $qT$ , the relation among these variable is given as,

$$T_{tot} = ((M - 1)(1 - q) + 1)T \quad 5.2.3$$

Denoting the original continuous signal  $s(t)$ , defined on  $0 \leq t \leq T_{tot}$  and its  $m^{th}$  overlapped segment as,

$$s_m(\tau) = s(\tau + (m - 1)(1 - q)T) \quad 0 \leq \tau \leq T, \quad m = 1 \text{ to } M \quad (5.2.4)$$

That is, each segment is defined over a time interval of  $[0, T]$ , and the  $m^{th}$  time interval is taken from the original signal starting at time  $(m-1)(1-q)T$ . The

windowing and sampling of each of the overlapping segments then can be achieved as,

$$x_{mj} = w(j\Delta t) \times s_m(j\Delta t) \quad m = 1 \text{ to } M, j = 0 \text{ to } n - 1 \quad (5.2.5)$$

where  $w(t)$ ,  $0 \leq t \leq T$  is a temporal weighting function of DFT and  $T = n\Delta T$ . The sampling of each overlapping segments yields a sampled ensemble of signals that can be used to estimate the spectral densities of the input and output signals [127,132,134].

In overlap averaging technique however, since the window  $w(t)$  modifies the amplitudes of the original measured signal, a scaling is required. This can be obtained by analyzing the effect that the window has on the measured original signal and requiring that the estimated spectral density reflect the same mean square value as the original signal. The spectral density of the windowed signal must be corrected by a factor. Defining the effective bandwidth of the signal as [132]

$$B_e = \frac{1}{T} \left( 1 + \frac{1}{2} \sum_{k=1}^K \frac{a_k}{a_0} \right) \quad (5.2.6)$$

where  $a_k$  defines the constants of the temporal weighting function. The correction parameter can be found as [132,133].

$$Q = \frac{T}{a_0^2 B_e} \quad (5.2.7)$$

For Hanning window  $K=1$  and the coefficients are,  $a_0=0.5$  and  $a_1=0.5$

In overlap averaging technique, the Discrete Fourier Transform (DFT) of  $m$  samples can be calculated in an extremely short time. The procedure is more effective than if

all the data points are used only once and it manifests this extra processing by producing smoother spectra than would be obtained if each data sample were used [121,127,132,134]. The extraction of the smoother spectra allows the determination of the accurate experimentally identified system models [60,127].

The success of the technique depends on the number of the averages that must be used in the estimation of the spectral densities. As the number of averages used in the estimation of the spectral density increases, the variance of the estimate decreases; thus the number of averages should be maximized for a specified sampling interval [121,132,134]. Obviously, the number of overlap should strictly be less than the window length specified by the sampling rate of the measurement,  $M_w$  [127]. The factors, influencing the selection of the window length includes storage space for measurements, the cost of obtaining measurements, or the time required to analyze signals. Figure 5.10 summarizes the algorithm considered for the nonparametric identification of the smart structures used throughout the thesis.

### **5.3.2.1 Nonparametric Identification for the Smart Beam**

The experimental transfer function of the smart beam is obtained by using the signals, an example was shown in Figure 5.6, signals through the method of spectral estimation. The plots of sample power spectral density functions  $S_{xx}$ ,  $S_{yy}$  and  $S_{xy}$  are shown in Figure 5.11. The spectral estimates are then used to calculate the experimental frequency response function. During the theoretical calculations the number of overlap averaging are selected to be as large as possible ( $M < 4096$ ). Figure 5.12 gives the bode plot of a sample experimental transfer function obtained.

In this thesis, unless stated otherwise, voltage is considered as the measurement units in the transfer function frequency response plots



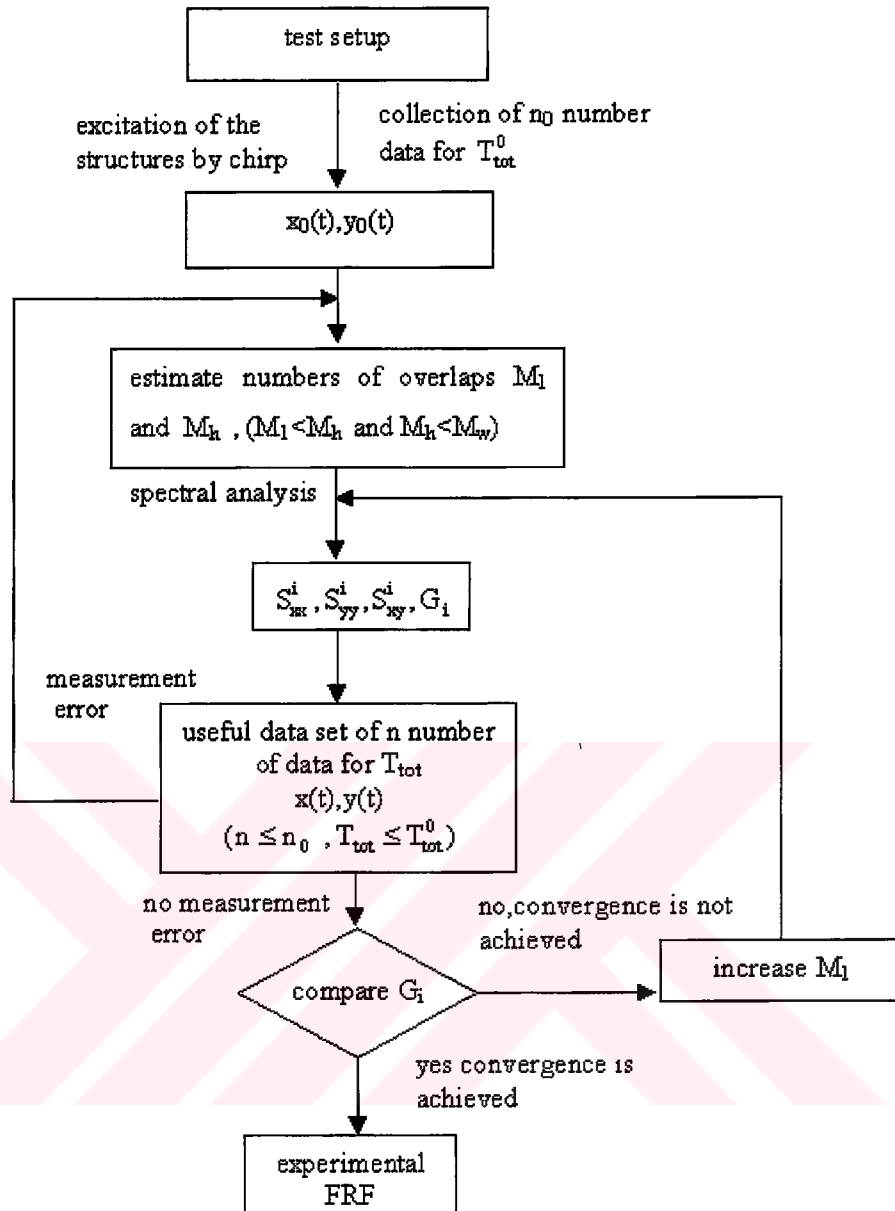


Figure 5.10. The algorithm for the method of spectral estimation of nonparametric identification used in the thesis ( $M_l$ ,  $M_h$  are the lower and higher estimate values for overlap averaging number respectively and  $M_w$  is the window length)

The accuracy of the method of spectral estimation depends largely on the number of overlap. Figure 5.13 gives the comparison of the effects of the number of overlaps on the experimental transfer functions of the smart beam. It can be seen that as the

number of overlap increases, the frequency response curve converges to each other. This is due to the decrease in the variance. The number of averages used to obtain the spectral density increases as the variance of the estimate decreases; so the number of averages should be maximized for a specified sampling interval. In this case however, the overlap averaging values larger than 2600 do not give appreciable differences.

By using the same experimental set up designed for the smart beam and the algorithm developed for method of spectral estimation, the transfer functions of the smart beam corresponding to three different tests in terms of the frequency range, the sampling rate and duration of the experiment are also calculated. Table 5.1 describes the parameters of the measurements conducted. The bode plots of the resulting experimental transfer functions are shown in Figure 5.14. As expected for each measurement, the technique predicts the same poles and zeros for the smart beam, only a slight deviation around the first zero of the system is observed. This deviation may be attributed to differences in the window length and the frequency range.

Table 5.1. The tests conducted for the nonparametric identification of smart beam

Test no	Frequency range (Hz)	Duration of the test (s)	Sampling rate (Samples/s)	Number of overlaps
1	0.1-150	120	4096	2600
2	1-150	60	2048	1600
3	1-150	30	1024	650

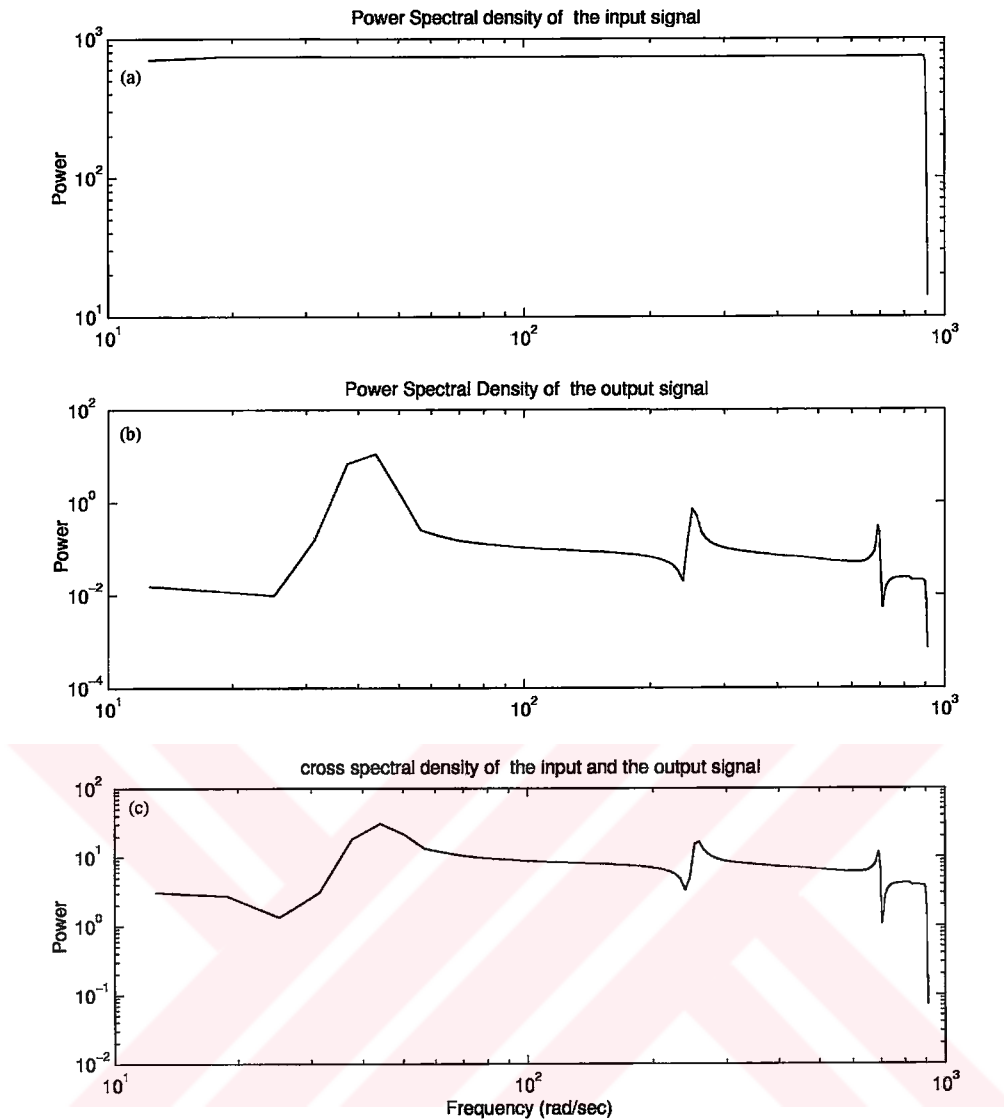


Figure 5.11. Sample power spectral densities of the input and the output of the smart beam

- The spectral density of the input,  $S_{xx}$
- The spectral density of the output,  $S_{yy}$
- The cross spectral density,  $S_{xy}$

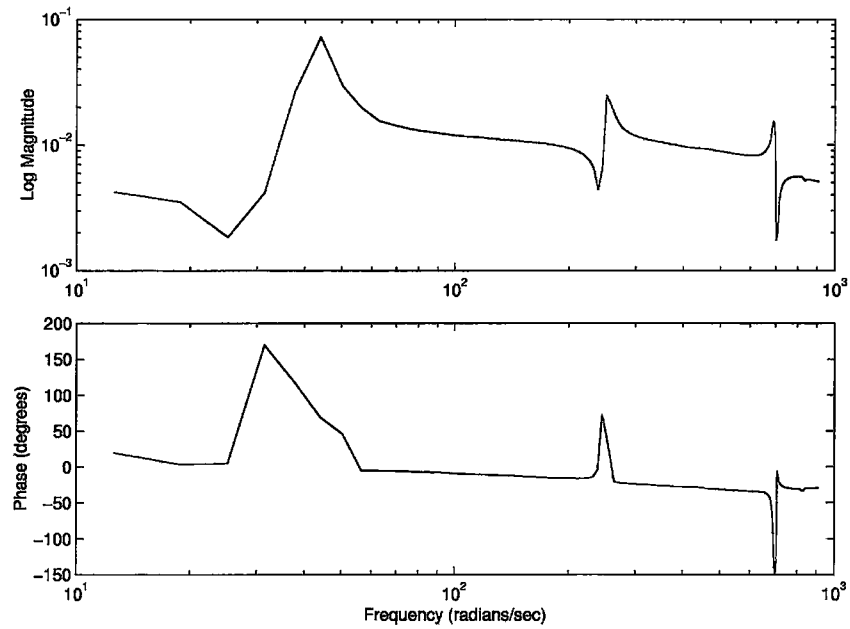


Figure 5.12. Bode plot of a sample experimental transfer function of the smart beam

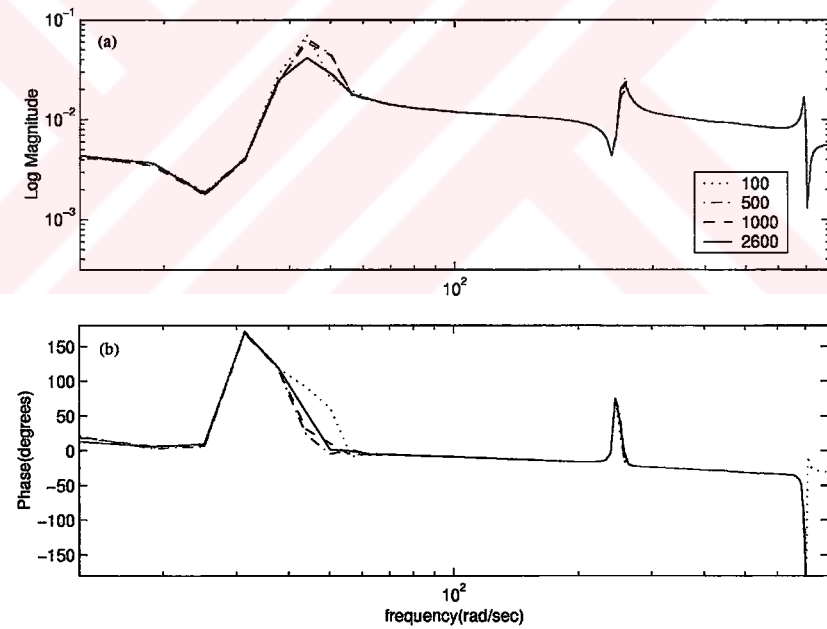


Figure 5.13. The influences of the overlap averaging number on the experimental transfer functions of the smart beam

a. Magnitude

b. Phase

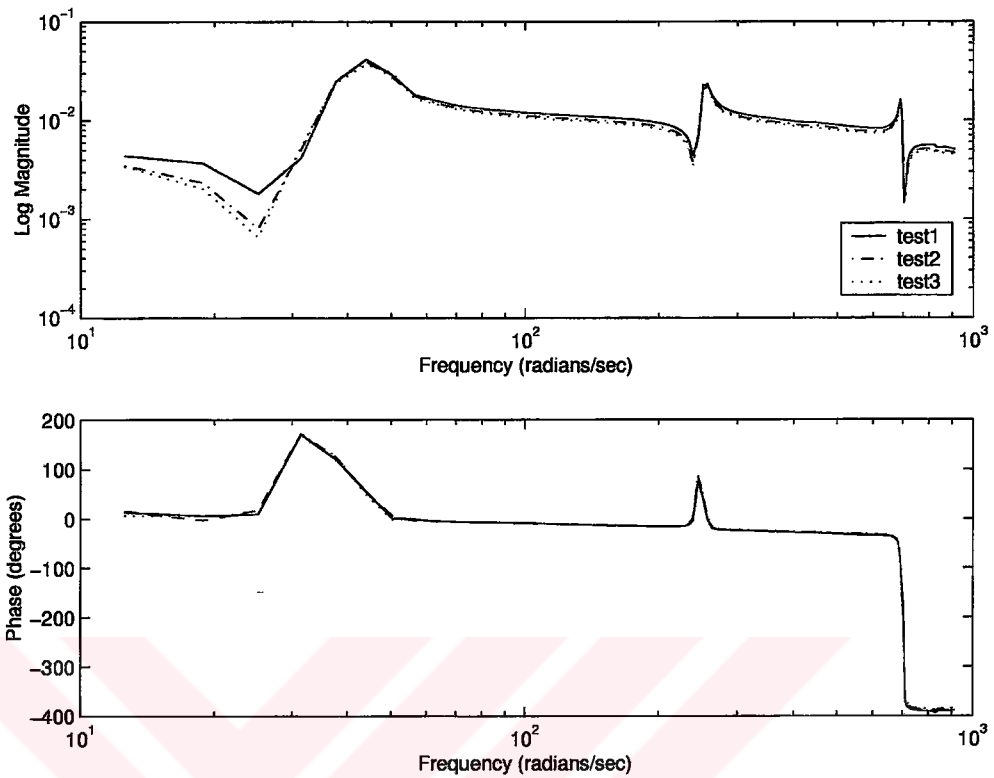


Figure 5.14. The comparison of the influences of the different measurements on the experimental transfer functions of the smart beam

### 5.3.2.2 Nonparametric Identification for the Smart Fin

By using the time domain representations of the input and the output signals obtained for the smart fin which are shown in Figure 5.8, the spectral estimates of the smart fin are calculated. During theoretical calculations 650 overlap averages are used for the determination of the power spectral densities  $S_{xx}$ ,  $S_{yy}$  and  $S_{xy}$ . The sample power spectral densities of the smart fin are shown in Figure 5.15. The bode plots of the sample experimental transfer functions corresponding to the strain gage locations (1) and (2) are shown in Figure 5.16.

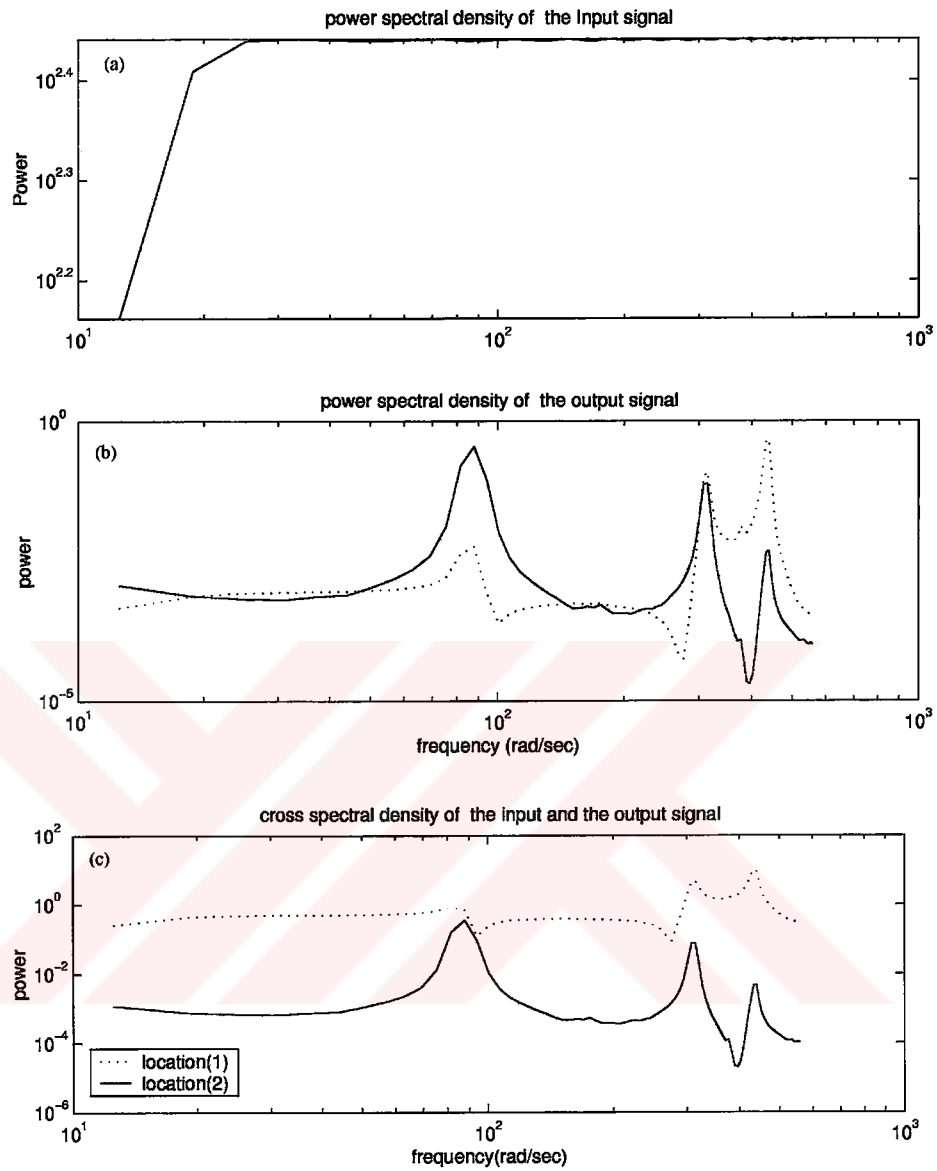


Figure 5.15. Sample power spectral densities of the input and the output of the smart fin (dotted: Strain gage measurements at location (1), solid: Strain gage measurements at location (2))

- The spectral density of the input,  $S_{xx}$
- The spectral density of the output,  $S_{yy}$
- The cross spectral density,  $S_{xy}$

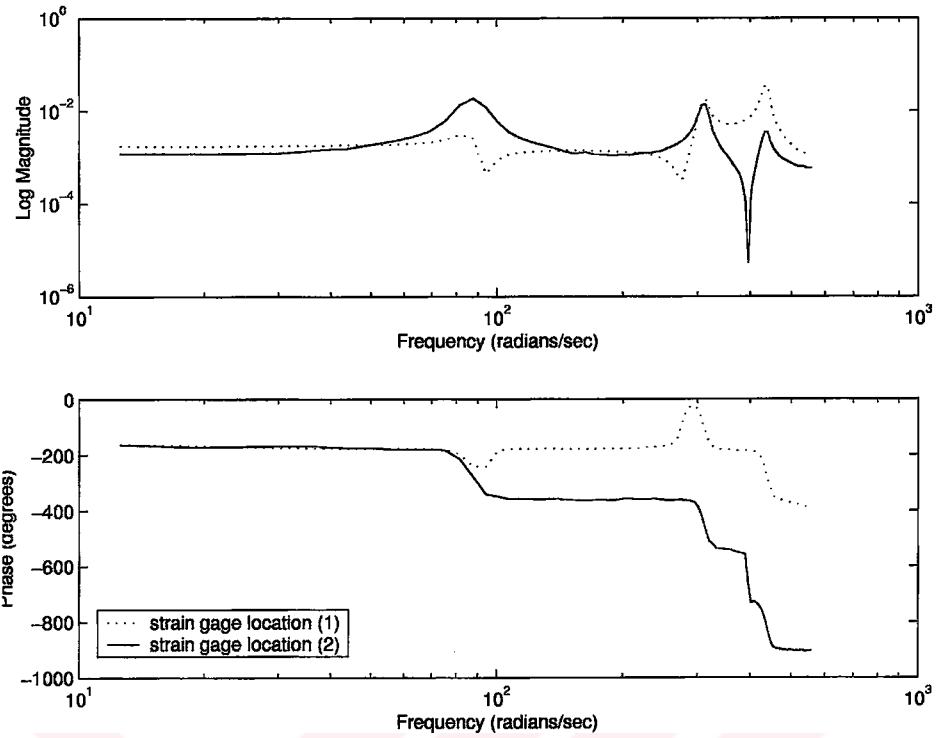


Figure 5.16. The bode plots of the sample experimental transfer functions of the smart fin (dotted: Strain gage measurements at location (1), solid: Strain gage measurements at location (2))

#### 5.4 Frequency Domain Least Squares Curve Fitting Technique

The accurate model for the system can be obtained by curve fitting to each nonparametric SISO transfer functions [58,60]. In this thesis, the experimental transfer functions obtained for the smart structures in the Section 5.2 are considered for this purpose.

The discrete transfer function representation for each experimental transfer function may be represented by the following form

$$g(z) = \frac{n(z)}{d(z)} \quad (5.3.1)$$

where  $n(z)$  and  $d(z)$  describes the polynomials of degree  $\leq p$  with unknown coefficients. Equation (5.3.1) can then be rewritten as [58,60],

$$g(z) = \frac{\sum_{j=0}^p n_j z^j}{z^p + \sum_{j=0}^p d_j z^j} \quad (5.3.2)$$

multiplying both sides by the denominator and rearranging the terms gives,

$$\sum_{j=0}^{p-1} d_j z^j g(z) - \sum_{j=0}^p n_j z^j = -g(z) z^p \quad (5.3.3)$$

equation 5.3.3 can be put in a compact form by defining the following variables [60].

Let,  $\{z\}_{i=1}^M$  represent the points on the unit surface obtained by mapping the discrete frequency points,  $\omega_i$  of the experimental transfer function as,

$$[Z] = \begin{bmatrix} \begin{Bmatrix} 1 \\ \vdots \\ 1 \end{Bmatrix} & \begin{Bmatrix} z_1 \\ \vdots \\ z_m \end{Bmatrix} & \dots & \begin{Bmatrix} z_1^p \\ \vdots \\ z_M^p \end{Bmatrix} \end{bmatrix} \quad (5.3.4)$$

Setting  $Z_0 = Z$  and deleting the last column of the matrix equation given in equation 5.3.4 and by defining the following variables,

$$\begin{aligned} D &= \text{diag}[g(z_1), \dots, g(z_M)] \\ \hat{n} &= [n_0, \dots, n_p]^T \\ \hat{d} &= [d_0, \dots, d_{p-1}]^T \\ y &= [g(z_1)z_1^n, \dots, g(z_M)z_M^n]^T \end{aligned} \quad (5.3.5)$$

equation (5.3.3) can be written in the following form.



$$(DZ_0 - Z) \begin{Bmatrix} \{\hat{d}\} \\ \{\hat{n}\} \end{Bmatrix} = -y \quad (5.3.6)$$

The form of equation (5.3.6) represents a standard least square problem. The vectors  $\{\hat{d}\}$  and  $\{\hat{n}\}$  can be estimated by solving equation (5.3.6). In the solution an iterative technique is considered. The resulting discrete transfer function can be transformed to continuous system by using bilinear transform [60,127].

In this thesis, the frequency domain least square technique is applied to the experimental frequency response functions. During the theoretical calculations Matlab<sup>®</sup>(v.6.0) package program is used to find the experimentally identified models for the smart structures. Figure 5.17 gives the flowchart of the least square curve fitting technique applied for the identification of the smart structures.

The least square curve fitting technique applied to the smart structures is iterative for the order of the system to be identified. The process is repeated until the desired accuracy between the experimental and the identified model is achieved. Thus, algorithm allows the specification of the minimal order models for the accuracy specifications at each frequency of the smart structures. The minimal order in state space realization is analogous to the number representing the sum of modes and residual modes contributing the response for a dynamical system.

In certain cases however, the numerical curve fitting algorithm may estimate the order than this number. This is due to the addition of over-damped poles to fit the DC gain of the experimental transfer function [127].

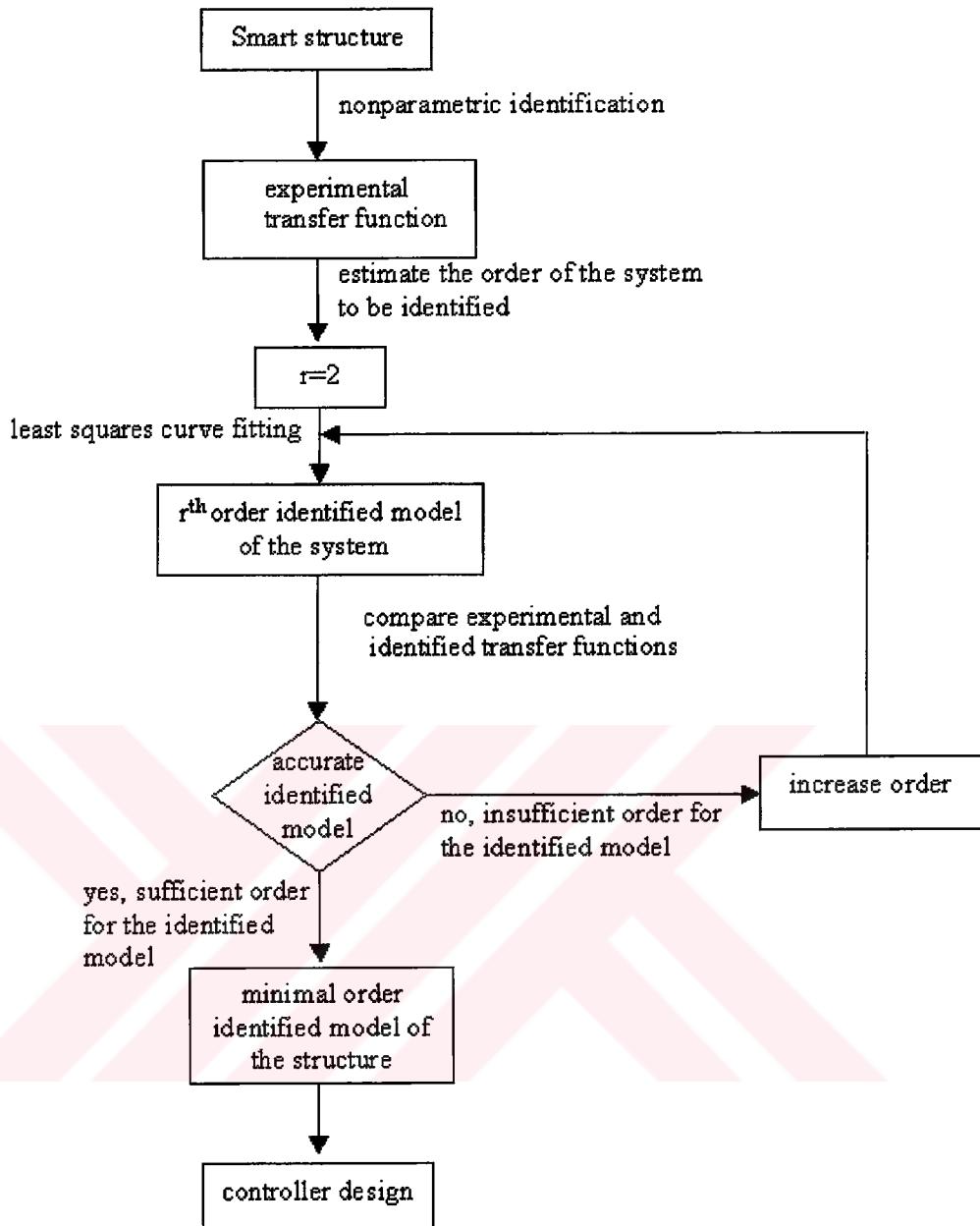


Figure 5.17. The algorithm used for the application of frequency domain least squares curve fitting technique to the smart structures

#### 5.4.1. System Identification for the Smart Beam

The least square curve fitting technique is applied to the experimental transfer function of the smart beam shown in Figure 5.12. In this technique, the aim is to find the minimal order that sufficiently matches with the experimental transfer functions. The identified minimal order transfer function obtained may then be used to find the state space representation of the system with some computational effort [80,127]. Figure 5.18 gives the effects of the influences of the system order estimation on the identified model of the smart beam. It can be seen that the 10<sup>th</sup> order identified model for the smart beam sufficiently matches with the experimental frequency response within the frequency range of interest. Thus the minimal order for the identified model for the smart beam is determined to be 10.

The Matlab<sup>®</sup> (v. 6.0) code used in the system identification of the smart beam is given in Appendix C.

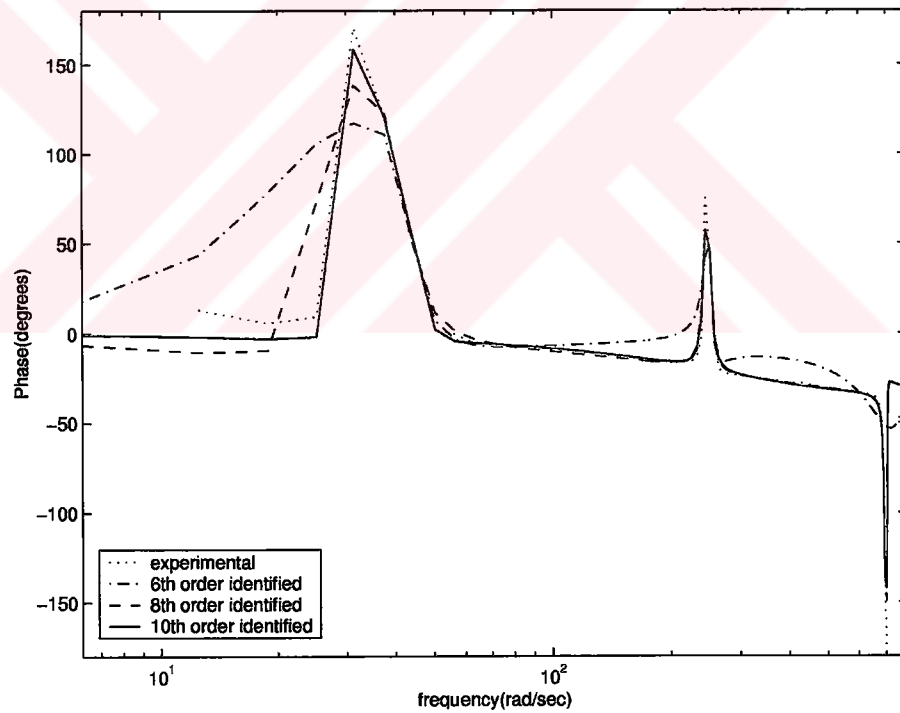
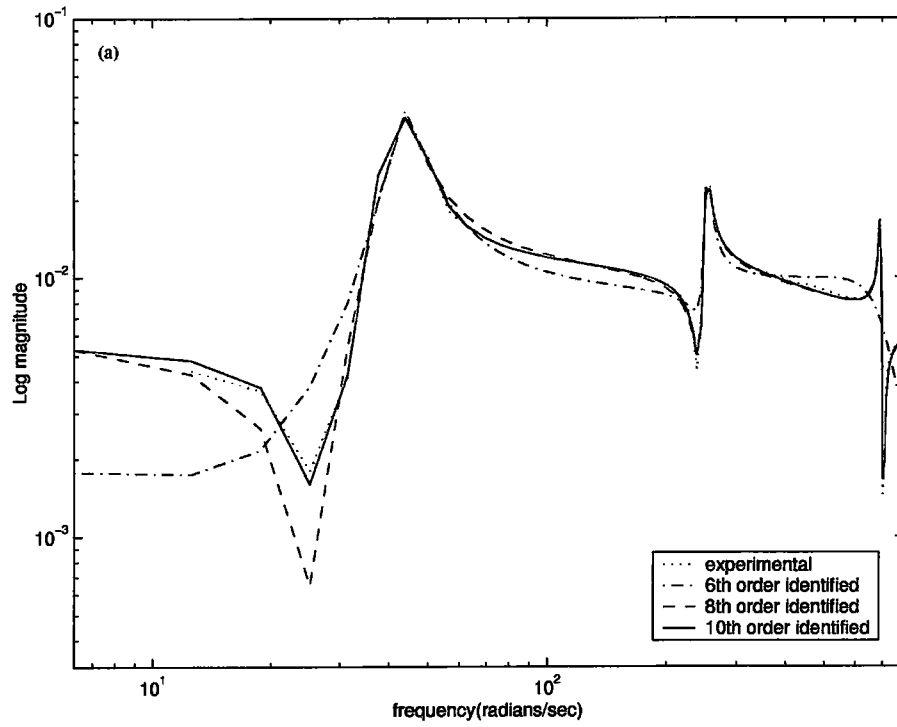


Figure 5.18. The influences of the order selection for the identified models of the smart beam

a. Magnitude

b. Phase

### 5.4.2 System Identification for the Smart Fin

The experimental frequency response functions of the smart fin given in Figure 5.16 are used to find the experimentally identified model of the smart fin. The application of the least square curve fitting technique results in 6<sup>th</sup> order transfer functions from the actuators to each sensor. The comparisons of these models with the experimental models are shown in Figure 5.19 and 5.20.

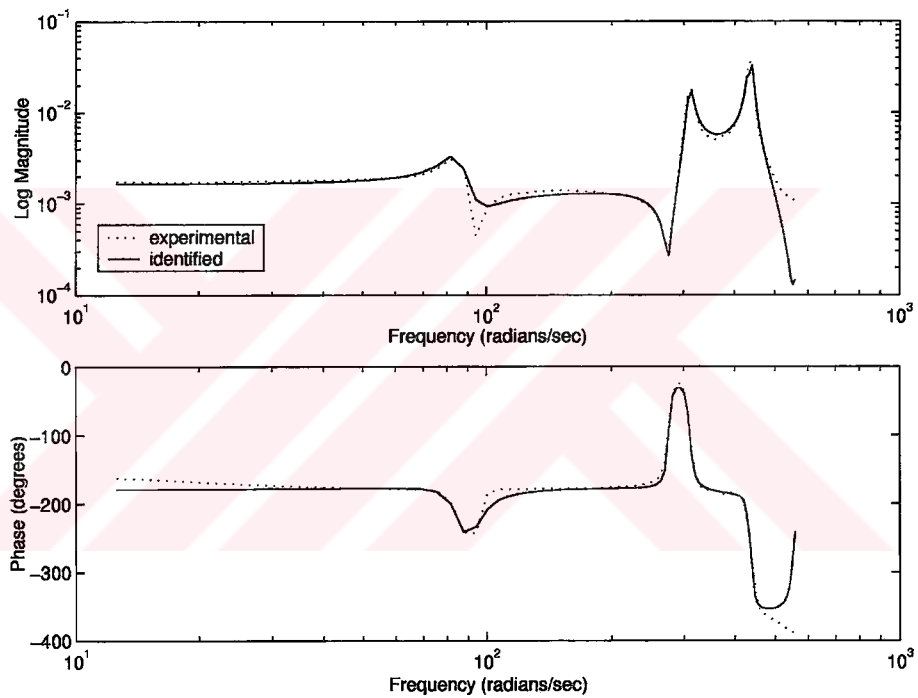


Figure 5.19. The comparison of the frequency responses of the experimental and 6<sup>th</sup> order identified models (Strain gage measurements at location (1))

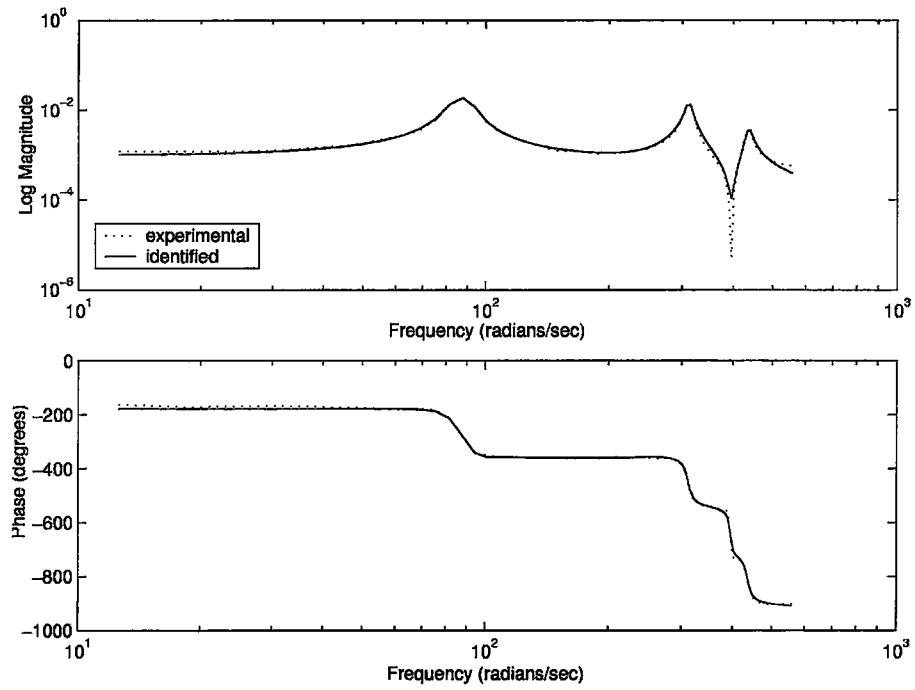


Figure 5.20. The comparison of the experimental and 6<sup>th</sup> order identified models of the smart fin (Strain gage measurements at location (2))

## 5.5 The Validation of the Finite Element Models of Smart Structures

The application of the system identification techniques allows the determination of the precise description of the dynamical characteristics of the smart structures. In this section, the undamped theoretical frequencies obtained from the finite element models of the smart structures and the experimental resonance frequencies are compared. The first three resonance frequencies are tabulated together with the experimentally determined modal damping ratios.

The comparison of the first three resonance frequencies and the modal damping ratios calculated for the smart beam is given in Table 5.2. The resonance frequencies and the modal damping ratios are also calculated for the smart fin. Table 5.3 gives the comparison of the frequencies together with the modal damping ratios.

Table 5.2. The comparison of the theoretical and experimental frequencies of the smart beam

FEM	Experimental	
Frequencies (Hz)	frequencies (Hz)	damping ratio (*)
7.3047	7.2885	$7.731 \times 10^{-2}$
44.112	40.065	$1.778 \times 10^{-2}$
117.28	110.622	$7.061 \times 10^{-3}$

(\*):  $\zeta_r = -\text{real}(\omega_r) / \text{mag}(\omega_r)$

Table 5.3. The comparison of the theoretical and experimental frequencies of the smart fin

FEM	experimental	
frequencies (Hz)	frequencies (Hz)	damping ratio
14.963	14.51	$4.800 \times 10^{-2}$
45.737	48.94	$2.023 \times 10^{-1}$
68.253	69.43	$1.792 \times 10^{-2}$

The frequencies obtained from the finite element models of the smart structures corresponding to the 1<sup>st</sup> and 3<sup>rd</sup> modes are close to the experimental values but the ones corresponding to the 2<sup>nd</sup> mode are different.

### 5.6. The Response of the Smart Beam by Assumed-Mode Summation Method

The finite element based modeling technique presented in this thesis offers three-dimensional fully coupled thermo-mechanical-electrical analysis of the smart structures. In order to highlight the advantages of the finite element based modeling technique developed in this thesis, the smart beam of the study is remodeled by using a technique available in the literature. The modal analysis based technique presented in [74,135] is considered for this purpose. The technique makes the use of the assumed mode-summation method developed for the proportionally damped smart beams. The assumed mode-summation method is known to yield accurate results for the analysis of the structures whose geometries are closed to those of beams [121,122]. During the adaptation of the assumed mode-summation method to the smart beam, the motion of the smart beam is assumed to be constrained on the horizontal plane and the passive portion of the smart beam is considered to be thin compared to its length so that it can be regarded as an Euler-Bernoulli beam. This assumption, leads to the reduction in the three-dimensional theories of the elasticity



and the piezoelectricity described in Chapter 3 to one-dimensional theories. This reduction implies the elimination of spatial variation of the anisotropic material and the piezoelectric properties of the piezoelectric patches. That is, the number of independent elastic constants associated with the piezoelectric patches is reduced from seven to one. The analysis also results in the reduction of two independent dielectric and three piezoelectric constants to one variable only, namely piezoelectric strain constant.

In this section, the results obtained by using the assumed mode-summation approach and those of developed finite element modeling are compared for the smart beam. Since the assumed mode-summation approach requires the specification of the modal damping ratios, the modal coordinate based finite element based modeling technique presented in Chapter 4 is also considered for the modeling of the smart beam. Table 5.4 gives the values for BM500 type piezoelectric actuators which are necessary for the theoretical calculations of the assumed mode-summation method.

Table 5.4. The properties of BM500 type piezoelectric patches [116]

Properties	Constant	Unit
Density: $\rho_p$	7730	kg/m <sup>3</sup>
Compliance: $S_{11}$ ( $S_{11}=1/C_{11}$ )	$15.5 \times 10^{-12}$	m <sup>2</sup> /N
Piezoceramic strain constant: $d_{31}$	$-160 \times 10^{-12}$	C/N

Figure 5.27 shows the comparison of the responses of the smart beam obtained by using these approaches, in terms of the mid-tip point displacement. It can be seen from the figure that the results obtained by using the mode summation approach significantly over-estimates the resonance frequencies of the smart beam. These discrepancies may be attributed to the elimination of the spatial variations of the material properties of the piezoelectric patches that eventually yields to the

inaccurate calculation of the stiffness of the smart beam. Table 5.5 gives the comparison of the theoretically calculated resonance frequencies together with the experimentally determined frequencies of the smart beam.

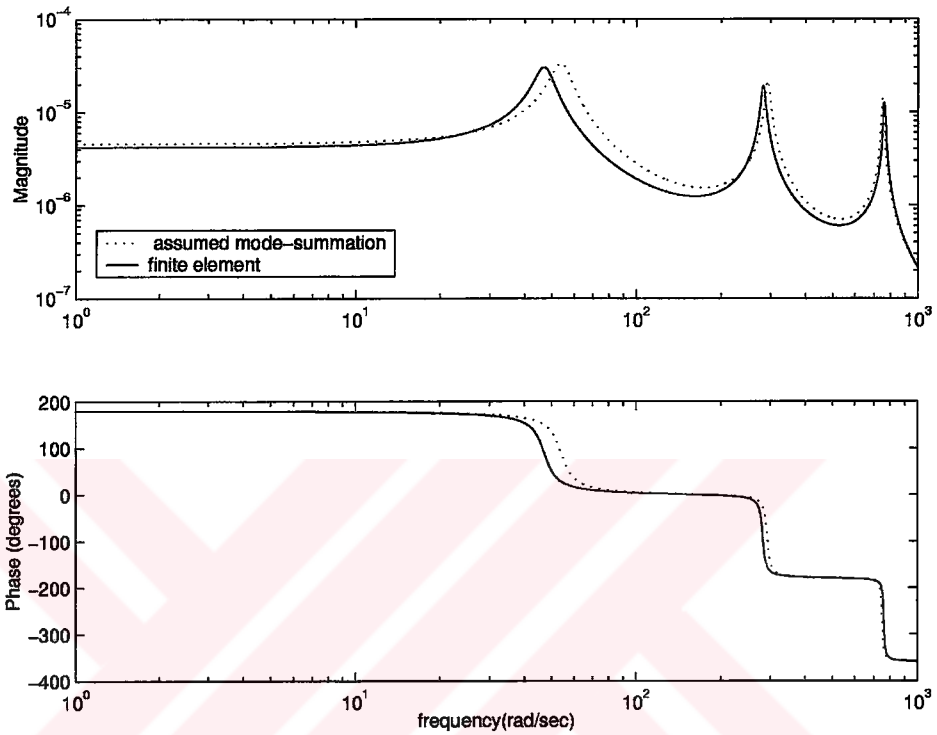


Figure 5.21. The comparison of the responses of the smart beam (the mid-tip displacement response with  $\zeta_1=7.730910^{-2}$ ,  $\zeta_2=1.778410^{-2}$  and  $\zeta_3=7.060510^{-3}$ )

Table 5.5. The comparison of the resonance frequencies of the smart beam

Frequencies (Hz)	Finite Element	Assumed Mode-Summation	Experimental
$f_1$	7.305	8.673	7.2885
$f_2$	44.112	46.371	40.065
$f_3$	117.280	119.37	110.622

In addition to the inaccurate calculation of the stiffness of the smart beam, the assumed-mode summation method also requires the elimination of the lateral deformations of the piezoelectric patches under the application of the electric field. Thus, the omission of the lateral deformations may also lead to inaccurate calculation of the bending moment distribution due to the piezoelectric actuation. It is evident that all those simplifications and omissions cause erroneous results.

### **5.7 The Tuning of the Finite Element Model of the Smart Beam**

This section deals with the determination of the factors that influences the accuracy of the finite element based theoretical models and explains the techniques used for tuning the theoretical response with the experimental data.

The unmodeled effects like the cable weights may influence the accuracy of the theoretical models. The exclusion or the improper interpretation of the damping characteristics including, the modal damping ratios ( $\zeta_r$ ) reduces the effectiveness of the theoretical models. In order to improve the accuracy of the theoretical models, these effects should systematically be incorporated into the analysis.

Another impediment in the accurate modeling of the smart structures designed in this thesis is the hysteresis behavior of the piezoelectric patches. The piezoelectric actuators exhibit the hysteresis nonlinear behavior in their response to applied electric field [3,16,22]. The hysteretic behavior of the piezoelectric actuators results in the mismatches between the theoretical and the experimental transfer functions that influence the effectiveness of the closed loop controllers designed to suppress the vibrations of the smart structures if not properly taken into account [15,17].

The experimentally identified models can be used to tune the accuracy of the finite element based theoretical models of the smart structures. The tuning of the response of the theoretical models deals with the incorporation of the experimental models with the theoretical models. In this thesis, the tuning of the theoretical models is achieved at the three stages. While the first stage focuses on the influences of the hysteretic nature of the piezoelectric actuators on the response, the second deals with the compensation of the cable mass effects on the response. The last stage in the tuning algorithm involves the correction of the damping characteristics of the theoretical models. The following section details on the method of tuning the response of the smart beam used in the thesis.

### **5.7.1 The Influences of The Hysteresis Effect: LVDT Tests on the smart Beam**

The piezoelectric actuators offer a number of benefits for applications in active vibration control of aerospace structures. Their high stiffness results in high actuator authority and excellent integration to the structures. However, the piezoelectric actuators exhibit the material specific nonlinearities in their response. This is observed in the form of hysteresis [3,16,22]. LVDT (Linear Variable Differential Transducer) tests are generally considered to investigate the hysteresis nonlinear behavior of the piezoelectric actuators [15,22,74].

In this thesis, the LVDT tests were conducted in Sensor Technologies Limited laboratories for the determination of the hysteresis effects on the piezoelectric actuators of the smart beam. During the tests, piezoelectric actuators are driven automatically by  $\pm 200\text{V}$  a LabVIEW<sup>®</sup> program controls the process for hysteresis loop experiment. During the experiments, the magnitude of the loop was limited with a maximum applicable electric field and the rate of change of the magnitude was very slow. Figure 5.22 gives the data acquisition used in the LVDT tests conducted for the smart beam.

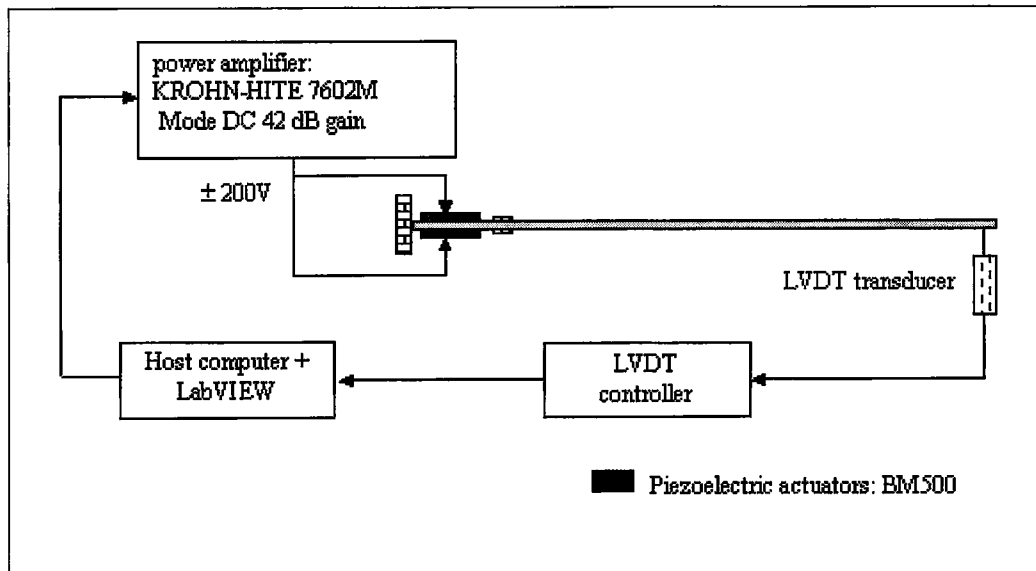


Figure 5.22. The data acquisition of the LVDT tests for the smart beam.

By using the setup shown Figure 5.22 various hysteresis loop experiments were conducted. Figure 5.23 gives the sample results of the hysteresis loop experiments conducted. The slight differences observed between the hysteresis loops reveals that depending of the history of the excitation, one of the possible expansions shown in Figure 5.29 can be the result of a specific voltage applied to the patches. This behavior is typical to the materials that experience the hysteresis nonlinearity with memory [72,73,74]. Hence BM500 type actuators used in the thesis exhibits hysteresis nonlinearity with memory in its response to the applied electric field.

It can be seen from these curves that, the hysteretic response of the smart beam may be approximated by the first and higher order curves. While in the range approximately from 0 to 100V the response can be approximated by the first order, for the actuation values approximately from 100V to 200 V the response is characterized by higher order curves. Since the range of the linearity changes for each sample of records, these ranges are not sharp.

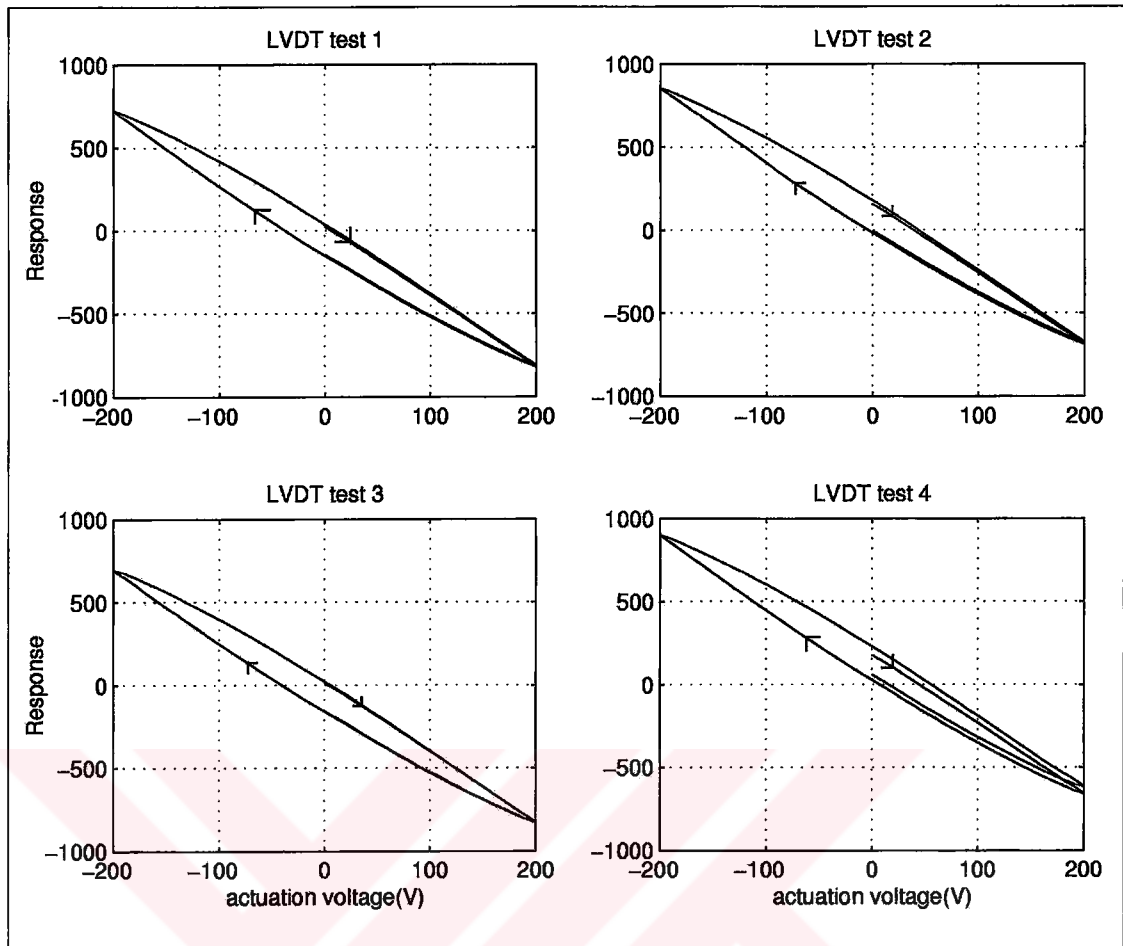


Figure 5.23. The hysteresis nonlinear behavior of the smart beam: The samples of the LVDT tests conducted.

The results of the LVDT tests indicates that that, the linear relationship between the piezoelectric actuation and the response of the smart structure predicted by the theoretical analysis conducted in Chapter 3, is valid only for the low range of the actuation voltage. Thus, if a relatively high voltage values is applied to the actuators, the relationship exhibits the hysteresis nonlinear behavior.

Generally closed loop controllers reduce the hysteresis effects on the system, if properly taken into account during the design stage. These effects can be included in the analysis as the phase lag, which causes instability if the phase margin is not taken large enough [15,74]. In this thesis, the hysteresis effects of the piezoelectric

patches are included in the analysis as the modeling uncertainties at the design stage of the closed-loop controllers.

### 5.7.2 The Influences of the Cable Masses on the Response of the Smart Beam

In this thesis, the effects of the cable masses on the response of the smart beam are simulated by the addition of the spatially distributed mass elements on the finite element model of the smart beam developed in Chapter 3. The mass element MASS21, available in ANSYS® (v. 5.6) is considered for this purpose. Figure 5.24 gives the orientation and the positive sign convention for the point mass element. The distribution of the mass elements on the finite element model of the smart beam is shown in Figure 5.31. In this figure,  $m_1$  represents the amount of the mass distributed on 63 mass elements to account for the effects of the actuator cables and  $m_2$  gives the amount of mass distributed on 4 elements to include the effects of the sensor cables. The effects of the tape mass are also considered by using 26 mass elements. In this model, the amount of the tape mass is represented by  $m_3$ .

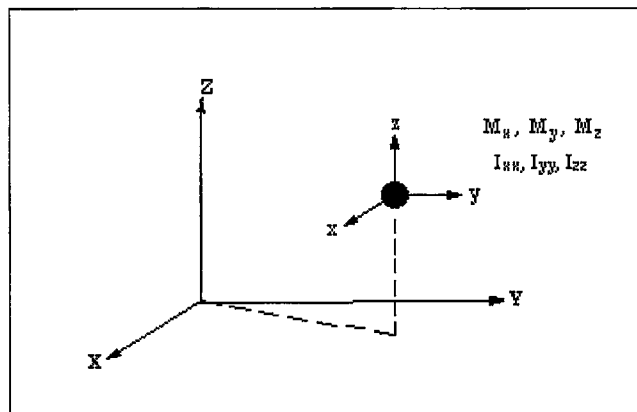


Figure 5.24. The positive sign convention and the orientation of the point mass element, MASS21 used in the thesis.

During the theoretical calculations involving this element, the mass is assigned to z direction only. The influences of the masses in other directions and the effects of the rotatory inertia are not included.

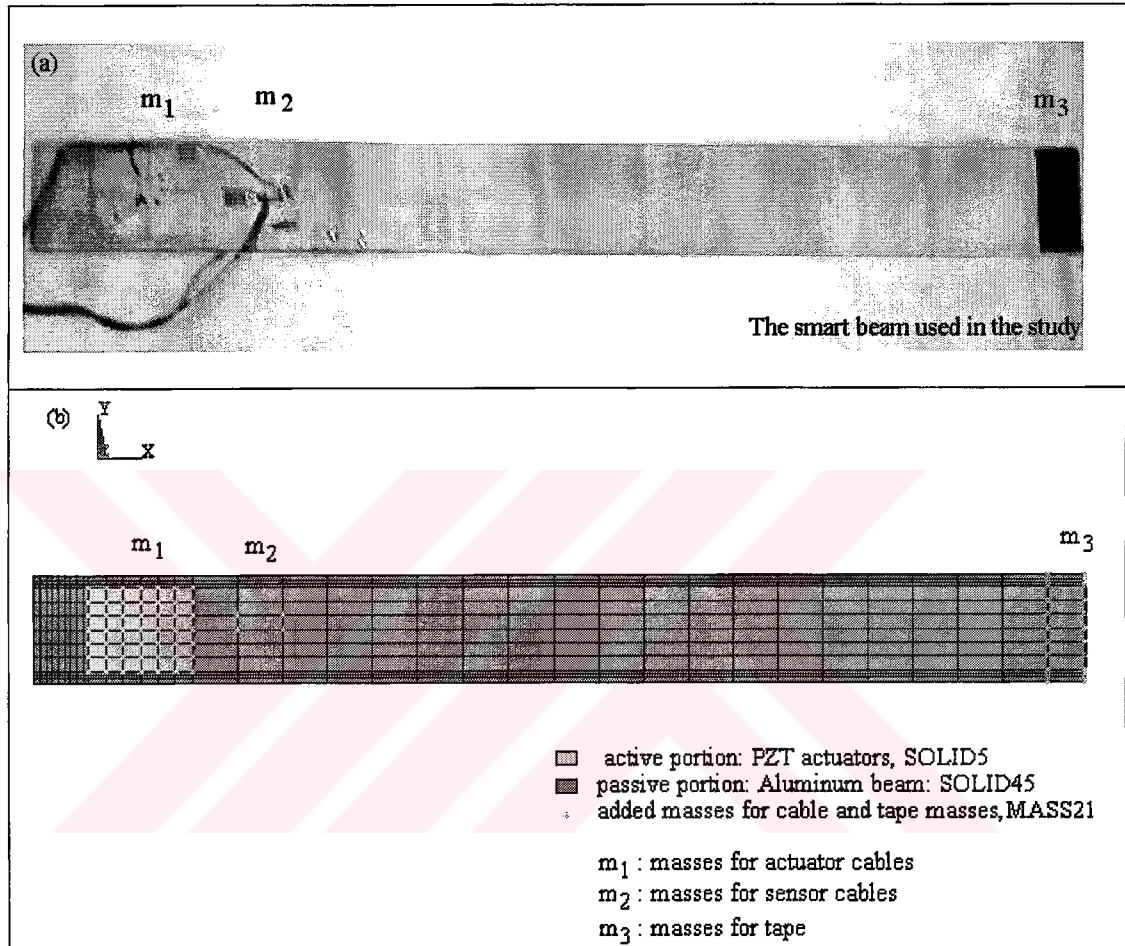


Figure 5.25. The smart beam and the configuration of the mass elements on the finite element model of the smart beam ( $m_1=6\text{gr}$ ,  $m_2=4\text{gr}$ ,  $m_3=1\text{gr}$ )

a. Smart beam

b. The finite element model of the smart beam (93 MASS21, 420 SOLID45, 72 SOLID5 elements)



Since ANSYS® (v.5.6) software does not allow the specification of the modal damping ratios associated with the modes of the structure for analyses involving the coupled field elements, the influences of damping present in the smart structures can only be analyzed through the specification of the mass,  $\gamma$  and stiffness damping constants,  $\beta$ . The preliminary analysis conducted for the analysis of the smart beam showed that the proportional damping values of  $\gamma=2\times 10^{-4}$  and  $\beta=1\times 10^{-4}$  yield closer results to the experimental data. For this reason, unless stated otherwise, these proportional damping constant values are used in the theoretical calculations wherever appropriate. Figure 5.26 shows the influences of the cable weights on the response of the smart beam, in terms of the longitudinal strain, together with the experimental frequency response. It can be seen from the Figure 5.26 that the addition of the cable weights not only shifts the resonance frequencies to slightly smaller values, but also reduces the amplitudes at the first and second resonance frequencies. Table 5.6 gives the influences of the cable masses on the first three undamped natural frequencies of the smart beam together with the experimentally determined frequencies. It can be seen in this Table 5.6 that, the addition of the mass elements to account for the cable masses improves the theoretical frequency values.

Figure 5.26, also reveals the information about the hysteresis effects. The hysteretic nature of the PZT patches results in phase shifts in the response of the smart beam [72,73,74].

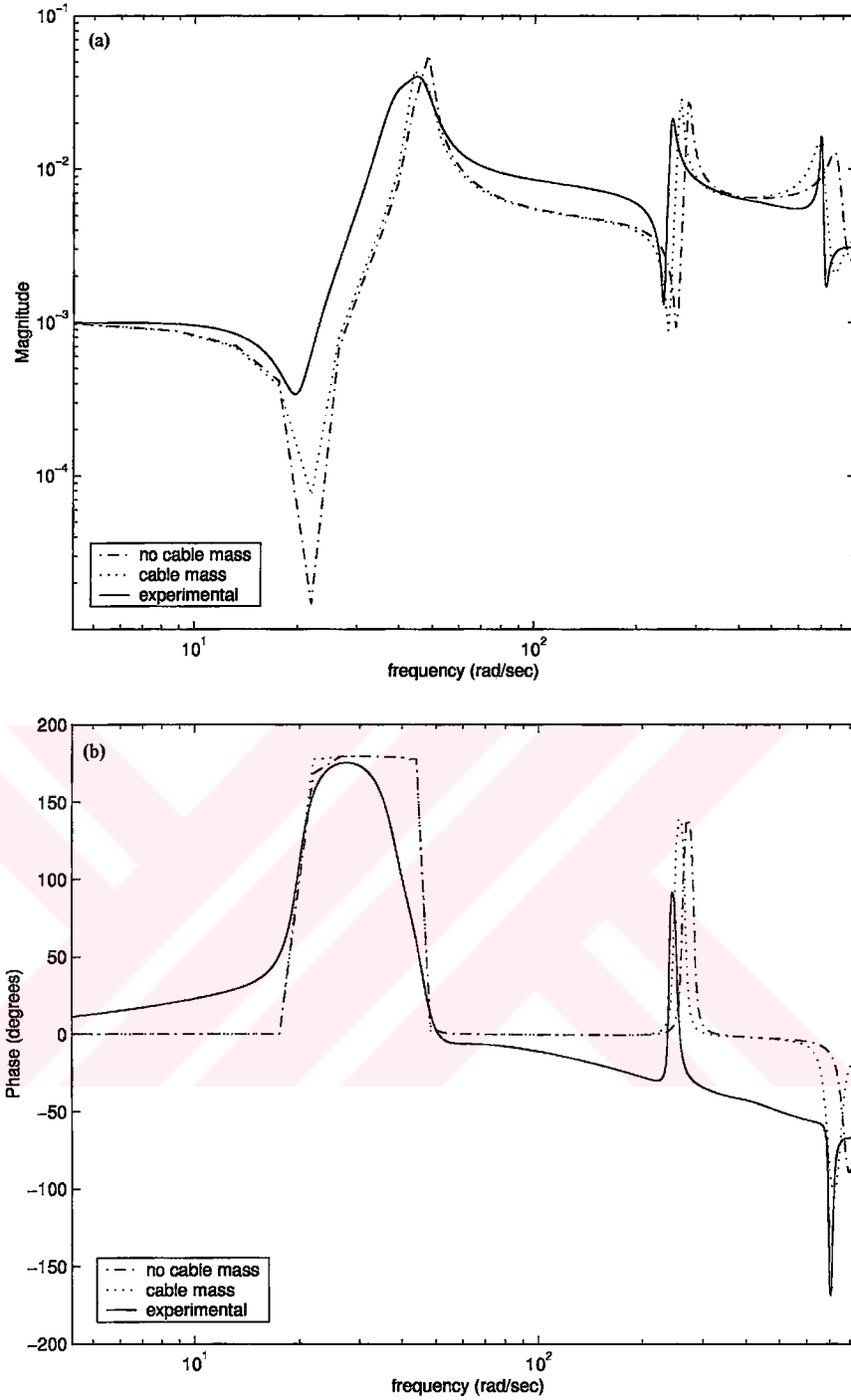


Figure 5.26. The effects of the cable mass on the response of the smart beam (the response at the strain gage location of  $x_s = 97\text{mm}$ ,  $y_s = 25.5\text{mm}$ , the theoretical model with damping values of  $\gamma = 2 \times 10^{-4}$  and  $\beta = 1 \times 10^{-4}$ ).

a. Magnitude

b. Phase

Table 5.6. The comparison of the finite element and experimental frequencies of the smart beam

Frequencies (Hz)	Finite Element Modeling		Experimental
	without cable mass	Cable Mass	
$f_1$	7.3047	7.2798	7.2885
$f_2$	44.112	42.631	40.065
$f_3$	117.28	111.8	110.622

It can be seen from Figure 5.32 that, although the inclusion of the cable weights improves the theoretical frequencies, the theoretical response still needs to be tuned in terms of damping. This is necessary for the success of the closed loop controller to be designed to suppress the vibrations of the smart beam.

### 5.7.3 The Influences of the Damping on the Response of the Smart Beam

Since the finite element modeling techniques make no damping predictions of the damping in the system [59], they offer less accurate results in the determination of the input/output transfer function parameters such as the zeros and phase-frequency response. This profoundly influences the performance of the controller designed [57,58]. In order to improve the response obtained from the theoretical models, the experimentally obtained damping models should be used. In this thesis, the theoretical models obtained through the modal coordinate based modeling technique, is considered in the determination of the theoretical transfer functions. By using the results of the experimental values obtained the damping characteristics of the functions are improved.

The modal coordinates based system models retain the physical correspondence between the theoretical model and the test structure a relation that is lost in nodal

coordinates based models. The modal coordinate based models allow the specification of the desired number of modes contributing to the response under consideration. This allowance always results in smaller order models than those of nodal coordinate based technique. Another advantage is that, by assigning different modal damping ratios associated with the modes of the structure, the modal coordinate based technique offers greater flexibility in tuning the theoretical model to the experimental data [59,121].

This thesis considers system identification for the determination of the damping characteristics of the smart structures. The damping characteristic can also be estimated within acceptable accuracy by a trial and error procedure through half power point circle fit technique [121,122].

Unlike experimental techniques, in the finite element model based techniques all the possible degrees of freedoms and their derivatives can be found by using the same theoretical model with some more computational effort. The transfer functions in terms of displacement and/or strain may be obtained by using the modal coordinates based modeling technique given in Chapter 4. The SISO transfer function between the  $i^{\text{th}}$  sensor and  $j^{\text{th}}$  actuator can be obtained by using equation 5.5.1.

$$G(s) = \sum_r^m \frac{{}_r A_{ij}}{s + \lambda_r} + \sum_r^m \frac{{}_r A_{ij}^*}{s + \lambda_r} \quad (5.5.1)$$

here, the modal participation constants can be given as,

$${}_r A_{ij} = \{\phi_i\}_{1 \times np} \{\phi_j\}_{np \times 1} \quad \text{and} \quad {}_r A_{ij}^* = \{\phi_i^*\}_{1 \times np} \{\phi_j^*\}_{np \times 1} \quad (r = 1 \text{ to } m) \quad (5.5.2)$$

where  $(^*)$  defines the complex conjugate and  ${}_r A_{ij}$  gives the modal participation constant of the  $r^{\text{th}}$  mode of vibration of the smart beam. Since transfer functions evaluated for the strain and displacement at the same point share the same system

matrix, the transfer functions have the same poles. However, because the output vectors defined for the strain and displacement formulations are different, the modal participation constants associated with the  $r^{\text{th}}$  mode of vibration may not coincide. These differences in the strain and displacement formulations may yield to the mismatches between the zeros of the transfer functions. This situation is shown in Figure 5.33. It can be seen from Figure 5.27 that both flexural displacement and strain transfer functions evaluated at the strain gage location give the same resonance frequencies. But the zeros do not coincide. Figures 5.28 and Figure 5.29 give the mass normalized theoretical mode shapes of the smart beam for flexural displacement and strain respectively.

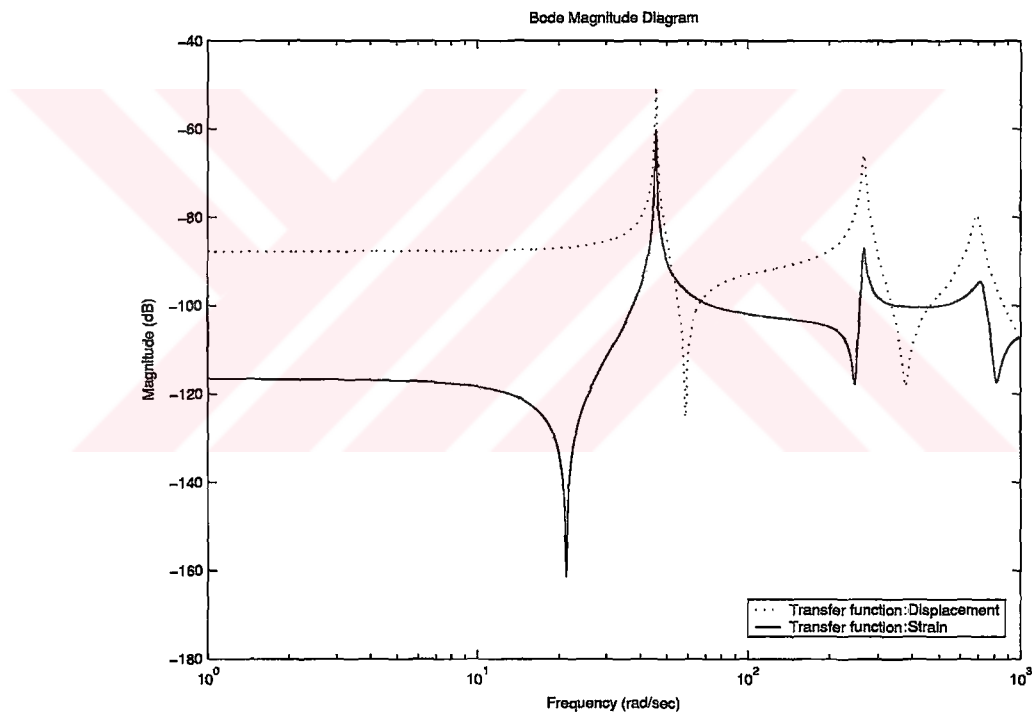


Figure 5.27. The comparison of the strain and displacement transfer functions of the smart beam at the strain gage location ( $\gamma=2 \times 10^{-4}$  and  $\beta=2 \times 10^{-4}$ )

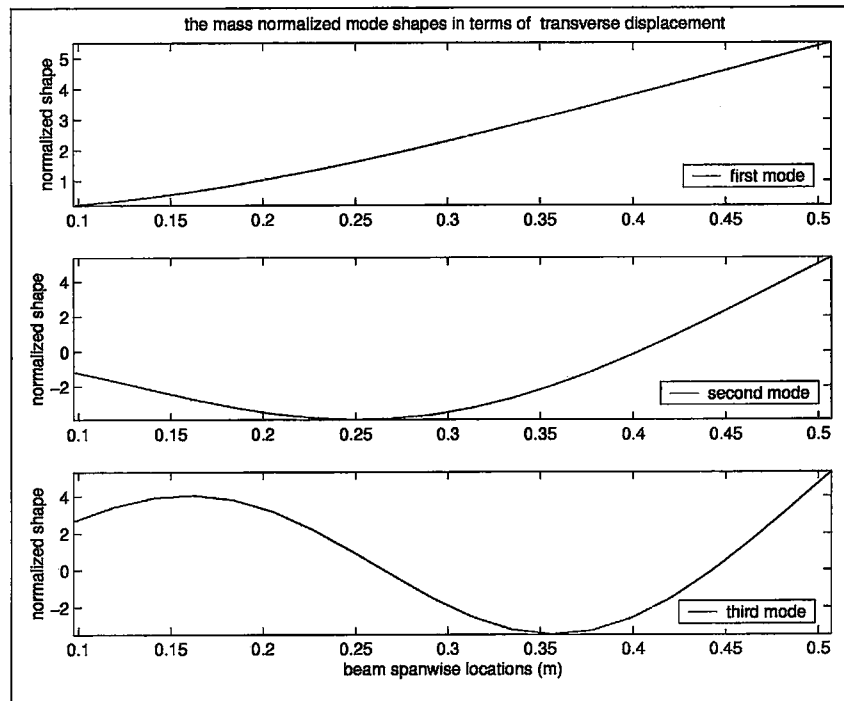


Figure 5.28. The first three theoretical mode shapes of the smart beam (flexural displacement)

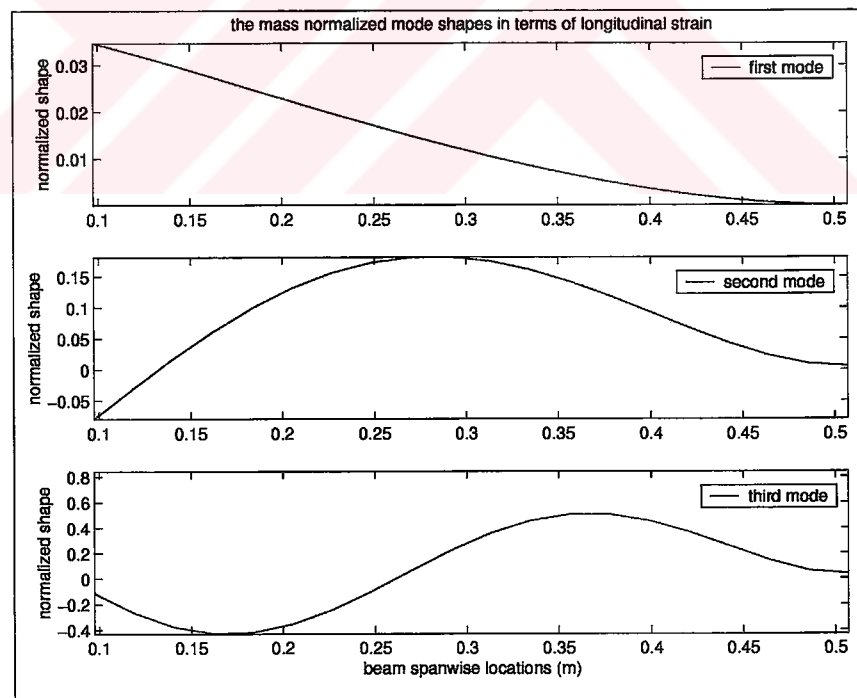


Figure 5.29. The first three theoretical mode shapes of the smart beam (longitudinal strain evaluated on aluminum beam,  $\epsilon_x$ )

Since the strain and displacement transfer function models developed for the smart beam share the same system matrix, a linear transformation from the displacement to the strain transfer functions can be obtained at the same measurement locations. In this case, the strain-displacement transfer function  $G_\tau(s)$  that relates the displacement transfer function  $G_\vartheta(s)$  to the strain transfer function,  $G_\theta(s)$  can be obtained. The relation between the strain transfer function  $G_\theta(s)$  and the displacement transfer function  $G_\vartheta(s)$  can be found to be:

$$G_\theta(s) = G_\tau(s)G_\vartheta(s) \quad (5.5.3)$$

where  $G_\tau(s)$  is the strain–displacement transfer function and has the following form.

$$G_\tau(s) = \frac{K_\theta \prod_{i=1}^m (s^2 / \theta_i^2 + 2\eta_i s / \theta_i + 1)}{K_\vartheta \prod_{j=1}^m (s^2 / \vartheta_j^2 + 2\eta_j s / \vartheta_j + 1)} \quad (5.5.4)$$

Where,  $K_\theta$  and  $K_\vartheta$  describes the open loop gain constant for the strain and displacement transfer functions. In this formulation,  $\theta_i$  and  $\vartheta_j$  symbolizes the zeros of the strain and displacement transfer functions and  $\eta_i$  gives the damping ratio associated with the zeros of the transfer functions. In this thesis, while the open loop gains and the zeros of the transfer function are obtained from the finite element model of the smart beam, the damping ratios associated with the poles and the zeros of the transfer function are obtained experimentally.

The technique developed in the thesis, relaxes the apparent restriction of the finite element code ANSYS in the description of the appropriate damping characteristics of the smart beam and allows the tuning of the finite element based model with the experimentally determined modal damping ratios. During the analysis, first the

transfer function in terms of displacement is extracted through modal coordinate based technique. Then by using the finite element model, the displacement to strain transfer function is obtained. The flowchart of the algorithm is given in Figure 5.30.

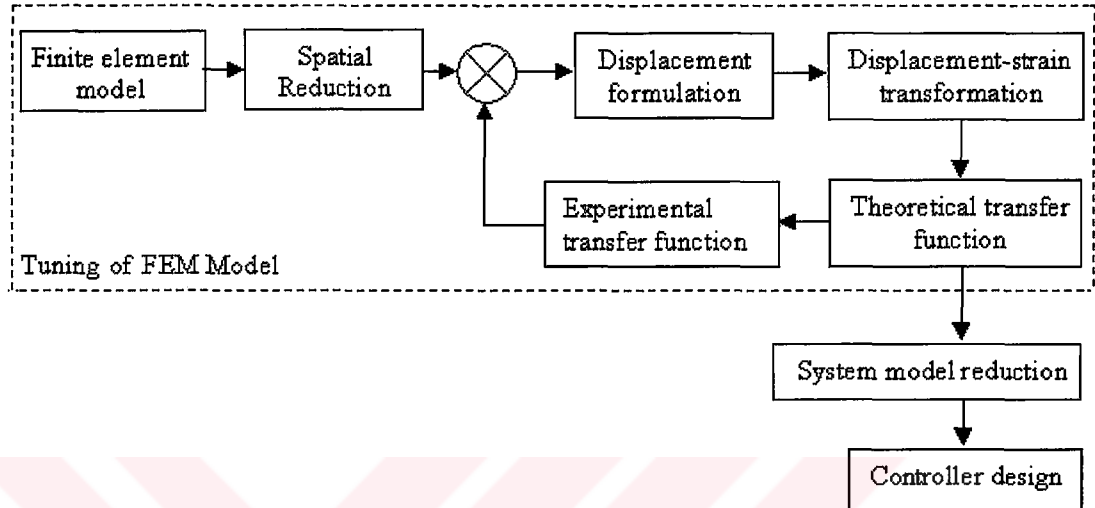


Figure 5.30. The algorithm used in the determination of the tuned theoretical response of the smart beam

During the theoretical calculations, the finite element model of the smart beam with Rayleigh damping multipliers of ( $\gamma=2\times 10^{-4}$  and  $\beta=2\times 10^{-4}$ ) is tuned with the experimentally determined modal damping ratios of  $\zeta_1=7.7309\times 10^{-2}$ ,  $\zeta_2=1.7784\times 10^{-2}$  and  $\zeta_3=7.0605\times 10^{-3}$ . The resulting transfer functions so obtained are compared with the experimental frequency response function. The transfer functions of the smart beam are shown in Figure 5.37. The transfer functions include the displacement, displacement to strain and strain.

The comparisons of the experimental model with the theoretical model of  $\gamma=2\times 10^{-4}$  and  $\beta=2\times 10^{-4}$  and the tuned theoretical model of  $\zeta_1=7.7309\times 10^{-2}$ ,  $\zeta_2=1.7784\times 10^{-2}$   $\zeta_3=7.0605\times 10^{-3}$  are shown in Figure 5.38. It can be seen that, apart from the hysteresis effects observed on the experimental transfer functions, the tuned



theoretical model is in good agreement with the experimental values. Table 5.7 gives the comparison of the parameters of the smart beam.

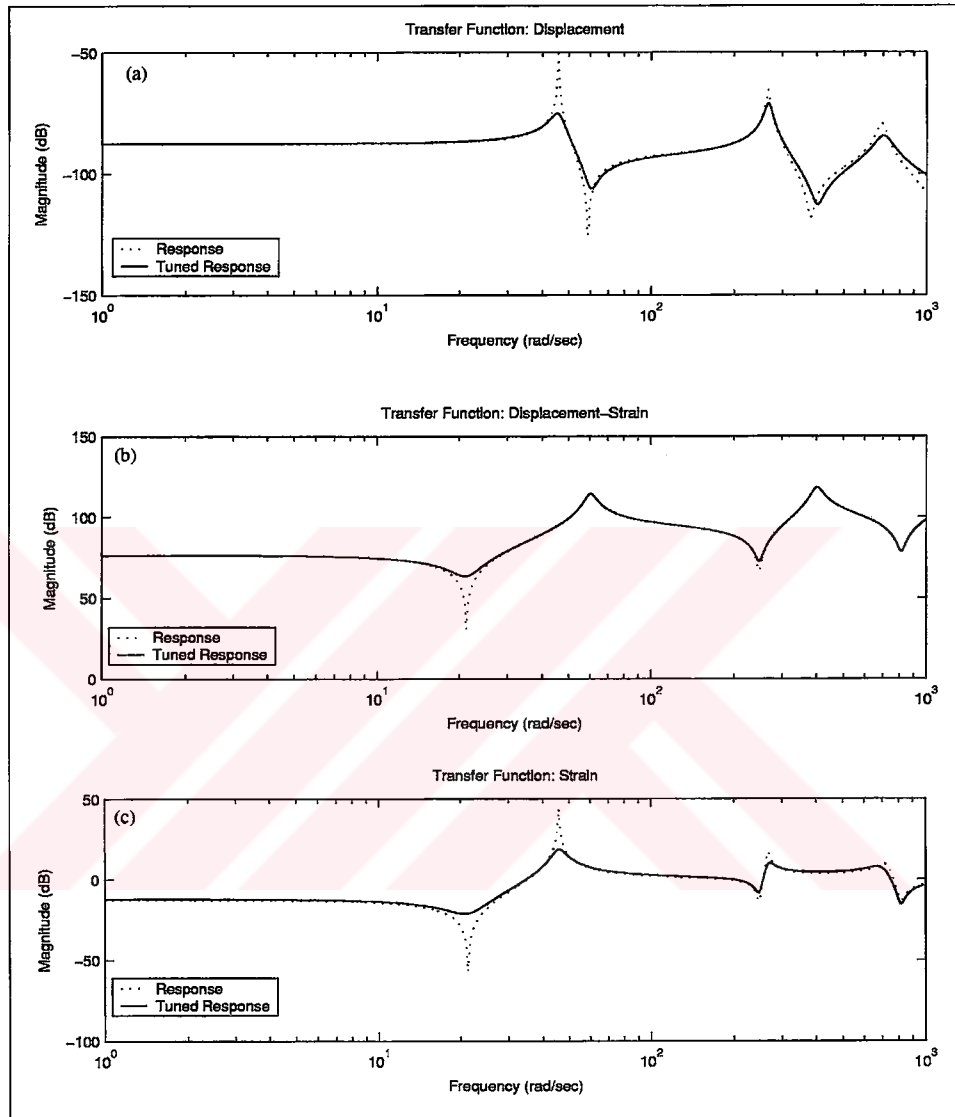


Figure 5.31. The transfer functions of the smart beam obtained in the thesis (the response at the strain gage location of  $x_s=97\text{mm}$ ,  $y_s=25.5\text{mm}$ )

- a. Displacement transfer function,  $G_g(s)$
- b. Displacement-strain transfer function,  $G_r(s)$
- c. Strain transfer function,  $G_\theta(s)$

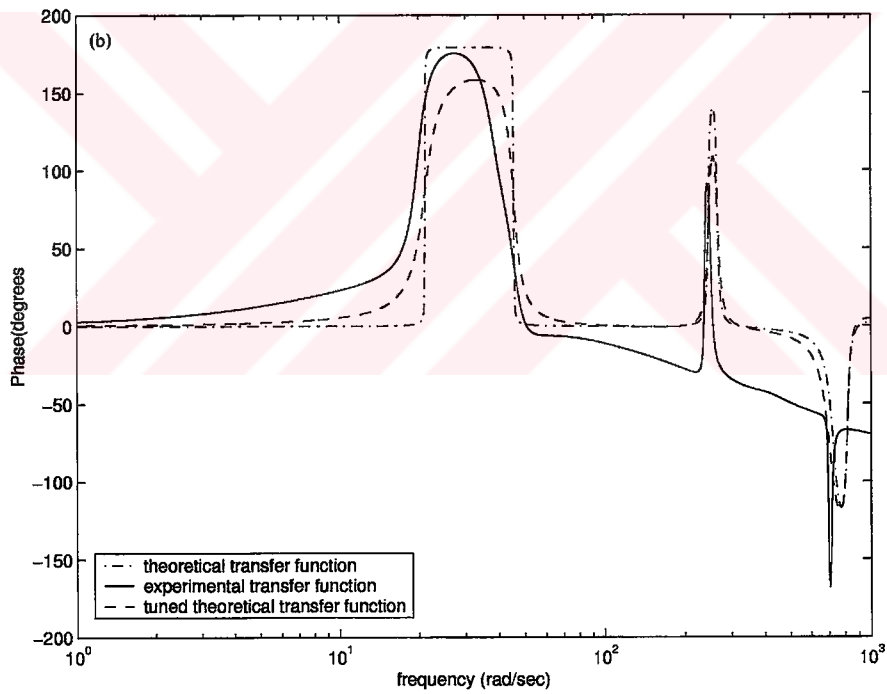
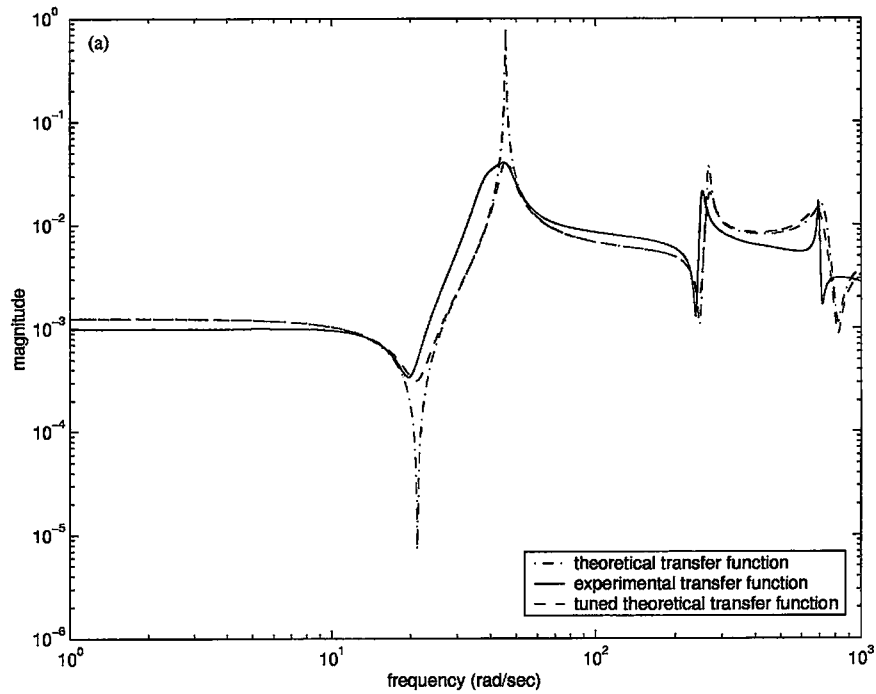


Figure 5.32. The comparison of the theoretical, tuned theoretical and experimental transfer functions of the smart beam

a. Magnitude

b. Phase

Table 5.7. The comparison of the parameters of the smart beam

$f_r$ (Hz)	FEM (tuned)		experimental		experimental	
	Poles	Zeros	poles	zeros	$\zeta_r$	$\eta_r$
$f_1$	7.2798	3.285	7.2885	3.078	$7.731 \times 10^{-2}$	$8.355 \times 10^{-2}$
$f_2$	42.631	39.42	40.065	38.08	$1.778 \times 10^{-2}$	$9.951 \times 10^{-3}$
$f_3$	110.9	129.6	110.622	113.44	$7.061 \times 10^{-3}$	$1.191 \times 10^{-2}$

### 5.8 Overview of Finite Element and System Identification Techniques Applied to Smart Structures

In this thesis, the system models of the smart structures are obtained by using both the finite element based theoretical and system identification approaches. Each of techniques presented has different characteristics. Table 5.8 summarizes the advantages and disadvantages of the techniques considered in the thesis.

The applications of both finite element and system identification approaches are generally required in the reliable design and analysis smart structures for active vibration control. In the smart structures applications, the finite element approach is generally applied at the design stage of the smart structures. The system identification approach is usually considered in the determination of the accurate model of the system to be controlled.

Table 5.8. The system modeling techniques for smart structures

Model	advantages	disadvantages
Finite Element	<ul style="list-style-type: none"> <li>• No prior knowledge for the parameters of system is required.</li> <li>• Gives the optimal Sensor-actuator locations and actuator size</li> <li>• Determines the accurate undamped frequencies and gives mode shapes.</li> <li>• Sensor types are not fixed. Determines all the degrees of freedoms and derivatives as the output.</li> <li>• Used to determine the maximum admissible piezoelectric actuation value to secure the integrity of the piezoelectric actuators</li> <li>• The results can be tuned</li> </ul>	<ul style="list-style-type: none"> <li>• Accurate mathematical model for the process is required.</li> <li>• Precise description of the system including material and actuator properties must be prescribed.</li> <li>• Excessive numerical calculations may be involved.</li> <li>• Makes no damping predictions</li> <li>• Hysteresis effects can not be included</li> </ul>
System identification	<ul style="list-style-type: none"> <li>•No prior knowledge for the parameters of system is required.</li> <li>•Accurate mathematical model for the process is not required.</li> <li>•Precise description of the system including material and actuator properties are not needed</li> <li>•Makes correct damping predictions</li> <li>•The linearized Hysteresis models can be obtained.</li> </ul>	<ul style="list-style-type: none"> <li>•The optimal Sensor and actuator locations can not be found directly.</li> <li>•Sensor types and locations are fixed.</li> <li>•The maximum admissible piezoelectric actuation value can not be determined.</li> <li>•Expensive equipment and excessive signal processing is needed.</li> </ul>

## 5.9 Conclusions

This chapter was served to lay down the fundamentals of the spectral method of nonparametric identification and least square curve fitting techniques, which give the accurate system models of the smart structures when the finite element modeling becomes insufficient. The results of the system identification were then used to tune the accuracy of the finite element model of the smart beam.

It was shown that the appropriate actuation patterns and the actuation levels that excite the structures in their modes could effectively be determined by using the finite element based models.

In this thesis, the system identification of the smart structures was achieved in two stages. First the frequency responses of the experimental transfer functions were found by using the method of nonparametric identification. Then the experimentally identified system models of the smart structures were calculated through the application of the frequency domain least square curve fitting technique.

The spectral estimation method of the nonparametric identification was used to determine the experimental transfer functions of the smart structures. It was shown that the application of the technique allowed the elimination of the spurious noise presented on the output signals and resulted in smoother frequency response for the experimental transfer functions of the smart structures.

The experimental transfer functions of the smart structures were then used in the determination of the identified SISO transfer functions. During the determination of the identified models, the method of frequency domain least squares curve fitting technique was applied to obtain the minimal order experimentally identified models of the smart structures. In this thesis, the experimentally identified models, in

addition to their direct applicability to the control design problems, were shown to have great flexibility in the tuning of the theoretical models.

The validity of the finite element based modeling used in the thesis was confirmed by comparing the first three theoretical and experimentally determined frequencies of the smart structures. While the frequency values associated with the first and third modes were determined to be in good agreement with the experimental results, but the frequency values corresponding to the second mode for the smart beam and smart fin were found to be slightly different than those of the experimental. These differences were attributed the unmodelled effects like cable masses.

It was shown that the unmodeled effects such as the cable masses, damping and hysteresis were profoundly influenced the accuracy of the finite element based theoretical model of the smart beam.

The addition of the mass elements to account for the effects of the unmodeled cable weights were determined to improve the response of the smart beam significantly.

It was further shown that the modal coordinate based technique developed in this thesis, relaxed the apparent restriction of the ANSYS software in the modeling of the damping characteristics of the smart beam and allowed the tuning of the damping characteristics of the finite element based theoretical model.

The LVDT tests were conducted to quantify the hysteretic nature of the piezoelectric actuators. By considering the results of the LVDT tests, it was shown that the linear relationship predicted by the theoretical analysis presented in Chapter 3 can be considered to be valid only for the low range of the actuation voltage. Thus, if a relatively high voltage value is applied to the actuators of the smart beam, the relationship exhibits the hysteresis nonlinear behavior. The hysteresis effects were observed in the form of the phase shifts on the frequency response of the smart beam.

The method of tuning the response of the smart beam could also be applied for the finite element based theoretical models of the smart plate and smart fin with equal ease. But, since the LVDT tests associated with these articles were not available, the tuning of those specimens was not presented.

Since the strain gages modeled in half wheatstone bridge configuration yields good performance at relatively low cost, the strain gages modeled in this configuration were considered in the thesis. However, the utilization of very small accelerometers bonded on the surface of the structures is also known to yield precise vibration sensing for system identification and vibration control. But the cost of the accelerometers and the peripheral devices, like charge amplifiers made the utilization of these devices in the design of smart structures considered impossible for the current study.

Another reason for the selection of the strain gages in the vibration sensing of the smart structures is their excellent compatibility with the commercial controller unit SS10, a product of Sensor Technologies Limited Canada, used for the implementation of the controller designed for the active vibration control of the smart structures in this thesis.

## CHAPTER 6

### DESIGN FOR ACTIVE VIBRATION CONTROL OF SMART STRUCTURES

#### 6.1 Introduction

The objective of this chapter is to present the design of robust controllers that effectively suppresses the vibrations of the smart structures. Based on structural and control models developed in Chapters 3 and 5 respectively, the vibration suppression is achieved by the application of robust PID and  $H_\infty$  controllers described in Chapter 4. The effectiveness of those controllers in the vibration suppression and in the modeling of the uncertainties is also compared.

In the design of a closed loop systems, it is generally desirable that the system should exhibit errors, which are very small, in the response to the input signal. The system dynamics should also remain relatively insensitive to the modeling errors or the changes in the system parameters. Furthermore, the undesirable disturbances such as high frequency sensor noises should be attenuated. The performance objectives of a closed-loop system include the determination of the frequency range and weights for which the controller affects the output in order to obtain the desired results.



Depending on the mission requirements, modeling and operating conditions, the selection of error signals and performance weights for the smart structures varies considerably. Thus, the specification of the proper performance weightings has the ultimate importance to achieve the performance objectives.

Since the response of a linear time invariant system is dominated by the resonance frequencies closer to the imaginary axis, the aim in the design of the closed loop controllers is to minimize the response in the lower frequency range where first three resonance frequencies of the smart structures resides in, while making minimal changes to the response at the higher frequencies. The thesis uses Matlab<sup>®</sup> (v.6.0) software to design the controllers.

## **6.2 The Series Compensator Design for the Vibration Control of the Smart Beam: PID Compensators**

The objective of this section is to examine the techniques that can be used in the design of a series compensator, or equivalently, a controller that suppresses the vibrations due to the first two modes of the smart beam. In order to determine the most effective compensator, various designs are examined for their effectiveness in vibration control. During the calculations, unless stated otherwise, the experimentally identified model of the smart beam is used. The series compensators considered in this thesis include Proportional (P), Proportional Integral (PI), Proportional Derivative (PD) and Proportional Integral Derivative (PID). In this section, the influences of the controller gain variations on the performances of the closed-loop systems are fully dealt with. During the course of work, Nyquist stability criterion is applied for each compensator design to ensure the absolute stability of the closed-loop systems.

The series compensator design considered in this thesis, deals with the modification of the open-loop frequency response of the smart beam to obtain the desired frequency response shape. This process is known as the loop shaping method of design [124,127]. The method of design is based on the satisfaction of the performance specifications by means of a trial and error procedure through the addition of new poles and zeros.

### 6.2.1 Proportional Compensator

The simplest element among the series compensators is the proportional compensator. The element is just a constant gain. The transfer function of the proportional compensator is described as

$$K(s) = K_p \quad (6.2.1)$$

where  $K_p$  symbolizes the proportional gain constant of the compensator. Figure 6.1 gives the block diagram of the P compensator system used in the study.

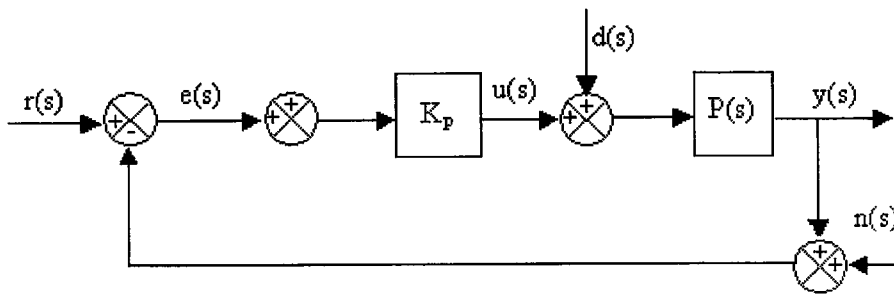


Figure 6.1. The block diagram representation of the P-compensated system for the smart beam

In this chapter, unless stated otherwise, the frequency responses of the theoretical open and closed loop transfer functions are compared by calculating the frequency responses of the transfer functions within the frequency range of interest. Hence, no other disturbances are considered in the theoretical calculations.

In order to investigate the influences of the gain variation on the P-compensated system, the closed loop responses for three gain values  $K_p=10$ ,  $K_p=30$  and  $K_p=50$  are calculated and the results are shown together with the open-loop response in Figure 6.2. Although the proportional gain slightly reduces the response levels at the first two resonance frequencies, it significantly increases those at the third frequency. It can also be seen from the figure that the proportional gain shifts the first resonance frequency to smaller frequencies. Thus, it can be concluded that the application of the simple proportional compensator becomes insufficient to yield adequate results for the vibration control of the smart beam under consideration.

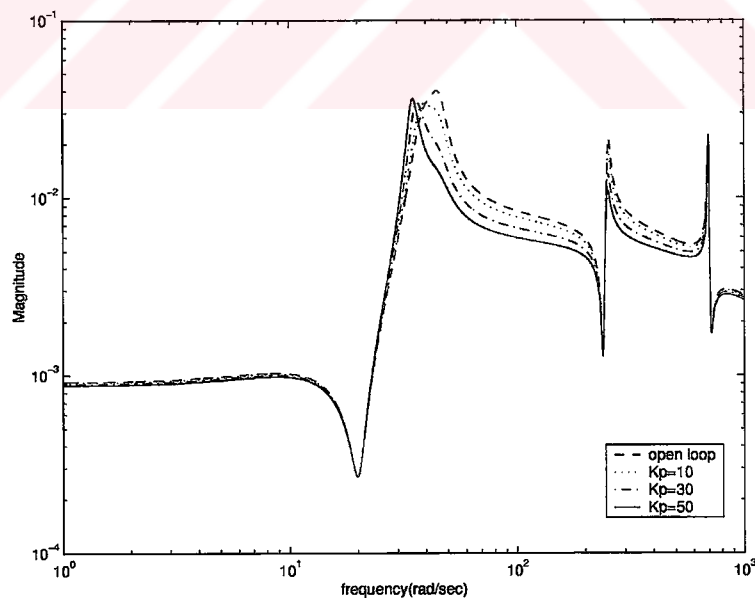


Figure 6.2. The comparison of the effects of the proportional gain on the P-compensated system for the smart beam

### 6.2.2 Proportional and Integral Controller

The method of increasing the loop gain at low frequencies while making minimal changes to the response at the high frequencies is provided by a PI or lag compensator. Figure 6.3 gives the block diagram of the PI-controlled system considered in the study. The PI or lag compensators consists of the proportional term and an integral or reset term. The transfer function of a PI compensator is given by

$$K(s) = \frac{K_p(s + K_i)}{s} \quad (6.2.2)$$

A PI compensator has high gain at lower frequencies and as frequency increases the gain approaches asymptotically to that of P compensator. Furthermore, the presence of the free integrator at the denominator provides improved steady state behavior [12,122].

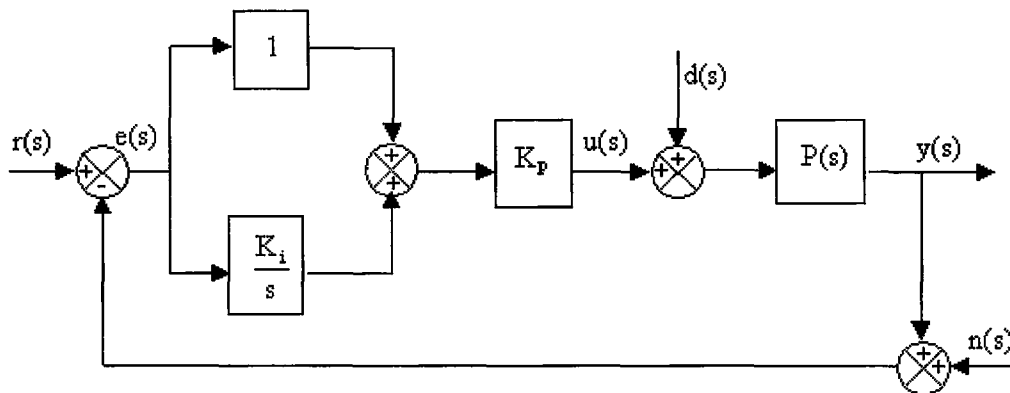


Figure 6.3. The block diagram representation of the PI-compensated system for the smart beam

The effectiveness of the PI compensator in the vibration control of smart beam is examined by considering the influences of the PI compensator gain variation on the response of the PI-compensated system. First the effect of changing  $K_p$  is investigated. Three different cases, which correspond to the proportional gain constant values of  $K_p=30$ ,  $K_p=60$  and  $K_p=100$  are considered. In each case, the integral constant is taken as  $K_i=60$ . The closed loop responses are shown in Figure 6.4 together with the open-loop response.

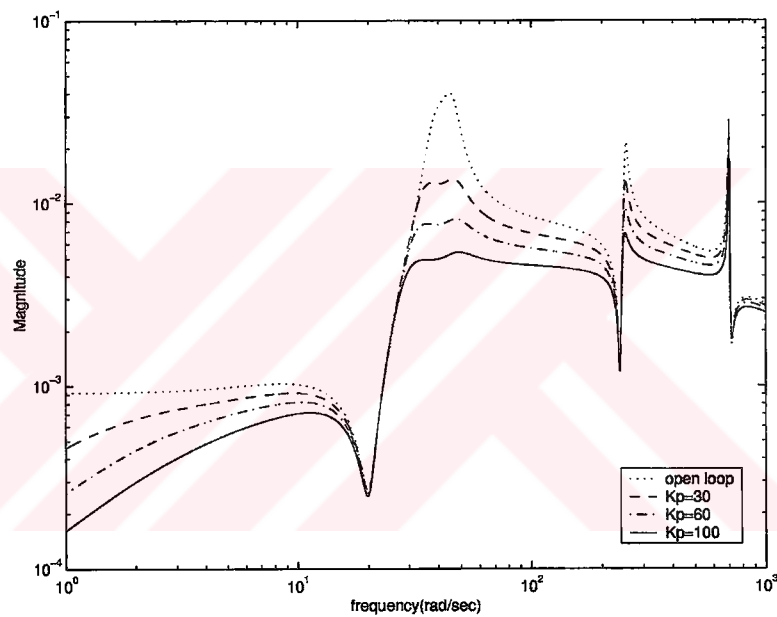


Figure 6.4. The comparison of the effects of the proportional gain  $K_p$  on the PI-compensated system for the smart beam

Then, the proportional gain is kept constant at  $K_p=60$  and three different integral gains are analyzed as  $K_i=40$ ,  $K_i=80$  and  $K_i=110$ . The resulting curves are shown in Figure 6.5 together with the open-loop response. The analysis of Figures 6.4 and 6.5 reveals that

the addition of the integral term to the P compensator offers an improved response at lower frequency range resulting the reduced peak response levels, but as the frequency increases the closed-loop response increases and gets close to that of P compensator. That is, similar to P compensators PI compensator also excites higher frequencies. This result may be attributed to the closeness of the P and PI compensator loop gains at high frequencies. Thus, despite of the improved response at lower frequencies, the excitation of the higher frequency modes also limits the potential use of the PI compensators in the vibration control of the smart beam.

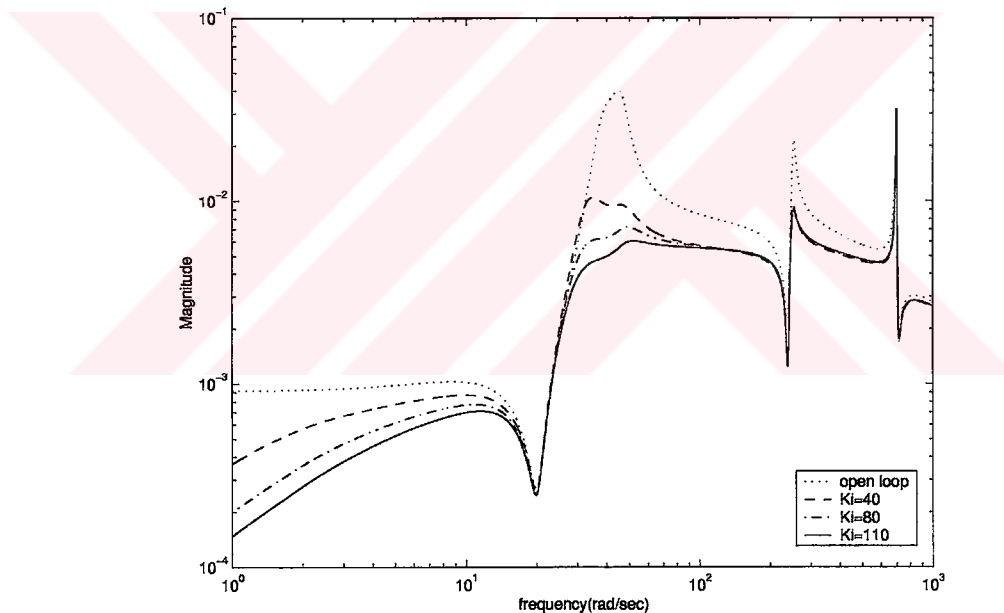


Figure 6.5. The comparison of the effects of the proportional gain  $K_i$  on the PI-compensated system for the smart beam

### 6.2.3 Proportional and Derivative Compensator

The last basic compensator is the derivative or lead compensator. In addition to the proportional term, the PD or the lead compensator also includes a derivative term. The transfer function of the PD controller is known to be

$$K(s) = K_p(1 + K_d s) \quad (6.2.3)$$

In principle, the addition of the derivative term improves the high frequency loop gain characteristics of the P controller. Figure 6.6 shows the block diagram architecture of the PD compensator used in the study.

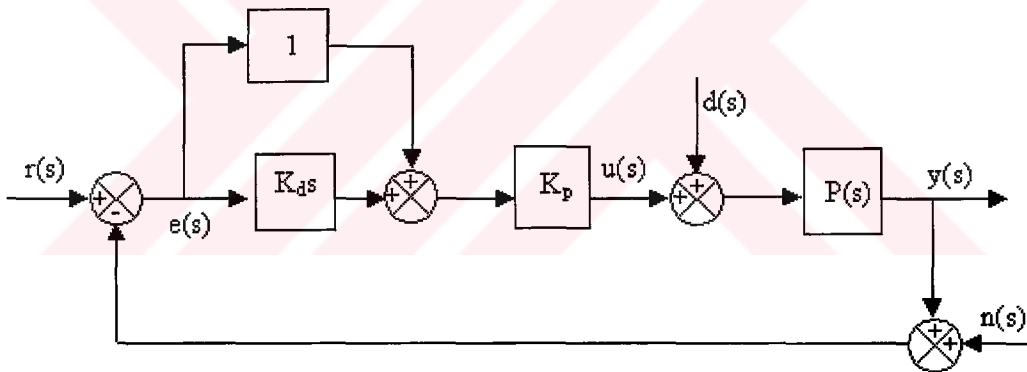


Figure 6.6. The block diagram architecture of the PD-compensated system for the smart beam

Similar to the analysis conducted for the P and PI-controlled systems, the effectiveness of the PD compensator is investigated by considering the gain variations of the compensator.

Figure 6.7 shows the effects changing of  $K_p$  on the response of the PD-controlled system. During the analysis, the response of the PD-controlled system is calculated by considering three different proportional gain values of  $K_p=10$ ,  $K_p=30$  and  $K_p=50$  for a fixed value of the derivative gain  $K_d=3/1000$ .

The effects of  $K_d$  variation on the response of the PD-compensated system is also analyzed by considering three different values of proportional gains of  $K_d=2/1000$ ,  $K_d=3/1000$  and  $K_d=4/1000$  for a fixed value of the proportional gain  $K_p=10$  the closed loop responses so obtained is given in Figure 6.8 together with the open-loop response. It is evident from Figure 6.7 and 6.8 that the addition of the derivative term allows the suppression of the peak response levels at higher frequency range, but the first frequency value increases as the proportional gain value increases. Since, the loop gain of the PD controller approaches to the gain of the P compensator as the frequency reduces, the performance of the PD-controlled system is not as effective as the PI-compensated system at lower frequencies.

Therefore, the most effective compensator design for the vibration control of the smart beam should include the proportional, derivative and integral terms. This can be achieved through the application of the PID compensators.



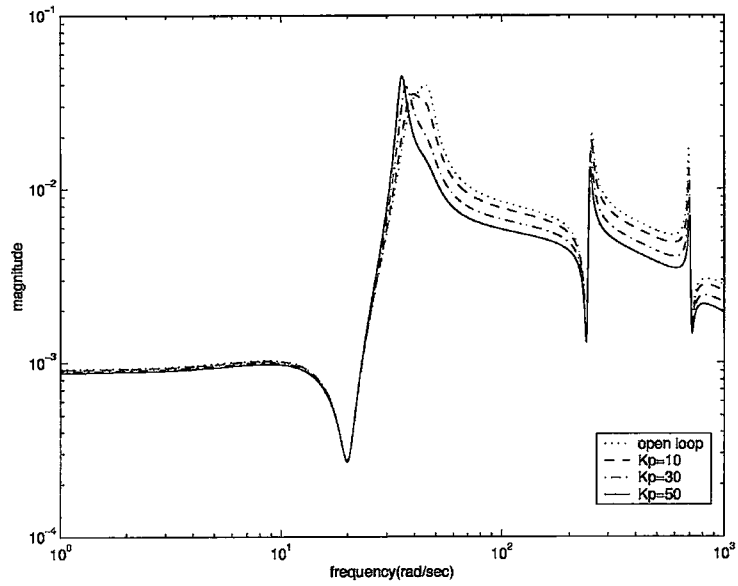


Figure 6.7. The comparison of the effects of the proportional gain  $K_p$  on the PD-compensated system for the smart beam

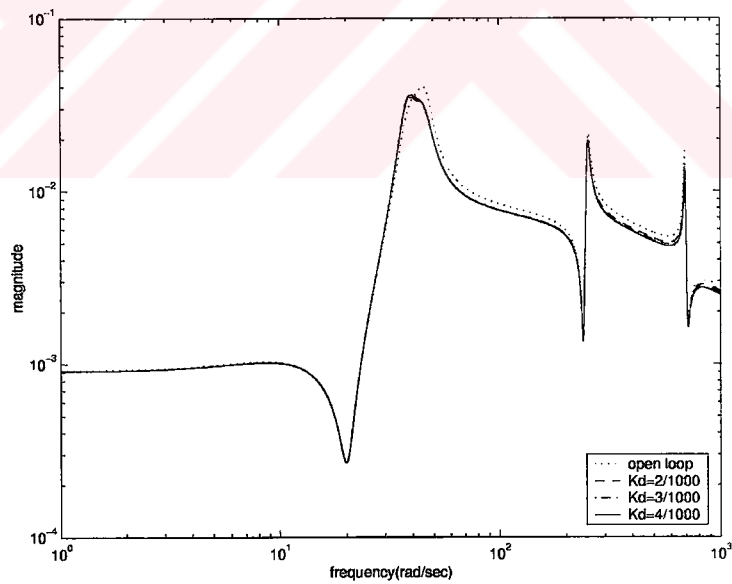


Figure 6.8. The comparison of the effects of the proportional gain  $K_d$  on the PD-compensated system for the smart beam.

### 6.2.4 Proportional, Integral and Derivative Compensators

This section investigates the effectiveness of the PID controller schemes that are designed to suppress the vibrations of due to the first two modes of the smart beam. Figure 6.9 shows the block diagram architecture of the PID-compensated system considered in this thesis for the smart beam.

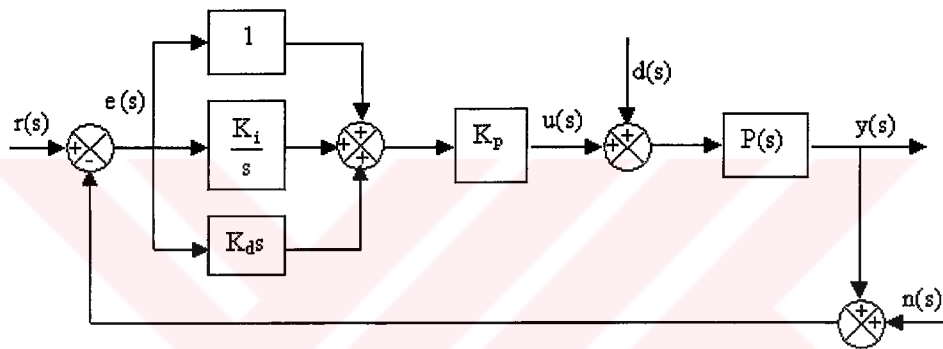


Figure 6.9. The block diagram architecture of the PID- compensated system for the smart beam

In order to investigate the effects of the PID gains on the closed-loop response of the PID-controlled system, three different gain configurations are considered and, the results obtained are plotted together with the open-loop response of the smart beam for each configuration.

First the effects of  $K_p$  variation are investigated. Three different cases, which correspond to the proportional gain values of  $K_p=10$ ,  $K_p=30$  and  $K_p=50$ , are used. In

each case, the integral and derivative gain values are kept constant as  $K_i=70$  and  $K_d=3/1000$ . The responses so obtained are shown in Figure 6.10.

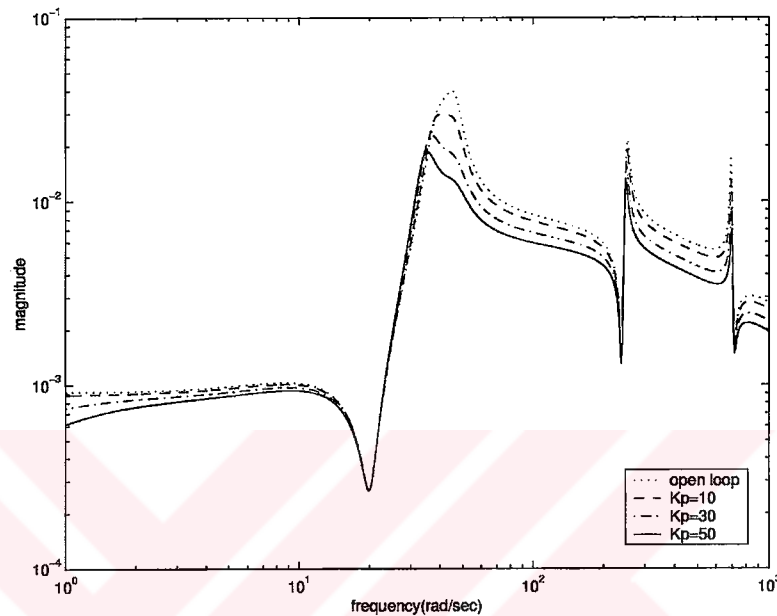


Figure 6.10. The comparison of the effects of the proportional gain  $K_p$  on the PID-controlled system for the smart beam

Next the proportional and derivative gains kept constant as  $K_p=60$  and  $K_d=3/1000$  and three integral gains of  $K_i=10$ ,  $K_i=30$  and  $K_i=50$  are analyzed. Figure 6.11 gives the results.

Then the proportional and integral gains are kept constant as  $K_p=80$  and  $K_i=30$  and three derivative gains are considered as  $K_d=2/1000$ ,  $K_d=3/1000$  and  $K_d=4/100$ . Figure 6.12 shows the results. It can be seen from Figures 6.10 to 6.12 that the PID

compensators can be used for the suppression of the vibrations due to the first two modes.

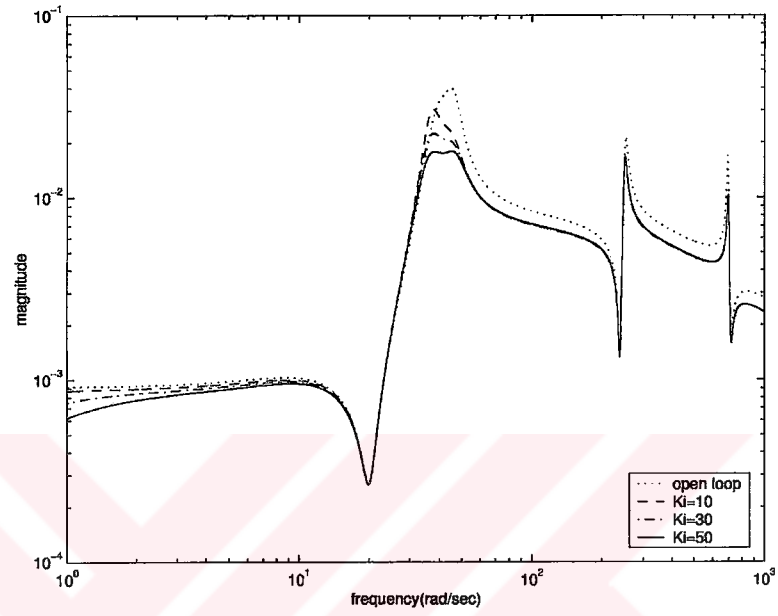


Figure 6.11. The comparison of the effects of the proportional gain  $K_i$  on the PID-compensated system for the smart beam

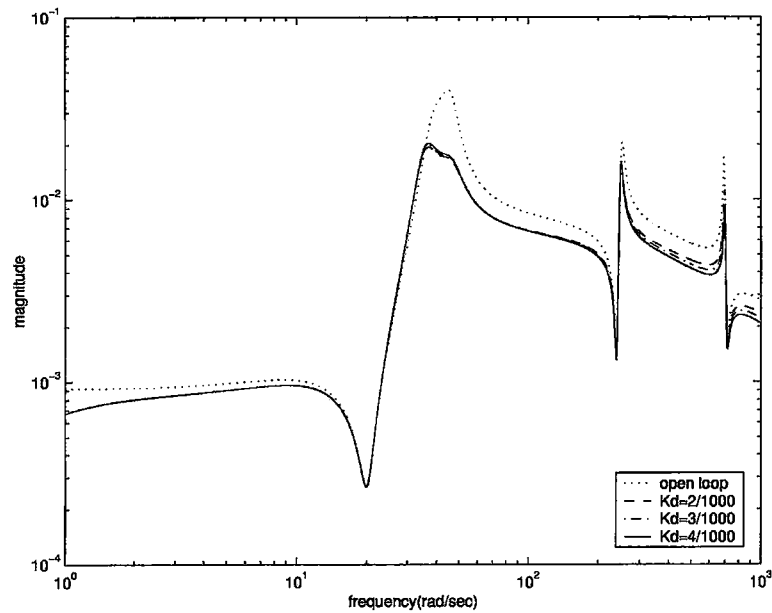


Figure 6.12. The comparison of the effects of the proportional gain  $K_i$  on the PID-compensated system for the smart beam

In order to compare the effectiveness of the series compensators in the vibration control of smart beam, the open loop and closed-loop responses of three series compensators are calculated and the results are shown in Figure 6.13. The series compensators considered include a PI having the gain values of  $K_p=30$ ,  $K_i=70$ , a PD with the gains values of  $K_p=30$ ,  $K_d=3/1000$  and a PID  $K_p=30$ ,  $K_i=70$ ,  $K_d=3/1000$ . The frequency dependency of the series compensators considered are also given in Figure 6.14. It can be seen from the Figures 6.13 and 6.14 that the applications of the PID compensators allow the simultaneous suppression of the first three modes of vibration. This is due to the high loop gains at lower and higher frequencies.

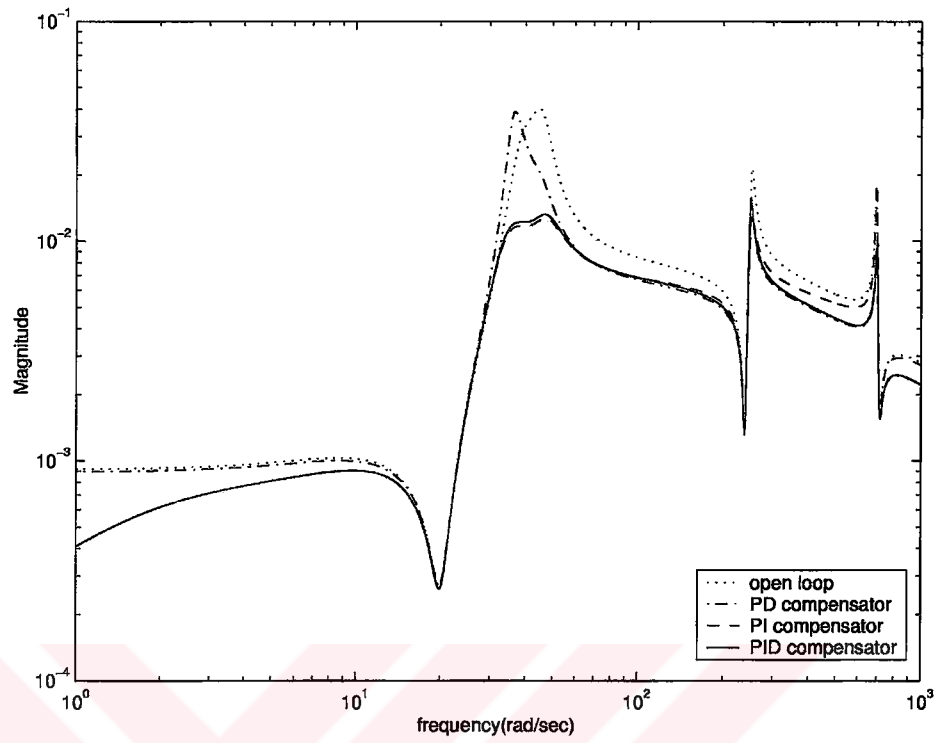


Figure 6.13. The comparison of the open and closed-loop frequency responses for the beam (PI:  $K_p=30$ ,  $K_i=70$ ), (PD:  $K_p=30$ ,  $K_d=3/1000$ ), (PID:  $K_p=30$ ,  $K_i=70$ ,  $K_d=3/1000$ )

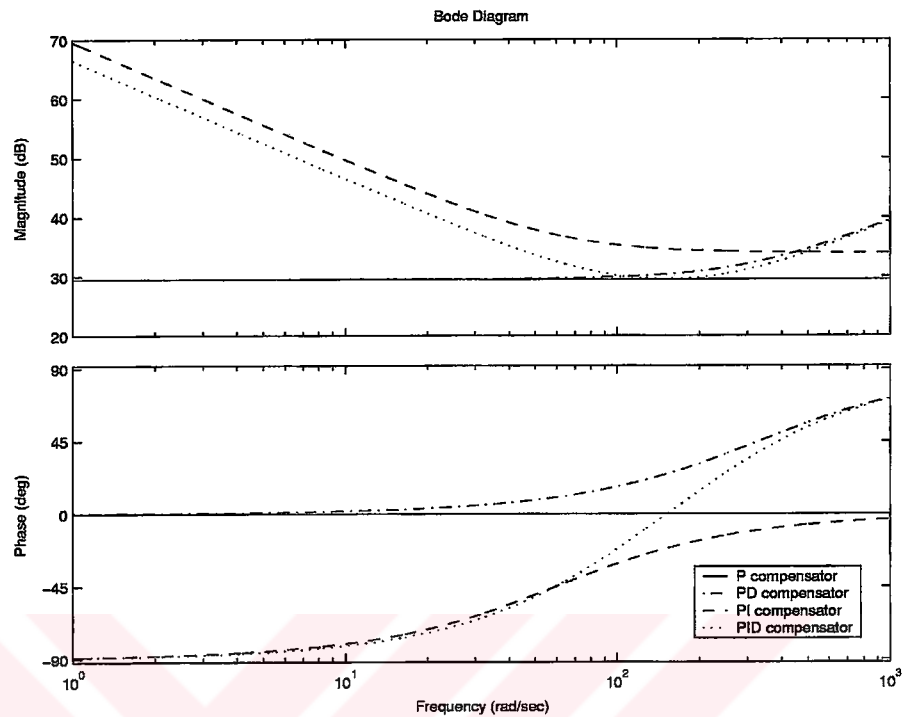


Figure 6.14. The comparison of the frequency responses of the series compensators used in the thesis (P:  $K_p=30$ ), PI:  $K_p=30$ ,  $K_i=70$ ), (PD:  $K_p=30$ ,  $K_d=3/1000$ ) and (PID: ( $K_p=30$ ,  $K_i=70$ ,  $K_d=3/1000$ ))

The responses of the PID-controlled systems to the unit-impulse are also calculated for the three PID compensator gains and the time domain results so obtained are compared with the open loop response in Figure 6.15. It can be seen from Figure 6.15 that as the PID compensator gains increase, the closed-loop response gets less oscillatory and the settling time reduces.

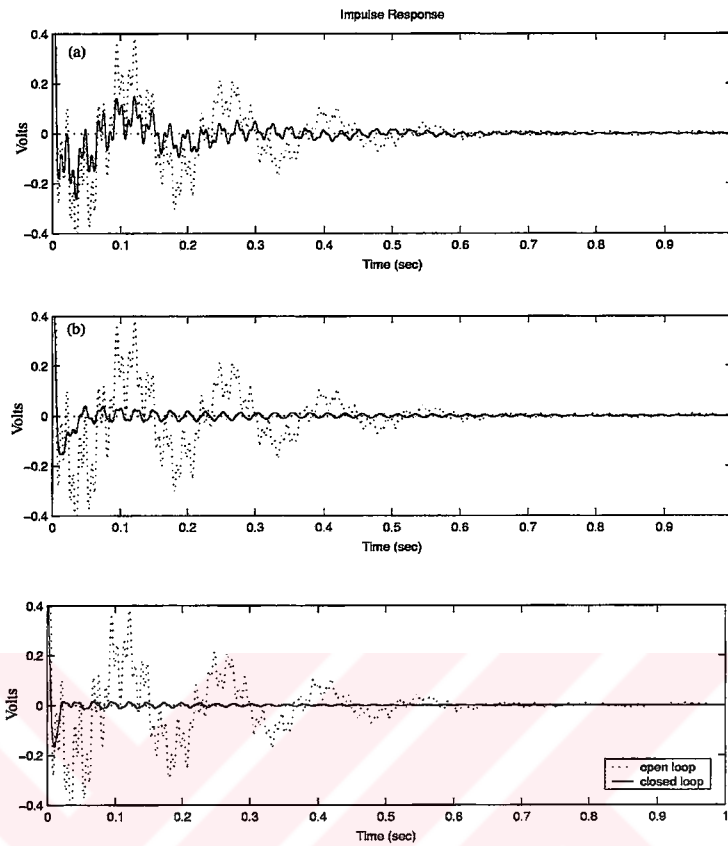


Figure 6.15. The comparison of the time domain responses of PID-compensated systems

- a. PID compensator with the gain of  $K_p=50$ ,  $K_i=60$ , and  $K_d=3/1000$
- b. PID compensator with the gain of  $K_p=150$ ,  $K_i=150$ ,  $K_d=3/1000$
- c. PID compensator having the gain of  $K_p=300$ ,  $K_i=300$ , and  $K_d=5/1000$

Generally, the closed-loop controllers are known to reduce the modeling errors such as the one observed for the smart beam due to the hysteresis. The experimentally identified model of the smart beam obtained in Chapter 5 inherently included the hysteresis nonlinearities associated with the piezoelectric actuators in a linearized form. Experimentally identified models and the tuned theoretical model, which does not



include any information related to the hysteresis, are considered to investigate the effectiveness of the PID compensators on the modeling errors due to hysteresis. The closed-loop responses of these models are compared for the same PID compensator.

Representing the closed loop transfer function calculated for the experimentally identified model of the smart beam by  $\tilde{\Omega}(s)$  and symbolizing, the closed loop transfer function calculated for the theoretical model with  $\Omega(s)$  the relative error  $\kappa(s)$  between the closed-loop models for the same PID compensator can be described as

$$\kappa(s) = \frac{\tilde{\Omega}(s) - \Omega(s)}{\tilde{\Omega}(s)} \quad (6.2.4)$$

The closed-loop responses of various PID compensators are used to determine the influence of the closed loop gain variation on the relative error. Three PID compensators used for this purpose. The first compensator have the gains of  $K_p = 50$ ,  $K_i = 60$  and  $K_d = 3/1000$ , the gain values associated with second compensator are  $K_p = 100$ ,  $K_i = 100$  and  $K_d = 3/1000$ , and the third compensator is assumed to have the gain values of  $K_p = 300$ ,  $K_i = 300$  and  $K_d = 5/1000$ . The resulting plots are shown in Figure 6.16. It is evident from Figure 6.16 that as the loopgain of the PID-compensated system increases the relative error reduces.

The hysteresis effects can also be included in the design as the phase lag that causes instability if the phase margin is not taken large enough [72,73]. Hence, the hysteretic nature of the piezoelectric actuators results in unmodeled phase lag whose presence may cause instability in a closed-loop control system if the phase margin is not large enough. In principle, the derivative term existing in the PD and PID compensators improves the effects of the additional phase lag due to hysteresis over a limited frequency range.

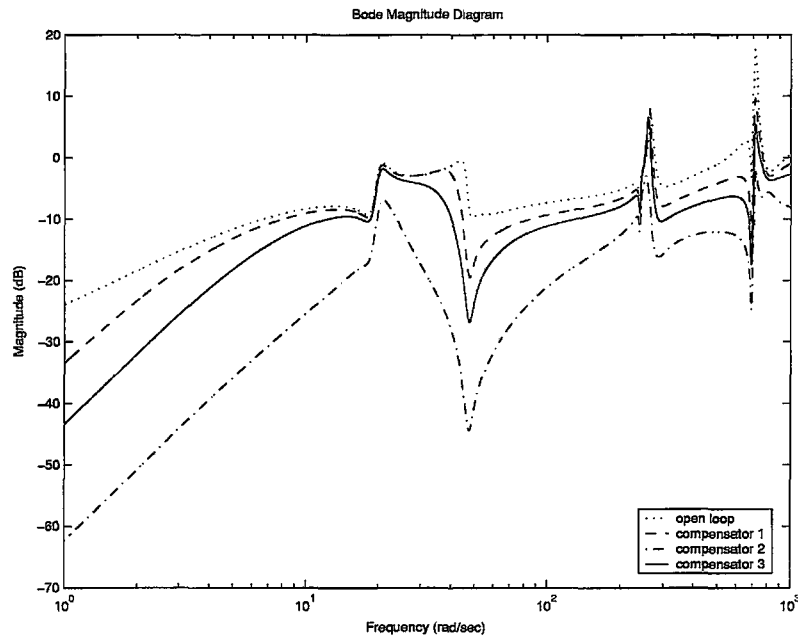


Figure 6.16. The influences of the gain variations on the relative error for the PID-compensated system models of the smart beam

Compensator 1:  $K_p = 50$ ,  $K_i = 60$  and  $K_d = 3/1000$ ,

Compensator 2:  $K_p = 100$ ,  $K_i = 100$  and  $K_d = 3/1000$ ,

Compensator 3:  $K_p = 300$ ,  $K_i = 300$  and  $K_d = 5/1000$

The PID compensators are designed for the suppression of the vibrations due to first two modes of smart beam without exciting the third mode. In order to investigate the effectiveness of the compensators at the higher frequencies, the compensators should be applied to the higher order model that contains the effects of the higher frequencies. Since the experimentally identified model obtained in Chapter 5 includes the first three modes of the smart beam only, the tuned theoretical model of the smart beam obtained in Chapter 5 is considered for this purpose. The tuned theoretical model is extended to include the first 5 modes of vibration. Figure 6.17 shows the comparison of the theoretically calculated open-loop response and the closed-loop response of the PID-

compensated system. During the theoretical calculations, the PID compensator is assigned to have the gain values of  $K_p=100$ ,  $K_i=150$  and  $K_d=1/1000$ . It is evident from the figure that the PID-controlled system suppresses the peak response levels at lower frequencies as well as, those at the higher frequencies. The analysis conducted for this gain values are repeated for all PID compensator designs considered in this thesis and the analyses are found yield similar results.

### **6.2.5 Robustness Analysis of PID Compensators**

This section is devoted to the evaluation of the robustness of the PID compensators designed for the vibration control of the smart beam. During the theoretical calculations both classical frequency response and modern robustness analyses are considered.

#### **6.2.5.1 The Classical Frequency Response Analysis of the PID-Compensated System**

In the classical frequency response analysis, the good controller design results in large loop gain for as large a frequency range as possible together with large gain margins (GM) and phase margins (PM) indicating that the loop gain avoid  $s=-1$  point. The limitations on the range of the loop gain include the actuator limits and the modeling inaccuracies [124,125,129]. In classical control, gain and phase margins are used as a design criteria. During the evaluation of the relative stability measures the Bode, Nyquist diagrams or Nichols plots may be considered [124,129] In the classical frequency response analysis, For good performance, PM values from  $30^\circ$  to  $60^\circ$  and the GM values larger than 6dB values are considered [129,130].

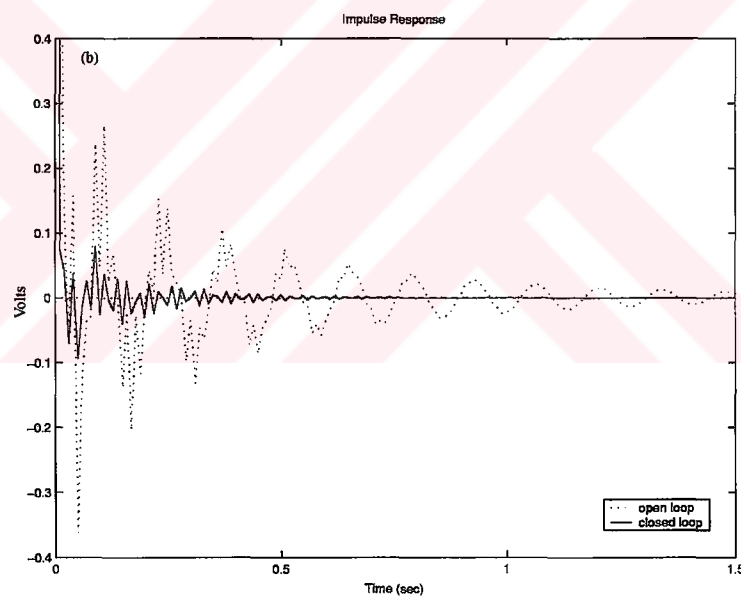
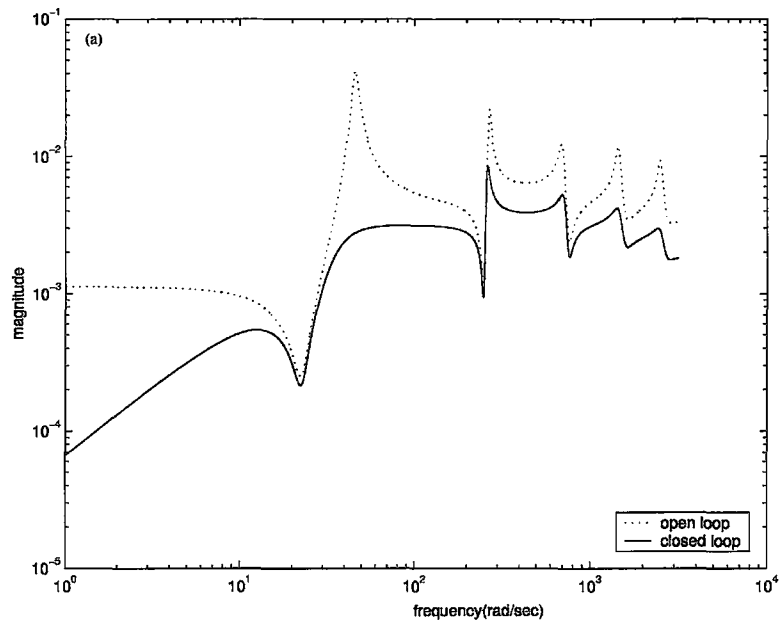


Figure 6.17. The influences of the higher frequencies on the PID-controlled system for the smart beam ( $K_p=100$ ,  $K_i=150$ ,  $K_d=1/1000$ )

- a. The comparison of the open and closed-loop frequency response
- b. The comparison of the open and closed-loop impulse response

Nichols plots combine the characteristics of Nyquist and Bode plots by producing a single plot that gives logarithmic gain plotted against phase shift. In Nichols diagrams the gain crossover point corresponds to the point where the loop gain intersects 0 dB axis and the phase cross over point is the point where  $G(s)$  intersects  $-180^\circ$  axis. Thus, the phase margin is the horizontal distance between the gain cross over point and the critical point ( $s=-1$  or, 0 dB,  $-180^\circ$ ). The gain margin is the distance between the phase crossover and the critical point. Similarly, the bandwidth of the system can also be found as the intersection of the  $G(s)$  and  $-3\text{dB}$  axis. Nichols plot is commonly used in the feedback controller design owing to its ease in the usage, [74,124,125].

In order to investigate the relative stability characteristics of the PID compensators designed for the vibration control of the smart beam, two cases are considered and compared for both theoretical and experimentally identified models of the smart beam. The utilization of the tuned theoretical model and the identified models developed in Chapter 5 allows one to investigate the effects of the modeling errors on the robustness issues in the classical frequency response analysis for the compensator designs.

The first case involves the performance analysis of a PID compensator having gains of  $K_p=50$ ,  $K_i=60$ ,  $K_d=3/1000$ . The comparison of the Nichols plots of the loop gains for the closed-loop experimentally identified and theoretical models are shown in Figure 6.18. It can be seen from the figure that the Nichols plots of both theoretical and experimental models, fall in a region far away from the critical point so the closed loop models have very large gain and phase margins. The second case involves the analysis of the closed loop model of the PID compensators with higher controller gains of  $K_p=300$ ,  $K_i=300$ ,  $K_d=5/1000$ . The comparison of the loop gains of the identified and the theoretical models of the smart beam for PID compensator are shown in Figure 6.19. Similar to the previous case, the models have very large phase and gain

margins. Although the increase in the gain values shift the Nichols plots to the higher loop gain values, the position relative to the critical point remains almost unchanged.

The classical robust performance tests are also conducted for the PID compensators and the results obtained for the theoretical and experimentally identified models are shown in Figure 6.20 and 6.21. Figure 6.20 gives the effects of the PID gain variations on the sensitivity function. It can be seen from Figure 6.20 that as the PID gain values increase, the magnitude of the sensitivity function decreases. That is, the increase in the gain values may be considered to improve the disturbance rejection characteristics of the closed loop system especially at the moderate frequency range (from 0 Hz to 17 Hz).

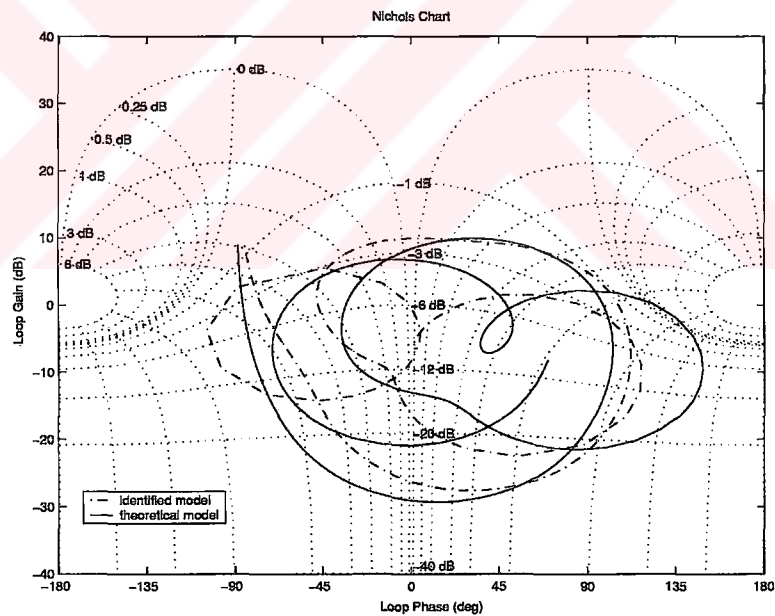


Figure 6.18. The comparison of the loop gains of the identified and the theoretical models of the smart beam for PID compensator with the gain values of  $K_p=50$ ,  $K_i=60$ , and  $K_d=3/1000$ .

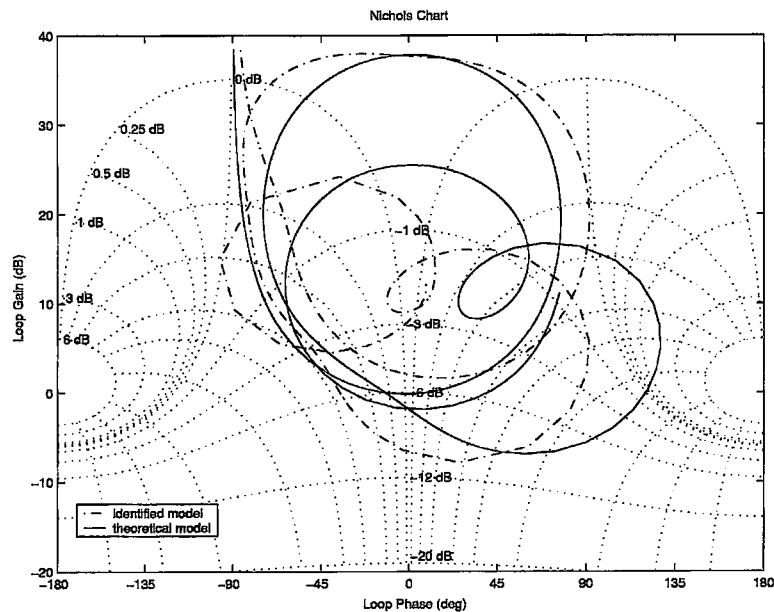


Figure 6.19. The comparison of the loop gains of the identified and the theoretical models of the smart beam for PID compensator with the gain values of  $K_p=300$ ,  $K_i=300$  and  $K_d=5/1000$ .

The influences of the PID compensator gain variations on the complementary sensitivity function are also compared and the results are shown in Figure 6.21 for the same gain values considered in Figure 6.20. It can be seen from Figure 6.21 that while the input tracks the output of the system very well in the moderate frequency range (from 0 Hz to 17 Hz), the noise rejection property of the system reduces. Since the sensor noise is known to be effective in relatively higher frequencies, where the complementary sensitivity function has of its smallest values, the compensator having the PID compensator gains of  $K_p=300$ ,  $K_i=300$  and  $K_d=5/1000$  is considered to have good noise rejection characteristics. Furthermore, the sensitivity and complementary sensitivity characteristics of the closed-loop system are shown to remain almost insensitive to the mismatches observed between the tuned and the experimentally identified model of the smart beam.

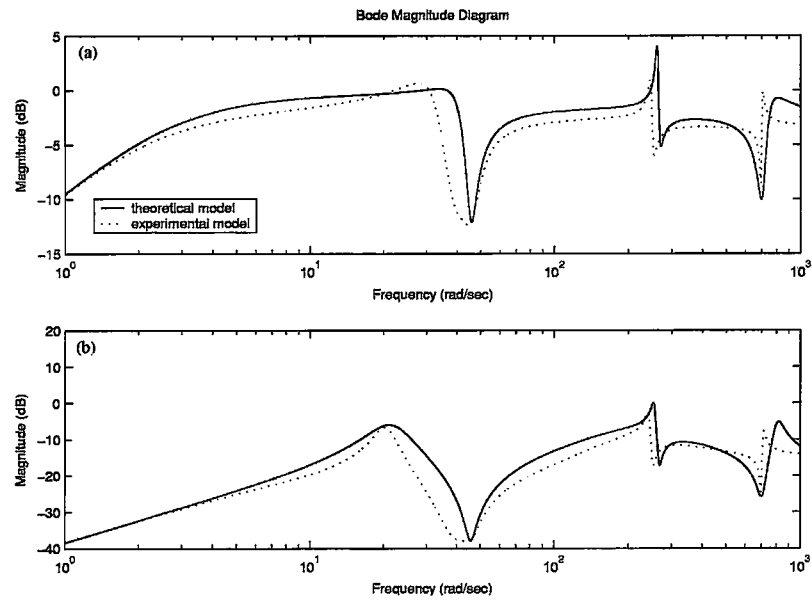


Figure 6.20. The comparison of the effects of the gain variations on the sensitivity function of the PID- compensated systems for the smart beam

a.  $K_p = 50$ ,  $K_i = 60$  and  $K_d = 3/1000$

b.  $K_p = 300$ ,  $K_i = 300$  and  $K_d = 5/1000$



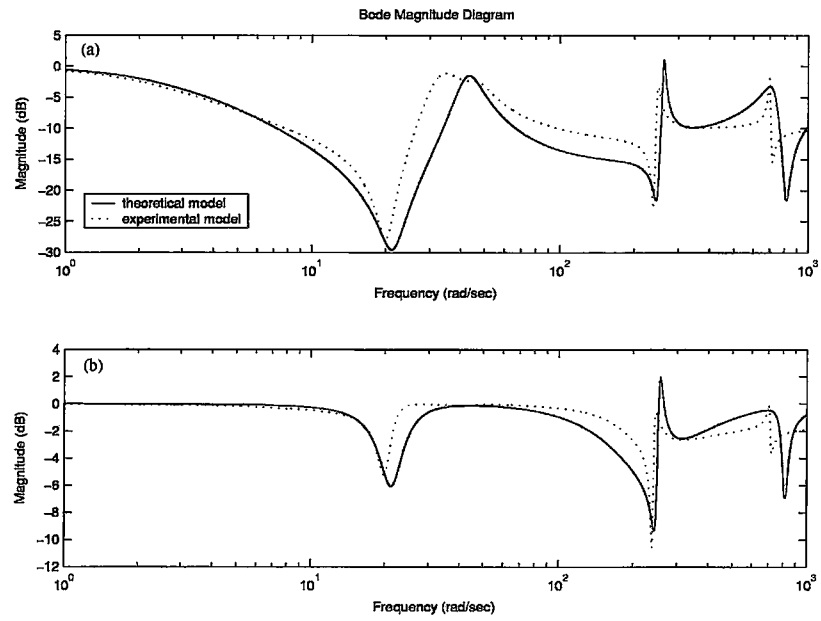


Figure 6.21. The comparison of the effects of the gain variations on the complementary sensitivity functions of the PID-controlled systems for the smart beam

a.  $K_p = 50$ ,  $K_i = 60$  and  $K_d = 3/1000$

b.  $K_p = 300$ ,  $K_i = 300$  and  $K_d = 5/1000$

### 6.2.5.2 The Modern Frequency Response Analysis of the PID-Compensated System

Based on the method described in Chapter 4 the modern robustness analysis of the PID-compensated models developed for smart beam is also conducted. During the analysis the set of plants in which the true plant, is assumed to lie is given by the multiplicative uncertainty model as,

$$\tilde{P}(s) = (1 + \Delta(s)W_2(s))P(s) \quad (6.2.5)$$

where  $\tilde{P}(s)$  gives the perturbed model of the smart beam and  $P(s)$  symbolizes the nominal transfer function of the smart beam. In this formulation, the modeling uncertainties are represented by the norm bounded  $\Delta(s)$  block satisfying  $\|\Delta(s)\|_\infty \leq 1$  condition and  $W_2(s)$  describing the uncertainty weighting transfer function. The application of the weighting transfer function  $W_2(s)$  allows the specification of the frequency dependent uncertainty profile. The interaction of the nominal transfer function  $P(s)$ , with  $W_2(s)$  gives the system model of the smart beam including the modeling uncertainties. During the modeling, it is further assumed that a performance weight is also applied output of the system to improve the frequency dependent performance profile of the compensator. Representing the weighting transfer function associated with the performance weight by  $W_1(s)$ , Figure 6.22 shows the block diagram representation of the perturbed model of the smart beam.

In the modern robustness analysis, the performance and additive weights are determined first. Figure 6.23 gives the comparison of the performance weight together with the open-loop response of the smart beam. The application of this weight improves the response at the lower frequency range (0 Hz to 130 Hz) without affecting

the response at higher frequencies (>130 Hz). The comparison of the additive weight,  $W_2(s)$  together with the open-loop response of the smart beam is shown in Figure 6.24. It can be seen in Figure 6.24 that, as the frequency increases the uncertainty increase. This indicates better system modeling at lower frequencies.

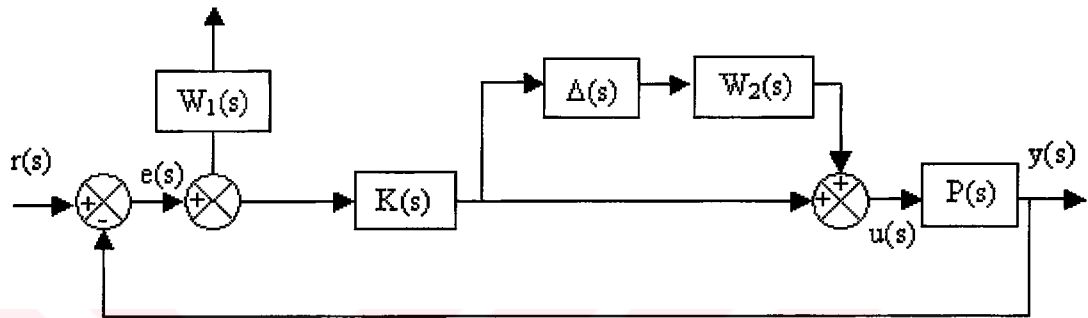


Figure 6.22. The block diagram representation of the perturbed model for the smart beam.

Then the transfer functions associated with these weights are calculated. The results are given in equation (6.2.6) for the performance weight  $W_1(s)$  and in equation (6.2.7) for the additive weight,  $W_2(s)$ .

$$W_1(s) = \frac{0.0002869s^3 + 54.09s^2 + 5.892 \times 10^4 s + 8.404 \times 10^6}{s^3 + 1.861e004s^2 + 9.381e006s + 7.8 \times 10^8} \quad (6.2.6)$$

$$W_2(s) = \frac{0.003704s^3 + 2.669s^2 + 918.5s + 3.146 \times 10^4}{s^3 + 726.4s^2 + 3.393 \times 10^5 s + 1.059 \times 10^7} \quad (6.2.7)$$

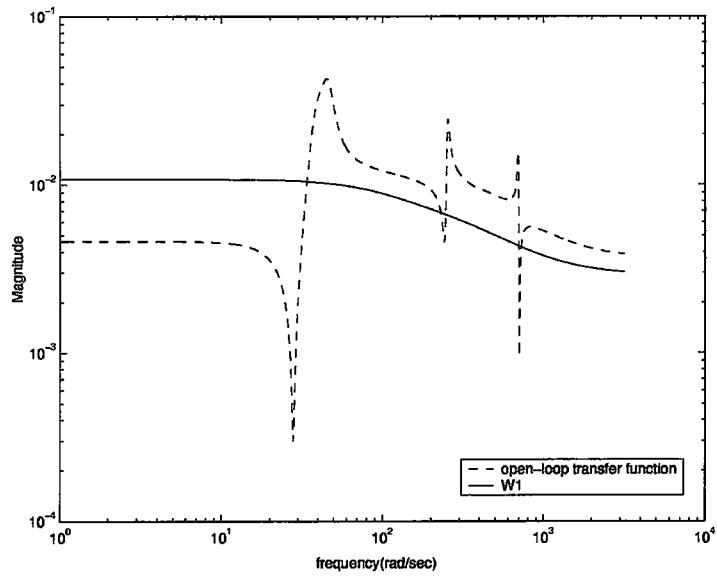


Figure 6.23. The comparison of the performance weight  $W_1(s)$  and the open-loop transfer function of the smart beam

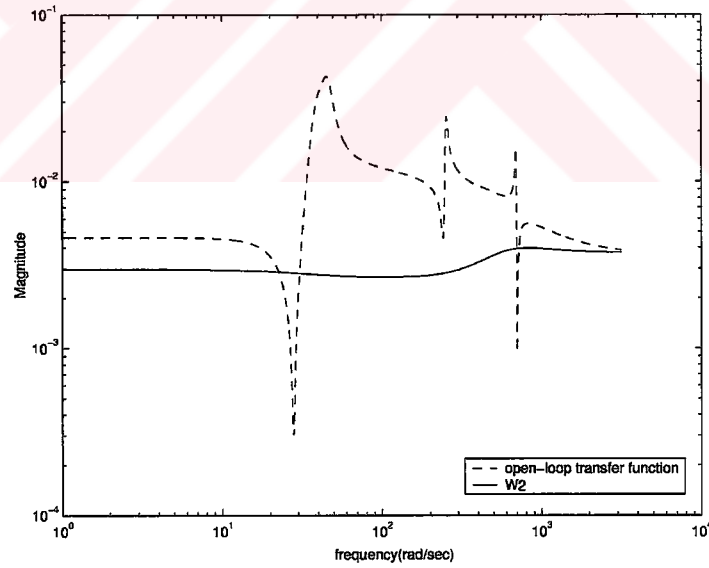


Figure 6.24. The comparison of the additive weight  $W_2(s)$  and the open-loop transfer function of the smart beam

The robust stability and performance criteria shown in Chapter 4 for multiplicative uncertainty models are examined on the perturbed model of the smart beam shown in Figure 6.22. For this reason, the effects of the PID-compensator gain variations on the robust stability and performance of the smart beam model are analyzed. During the calculations the experimentally identified model of the smart beam is assumed to describe the nominal model and the perturbed system is represented by the weights given in equations (6.2.6) and (6.2.7).

The effects of the compensator gain variations on the robust stability and performance parameters for the PID-compensated model for the smart beam are analyzed by considering four PID compensators. The first compensator is assumed to have the gains of  $K_p=50$ ,  $K_i=60$  and  $K_d=3/1000$ , the gain values associated with the second are  $K_p=150$ ,  $K_i=150$  and  $K_d=3/1000$  and the third compensator is considered with the gain values of  $K_p=200$ ,  $K_i=200$  and  $K_d=3/1000$ . The last compensator is assigned to have the highest gain values as  $K_p=300$ ,  $K_i=300$  and  $K_d=5/1000$ . Figure 6.25 gives the results.

It can be seen from Figure 6.24 that the necessary and sufficient conditions for the robust stability  $\|W_2(s)T(s)\|_\infty < 1$ , and the robust performance conditions,  $\|W_1(s)S(s) + |W_2(s)T(s)\|_\infty < 1$ , hold true for all compensators considered in the analysis. Furthermore, It is also evident from Figure 6.25 that as the compensator gain values increase, the robust stability increase but robust performance reduces. Hence, by considering the robust stability and performance criteria it can be concluded that the increase in the compensator gain reduces the stability but improves robust performance. It can be seen from the figure that both robust stability and do not reach the robust stability limits for the compensators used in the analysis. That is, the PID-compensated model for the smart beam is determined to have the robust stability and performance properties.

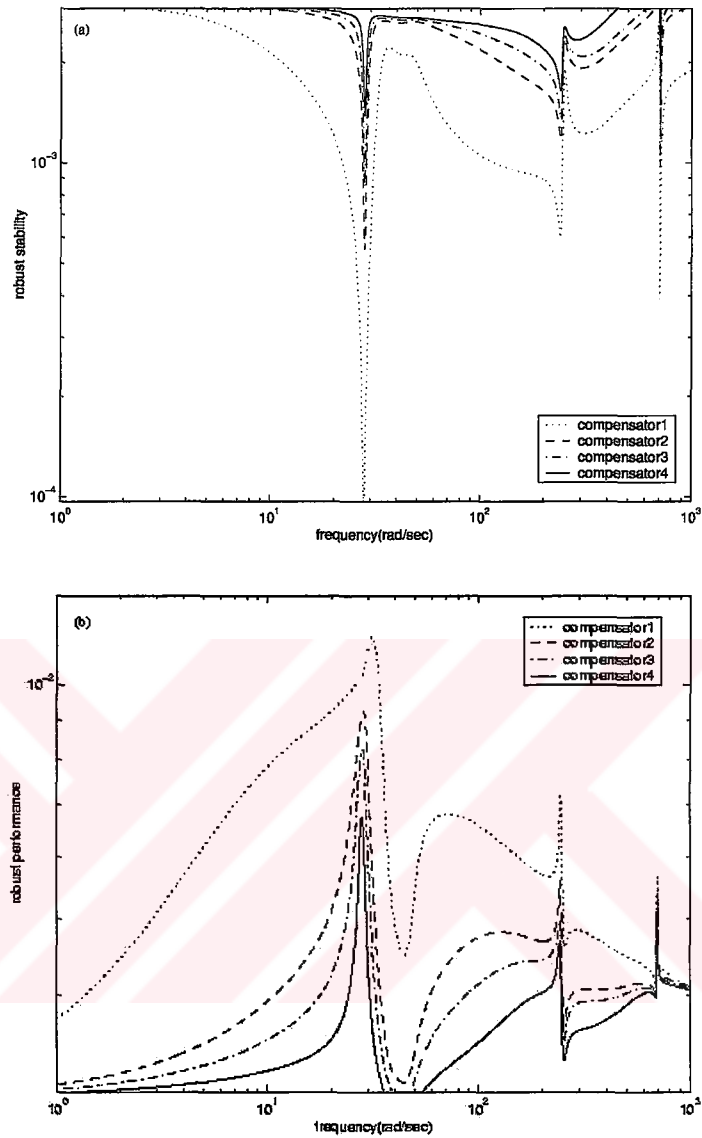


Figure 6.25. The effects of the gain variations on the robust stability and performance of the PID-compensated system model for the smart beam (compensator 1:  $K_p=50$ ,  $K_i=60$  and  $K_d=3/1000$ , compensator 2:  $K_p=150$ ,  $K_i=150$  and  $K_d=3/1000$ . compensator3:  $K_p=200$ ,  $K_i=200$  and  $K_d=3/1000$ , compensator 4:  $K_p=300$ ,  $K_i=300$  and  $K_d=5/1000$ )

a. Robust stability:  $|W_2(s)T(s)|$

b. Robust performance:  $|W_1(s)S(s)| + |W_2(s)T(s)|$

### 6.3 $H_\infty$ Optimal Control design for the Smart Beam

Although PID compensators are shown to yield satisfactory results for the control of vibration of the smart beam, the PID compensators does not necessarily yield to optimal results [124,128]. Hence,  $H_\infty$  controller design which offers, the optimal solutions to the vibration control problems [59,60,129] is also considered. Based on the theory presented in Chapter 4, this section presents the application of the  $H_\infty$  controller design for the vibration control of the smart beam. The robust performances of the PID compensator and the  $H_\infty$  controller are also compared.

The aim in the  $H_\infty$  controller design is to suppress vibrations due to the first two modes of the smart beam within the frequency range of interest hence, reducing the settling time. In the  $H_\infty$  controller design, the aim is to minimize the  $H_\infty$  norm of the transfer function describing the relation between the inputs and the outputs of a multi input multi output system.

Figure 6.26 shows the block diagram formulation of the closed loop control problem in  $H_\infty$  framework. In this figure,  $SYS_{\text{beam}}$  defines the nominal smart beam model, and  $W_{\text{add}}$  describes the weight of the uncertainties added to the system. The additive uncertainty weight  $W_{\text{add}}$  is included to account for the unmodeled or truncated high frequency modes. The interaction of the nominal transfer function  $SYS_{\text{beam}}$ , with the uncertainty structure  $\Delta$  defines the system model of the smart beam including the uncertainties. In the modeling,  $W_{\text{per}}$  symbolizes the performance weight applied to strain gage measurements

In the  $H_\infty$  control design technique applied to the smart beam,  $W_d$  describing the weight added to the disturbance is taken to be 1 indicating that the order of the disturbance acting on the system and the input signal produced by the controller is the same.

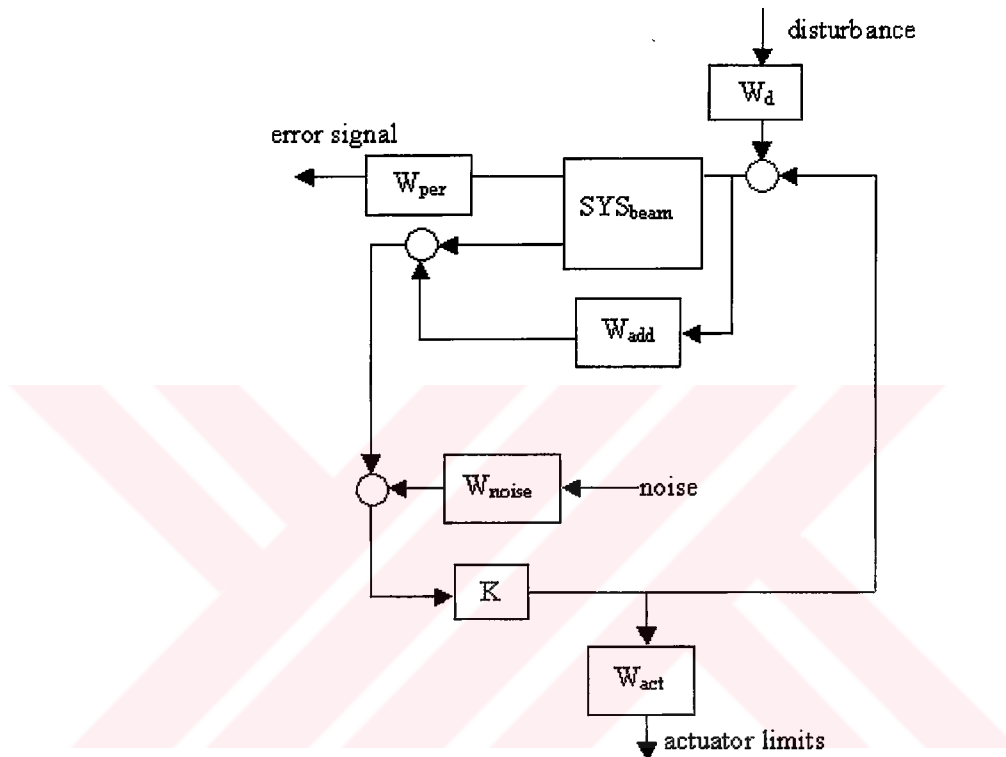


Figure 6.26. The  $H_\infty$  control formulation for the smart beam

In Figure 6.26  $W_{act}$  symbolizes the weight applied to the actuator signals in order to limit the actuator authority. This weight is chosen to be  $1/250$  representing the upper limit for the actuation voltage of 250V. Furthermore,  $W_{noise}$ , symbolizing the noise to signal ratio is selected to be 0.01.



During the  $H_\infty$  controller design for the smart beam, the performance weight given in equation (6.2.6) and the additive weight described by equation (6.2.7) are considered. The applications of these weights results in the minimization of the strain gage outputs at lower frequencies (0Hz to 130Hz) while making minimal changes at higher frequencies (>130Hz).

In  $H_\infty$  controller design, a scaling factor applied to the nominal model system model may be required to avoid the numerical difficulties involved in the optimal  $H_\infty$  controller algorithm [60,127]. For a linear time invariant systems, the scaling corresponds to the multiplication of the input signal. Furthermore, the controller is generally designed by using the lowest possible order for system model representing the dynamical characteristics of the system model to reduce the numerical inaccuracies. But the controller so obtained, is usually tested on the higher order model representing the model closer to the true system. This secures the success of the controller prior to the implementation of the controller.

In the design calculations performed for the smart beam, the additive weight given in equation (6.2.6) and performance weight described by equation (6.2.7) are considered. During the theoretical calculations, scaling factor of 100 is applied to the 10<sup>th</sup> order identified model of the smart beam developed in Chapter 5 and the performance and the additive weights. That is, during the calculations for the  $H_\infty$  controller, the nominal system model of the smart beam is taken to be  $SYS_{beam}=100 \times P(s)$  and the performance and the weights are adjusted to be  $W_{per}(s)=100 \times W_1(s)$  together with  $W_{add}(s)=100 \times W_2(s)$ .

The inclusion of these weights in the system model of the smart beam yields to the formulation of the standard  $H_\infty$  control problem presented in Chapter 4. The application of the standard  $H_\infty$  solution techniques to 10<sup>th</sup> order experimentally identified model of

the smart beam leads to the determination of a 16<sup>th</sup> order  $H_\infty$  controller. By using standard model reduction techniques, the controller is reduced to 6<sup>th</sup> order. Figure 6.27 gives the bode diagram of the  $H_\infty$  controller obtained. The comparison of the open and closed-loop frequency responses are shown in Figure 6.28.

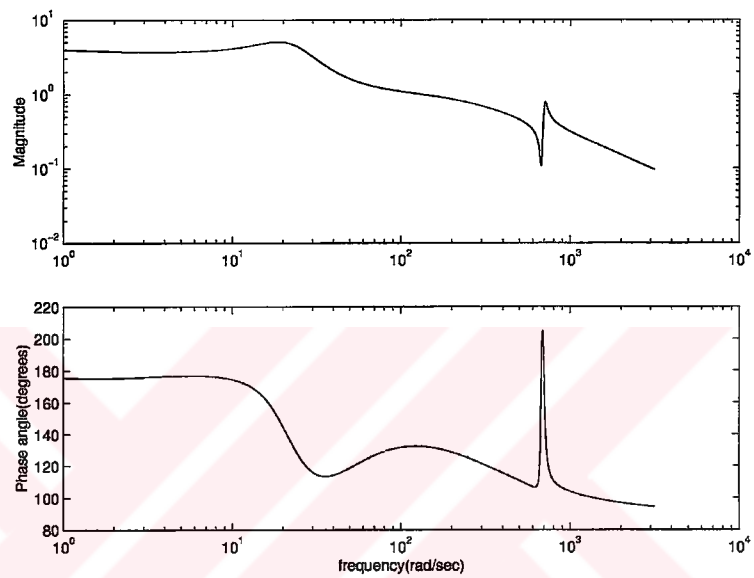


Figure 6.27. The 6<sup>th</sup> order  $H_\infty$  controller designed in the study

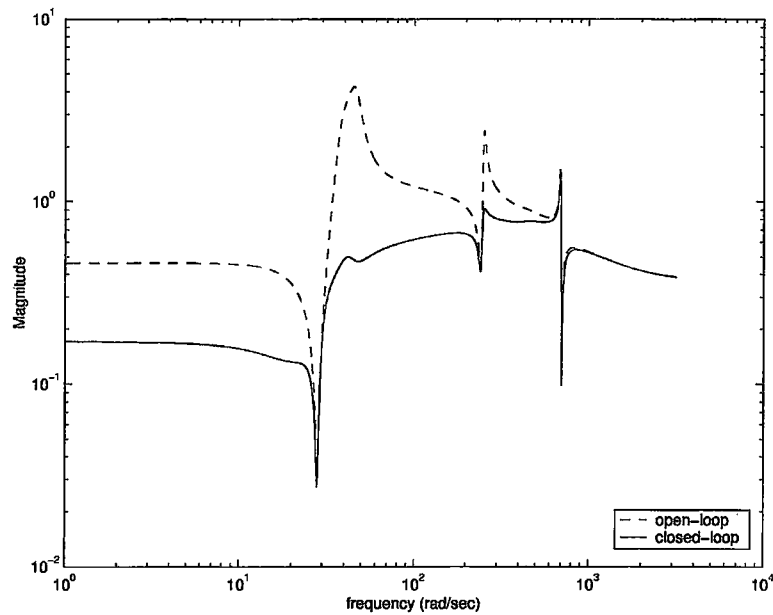


Figure 6.28. The comparison of the open and closed-loop responses of  $H_{\infty}$  -controlled system for the smart beam

### 6.3.1 The Robustness analysis of the $H_{\infty}$ -Controlled System for the Smart Beam

In order to test the robustness of the  $H_{\infty}$ -controller the structural singular value ( $\mu$ ) of the system is calculated across the frequency range of interest. A closed loop system is said to have the robust performance that is, the stability and the performance specifications are satisfied in the presence of the uncertainties defined if  $\mu$  value is less than 1 within the frequency range of interest. Figure 6.29 show that, the closed loop system designed for the smart beam has robust stability and robust performance properties [129,136].

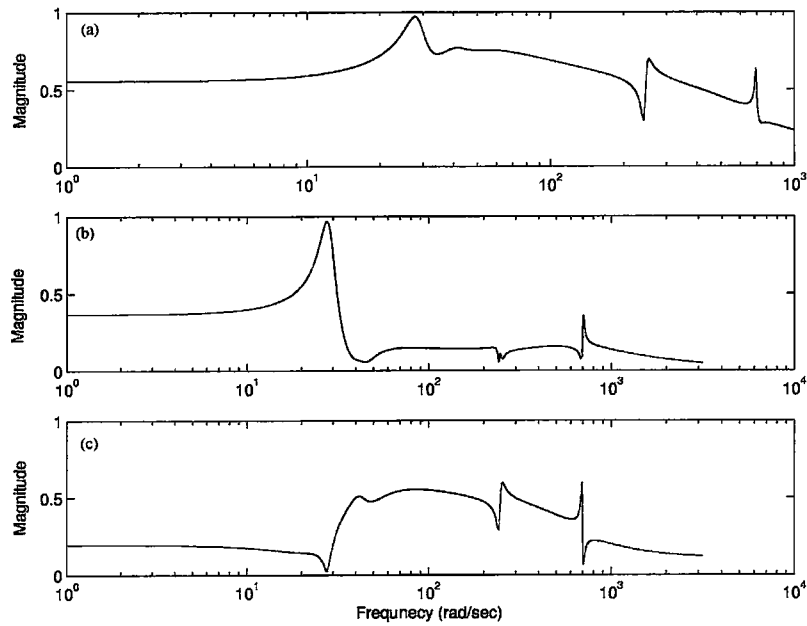


Figure 6.29. The structured singular value ( $\mu$ ) of the closed-loop system for the smart beam

- a. Robust performance
- b. Robust stability
- c. Nominal Performance

### 6.3.2 The Comparison of the PID Compensator and the $H_\infty$ Controller for the Smart Beam

In order to compare the performances of the PID-compensator and  $H_\infty$  controller for the vibration control of the smart beam, a test case is considered. The case considers 12<sup>th</sup> order nominal scaled model for the smart beam  $SYS_{\text{beam}}$  in the PID compensator design and the maximum actuator gain value of the PID-compensator is set to the maximum actuator gain of the optimal  $H_\infty$  controller shown in Figure 6.27.

The serial compensator design is resulted the PID gains of  $K_p=0.5$ ,  $K_i=9.6$  and  $K_d=1/1000$ . Figure 6.30 gives the comparison of the frequency responses of the PID-compensator and the  $H_\infty$  controller. By using the PID-compensator and the  $H_\infty$  controller, the closed-loop responses of the smart beam are calculated. The comparison of the open-loop, PID-compensated and  $H_\infty$  controlled and closed loop systems for the smart beam are shown in Figure 6.31. It can be seen from Figure 6.31 that for the same maximum controller gain levels, the  $H_\infty$  controller results in better attenuation levels at the first two resonance frequencies of the smart beam than those of the PID-compensated model

Table 6.1 summarizes the results in terms of the reduction in the attenuation levels at the first three modes of vibration.

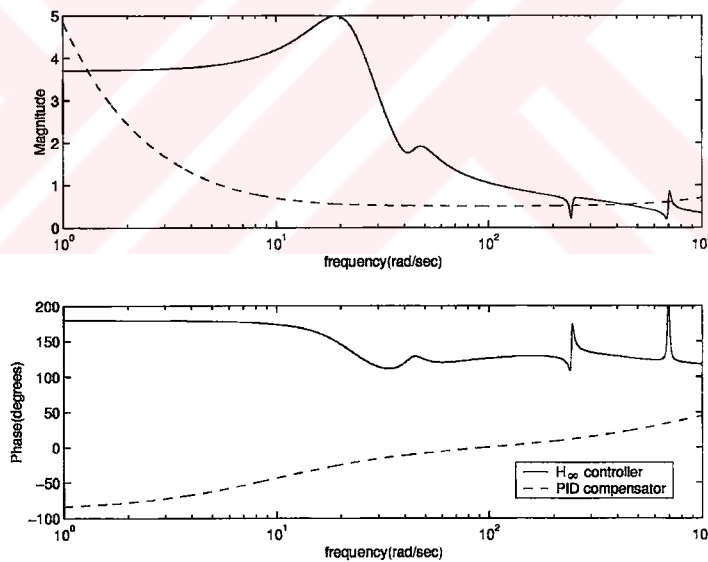


Figure 6.30. The comparison of the responses of the PID-compensator with the gains of  $K_p=0.5$ ,  $K_i=9.6$  and  $K_d=1/1000$  and the optimal  $H_\infty$  controller for the smart beam

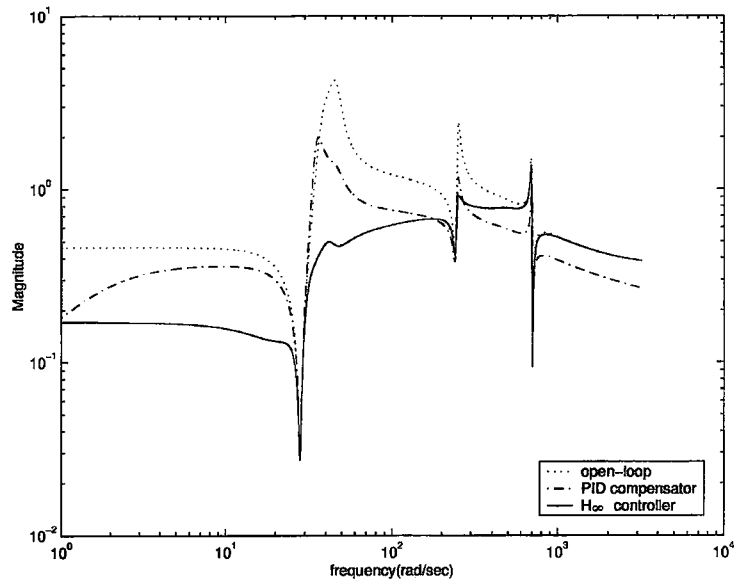


Figure 6.31. The comparison of the open and closed-loop responses of the smart beam

Table 6.1. The comparison of the effectiveness of the PID-compensator and  $H_\infty$  controller on the vibration control of the smart beam

Frequencies	Attenuation levels	
	PID-compensator (*)	$H_\infty$ controller
$f_1$	2.25	8.56
$f_2$	2.06	2.67
$f_3$	1.64	1.16

(\*) PID-compensator with the gains of  $K_p=0.5$ ,  $K_i=9.6$  and  $K_d=1/1000$

As it was discussed in Chapter 4, that the major advantage of the  $H_\infty$  controllers over the PID-compensators is observed in the modeling of the uncertainties. Unlike PID compensator design, The  $H_\infty$  controller design allows the inclusion of the modeling uncertainties in the closed-loop system during the design stage systematically.

Since the  $\mu$  analysis conducted for the  $H_\infty$  controller designed requires the specification of the proper transfer functions for the controllers, that is the controller transfer function with the order of the denominator is larger than that of the denominator, the  $\mu$  analysis is not conducted for the PID-compensated model of this section. Instead, the perturbed model for the smart beam shown in Figure 6.22 is considered. During the robustness analysis of the PID-compensated system model developed in this section, the scaled nominal system model of the smart beam  $S_{\text{beam}}$  and scaled performance  $W_{\text{per}}$  and additive weights  $W_{\text{add}}$  are considered. Figure 6.32 gives the robust stability and performance plots.

It is evident from the figure that the PID-compensated model with the gain values of  $K_p=0.5$ ,  $K_i=9.6$  and  $K_d=1/1000$  does not satisfy the robust performance criteria that is the robust performance parameter reaches to maximum value larger than one. Thus, in order to improve the robust performance the gain values should be increased. By considering the results obtained from the test case, it can be concluded that the PID-compensator should have gain values considerably larger than that of  $H_\infty$  controller to achieve the robust performance requirement. In this case, the PID-compensator gain values however are bounded by the actuator limits and the robust stability criteria.

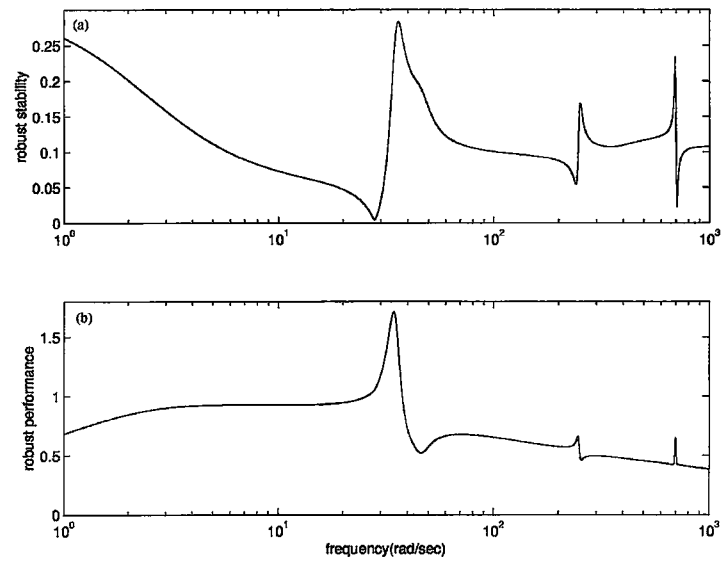


Figure 6.32. The robust stability and performance tests for the PID-compensated model with the gains of  $K_p=0.5$ ,  $K_i=9.6$  and  $K_d=1/1000$  for the smart beam

a. Robust stability:  $|W_{\text{add}}(s)T(s)|$

b. Robust performance:  $|W_{\text{per}}(s)S(s)| + |W_{\text{add}}(s)T(s)|$



## 6. 4 Vibration Control of the Smart Fin

Based on the model obtained in Chapter 5, an  $H_\infty$  controller is also designed for the smart fin. The goal of the controller is to attenuate the vibrations of the fin at its first two natural frequencies (in the range from zero to 60 Hz) and gain stabilize the unmodeled high frequency modes.

### 6.4.1 $H_\infty$ Optimal Controller Design for the smart fin

In  $H_\infty$  controller design for the smart fin, the performance objective is to minimize the maximum frequency response of the first two modes of the smart fin at the sensor locations. Figure 6.33 shows the formulation of the closed loop control in  $H_\infty$  framework.

In Figure 6.33,  $SYS_{fin}$  defines the nominal smart fin model,  $W_{per}$  represents a performance weight on the strain gage sensors to achieve the performance objective. For both strain gage output channels, magnitude of the  $W_{per}$  weights are shown in Figure 6.34 together with the open-loop response. These weights are selected to achieve attenuation in the peak frequency response of the closed loop system. An additive uncertainty is included in the problem formulation to account for the unmodeled high frequency modes and modeling errors within the controller bandwidth. This weight is selected to have a magnitude greater than the structural modes above 500 rad/sec. If robust stability of the closed-loop system is achieved for this additive uncertainty model, the flexible modes of the structure will be gain stabilized above 500 rad/sec. Figure 6.35 shows the magnitude of  $W_{add}$  versus the frequency response of the transfer function from the piezoelectric actuators to both strain gage sensors. To limit the actuator command signal in the control design process to 250 volts,  $W_{act}$  in Figure 6.33 is chosen as 1/250.

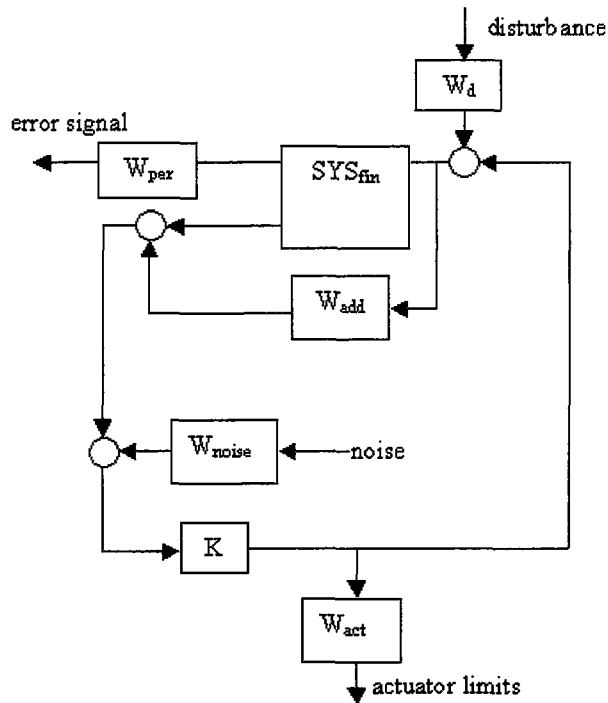


Figure 6.33. The block diagram formulation of the  $H_\infty$  control problem for the smart fin

During the design, the weights on the disturbance input  $W_{dist}$  is taken to be 1. This indicates that the input disturbance is expected to be in the same order of magnitude as the controller signals. The strain gage signals have a signal to noise ratio of 100 on both channels, therefore,  $W_{noise}$  in Figure 6.33 is taken as a  $2 \times 2$  diagonal matrix with 0.01 as the diagonal elements for each output channel. A 12<sup>th</sup> order controller is obtained by applying the standard solution techniques to the system formulated in Chapter 4. This controller is tested on a 10<sup>th</sup> order model of the smart fin obtained from the experimental data by using system identification as explained in Chapter 5. Open and closed loop frequency responses for both channels are shown in Figure 6.36 and Figure 6.37.

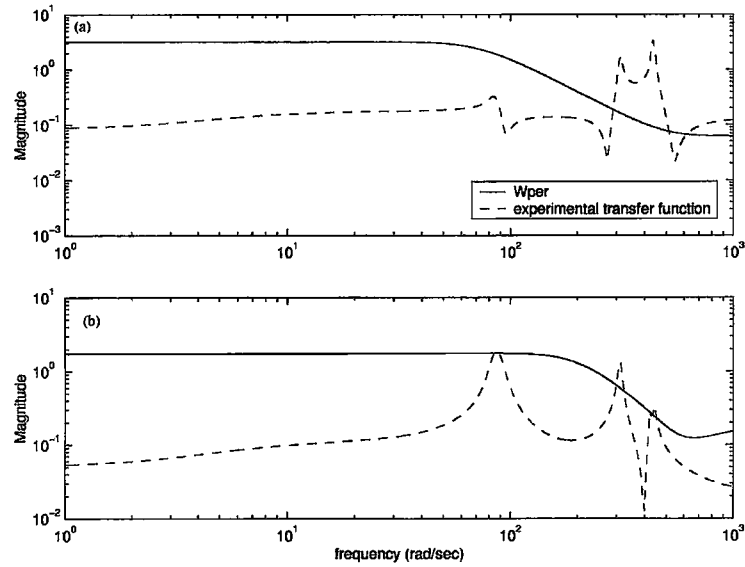


Figure 6.34. The comparison of the performance weight  $W_{per}$  and the experimental smart fin transfer functions at the strain gage locations

- a. Location (1)
- b. Location (2)

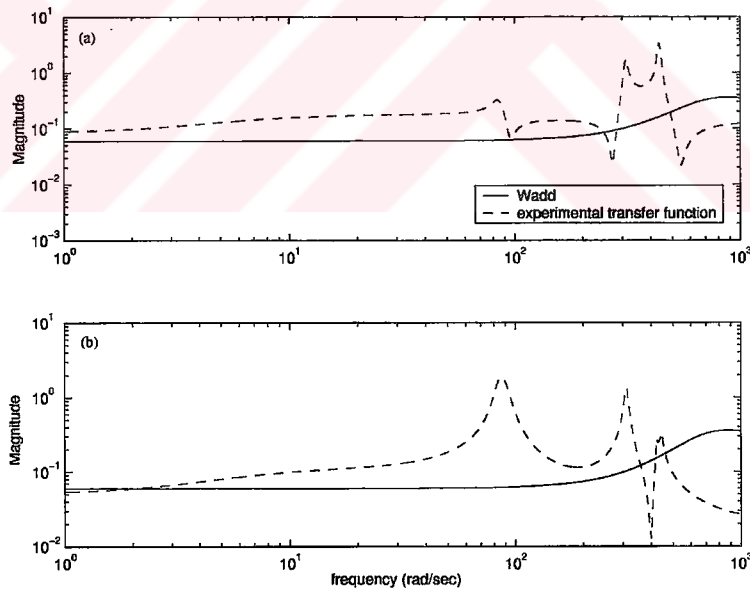


Figure 6.35. The comparison of the performance weight  $W_{add}$  and the experimental smart fin transfer functions at the strain gage locations

- a. Location (1)
- b. Location (2)

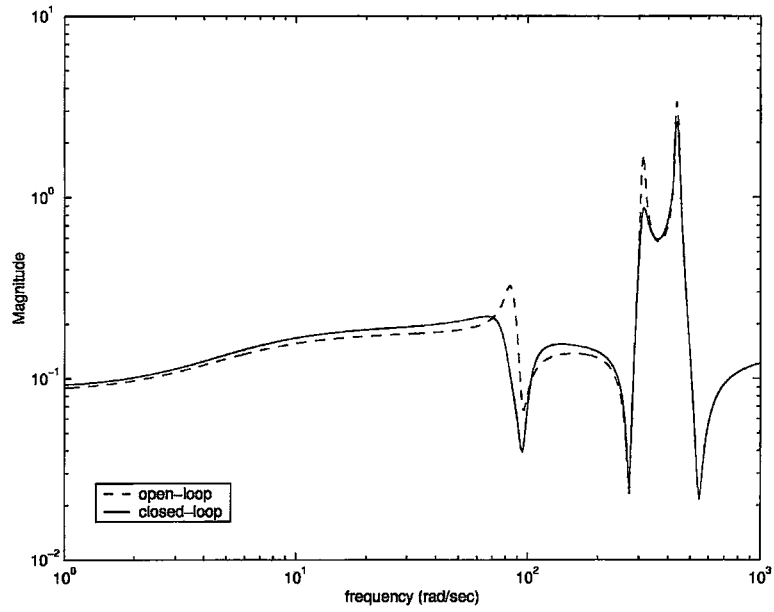


Figure 6.36. The comparison of the open and closed loop responses of the smart fin for the strain gage at location (1)

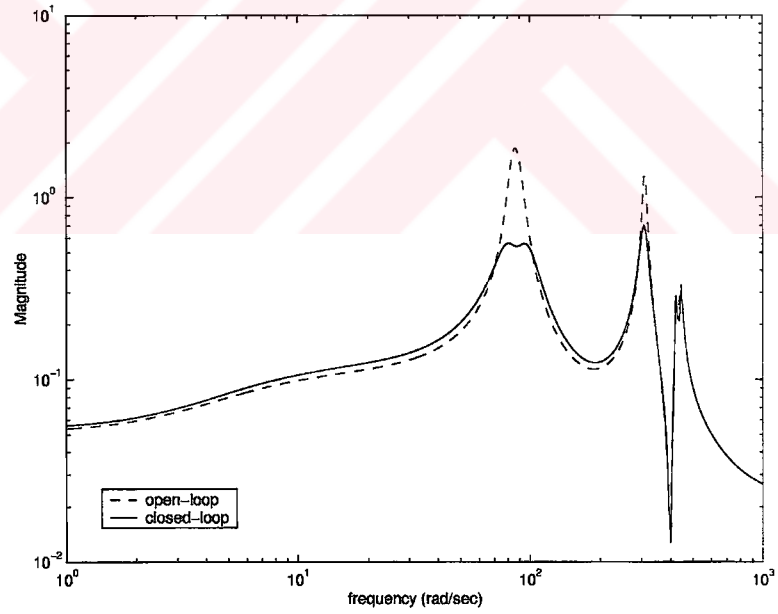


Figure 6.37. The comparison of the open and closed loop responses of the smart fin for strain gage location (2)

It is evident from Figures 6.36 and 6.37 that the application of the  $H_\infty$  controller results in the attenuation in the peak response levels associated with the resonance frequencies of the smart fin. Table 6.2 summarizes the results obtained in terms of the attenuation levels for the strain gage outputs at the locations (1) and (2). It can be seen from the table that the single input two outputs closed-loop model achieves the best performance in terms of the attenuation levels at the resonance frequencies of the smart fin at the location (2). Figure 3.38 gives the frequency responses of the controllers.

Table 6.2. The comparison of the attenuation levels achieved by the  $H_\infty$  controller designed for the smart fin

frequencies	Strain gage location (1)			Strain gage location (2)		
	$f_1$	$f_2$	$f_3$	$f_1$	$f_2$	$f_3$
Attenuation levels(*)	1.61	1.93	2.12	3.36	1.89	1.20

(\*) closed-loop response/open-loop response

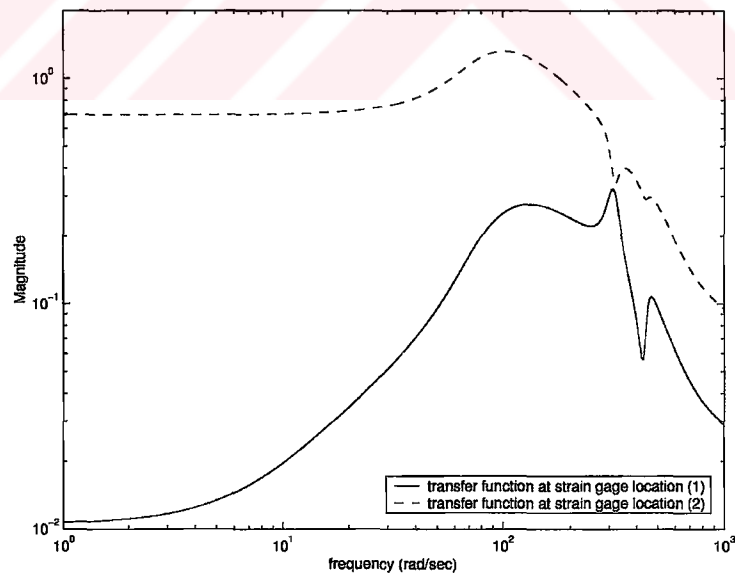


Figure 6.38. The comparison of the frequency responses of the 12<sup>th</sup> order  $H_\infty$  controllers applied to the strain gage locations

## 6.4.2 Robustness Analysis of the $H_\infty$ Controller

$\mu$ -analysis results are given in Figure 6.39. It can be seen that  $\mu$  has a peak value of approximately one. This indicates that the robust performance requirements are satisfied for the closed loop system.

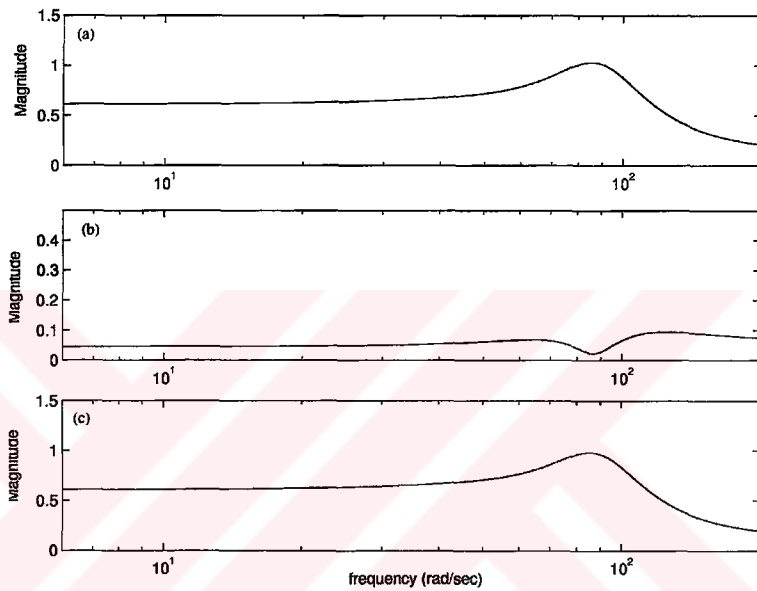


Figure 6.39. Structural singular value ( $\mu$ ) of the closed loop system of the  $H_\infty$  controller designed for the smart fin.

- a. Robust performance
- b. Robust stability
- c. Nominal performance

## 6.5 The Real time implementation of $H_\infty$ Controller the Smart Beam

This section describes the experimental work conducted for the implementation of the  $H_\infty$  controller designed for the active vibration control of the smart beam. The  $H_\infty$  controller designed in this chapter, is implemented in the structural dynamics laboratory in the department of Aeronautical Engineering, METU. Figure 6.40 shows the block diagram representation of the experimental setup used for the implementation of controller. The experimental setup consists of control system unit (SS10) and a High Voltage Power Amplifier (SA10). Appendix D gives the necessary data for the real-time implementation of the  $H_\infty$  controller.

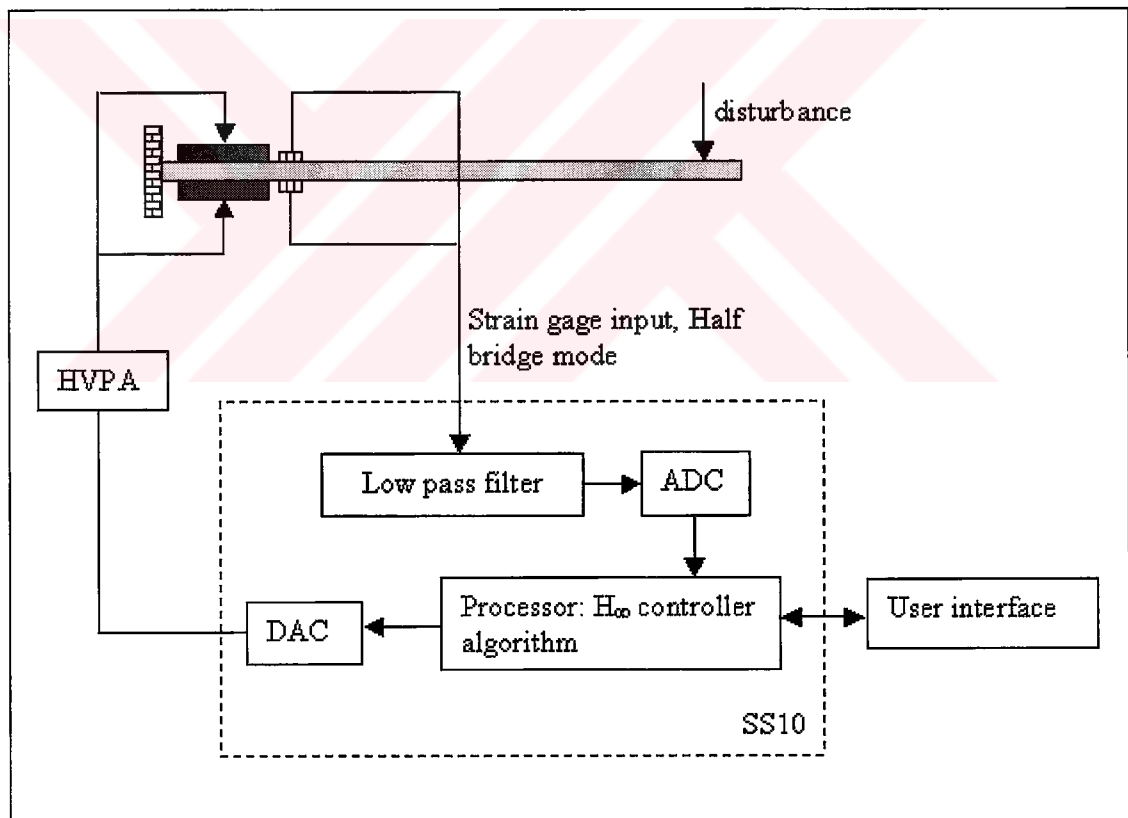


Figure 6.40. The block diagram representation of the experimental setup for active vibration control of the smart beam.

The Control system unit (SS10) used in the thesis is designed by Sensor Technologies Limited of Canada to accommodate up to eight strain gage inputs in wheatstone bridge configuration for four low power actuator outputs. SS10 is designed to tolerate heavy computing applications of real-time signal processing and control. The unit consists of an intel CPU (266 MHz), RAM up to 64 MB, High speed ADC (Analog–Digital Conversion), DAC (Digital-Analog Conversion) boards and has C or C++ code, which makes the development and the implementation of real-time complex algorithms like  $H_\infty$  possible. The controller unit contains first order low pass filter with the cut off frequency of 80 Hz.

During the closed-loop tests conducted the strain gage signals collected, were low-pass filtered and converted to digital ones before they were fed to the signal processing unit which includes the  $H_\infty$  control algorithm for active vibration control. The digital controller outputs calculated according to the algorithm were then converted to the analog ones by a high speed DAC board. The piezoelectric actuator inputs were amplified to the desired levels by a High Voltage Power Amplifier to achieve the high voltage requirements for the active vibration control of the smart beam.

During the tests, SS10 was controlled by a host computer using RS232 connection. The high voltage power amplifier, SA10 designed by Sensor Technologies Limited of Canada provided the high voltage drive for the piezoelectric actuators throughout the tests.

The open and closed-loop responses of the smart beam in terms of strain gage output voltage to the initial tip displacement value of 2 cm were measured for 20sec by using the experimental setup and the results obtained are shown in Figure 6.41. It can be seen from the figure that despite of the presence of the noise present in the environment, the controller effectively suppresses the vibrations of the smart beam.



In order to remove noise from the signal a low-pass analog filter should be used. In this case, the filter could be connected between the output of the controller unit and the HVPA.

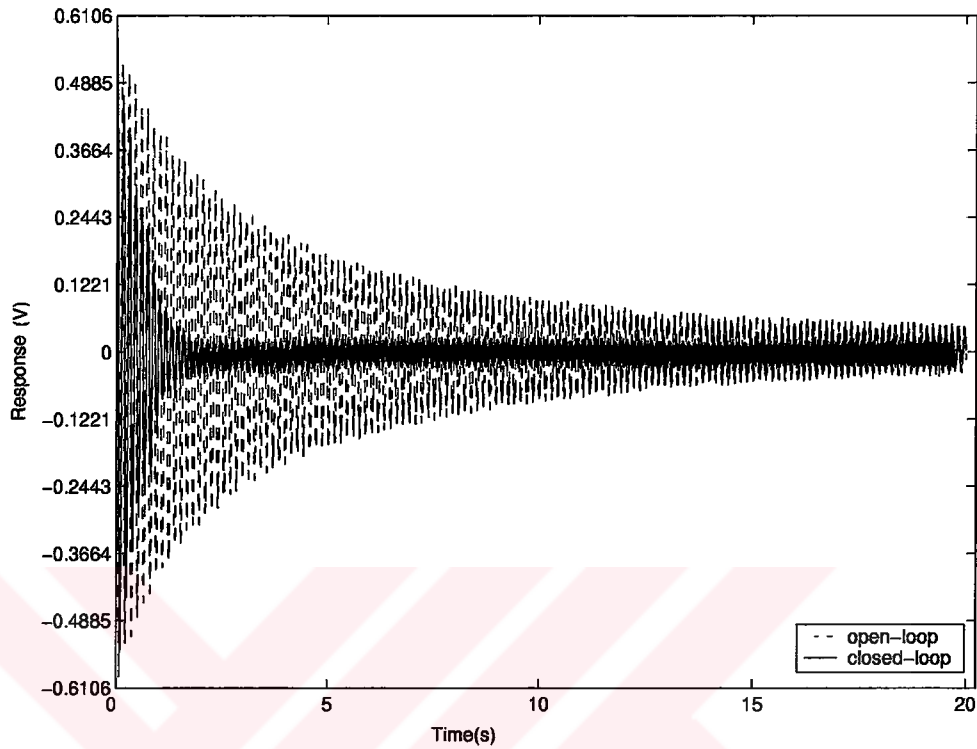


Figure 6.41. The comparison of the open and closed responses of the  $H_\infty$  controlled smart beam (response to the initial tip displacement of 2 cm).

## 6.6 Conclusions

This chapter presented active vibration control of the smart structures considered in the thesis. Based on the structural and experimental models developed, the series compensator and  $H_\infty$  control design techniques were examined for their effectiveness in the vibration control of the smart structures.

The study first analyzed the effectiveness of the PID compensators in the vibration control of the smart beam. Although the PID compensators were shown to reduce

the modeling errors existing between the experimental and the theoretical models developed for the smart beam and produced satisfactory results in the vibration control, the difficulties in the modeling of the uncertainties and the inherent difficulties of the technique in the determination of the optimal solutions were shown to limit their potential use in the active vibration control of smart structures. The  $H_\infty$  control design technique however offered the optimal, robust solutions for the vibration control of the smart beam by relaxing the apparent restrictions of the PID compensators in the modeling of the uncertainties.

Hence,  $H_\infty$  control design technique was also applied to the smart fin. Because of the difficulties in the development of the accurate finite element model of the smart fin, the experimentally identified models were considered in the design of the  $H_\infty$  controllers. The thesis was focused on the accurate modeling of the uncertainties within the  $H_\infty$  control design framework. The designed controllers were found to suppress the vibrations due to the first two modes of the smart fin. By using structured singular value ( $\mu$ ) analysis, it was also shown that the controllers designed guaranteed the robust performance of those systems in the presence of uncertainties.

The time domain implementation of the  $H_\infty$  controller designed for the smart beam also verified the effectiveness of the technique. It was shown both theoretically and experimentally that despite of the presence of the uncertainties the controller results in the attenuation of the response of the smart beam. The high noise levels observed in the open and closed-loop response measurements indicated the need for the consideration of the effective means of the noise removal in the signals. One way to achieve this might be the application of the analog low pass filter to the output of the controller unit. Because of the high costs of the analog filters suitable for the current noise problem, the appropriate noise removal could not be handled in the current study.

Unlike passive surface damping treatment methods, which can be used to suppress vibration due to the single frequency generally first mode within the frequency range, in addition to the superiority of the technique in the modeling of the uncertainties, the application of the  $H_\infty$  controller allows simultaneous suppression of the desired number of modes within the frequency range while making minimal change at higher frequencies.



## **CHAPTER 7**

### **CONCLUSIONS**

#### **7.1 General Conclusions**

This study aimed to investigate some applications of smart structures in aerospace engineering. The smart structure models were considered to be finite and flat aluminum beam-like and plate-like structures with surface bonded PZT (Lead-Zirconate-Titanate) patches. The smart structures were studied in cantilevered configuration.

The first part of the thesis presented a finite element based modeling technique for the analysis and design of the smart structures. By using ANSYS® (v.5.6) software, the study described the effects of the piezoelectric patches on the response of the smart structures. It further explained the influences of the patch size, placement of patches and suitable sensor types and locations. The study focused on the accurate representation of anisotropy and electro-mechanical coupling inherent to piezoelectric materials and their effects on the smart structures.

It was shown in the thesis that the piezoelectric actuation generates significant transverse and normal stresses in the vicinity of the region where the piezoelectric patches interfaces with the passive structures. Thus any exclusion of these stresses such as the modeling of the smart structures through the plane stress approach may yield to inaccurate results.

Although the modeling of the passive portions of the smart structures by using linear prismatic elements with extra displacement shapes was shown to be a correct approach for the simple smart structures considered such as the ones considered in the thesis, the difficulties in the modeling of the irregular geometries by using these elements and the increased computing time limit their potential applications on realistic aerospace structures.

In this thesis, the finite element method was shown to be especially advantageous in dealing with the multiple design parameters of the smart structures. By enabling the parametric design feature, the placement and size of the piezoelectric patches on the response of the smart structures could be obtained. The determination of the maximum admissible piezoelectric actuation value, which effectively gives the actuator limits, was appeared to be another advantage of the technique.

The modal analysis based sensor and actuator placement technique considered in this thesis is not a formal optimization. It gives satisfactory results for the simple structures like the smart structures considered in the thesis. The extension of the technique to the realistic structures is very difficult.

The second part of the thesis described the experimental work conducted to validate the theoretical models. In this part, the factors affecting the accuracy of the theoretical models were investigated. During the course of work, the models of the smart structures were also synthesized from identified single-input, single-output transfer functions, which were obtained by curve fitting to the experimental data in the frequency domain. The identified models were then used only to tune the accuracy of the developed theoretical models. The effectiveness of the method of spectral estimation in the elimination of the spurious noise was shown. It was further stated that the system identification technique could be used when the finite element method becomes insufficient.

The validity of the finite element based modeling was confirmed by comparing the first three theoretical and experimentally determined frequencies of the smart structures. While the frequency values associated with the first and the third modes were shown to be in good agreement with the experimental results, the frequencies corresponding to the second mode were found to be slightly different. These differences were attributed to the unmodelled effects like cable masses.

The probable deficiencies in the determination of an accurate finite element model of the smart structures were determined to be the exclusion or improper modeling of the cable mass and/or damping.

It was shown that the tuning algorithm developed in the thesis could effectively be used to tune the accuracy of the theoretical models. Another impediment to the accurate modeling of the smart structure was shown to be the hysteresis effects of the piezoelectric patches.

The LVDT tests conducted had indicated that the linear relationship between the piezoelectric actuation and the response predicted by the finite element models holds true only for the low actuation voltage values. Hence, if a relatively high voltage values is applied to the patches, the relationship inevitably exhibits nonlinear behavior. The hysteresis in the piezoelectric material, used in the thesis was determined to have a form of nonlinearity with memory BM500.

By using the models developed in the first and second part, the third part detailed on the design of PID compensators and  $H_\infty$  controllers that suppresses vibrations of the smart structures due to the first two flexural modes of vibrations. The influences of the modeling uncertainties in robust performances of the systems were fully dealt with.

In the third part of the thesis, first the performances of the PID compensators and  $H_\infty$  controllers in the vibration control of smart beam were investigated by

considering the theoretically developed and experimentally obtained models. It was shown that the  $H_\infty$  controller design was offered optimal, robust solutions for the vibration control of smart beam by relaxing the apparent restrictions of the PID compensators in the modeling of the uncertainties. The  $H_\infty$  controllers were then considered in the suppression of the vibrations of the smart plate and smart fin. Based on the experimentally identified models,  $H_\infty$  controllers were designed. It was shown that the designed controllers guaranteed the robust performance in the presence of the uncertainties.

The time domain implementation of the  $H_\infty$  controller designed for the smart beam was verified the effectiveness of the technique. It was also shown that despite of the presence of the noise levels present in the environment the controller results in the attenuation of the response of the smart beam.

It was shown in the study that unlike the passive surface damping treatment methods, which can be tuned to suppress vibration due to the single frequency within the frequency range, in addition to the superiority of the technique in the modeling of the uncertainties, the application of the  $H_\infty$  controller allows the simultaneous suppression of the desired number of modes within the frequency range while making minimal change at higher frequencies.

The high noise levels observed in the open and closed-loop response measurements indicated the need for the consideration of the effective means of the noise removal in the signals. One way to achieve was recommended to be the application of the analog low pass filter to the output of the controller unit. Because of the high costs of the analog filters suitable for the current noise problem, the appropriate noise removal could not be handled in the current study.

Furthermore, the PID compensators for the smart beam and  $H_\infty$  controller designed to suppress the vibrations of the smart fin due to its first two modes could not be implemented. The software developments for the PID compensators and single input-multi output  $H_\infty$  controllers to be used in the smart controller unit SS10 should be done.

## **7.2 Recommendations for the Future Work**

It is believed that the results of the current study may serve as a precursor for the achievement of the following subjects.

The linear theory of piezoelectricity may be refined to include the effects of the induced potential, which is crucial for the analysis of the smart structures undergoing large deformations. Furthermore the influences of the thermal stresses on the response of the smart structures may also be investigated.

In order to eliminate the errors determined in the modelling of the solid-shell hybrid models, the offset modelling techniques for these models should be improved or shell piezoelectric elements having quadratic displacement and voltage behaviour must be developed. This is expected to improve the correctness and easiness of the smart structure models to be developed for the complicated realistic aerospace structures.

The control models developed for the suppression of the in-vacuo vibrations may be extended to include the effects of aeroelastic effects. Hence aeroservoelastic studies may be conducted by considering the smart structures.

An  $H_\infty$  control with accurate nonlinear model in driving piezoelectric actuators to resolve the hysteresis problem may be developed.



## REFERENCES

- [1] H. R. Clauser, "Modern Materials Concepts make Structure Key to progress", *Materials Engineering*, Vol. 68, pp. 38-42, Nov. 1968
  
- [2] C. R. Crowe and J. M. Sater, "Smart Aircraft Structure", *The NATO Research and Technology organization, AGARD Conference on Future Aerospace Conference Future Aerospace Technology*, Apr. 14-16, 1997, Paris, France
  
- [3] T. S. Koko, A. Berry, P. Masson, U. O. Akpan, L. Guertin and J. Szabo, "Sensors and Actuators for Active Noise and Vibration Control in Ship Structures", *2<sup>nd</sup> CanSmart Workshop Smart Materials and Structures*, pp1-10, Sept. 14-15, 1999, St Hubert, Qubec, Canada
  
- [4] S. R. Hamilton, D. Nikanpour and S. Lapensee, "Application of Shape Memory alloys as Space Based Actuators and Mechanisms", *2<sup>nd</sup> CanSmart Workshop Smart Materials and Structures*, pp. 123-138, Sept 14-15 1999, St Hubert, Qubec, Canada
  
- [5] D. Z. Li and Z. C. Feng, "Dynamic Properties of Pseudoelastic Shape Memory Alloys", *The 6<sup>th</sup> International Conference on Recent Advances in Structural Dynamics*, pp. 1629-1639, Southhampton England, 1997

- [6] Z. W. Zhong and C. Mei, "Investigation of The Reduction in Thermal Deflection and Random Response of Composite Plates at Elevated Temperatures Using Shape Memory Alloys", pp. 1641-1655, *The 6<sup>th</sup> International Conference on Recent Advances in Structural Dynamics*, pp. 1629-1639, Southampton England, 1997
- [7] D. X. Jiang, M. Muallavey, D. Xu, A. Yousefi-Koma, D. Nikanpour and G. Akras, "Application of Shape Memory alloy for the Vibration Control of A Cantilever Beam", *CanSmart Workshop Smart Materials and Structures*, pp. 31-37, Oct. 2001 St Hubert, Quebec, Canada
- [8] D. X. Jiang, M. Muallavey and D. Nikanpour, "Optimization and Dynamic Analysis of Shape Memory Alloy Strips on Cantilevered Aluminum Beam", *CanSmart Workshop Smart Materials and Structures*, pp. 197-201, Oct. 2001 St Hubert, Quebec, Canada
- [9] D. P. Garg and G. L. Anderson, "Innovations in Structural Damping and Vibration Control Techniques", *CanSmart Workshop Smart Materials and Structures*, pp. 1-12 Sept 197-202, Oct. 2001 St Hubert, Quebec, Canada
- [10] J. P. Coultier, D. L. Don, M. Yalçintaş and P. J. Bierman, "An Experimental Investigation of Electrorheological Material Based Adaptive Plates", *Adaptive Structures and Material Systems*, Vol.35, ASME, 1993
- [11] S. A. Austin, "The Vibration Damping Effect of Electrorheological Fluid", *Journal of Sound and Vibration*, 198, Vol. 115, pp. 136-141, Jan. 1993
- [12] A. Baz J-J Bo, "The Concept and Performance of Active Constrained Layer Damping Treatments", *Sound and Vibration*, 198, Vol. 115, pp. 18-21, Jan. 1993

- [13] N. Wereley, G. M. Madhavan, "Hysteresis Modeling of Semiactive Magnetorheological Helicopter Lag Dampers ", *Journal of Intelligent Material Systems and Structures*, Vol. 10, pp. 624-633, 1999
- [14] J. Crassidis, A. Baz, N. Wereley, "Control of Active Constrained Layer Damping", *Journal of Vibration and Control*, 198, Vol. 6, pp. 113-136, 2000
- [15] N. Mrad and W. J. Bock, "Fiber Optic Sensors For Structural Applications", *2<sup>nd</sup> CanSmart Workshop Smart Materials and Structures*, pp99-112, Sept. 14-15, 1999, St Hubert, Quebec, Canada
- [16] T. Ikeda, "Fundamentals of Piezoelectricity", *Oxford University Press*, 1996
- [17] T. Bailey, J. E. Hubbard, "Distributed Piezoelectric-Polymer Active Vibration Control of a Cantilever Beam." *Journal of Guidance, Control and Dynamics*, Vol. 8, No. 5, pp. 605-611, 1985
- [18] S. E. Burke and J. E. Hubbard, "Active Vibration Control of a Simply Supported Beam Using Spatially Distributed Actuator ", *IEEE Control Systems Magazine*, pp. 25-30, Aug. 1987
- [19] S. E. Burke and J. E. Hubbard, "Distributed Transducer Control Design for Thin Plates", *SPIE Conference on Electro-Optical Materials for Switches Coatings, Sensor Optics and Detectors*, 1307, pp. 222-231, 1990
- [20] C. K. Lee, "Theory of Laminated Piezoelectric Plates for the Design of Distributed Sensors/Actuators. Part I: Governing Equations and Reciprocal Relationships", *J. Acoust. Am.* 87(3), pp. 1144-1157, Mar. 1990

- [21] S. E. Miller, H. Abramovich, and Y. Oshman, "Active Distributed Vibration Control of Anisotropic Piezoelectric Laminated Plates", *Journal of Sound and Vibration*, Vol. 183, no. 5, pp. 797-817, 1995
- [22] D. F. Jones, S. E. Prasad and J. B. Wallace, "The Applications of Advanced Materials in High Technology Society": *Trans Tech Publications*, Vol.1, Chapter: Piezoelectric Materials and Their Applications, 1996
- [23] M. R. Steel, F. Harrison and P. G. Harper, "The Piezoelectric Bimorph: An experimental and theoretical study of its quasistatic response", *J. Phys. D: Appl. Phys.*, Vol. (11), pp. 979-989, 1978
- [24] S. Yoshikawa and T. ShROUT, "Multilayer Piezoelectric Actuators and reliability", *The 34<sup>th</sup> AIAA/ASME/ASCE/AHS/ASC Structures, Structural Dynamics, and Materials Conference AIAA/ASME Adaptive Structures Forum*, Part 6, pp. 3581-3586, Lajolla, CA, Apr. 1993
- [25] K. Uchino, "Reliability of Ceramic Actuators", Proceedings of ISAF 10, East Brunswick, NJ, 1996
- [26] *MST News special issue*, "Recent Developments in Piezoceramic Actuators-Comparison Among USA, Japan and Europe", Nov. 1995
- [27] S. Chandran, V. D. Kugel and L. E. Cross, "Characterization of the Linear and Nonlinear Dynamic Performance of RAINBOW Actuator", Proceedings of ISAF 10, East Brunswick, NJ, 1996
- [28] V. D. Kugel, Q. M. Zhang, B. Xu, S. Chandran and L. E. Cross, "Behavior of Piezoelectric Actuators Under High Field", Proceedings of ISAF 10, East Brunswick, NJ, 1996

- [29] Q. Wang, B. Xu, V. D. Kugel and L. E. Cross, "Characteristics of Shear Mode Piezoelectric Actuators", Proceedings of ISAF 10, East Brunswick, NJ, 1996
- [30] V. D. Kugel, S. Chandran and L. E. Cross, "A Comparative Analysis of Piezoelectric Bending Mode Actuators", SPIE Proceedings on Smart Structures and Materials section: Smart Materials Technologies, no. 3040-90, 1997
- [31] C. D. Near, "Piezoelectric Actuator Technology", *SPIE Smart Structures and Materials Conference*, Feb. 27, 1996
- [32] B. Mukherjee, W. R. Ren, G. Yang, S. Liu and A. J. Massy, "Nonlinear Effects in Piezoelectric Ceramics: Dependence of Properties on Applied Field and Stress", *CanSmart Workshop Smart Materials and Structures*, pp. 169-176, Oct. 2001 St Hubert, Qubec, Canada
- [33] C. J. Swiger and R. L. Forward, "Electronic Damping of Orthogonal Bending Modes in Cylindrical most-Theory", *Journal of Spacecraft and Rockets*, Vol.18
- [34] M. C. Dökmeci, "Theory of Vibrations of Coated, Thermopiezoelectric Laminae", *Journal of Math. Phys.*, Vol. 9, pp. 109-126 Jan. 1978
- [35] M. C. Dökmeci, "Certain Integral and Differential Types of Variational Principles in Nonlinear Piezoelectricity", *IEEE transactions on Ultrasonics, Ferroelectrics and Frequency Control* Vol. (6), pp. 775-787, Nov. 1988
- [36] E. F. Crawley, J. Louis, "Use of Piezoelectric Actuators as Elements of Intelligent Structures." *AIAA Journal* Vol.125, no.10, pp. 1373-1385, Oct. 1989

- [37] E. K. Dimitridis C., R. Fuller, C. A. Rogers “ Investigation on Active Control of Sound Transmission through Elastic Plates using Piezoelectric Actuators Embedded in Composites”, *AIAA Conference*, no. AIAA-89-1062, 1989
- [38] E. K. Dimitridis C., R. Fuller, C. A. Rogers “Piezoelectric Actuators for Distributed Vibration excitation of Thin Plates”, *Journal of Vibration and Acoustics*, Vol. 113, pp. 100-107, Jan. 1991
- [39] J. Pan C H. Hansen and S. D. Snyder, “ A Study of the Response of a Simply Supported Beam to Excitation by a Piezoelectric Actuator”, *Journal of Intelligent Materials and Structures*, Vol.3, Jan 1992
- [40] M. K. Kwak, W. T. Schlaegel and A. Das, “A Testbed for the Dynamics and Control of Flexible Multibody Systems ”, *The 34<sup>th</sup> AIAA/ASME/ASCE/AHS/ASC Structures, Structural Dynamics, and Materials Conference AIAA/ASME Adaptive Structures Forum*, Part 6 Lajolla, CA., pp. 3570-3580, Apr.1993
- [41] S. Kalaycıoğlu, “Dynamic Modeling and Vibration Suppression for Plate Type Structures Using PZT”, *Canadian Space Agency technical Report*, Nov. 14, 1996
- [42] A. Yousefi-Koma and G. Vukovich, “ Experiments on Active Vibration Control of Smart Structures Using Wave Method”, *Canada-US CanSmart Workshop Smart Materials and Structures proceedings*, pp.119-132, Sept. 1998 Montreal Quebec Canada

- [43] H. Allik and T. R. Hughes “ Finite Element Method for Piezoelectric Vibration”, *Journal of Numerical Methods in Engineering* Vol.2, pp. 151-157, 1970
- [44] H. Allik and K. M. Webman and J. T. Hunt “Vibrational response of Sonar Transducers Using Piezoelectric Transducers”, *Journal of Acoustic Society of America*, Vol. 56, pp. 1782-1791, 1974
- [45] H. S. Tzou and M. Gadre, “ Finite Element Modeling of Nonlinear Active and Passive Dampers Applied to Vibration Control”, *Computers and Structures*, Vol. 28, pp. 453-460, 1988
- [46] H. S. Tzou, “Integrated Distributed Sensing and Active Vibration Suppression of Flexible Manipulators Using Distributed Piezoelectrics”, *Journal of Robotic Sys*, Vol.6, pp.745-767, 1989
- [47] W-S. Hwang and C. P. Hyun, “ Finite Element Modeling of Piezoelectric Sensors and Actuators”, *AIAA Journal*, Vol. 31, pp. 930-937, May. 1993
- [48] D. K. Shah W. S. Chan and S. P. Joshi, “Finite Element Analysis of Plates with Piezoelectric Layers”, *The 34<sup>th</sup> AIAA/ASME/ASCE/AHS/ASC Structures, Structural Dynamics, and Materials Conference AIAA/ASME Adaptive Structures Forum*, Part 6 Lajolla, CA., pp. 3189-3197, Apr. 1993
- [49] A. Suleman and V. B. Venkayya, “A Simple Finite Element Formulation for a Laminated Composite with Piezoelectric Layers”, *Journal of Intelligent Materials, Systems and Structures* Vol.6, pp. 776-782, 1995

- [50] ANSYS® Users Manual (version 5.6) *ANSYS Inc.*, South pointe 275 Technology Drive Canonsburg, PA 15317
- [51] Wang H. Jen C.K. “Design and Fabrication of Composites for Static Shape Control: Final Report”, June 1996, *Sensor Tech Limited BM Hi-Tech Division*, Ontario Canada
- [52] S. E. Prasad, J.B. Wallace, B. E. Petit, H. Wang C. K. Jen. Kalaycioğlu, M. Giray “Development of Composite Structures for Static Shape Control.” *SPIE, Far East and Pacific Rim Symposium on Smart Materials, Structures and MEMS*, 1996 (Bangor, India)
- [53] Ş. Utku, “Incorporating Intelligence into Engineering Products: Adaptive Structure”, *Fulbright Lectures*, spring 1998
- [54] R. L. Bravo, A. Vaz, S. Leatherland and M. Dokainish, “Active Vibration Suppression of A smart Truss Structures”, Canada-US *CanSmart Workshop Smart Materials and Structures* proceedings, pp.81-90, Sept. 13-14. 1999 Montreal Quebec Canada
- [55] P. E. Tenzer and B. Mrad, “Application in Inchworm Precision Pointers”, Canada-US *CanSmart Workshop Smart Materials and Structures* proceedings, pp. 77-84, Oct. 2001 Montreal Quebec Canada
- [56] A. Suleman, S. Burns, D. Waecher, R. Blacow, B. Yan and S. E. Prasad “Flexural Brake Mechanism For Inchworm Actuator”, Canada-US *CanSmart Workshop Smart Materials and Structures* proceedings, pp. 125-132, Oct. 2001 Montreal Quebec Canada



- [57] M. Bai and G. M. Lin “ The Development of DSP-Based Active Small Amplitude Vibration Control”, *journal of Sound and Vibration*, 198, Vol. 4, pp. 411-427, 1996
- [58] G. F. Franklin and J. D. Powell, “Digital Control of Dynamic Systems”, *Addison-Wesley Publishing Company*, second edition, 1990
- [59] J. Dosch, D. Leo and J. Inmann, “Modeling and Control for Vibration Suppression of a Flexible Active Structure.” *Journal of Guidance, Control and Dynamics*, Vol. 18, pp. 340-346, Apr. 1995
- [60] V. Nalbantoğlu, *Ph.D. Thesis*, “Robust Control and System Identification for flexible structures” University of Minnesota, 1998
- [61] S. Hanagud, M. W. Obal, and A. J. Calise, “Optimal Vibration Control by the Use of Piezoceramic Sensors and Actuators”, *Journal of Guidance, Control and Dynamics*, Vol.15, no: 5, pp. 1199-1206, Oct. 1992
- [62] S. Devasia, T. Meressi, B. Paden and E. Bayo, “Piezoelectric Actuator Design for Vibration Suppression: Placement and Sizing”, *Journal of Guidance, Control and Dynamics*, Vol. 16, pp. 859-864, Oct. 1993
- [63] M. Sunar and S. S. Rao, “Distributed Modeling and Actuator Location for Piezoelectric Control Systems, *AIAA Journal*, Vol.34 no: 10. 1996
- [64] S. Kalaycıoğlu and A. Misra “Approximate Solutions for Vibrations of Deploying Appendages.” *Journal of Guidance Control and Dynamics, AIAA*, Vol.14 no.2, pp.287-293, 1991

- [65] N. C. Singer, *Ph.D. Thesis*, "Residual Vibration Reduction in Computer Controlled Machines" MIT Artificial Intelligence Laboratory, Feb. 1989
- [66] S. Kalaycıoğlu, M. M. Giray and H. Asmer, "Time Delay Control of Space Structures Using Embedded Piezoelectric Actuators and Fiber optic Sensors." *SPIE's 4<sup>th</sup> Annual Symposium on Smart Structures and Materials*, Mar. 1997
- [67] Y. K. Kang H. C Park, W. Hwang K. S. Han, "Optimum Placement of Piezoelectric Sensor/Actuator for Vibration Control of Laminated Beams", *AIAA Journal*, Vol.34 pp.1921-1925, Sept. 1996
- [68] K. Xu and T. Igusa, "Optimal Placement and Gains of Sensors and Actuators for Feedback Control", *Journal of Guidance, Control, and Dynamics*, Vol. 17, pp. 929-934, Oct. 1994
- [69] W-S Hwang, W. Hwang H. C. Park, "Integration of Composite Design with the Intelligent System Concept", *The 34<sup>th</sup> AIAA/ASME/ASCE/AHS/ASC Structures, Structural Dynamics, and Materials Conference AIAA/ASME Adaptive Structures Forum*, Part 6, pp.3534-3539, Lajolla, CA, Apr.1993
- [70] H-P. Xie, *Msc. Thesis*, "Flexible dynamic Modeling and Control for the Remote Manipulator System Vibrations in the Space Shuttle Remote Manipulator System", Concordia University, 1996
- [71] M. Mollaem, K. Khorasani and R. Patel, "An Integral Manifold Approach for Tip- Position Tracking Control of Flexible Multi- Link Manipulators", *IEEE Transactions on Robotics and Automation*, Vol.13, no.6, Dec. 1997

- [72] P. Ge and M. Jouaneh, "Tracking Control of a Piezoceramic Actuator", *IEEE Transactions on Control Systems Technology*, Vol. 4, pp. 209-216, 1996
- [73] H. Hu and R. B. Mrad, "Preisach Modeling of Hysteresis in a Piezoceramic Actuator", *Canada-US 2<sup>nd</sup> CanSmart Workshop Smart Materials and Structures* proceedings, 1999 Montreal Quebec Canada
- [74] S-B. Choi S.-S. Cho and Y-P. Park, "Vibration and Position Tracking Control of Piezoceramic- Based Smart structures Via QFT", *Journal of Dynamic Systems, Measurement and Control* ,Vol. 121, pp.27-33, Mar. 1999
- [75] B. A. Francis, "Lecture Notes in Control and Information Sciences: A course in  $H_\infty$  Control Theory", Springer-Verlag, 1987
- [76] B. Mei and B. R. Mace, "Reduction of Control Spillover in Active Vibration Control of Distributed Structures using Multioptimal Schemes", *Journal of Sound and Vibration*, Vol.251, pp 184-192, 2002
- [77] Y. Yaman, T. Çalışkan, V. Nalbantoğlu, D. Waechter, E. Prasad, "Active Vibration Control of a Smart Beam", *Canada-US CanSmart Workshop Smart Materials and Structures* proceedings, pp.137-147, Oct. 2001 Montreal Quebec Canada
- [78] Y. Yaman, T. Çalışkan, V. Nalbantoğlu, D. Waechter, D. Ülker, E. Prasad, B. Yan "Active Vibration Control of Smart Plates By Using Piezoelectric Actuators", *ESDA2002 6<sup>th</sup> Biennial Conference on Engineering Systems Design and Analysis*, proceedings, July 2002, Istanbul.

- [79] S. Sivrioğlu, N. Tanaka and I. Yüksek, “ Acoustic Power Suppression of a Panel Structure Using  $H_{\infty}$  Output Feedback Control”, *Journal of Sound and Vibration*, Vol.249, pp 885-897, 2002
- [80] D. Bean and N.J. Wood, “Vortex Control Technique for the Alleviation of Fin Buffet”, *Journal of Aircraft*, Vol. 100, Nov. 1993
- [81] A-M Mc Gowan, L. G. Horta, J. S. Harrison and D. L. Raney, “Research Activities Within NASA’s Morphing Program”, *RTO AVT Specialists Meeting on Structural Aspects of Flexible Aircraft Control RTO MP-36*, Ottawa, Canada, Oct. 1999
- [82] R. W. Moses, “NASA Langley Research Center’s Contributions to International Active Buffeting Alleviation Programs”, *RTO AVT Specialists Meeting on Structural Aspects of Flexible Aircraft Control RTO MP-36*, Ottawa, Canada, Oct. 1999
- [83] A. Suleman “Application of Smart Composites in Panel Flutter Suppression”, Canada-US *CanSmart Workshop Smart Materials and Structures* proceedings, pp.81-90, Sept. 10-11. 1998 Montreal Quebec Canada
- [84] A. Suleman, A. P. Costa, C. Crawford, R. Sedaghati, “Wind Tunnel Aeroelastic Response of Piezoelectric and Aileron Controlled 3-D Wing” *CanSmart Workshop Smart Materials and Structures* Proceedings, Sep. 1998
- [85] K.L. Roger, “Airplane Mathematical Modeling Methods for Active Vibration Control Design”, *AGARD-CP-228*, Aug. 1977

- [86] M.L. Baker, P. J. Goggin and B. A. Winther, "Aeroservoelastic Modeling, Analysis and Design Techniques for Transport Aircraft", *RTO AVT Specialists Meeting on Structural Aspects of Flexible Aircraft Control RTO MP-36*, Ottawa, Canada, Oct. 1999
- [87] J. K. Dürr U. Schmidt, H. W. Zaglauer and J. Becker, "Active Fin Buffeting Alleviation for Fighter Aircraft", *AVT Symposium on Active Control Technology for Enhanced Performance Operation Capabilities of Military Aircraft, Land Vehicles and Sea Vehicles*, 8-11 May 2000, Braunschweig, Germany
- [88] W. Luber and J. Becker, "Flight Control Design Optimization with Respect to Flight and Structural Dynamics Requirements", *AIAA 96-4047, 6<sup>th</sup> AIAA/NASA Symposium on Multidisciplinary Analysis and Optimization*, MDO, Bellevue, WA, USA, Sept. 1996
- [89] W. Luber and J. Becker, "An Integrated Design Procedure for Aircraft Structure Including the Influence of Flight Control System on Aircraft Flutter", *RTO AVT Specialists Meeting on Structural Aspects of Flexible Aircraft Control RTO MP-36*, Ottawa, Canada, Oct. 1999
- [90] F. Nitzche, D. Zimcik, S. Liberatore, "Finite Element Approach for the Design of Control Algorithms for Vertical Fin Buffeting Using Strain Actuation", *AVT Symposium on Active Control Technology for Enhanced Performance Operation Capabilities of Military Aircraft, Land Vehicles and Sea Vehicles*, 8-11 May 2000, Braunschweig, Germany
- [91] MSC/NASTRAN<sup>®</sup> *user manual (version 70.7)*, MacNeal-Schwendler Corporation 815 Colorado Boulevard Los Angeles, CA 90041-1777

- [92] S. Hanagoud and S. M. Noyer, "Offset Piezoceramic Stack Actuators and Acceleration Feedback Control for Tail Buffet Alleviation of a High Performance of Twin Tail Aircraft: Robustness Issues", *AVT Symposium on Active Control Technology for Enhanced Performance Operation Capabilities of Military Aircraft, Land Vehicles and Sea Vehicles, 8-11 May 2000, Braunschweig, Germany*
- [93] R. T. Britt, J. A. Volk, D. R., Dreim and K. A. Applewhite, "Aeroservoelastic Characteristics of the B2 Bomber and Implications for Future Large Aircraft", *RTO AVT Specialists Meeting on Structural Aspects of Flexible Aircraft Control RTO MP-36, Ottawa, Canada, Oct. 1999*
- [94] B. Nam, P. C. Chen and D. D. Liu, "Active Flutter Suppression Using ASTROS with Smart Structures and ASE Modules",
- [95] E. H. Johnson, V. B. Venkayya, "Automated Structural Optimization System (ASTROS), Theoretical Manual", *AFWAL -TR-96-88-3028, Vol.1, Dec., 1988*
- [96] G.D. Padfield, "Helicopter Flight Dynamics", *AIAA Education Series, 1996*
- [97] D. J. Walker and I. Postlethwaite, "Advanced helicopter Flight Control Using two degree of freedom  $H_{\infty}$  optimization", *Journal of Guidance Control and Dynamics, Vol.19, no. 2,pp. 461-468, 1996*
- [98] A. Büter, U-C Ehlert, D. Sachau and E. Breitbach, "Adaptive Blade Concepts Direct Twist and Chamber Variation", *AVT Symposium on Active Control Technology for Enhanced Performance Operation Capabilities of Military Aircraft, Land Vehicles and Sea Vehicles, 8-11 May 2000, Braunschweig, Germany*

- [99] Y. H. Yu, B. Gmelin and W. R. Spettstoesser, "Reduction of Helicopter Blade- Vortex Interaction Noise by Active Rotor Control Technology, *Progress in Aerospace Science* Vol.33, pp. 647-687, 1997
- [100] W. R. Spettstoesser, K. J. Schultz, B. Van der Wall and H. Bucholz, "Helicopter Noise Reduction by Individual Blade Control Selected Flight Test and Simulation Results", *AVT Symposium on Active Control Technology for Enhanced Performance Operation Capabilities of Military Aircraft, Land Vehicles and Sea Vehicles, 8-11 May 2000, Braunschweig, Germany.*
- [101] A. P. Costa, P. A. Moniz and A. Suleman "RPV Design Issues and Integration of Piezoelectric Adaptive Wing", *Canada-US CanSmart Workshop Smart Materials and Structures* proceedings, pp.93-103, Oct. 2001 Montreal Quebec Canada
- [102] A. S. Bicos, J. J. Tracy, "Structural Considerations for Sensor Selection and Placement", SPIE, Vol. 1170 *Fiber Optic Smart Structures and Skins II*, 1989
- [103] R. S. Rogowski, "On-Orbit Structural Health Monitoring", SPIE, Vol. 1370 *Fiber Optic Smart Structures and Skins III*, 1990.
- [104] B. Liang F.P. Sun and C. A. Rogers, " An Impedance Method for Dynamic Analysis of Active Material Systems", *Journal of Vibration and Acoustics*, Vol. 116, pp. 120-128, 1994

- [105] F. Sun, C. A. Rogers, and C. Liang, "Structural Frequency Response Function Acquisition via Electric Impedance Measurement of Surface-Bonded Piezoelectric Sensor/Actuator." *36th. AIAA/ASME/ASCE/AHS/ASC Structures Structural Dynamics, and Materials Conference and AIAA/ASME Adaptive Structures Forum*, Part 5 New Orleans, L. A. April 1995.
- [106] F. P. Sun, Z. Chaudhry, C. A. Rogers and M. Majmundar, "Automated Real-Time Structure Health Monitoring via Signature Pattern Recognition", *SPIE N. American Conference on Smart Structures and Materials, San Diego, CA., 26 Feb.-3 March, 1995*
- [107] F. P. Sun, Z. Chaudhry, C. Liang and C. A. Rogers, "Truss structure Integrity Identification Using PZT Sensor-Actuator", *Journal of Intelligent Material Systems and Structures*, Vol. 6, Jan 1995
- [108] Z. Chaudhry, T. Joseph, F. Sun, and C. A. Rogers, "Local-Area Health Monitoring of Aircraft via Piezoelectric Actuator/Sensor Patches", Paper No. 2443-29, *SPIE 1995 North American Conference on Smart Structures and Materials*, San Diego, CA, 26 Feb.-3 March, 1995.
- [109] Z. Chaudhry F. Lalande, A. Ganino and C. A. Rogers, " Monitoring the Integrity of Composite Patch Structural Repair Via Piezoelectric Actuators/Sensors", *36th. AIAA/ASME/ASCE/AHS/ASC Structures Structural Dynamics, and Materials Conference and AIAA/ASME Adaptive Structures Forum*, Part 5 New Orleans, L. A. April 1995
- [110] W. B. Spillman Jr., P. L. Fuhr, "Impact Detection and Location System for Smart Skin Applications", SPIE, Vol. 1370 *Fiber Optic Smart Structures and Skins III*, 1990.



- [111] P. Tsou, M. H. Shen, “ Structural Damage Detection and Identification Using Neural Network”, *AIAA/ASME/ASCE/AHS/ASC Structures Structural Dynamics, and Materials Conference and AIAA/ASME Adaptive Structures Forum*, Part 6 Lajolla, CA L. A. Apr. 19-22 1993.
- [112] A. S. Islam K. C. Craig “Damage Detection in Composite Structures Using Piezoelectric Materials”, *Journal of Smart Materials and Structures*, Vol. (3), 1994
- [113] S. L. McBride, N. Mrad and P. L. Rochon, “A Feasibility Study For Debris Impact and Damage Assesment In Space Structures”, *2<sup>nd</sup> CanSmart Workshop Smart Materials and Structures*, pp41-45], Sept. 10-11, 1998, St Hubert, Qubec, Canada
- [114] D. S. Nesculescu and R. F. Abreu, “A Feasibility Study For Debris Impact and Damage Assesment In Space Structures”, *2<sup>nd</sup> CanSmart Workshop Smart Materials and Structures*, pp 207-215, Sept. 13-14, 1999, St Hubert, Qubec, Canada
- [115] J.N. Reddy, “Mechanics of Composite Plates”, *CRC Press*, 1997
- [116] Sensor Technologies Limited. *Product Data Sheets*, 2002
- [117] E. L. Wilson, R. L. Taylor, W. P. Doherty and J. Ghaboussi, “ Incompatible Displacement Models”, *Numerical and Computer Methods in Structural Mechanics*, Academic Press Inc., pp. 43-57, 1973
- [118] I. D. Mayergoyz, “A New Scalar Potential Formulation for Three Dimensional Magnetostatic Problems”, *IEEE Transactions on Mechanics*, Vol. MAG-23, No.6, pp.3889-3894, 1984

- [119] S. P. Timoshenko and S. W. Krieger, "Theory of Plates and Shells", McGraw-Hill, second edition, 1959
- [120] R. D. Cook, "Finite Element Modeling for Stress analysis", John Wiley and Sons, *Inc.*, 1995
- [121] D.J. Ewins, "Modal Testing: Theory and Practice", Research Studies Press Limited, England, 1995
- [122] M. M. Maia, J. J. Silva "Theoretical and Experimental Modal Analysis", Research Studies Press Limited, Baldoc England, 1998
- [123] W. K. Gawronski, "Dynamical Control of Structures", Springer-Verlag, 1998
- [124] K. Ogata, "Modern Control Engineering", *Prentice Hall, New Jersey*. Third edition, 1990
- [125] J. Golten, A. Werwer, "Control System Design and Simulation", McGraw-Hill, 1991
- [126] C.E. Rohrs, J. L. Melsa and D.G. Shultz, "Linear Control Systems", McGraw-Hill, 1993
- [127] G. J. Balas, J. C. Doyle, K. Glover A. Packard and R. Smith, " $\mu$  Analysis and Synthesis Toolbox Matlab (version 3) ", *Mathworks Inc.*
- [128] K. J. Aström and T. Höggglund, "Automatic Tuning of PID Controllers", Instrument Society of America, Research Triangle Park, 1988
- [129] J. Doyle, B. Francis and A. Tanenbaum, "Feedback Control Theory.", Mac Millan publishing, New York, 1992

- [130] K. Zhou, J.C. Doyle, K. Glove “Robust and Optimal Control.” Prentice Hall, New Jersey, 1996
- [131] J.W. Dally W. F. Riley, “Experimental stress Analysis”, Mac Graw Hill Inc., 1978
- [132] P. H.Wirsching T. L. Paez and K. Ortiz, “Random Vibrations: Theory and Practice”, John Wiley and Sons, Inc., 1995
- [133] T. J. Cavicchi, “Digital Signal Processing”, John Wiley and Sons, Inc., 2000
- [134] D. E. Newland, “Random Vibrations and Spectral Analysis”, Longman Press, 1975
- [135] O. J. Aldraihem, T. Singh and Wetherhold, “Optimal Size and Location of Piezoelectric Actuators/Sensors”, *Journal of Guidance, Control, and Dynamics*, Vol. 23 no. 3 pp. 509, May-June 2000.
- [136] V. Nalbantoğlu, G. Balas, P. Thompson, “The role of performance criteria selection in the control of flexible structures”, AIAA Guidance and Navigation and Control Conference, San Diego, CA, pages 1-9,1996.

## APPENDIX A

### PIEZOELECTRIC, DIELECTRIC AND MATERIAL PROPERTIES OF BM500 PZT PATCHES

The precise modeling and the description of the smart materials ultimately affect the accuracy of the smart structure models. The properties of a piezoelectric patch depend on the direction of the applied electric field, displacement, stress and strain. This appendix gives the properties of the piezoelectric patch, BM500 produced by Sensor Technologies Limited of Canada. All the data related to the dielectric and piezoelectric constants of the piezoelectric patch which is considered throughout the thesis, is obtained from the PZT in mechanically clamped configuration [51,52,116]. A three dimensional piezoelectric model requires the specification elastic coefficient matrix, piezoelectric and the permittivity matrix that relates the scalar potential  $\psi$  to electric field,  $\xi$  through equation (3.1.4).

### A.1. Dielectric Constant, $[\epsilon]^s$ (Relative Permittivity)

The dielectric constant is the ratio of the permittivity of the material to the free permittivity free space and determined to be

$$[\epsilon]^s = \begin{bmatrix} 15.32 \times 10^{-9} & 0 & 0 \\ 0 & 15.32 \times 10^{-9} & 0 \\ 0 & 0 & 15.05 \times 10^{-9} \end{bmatrix} \text{ (F/m}^2\text{)}$$

Here, superscript 's' indicates the constants are evaluated at constant strain.

### A.2. Piezoelectric Stress Constant Matrix

The piezoelectric stress constant matrix is a  $6 \times 3$  matrix that relates the electric field to stress. The configuration of the actuator influences the determination of the piezoelectric constant matrix. Depending on the application two data sets namely, free and mechanically clamped data sets are available. During the study, the data for the mechanically clamped piezoceramic was used.

$$[e]^T = \begin{bmatrix} 0 & 0 & -5.4 \\ 0 & 0 & -5.4 \\ 0 & 0 & 15.8 \\ 0 & 0 & 0 \\ 0 & 12.3 & 0 \\ 12.3 & 0 & 0 \end{bmatrix}, \text{ (Coulomb/m}^2\text{)}$$

### A.3. Stiffness Matrix

The stiffness matrix incorporating the anisotropic material properties of the actuators are given below

$$[C_o] = \begin{bmatrix} 1.21 \times 10^{11} & 7.54 \times 10^{10} & 7.52 \times 10^{10} & 0 & 0 & 0 \\ & 1.26 \times 10^{11} & 7.50 \times 10^{10} & 0 & 0 & 0 \\ & & 1.11 \times 10^{11} & 0 & 0 & 0 \\ & & 2.30 \times 10^{10} & 2.11 \times 10^{10} & 0 & 0 \\ & \text{symmetric} & & 2.30 \times 10^{10} & 2.26 \times 10^{10} & 0 \\ & & & & & 2.26 \times 10^{10} \end{bmatrix},$$

(N/m<sup>2</sup>)

### A4. Curie Temperature:

The Curie temperature is the upper thermal bound of the piezoceramic material. At this temperature the crystal structure of the material changes from asymmetric to symmetric (nonpiezoelectric). Curie Temperature of BM500 is 193 °C.

### A5. Other Properties :

Thermal expansion Coefficient ( $\alpha_{11}$ ) and the density of the piezoelectric patch are taken to be  $\alpha_{11} = 4.0 \mu\epsilon / ^\circ\text{C}$  and  $\rho = 7730 \text{kg/m}^3$  respectively. Furthermore, the emissivity of the actuator is considered to be unity throughout the study.

## APPENDIX B

### THE EFFECTS OF ELEMENT TYPE SELECTION ON THE NATURAL FREQUENCIES

This section compares the effects of element type selection for the aluminum plate strips by calculating the natural frequencies of the structures. During the analysis, the plates are modelled in cantilevered configurations and the finite element results obtained by using ANSYS® (v.5.6) are compared with those available in the literature. In the analysis of the structures, three finite element model are considered each of which contains prismatic, SOLID45 and SOLID95 or shell elements, SHELL93 to model plates. Table B-1 compares the first three theoretical frequencies of a 500×50×2mm aluminum plate strip obtained by using finite element method together with the results available in the literature for the beam.

Table B-1 the first three theoretical frequencies of a 500×50×2mm aluminum plate

Referance(*)	FEM <sup>1</sup>	FEM <sup>2</sup>	FEM <sup>3</sup>
Frequencies	frequencies	Frequencies	Frequencies
6.5209	6.6726	6.5692	6.6482
40.864	41.720	41.097	41.631
114.43	112.09	114.94	110.99

(FEM1: Model with 126 nodes and 40 SOLID45 element, FEM2: Model with 165 nodes and 40 SHELL93 element, FEM3: Model with 393 nodes and 40 SOLID 98 elements),(\*): Formulas for Natural Frequencies and Mode Shapes, Van Nostrand and Reinhold Company, 1979.

It can be seen from the Table B-1 that The quadratic elements have the closer convergence than the linear solid element but the deviations between the model results remains in the order of 1.5 percent. Therefore, the linear elements with extra displacement functions can be considered for the aluminum plate strips within the accuracy of 1-2 percent for the modal analysis.





## APPENDIX C

### THE COMPUTER CODES FOR SYSTEM IDENTIFICATION

This appendix is prepared by using Matlab<sup>®</sup> software, therefore the subroutines and equations given in the following pages are provided in Matlab<sup>®</sup> (v.6.0) syntax

#### C-1. Nonparametric Identification

%input file recorded interms of the input and output must be in the workspace use the Labview Program shown in Figure 5.6 for data acquisition

% tprm1 and tprm2 are the truncation parameters for the experimental data

%nlap is the number of overlap (the number less than window length)

% tprm1 and tprm2 are the truncation parameters for the experimental data

% this is done to find the useful data set for the nonparametric identification

%flnm name of the file

%smplr is the sampling rate

flnm=input('the name of the data set(no extension please): ');

smplr=input('sampling rate is: ');

nlap=input('number of overlap is: ');

```

tim=input('duration of the experiment is: ');
tprm1=3;
tprm2=146;

wsh1=input(' press 1 to see the input plot for 10 sec: ');
while wsh1>0;
figure;
time=linspace(1,10,10*smp1r);
plot(time,flnm(1:10*smp1r,1)),xlabel('Time (s)'),ylabel('Input (V)')
%figure;
%plot(xb1(1:10*4096)),axis([1 10*4096 -10 10]);
wsh1=input('press 0 to see next plot: ');
end
wsh2=input('press 1 to see the output plot:');
while wsh2>0;
figure;
time=linspace(1,120,tim*smp1r);
plot(time,flnm(:,2)),xlabel('Time (s)'),ylabel('response (Volts)')
wsh2=input('press 0 to see next plot: ');
end
% the spectral analysis by using the time domain data
[P,F] = spectrum(flnm(:,1),flnm(:,2),smp1r,nlap,[],smp1r);

wsh3=input('press 1 to see the Power Spectral Density of the input Signal : ');
while wsh3>0;
    dump=P(:,1);
    dumf=2*pi*F(tprm1:tprm2);
    dump1=dump(tprm1:tprm2);

```

```

tf_estd=vpck(dump1,dumf);
figure;
vplot('liv,lm',tf_estd),xlabel('Frequency (rad/sec)'),ylabel('Power'),title('Power Spectral
density of the Input signal');
wsh3=input('press zero to see next plot: ');
end

```

```

wsh4=input('press 1 to see the Power Spectral Density of the Output Signal : ');
while wsh4>0;
dump=P(:,2);
dumf=2*pi*F(tprm1:tprm2);
dump1=dump(tprm1:tprm2);
tf_estd=vpck(dump1,dumf);
figure;
vplot('liv,lm',tf_estd),xlabel('Frequency (rad/sec)'),ylabel('Power'),title('Power Spectral
Density of Output signal');
wsh4=input('press zero to see next plot: ');
end
wsh5=input('press 1 to see the bode plot for the experimental data : ');
while wsh5>0;
Fr = F*2*pi;
dump=P(:,4);
dumf=2*pi*F(tprm1:tprm2);
dump1=dump(tprm1:tprm2);
tf_estd=vpck(dump1,dumf);
tf_est = vpck(P(:,4),Fr);
figure;
vplot('bode',tf_estd);

```

```

wsh5=input('press zero to see next plot: ');
end
wsh6=input('press 1 to see the frf for the experimental data :');
while wsh6>0;
figure;
var1=abs(dump1);
ax=[1 140 1e-3 1e-1];
semilogy(F(tpm1:tpm2),var1),axis(ax),xlabel('Frequency (Hz)'),ylabel('Response
(V)'),grid;
wsh6=input('Press 0 to see next plot: ');
end
wsh7=input('Press 1 to see the system identification results for the experimental data:')
while wsh7>0;
TFx=tf_estd;
figure;
% the least square curve fitting
runfitsys
%print -dps beam_id.eps
[A,B,C,D] = unpck(sys);
sysident10=sys;
D=0;
sysn=pck(A,B,C,D);
[num2,den2]=ss2tf(A,B,C,D);
[num,den] = ss2tf(A,B,C,D); % state space to transfer function
om = logspace(0,3.5,1000);
sys1 = frsp(sysident10,om);
sys2 = frsp(sysn,om);

```

```

wsh7=input('Press zero to see next plot: ');

end

wsh10=input('Press 1 to see the system identification results for the experimental data,
while wsh10>0;
A1=[abs(spoles(sysident))/(2*pi)];
A2=[abs(spoles(sysfem))/(2*pi)];
p1=sortrows(A1);
p2=sortrows(A2);
freqs=[p1 p2]
wsh10=input('Press 0 to continue: ');
end

wsh12=input('press 1 to see the nyquist plot of the experimental model: ')
while wsh12>0
[AI,BI,CI,DI]=unpck(sysident);
[numi,deni]=ss2tf(AI,BI,CI,DI);
figure;
nyquist(tf(numi,deni),om2),axis(ax2);
wsh12=input('Press 0 to continue: ');
end

```

## C-2 The subroutine for the least square curve fitting technique

```
%TFx =xtract(sel(TFsw41,1,1),1.1*2*pi,30*2*pi);%fit from 20 rad/sec to 188 rad/s
```

```
ord = input('Input order of the fit: ');
```

```
while ord>0
```

```
    sys = mfitsys(TFx,ord);
```

```
    sysg = frsp(sys,TFx);
```

```
    rofd(spoles(sys))
```

```
    for i = 1:1
```

```
        vplot('bode',sel(sysg,i,1),':',sel(TFx,i,1),'w')
```

```
    % subplot(211)
```

```
        title(num2str(i))
```

```
        pause
```

```
    end
```

```
    ord = input('Input order of the fit (Enter a negative number to exit): ');
```

```
end
```

## **APPENDIX D**

### **THE COMPUTER CODE USED IN REAL TIME IMPLEMENTATION OF $H_{\infty}$ CONTROLLER**

In this thesis, the  $H_{\infty}$  controller designed for the active vibration control of the smart beam is implemented by using the smart controller unit SS10. The controller unit, implements the  $H_{\infty}$  controller by using the computer code written in C language. This appendix gives the data, which is necessary for the real-time implementation of the  $H_{\infty}$  controller used for vibration control of the smart beam.

#### **D-1 The $H_{\infty}$ CONTROLLER**

The application of the  $H_{\infty}$  controller design technique resulted a 6<sup>th</sup> order controller. By using standard model reduction techniques the controller is further reduced to 4<sup>th</sup> order. The system model, which is necessary for the implementation of the controller unit, is given as follows.

The system matrix for the controller is,

$$A = \begin{bmatrix} -4.2407 & 25.6641 & -22.3859 & 11.4441 \\ -25.6641 & -0.5122 & 8.9394 & -4.4089 \\ -22.3859 & -8.9394 & -831.0786 & 535.6031 \\ 11.4441 & 4.4089 & 535.6031 & -374.8691 \end{bmatrix}$$

The input, output and direct transmission vectors are found to be

$$B^T = \{-6.9707 \quad -2.2874 \quad -19.1037 \quad 9.6078\}$$

$$C = \{6.9707 \quad -2.2874 \quad 19.1037 \quad -9.6078\}$$

$$D = \{-0.0019\}$$

## D-2 The Computer code

The controller is implemented by using the computer code written in C language. The computer code developed for this purpose is provided in C syntax.

```

/*=====
*
*           This program is used to test 8-ADC and
4-DAC of SBC0486
*
C version
*
*           GNU Development Tools of
the Redhat linux 6.2*
*=====
*
*/
#include <stdio.h>
#include <time.h>
#include <sys/io.h>

```



```

#include <sys/perm.h>
#include <stdlib.h>

#include <termios.h>
#include <unistd.h>

#include <signal.h>

#include <sys/types.h>
#include <sys/stat.h>
#include <fcntl.h>
#include <termios.h>
#include <string.h>
#include <time.h>

/***** Register Address, ADC & DAC of SBC0486 *****/

#define CFGINDEX 0x350
#define CFGPORT 0x351
#define ADCDONE 0x352
#define DACPORT 0x353
#define ADC_CONTROL 0x356
#define ADC_DATA_LOWBYTE 0x356
#define ADC_DATA_HIBYTE 0x357

#define HI_CLAMP_PT 4095 /* high limit for output */
#define LO_CLAMP_PT 0 /* low limit for output */

#define TIME_LIMIT 20

void Initialize_IOPort(void);
void Initialize_CFGINDEX_CFGPORT(void);

void DAC_Update(int);
int ADC_Sample(void);
void Initialize_DAC(void);

```

```

/**** End of Register Address, ADC & DAC of SBC0486 ****/

unsigned int DAC_Port = 0x3000;
unsigned int ADC_Port = 0x48;

void AD_DA_test(void);
void Choose_test_channel(void);
void Show_Channel(void);

/***** End Viscous Damping Vibration *****/
/***** Signal of Linux *****/
long int Cycle_number=0;
void SigHandler(int SigNum)
{
    Initialize_DAC();

printf("\n Cycle_number=%ld.", Cycle_number);
Cycle_number=0;
    Choose_test_channel();

    Show_Channel();

    alarm(TIME_LIMIT); /* Exit if it exceeds certain time */

printf("\nTest will last 30 seconds!\n");

    return;
}

void Choose_test_channel(void)
{
    int ch;
    struct termios old, new;

    tcgetattr(0, &old);
    new = old;

```

```

new.c_lflag &= ~ICANON;

new.c_cc[VMIN] = 1;
new.c_cc[VTIME] = 0;

tcsetattr(0, TCSANOW, &new);

/*
0x48 -- ADC 0;
0x49 -- ADC 1;
0x4A -- ADC 2;
0x4B -- ADC 3;
0x4C -- ADC 4;
0x4D -- ADC 5;
0x4E -- ADC 6;
0x4F -- ADC 7;

0x3000 -- DAC 0
0x7000 -- DAC 1
0x0b000 -- DAC 2
0x0f000 -- DAC 3
*/

/*****      Input Channel      *****/

printf("\nInputing 'n' will end the AD-DA test.");
printf("\nInput the Channel Number of STRAIN GAUGE INPUT or n:");

do {
    ch = getchar();
    printf("\n Your INPUT is : %c\n", ch);

    }while((ch != '1') && (ch != '2') && (ch != '3') && (ch !=
'4')
        && (ch != '5') && (ch != '6') && (ch != '7') && (ch !=
'8') && (ch != 'n'));

```

```

        if(ch == '1') ADC_Port = 0x48;
        else if(ch == '2') ADC_Port = 0x49;
        else if(ch == '3') ADC_Port = 0x4A;
        else if(ch == '4') ADC_Port = 0x4B;
        else if(ch == '5') ADC_Port = 0x4C;
        else if(ch == '6') ADC_Port = 0x4D;
        else if(ch == '7') ADC_Port = 0x4E;
        else if(ch == '8') ADC_Port = 0x4F;
        else if(ch == 'n') {
                tcsetattr(0, TCSANOW, &old);
                exit(EXIT_SUCCESS);
        }

printf("\nInputing 'n' will end the AD-DA test.");
printf("\nInput the Channel Number of OUTPUT or n:");
do {
        ch = getchar();
        printf("\n Your INPUT is : %c\n", ch);
        }while((ch != '1') && (ch != '2') && (ch != '3') && (ch !=
'4') && (ch != 'n'));

        if(ch == '1') DAC_Port = 0x3000;
        else if(ch == '2') DAC_Port = 0x7000;
        else if(ch == '3') DAC_Port = 0xb000;
        else if(ch == '4') DAC_Port = 0xf000;
        else if(ch == 'n') {
                tcsetattr(0, TCSANOW, &old);
                exit(EXIT_SUCCESS);
        }

        tcsetattr(0, TCSANOW, &old);
}

void Show_Channel(void)
{

```

```

        if (ADC_Port == 0x48) printf("\n Sampling ADC 0 or Strain
Gauge Input 1 \n");
        else if (ADC_Port == 0x49) printf("\n Sampling ADC 1 or Strain
Gauge Input 2\n");
        else if (ADC_Port == 0x4A) printf("\n Sampling ADC 2 or Strain
Gauge Input 3\n");
        else if (ADC_Port == 0x4B) printf("\n Sampling ADC 3 or Strain
Gauge Input 4\n");
        else if (ADC_Port == 0x4C) printf("\n Sampling ADC 4 or Strain
Gauge Input 5\n");
        else if (ADC_Port == 0x4D) printf("\n Sampling ADC 5 or Strain
Gauge Input 6 \n");
        else if (ADC_Port == 0x4E) printf("\n Sampling ADC 6 or Strain
Gauge Input 7\n");
        else if (ADC_Port == 0x4F) printf("\n Sampling ADC 7 or Strain
Gauge Input 8\n");
        else printf("\n  ADC-Port address is wrong! \n");

        if (DAC_Port == 0x3000) printf("\n Updating DAC 0 or OUTPUT
1\n");
        else if (DAC_Port == 0x7000) printf("\n Updating DAC 1 or OUTPUT
2\n");
        else if (DAC_Port == 0xb000) printf("\n Updating DAC 2 or OUTPUT
3\n");
        else if (DAC_Port == 0xf000) printf("\n Updating DAC 3 or OUTPUT
4\n");
        else printf("\n  DAC-Port address is wrong! \n");

        return;
    }

void Register_Signal(void)
{
    if(signal(SIGALRM, SigHandler) == SIG_ERR)
    {
        printf("\nCouldn't register signal handler!\n");
        exit(EXIT_FAILURE);
    }
}

```

```

    }
}

/***** Signal of Linux *****/

int main( void )
{
    Register_Signal();

    Initialize_IOPort();
    Initialize_CFGINDEX_CFGPORT();
    Initialize_DAC();

    AD_DA_test();

    return 0;
}

void Initialize_IOPort()
{
    if((iopl(3)) == -1)
    {
        printf("\nThe iopl(...) is not called rightly!\n");
        exit(EXIT_FAILURE);
    }

    printf("\nInitialize_IOPort()...passed!\n");
}

void Initialize_CFGINDEX_CFGPORT()
{
    unsigned int OriginalState;

    outb(0x00, CFGINDEX);          /* CFGINDEX Register of SBC0486 */

    OriginalState = inb(CFGPORT); /* CFGPORT Register of SBC0486 */
}

```

```

/* LED4 OFF, RS232 for COM1 and COM2 of SBC0486 */
outb((OriginalState & 0x0f), CFGPORT);

printf("\nInitialize CFGINDEX & CFGPORT...passed!\n");
printf("\nLED4 OFF, RS232 for COM1 and COM2 of SBC0486\n");

}

void Initialize_DAC()
{
    DAC_Update(2047); /* DAC of SBC0486 = 2.5v, High Voltage = 0v */
}

void AD_DA_test()
{
    FILE * fp;
    int AD_Input = 0;
    int DA_OUT = 0;

    float y = 0.0;
    float a11 = -4.2407;
    float a12 = 25.6641;
    float a13 = -22.3859;
    float a14 = 11.4441;
    /* float a15 = 10.8400 ;
    float a16 = -0.872;*/
    float a21 = -25.6641;
    float a22 = -0.5122;
    float a23 = 8.9394;
    float a24 = -4.4089;
    /* float a25 = 7.1140;
    float a26 = -0.2668;*/
    float a31 = -22.3859;
    float a32 = -8.9394;
    float a33 = -831.0786;
    float a34 = 535.6031;

```

```
/* float a35 = -0.3028;
float a36 = -0.0786;*/
float a41 = 11.4441;
float a42 = 4.4089;
float a43 = 535.6031;
float a44 = -374.8691;
/* float a45 = ;
float a46 = ;
float a51 = ;
float a52 = ;
float a53 = ;
float a54 = ;
float a55 = ;
float a56 = ;
float a61 = ;
float a62 = ;
float a63 = ;
float a64 = ;
float a65 = ;
float a66= ;
float B5 = ;
float B6 =;*/
float c1 =6.9707;
float c2 =-2.2874;
float c3 = 19.1037;
float c4 = -9.6078;
float x1 = 0;
float x2 = 0;
float x3 = 0;
float x4 = 0;
/*float x5 = 0;
float x6 = 0;*/
float D = -0.0019;
float B1 = -6.9707;
float B2 = -2.2874;
float B3 = -19.1037;
float B4 = 9.6078;
```



```

float ddt = 1.0/540.0;

float AD_I;

printf("\nAD-DA test!\n");

Choose_test_channel();

Show_Channel();
Cycle_number=0;
printf("\nTest will last 30 seconds!\n");

alarm(TIME_LIMIT); /* Exit if it exceeds certain time */

Initialize_DAC();

fp=fopen("tarkan.txt","wt");
do {

/* Strain Gauge senses the amplitude of vibration displacement
*
* Assume dt = 1*/

AD_Input = ADC_Sample();
AD_I = 20*(AD_Input -800); /* There is bias on the strain
gage */

/****** Make DAC output be in 0 -- 4095 *****/
/****** H_infinity algorithm *****/
x1 = x1 + (a11*x1 + a12*x2 + a13*x3 + a14*x4 /*+ a15*x5 + a16*x6 */+
B1*AD_I)*ddt;
x2 = x2 + (a21*x1 + a22*x2 + a23*x3 + a24*x4 /*+ a25*x5 + a26*x6 */+
B2*AD_I)*ddt;
x3 = x3 + (a31*x1 + a32*x2 + a33*x3 + a34*x4 /*+ a35*x5 + a36*x6 */+
B3*AD_I)*ddt;

```

```

    x4 = x4 + (a41*x1 + a42*x2 + a43*x3 + a44*x4 /*+ a45*x5 + a46*x6*/ +
B4*AD_I)*ddt;
/* x5 = x5 + (a51*x1 + a52*x2 + a53*x3 + a54*x4 + a55*x5 + a56*x6 +
B5*AD_I)*ddt;
    x6 = x6 + (a61*x1 + a62*x2 + a63*x3 + a64*x4 + a65*x5 + a66*x6 +
B6*AD_I)*ddt;
*/
    y = c1*x1 + c2*x2 + c3*x3 + c4*x4 /*+ c5*x5 +c6*x6*/ + D*AD_I;
    DA_OUT = 2047 + y;

    if(DA_OUT > 4095) DA_OUT = 4095;
    else if(DA_OUT < 0) DA_OUT = 0;

printf("input=%d...output= %d\n",AD_Input,DA_OUT);
fprintf(fp,"\n input= %d ... output=%d",AD_Input,DA_OUT);
    DAC_Update(DA_OUT);

Cycle_number++;
    }while (1);
fclose(fp);
    return;
}

void DAC_Update(int DA_Output)
{
    int loop;
    int DACDATA;
    unsigned int Test_bit;

    /****** MAX525 DAC of SBC0486 Start *****/
    /****** Initiate the DACCS and DACCLK of DACPORT *****/
    outb(0x06, DACPORT); /** DACCS = 0; DACCLK = 1 **/

    /* 0 to 0V; 2047/2048 to 2.5V; 4095 to +5V for DAC of SBC0486 */
    /* Load input register A, all DAC register updated of MAX525 */

```

```

/* 0x3000 -- DAC 0
   0x7000 -- DAC 1
   0x0b000 -- DAC 2
   0x0f000 -- DAC 3
*/

DA_Output = DA_Output | DAC_Port;

Test_bit = 0x8000;

/***** Send data to D/A serially *****/
for(loop = 15; loop >= 0; loop --)
{
    if(Test_bit & DA_Output) DACDATA = 0x01;
    else DACDATA = 0x00;
    outb((DACDATA | 0x04), DACPORT); /* DACCS = 0; DACCLK = 0 */
    Test_bit = Test_bit >> 1;
    outb((0x06 | DACDATA), DACPORT); /* DACCS = 0; DACCLK = 1 */
}
outb(0x02, DACPORT); /* DACCS = 1; DACCLK = 1 */
/***** DAC of SBC0486 end *****/
}

int ADC_Sample()
{
    int AD;

    /***** MAX197 ADC of SBC0486 *****/
    /** Channel 1/AD0; -5v - +5v; Aquisition Mode: Internally controlled
    **/
    /** AD Control register, and start aquisition and conversion of AD
    **/
    /* 0x48 -- ADC 0;
       0x49 -- ADC 1;
       0x4A -- ADC 2;
       0x4B -- ADC 3;
       0x4C -- ADC 4;

```

```

    0x4D -- ADC 5;
    0x4E -- ADC 6;
    0x4F -- ADC 7;
*/

outb(ADC_Port, ADC_CONTROL);

/***** Sample data from A/D 0 *****/
while(!(0x01 & inb(ADC_DONE)))
    { /* waiting for A/D conversion completion */
    }
AD = inb(ADC_DATA_HIBYTE);
AD = AD << 8;
AD += inb(ADC_DATA_LOWBYTE);
if(AD & 0x8000) AD -= 65535; /* Adjust minus number */
return (AD);
}

```

## VITA

The author was born in 1969 at Ankara, Turkey. He received his B.Sc. and Msc degree in Department of Aeronautical Engineering from METU in 1992 and 1995 respectively. He worked as an research asistant at the department of aeronautical engineering, METU from 1992 to 2002. His main areas of interest are theoretical and experimental stress analysis, structural dynamics, system identification, active vibration control and active aeroelastic control by using smart materials specifically piezoelectric ceramics.